Научном већу Института за физику у Београду

Предмет: Покретање поступка за избор у звање научни сарадник

Молим Научно веће Института за физику у Београду да покрене поступак за мој избор у звање научни сарадник.

У прилогу достављам:

1. Мишљење руководиоца лабораторије са предлогом комисије за избор у звање;
2. Биографске и стручне податке;
3. Преглед научне активности;
4. Елементе за квалитативну оцену научног доприноса;
5. Елементе за квантитативну оцену научног доприноса;
6. Списак објављених радова;
7. Податке о цитираности;
8. Копије објављених радова;
9. Копију докторске дисертације;
10. Уверење о стеченом високом образовању трећег степена докторских студија.

Београд,

07.04.2022.

С поштовањем,

Бокић Бојана

Бојана Бокић

Научном већу Института за физику у Београду

Предмет: Мишљење руководиоца лабораторије о избору др Бојане Бокић у звање научни сарадник

Др Бојана Бокић је запослена у Лабораторији за квантну биофотонику Института за физику у Београду. У истраживачком раду бави се квантном оптиком са посебним интересовањем за нелинеарну фотонику и примену комплексних структура у истраживањима из области физике материјала и оптичких телекомуникација. С обзиром да испуњава све предвиђене услове у складу са Правилником о поступку, начину вредновања и квантитативном исказивању научноистраживачких резултата истраживача МПНТР, сагласан сам са покретањем поступка за избор др Бојане Бокић у звање научни сарадник.

За састав комисије за избор др Бојане Бокић у звање научни сарадник предлажем:

[1] др Бранко Коларић, научни саветник, Институт за физику у Београду,

[2] др Драгана Јовић Савић, научни саветник, Институт за физику у Београду,

[3] др Душан Арсеновић, научни саветник, Институт за физику у Београду,

[4] проф. др Ђорђе Спасојевић, редовни професор Физичког факултета Универзитета у Београду.

Душан Арсеновић

др Душан Арсеновић

научни саветник / руководилац Лабораторије за квантну биофотонику

2. БИОГРАФСКИ И СТРУЧНИ ПОДАЦИ

Кандидат Бојана Бокић рођена је у Београду 05.07.1981. Основну школу и гимназију, природно-математички смер, завршила је у Неготину 2000. године. Исте године уписује Електротехнички факултет Универзитета у Београду. Дипломира 2008. године на студијском програму Електротехника и рачунарство – модул Наноелектроника, оптоелектроника и ласерска техника, одбранивши дипломски рад на тему *Примена ласера у медицини – Дијагностичке технике*, чиме стиче звање дипломираног инжењера електротехнике. 2010. године завршава Мастер академске студије на Електротехничком факултету Универзитета у Београду, на студијском програму Електротехника и рачунарство – модул Биомедицински и еколошки инжењеринг, одбранивши мастер рад на тему *Примена ласера и других снопних техника у дијагностичке и терапеутске сврхе у биомедицини.*

Од 1.октобра 2010. је запослена у Центру за фотонику Института за физику, као истраживач-приправник у Лабораторији за атомску и квантну оптику, са ангажовањем на пројекту основних истраживања ОИ171038 Министарства просвете, науке и технолошког развоја под називом *Холографске методе генерисања специфичних таласних фронтова за ефикасну контролу кохерентних ефеката у интеракцији атома и ласера*, под руководством др Дејана Пантелића. 2011. године кандидат уписује Докторске академске студије на Физичком факултету Универзитета у Београду, на смеру Квантна оптика и ласери, под менторством др Бранислава Јеленковића. Од 2013-2014. године била је ангажована на билатералном пројекту са Савезном Републиком Немачком под називом *Пропагација и локализација светлости у системима са комплексним фотоничним решеткама* под руководством др Драгане Јовић Савић.

Њена област истраживања је квантна оптика са посебним интересовањем за нелинеарну фотонику и примену комплексне светлости у истраживањима из области физике материјала и оптичких телекомуникација. Резултате свог истраживања публиковала је у шест радова категорије М21, два рада категорије М23, шест саопштења са међународног скупа категорије М33 и М34, и три саопштења са скупа од националног значаја категорије М64.

3. ПРЕГЛЕД НАУЧНЕ АКТИВНОСТИ

Кандидат Бојана Бокић се у свом научном раду бави проблематикама испитивања феномена који се односе на процес интеракције ласерског зрачења и специфичних таласних фронтова са материјалима различитог порекла.

У оквиру пројекта ОИ171038 под називом *Холографске методе генерисања специфичних таласних фронтова за ефикасну контролу кохерентних ефеката у интеракцији атома и ласера* Бојана Бокић је била ангажована на истраживањима фотонских структура биолошког порекла где је испитивана спектрална и просторна селективност нанометарских структура на површини крила лептира *Apatura ilia* и *Apatura iris*. Показано је да крило веома интензивно рефлектује светлост у уском спектралном и угаоном интервалу и даје путоказ за реализацију спектрално и угаоно селективних филтера. Ово истраживање је разултирало радом који је објављен у водећем међународном часопису:

- D. Pantelić, S. Ćurčić, S. Savić-Šević, A. Korać, A. Kovačević, B. Ćurčić, and **B. Bokić**, "*High angular and spectral selectivity of purple emperor (Lepidoptera: Apatura iris and A. ilia) butterfly wings*", Optics Express **19**, 5817 (2011).
  DOI: 10.1364/OE.19.005817
  ISSN: 1094-4087; **IF**: 3.669;

У оквиру истог пројекта Бојана је радила и на експерименту испитивања ефеката фемтосекундног ласерског снопа, таласне дужине из ултраљубичастог дела спектра и фреквенције 76 MHz, на два типа танких филмова на супстрату силицијума – једнослојном танком филму алуминијума, и вишеслојном танком филму који се састоји од пет алуминијум/титанијум бислојева (укупне дебљине 130 nm). Модификација површина мета је урађена сноповима ниских флуенци и различитим временима озрачавања. Формиране су периодичне површинске наноструктуре, периода око 315 nm и висине 45 nm. Ови експериментални резултати су објављени у водећем међународном часопису:

- Aleksander G. Kovačević, Suzana M. Petrović, **Bojana M. Bokić**, Biljana M. Gaković, Miloš T. Bokorov, Borislav Z. Vasić, Radoš B. Gajić, Milan S. Trtica, Branislav M. Jelenković, „*Surface nanopatterning of Al/Ti multilayer thin films and Al single layer by a low-fluence UV femtosecond laser beam*", Applied Surface Science **326**, str. 91-98 (2015).
  DOI: 10.1016/j.apsusc.2014.10.180
  ISSN: 0169-4332; **IF**: 6.182;

У оквиру билатералног пројекта са Немачком, под називом „*Пропагација и локализација светлости у системима са комплексним фотоничним решеткама*" Бојана Бокић је радила на експерименту са Еиријевим сноповима.

Главни циљ пројекта био је испитивање пропагације и локализације недифрагујућих снопова, креирање различитих фотонских структура са дефектима или кластерима дефеката као и различитих неуређених и квази-периодичних решетки а у циљу изучавања пропагације и локализације светлости у таквим структурама, и стварања директне везе са процесом процесуирања информација.

Бојана је изучавала, теоријски и експериментално, активну контролу самоубрзања Еиријевих снопова са оптички индукованим таласоводима, који садрже и различите типове

дефеката. Испитивања су рађена прво са једнодимензионалним Еиријевим снопом у кристалу литијум баријум ниобата. У кристалу су ласером уписивани различити таласоводи са периодичном променом индекса преламања и одговарајућим дефектима. Разматрала је како позитивни и негативни дефекти утичу на закривљење као и на убрзање зрака. Резултати су показали да са одговарајућом модификацијом индекса преламања, убрзање Еиријевих снопова може бити редуковано до формирања дискретних зрака. Резултати су објављени у једном раду и три саопштења са међународних скупова:

- Nemanja M. Lučić, **Bojana M. Bokić**, Dušan Ž. Grujić, Dejan V. Pantelić, Branislav M. Jelenković, Aleksandra Piper, Dragana M. Jović, Dejan V. Timotijević, „*Defect-guided Airy beams in optically induced waveguide arrays*“, Physical Review A **88**, br. 6 (2013).
  DOI: 10.1103/PhysRevA.88.063815
  ISSN: 2469-9934; **IF**: 2.777;
- Nemanja M. Lučić, **Bojana M. Bokić**, Dušan Ž. Grujić, Dejan V. Pantelić, Branislav M. Jelenković, Darko M. Vasiljević, Dejan V. Timotijević, Aleksandra Piper, Dragana M. Jović, „*Defect controlled Airy beam acceleration in optically induced waveguide arrays*“, PHOTONICA 2013, IV international School and Conference on Photonics, Beograd, Srbija, Avgust 26-30. (2013).
- Nemanja M. Lučić, **Bojana M. Bokić**, Dušan Ž. Grujić, Dejan V. Pantelić, Branislav M. Jelenković, Aleksandra Piper, Dragana M. Jović, Dejan V. Timotijević, „*Guiding of Airy Beams with Optically Induced Waveguide Arrays in the Nonlinear Crystal*“, 16th International Conference On Transparent Optical Networks (ICTON), Graz, Austria, July 06-10. (2014).
- Nemanja M. Lučić, **Bojana M. Bokić**, Dušan Z. Grujić, Dejan V. Pantelić, Branislav M. Jelenković, Aleksandra Piper, Dragana M. Jović, Dejan V. Timotijević, „*Airy beam propagation along one dimensional optically induced photonic lattice with defect* “, Oasis 5th Conference and Exhibition on Optics and Electro-Optics, MEDINANO, pp. 74-74, Izrael, March 03-04. (2015).

Након истраживања са једнодимензионалним Еиријевим сноповима прелази на истраживања са дводимензионалним Еиријевим сноповима у нелинеарном кристалу стронцијум баријум ниобата.

Испитивала је кохерентну и некохерентну суперпозицију два и четири дводимензионална Еиријева снопа, када су у фази као и када су у различитим фазама. Показала је да за разлику од линеарне суперпозиције, нелинеарна интеракција формира структуре налик солитонима, једно солитарно стање када су снопови у фази и солитарни пар када су снопови у различитим фазама. У наставку пројекта Бојана је радила и на експерименту са Еиријевим сноповима у фотонским структурама са различитим дефектима.

Након добијених експерименталних резултата, и њиховог поређења са нумеричким резултатима, уследила је обрада резултата као и припрема за публиковање. У оквиру овог истраживања написана су два рада и једно саопштење са међународног скупа:

- Falko Diebel, **Bojana M. Bokić**, Martin Boguslawski, Aleksandra Piper, Dejan V. Timotijević, Dragana M. Jović, Cornelia Denz, „*Control of Airy-beam self-acceleration by photonic lattices*”, Physical Review A **90** br. 3 (2014).
  DOI: 10.1103/PhysRevA.90.033802

ISSN: 2469-9934; **IF**: 2.777;

- **Bojana M. Bokić**, Falko Diebel, Dejan V. Timotijević, Aleksandra Piper, Martin Boguslawski, Dragana M. Jović, Cornelia Denz, „*Airy beams propagation in optically induced photonic lattices*", Nonlinear Optics And Its Applications VIII; And Quantum Optics III, vol. 9136 (SPIE), Brussels, Belgium, April 14-16, (2014).
- Falko Diebel, **Bojana M. Bokić**, Dejan V. Timotijević, Dragana M. Jović Savić, Cornelia Denz, "*Soliton formation by decelerating interacting Airy beams*", Optics Express **23**, br. 19, str. 24351-24361, (2015).
  DOI: 10.1364/OE.23.024351;
  ISSN: 1094-4087; **IF**: 3.669;

После истраживања са Еиријевим сноповима Бојана Бокић почиње сарадњу са др Бранком Коларићем на различитим пројектима из области фотонике и биофотонике. 2019. године је учествовала у дизајну експеримента који је проучавао интеракцију умрежених фотона и плазмонских наноструктура са циљем да објасни ефекат плазмонске резонанце на пропагацију увезаних фотона (тј. постојаност квантне корелације). Поред дизајна експеримента Бојана је активно учествовала и у анализи резултата. Ово истраживање је објављено у следећем часопису и једном саопштењу са међународног скупа:

- M. Remy, M. Cormann, W. Kubo, **B. Bokic**, Y. Caudano and B. Kolaric, "*Transmission of entangled photons studied by quantum tomography: do we need plasmonic resonances?*", Journal of Physics Communications, **3**, 065011, (2019).
  DOI: 10.1088/2399-6528/ab292f;
  ISSN: 2399-6528: **IF**(2019) = 1.13;
- M. Remy, **B. Bokić**, M. Cormann, W. Kubo, Y. Caudano, and B. Kolaric, „*Survival of quantum entanglement in transmission without plasmonic resonance*", 26th Central European Workshop on Quantum Optics, Paderborn University, Germany, June 3–7, (2019).

Бојана Бокић је проучавала и радијациону динамику пигмената инкорпорираних у транспарентна крила код разних врста *Cicada*. У раду публикованом као препринт (Arxiv) а послатом у *Proceedings of Royal Society B* (тренутно у рецензији) допринос Бојане Бокић је био анализа динамике екцитованог стања и успостављања корелације између морфологије/наноструктуре крила *Cicada* и оптичког одговора (трансмисије и флуоресценције). У оквиру овог истраживања написан је један рад и једно саопштење са међународног скупа:

- Sébastien R Mouchet, Charlotte Verstraete, **Bojana Bokic**, Dimitrije Mara, Louis Dellieu, Albert G Orr, Olivier Deparis, Rik Van Deun, Thierry Verbiest, Pete Vukusic, Branko Kolaric, „*Naturally occurring fluorescence in transparent insect wings*", arXiv preprint arXiv:2110.06086
- Dimitrije Mara, **Bojana Bokic**, Rik Van Deun, Pete Vukusic, Thierry Verbiest, Sébastien R. Mouchet and Branko Kolaric, ***Linear and Nonlinear Optical Response from Cicadas Transparent Wings***, Belgium Photonics Online Meetup - **bePOM**, 10-11 September 2020, Namur, Belgium, Virtual Poster Session, **Link:** http://hdl.handle.net/1854/LU-8674507

Успостављена сарадња са др Коларићем резултирала је и радовима објављеним 2022.године. У првом раду Бојана је учествовала у анализи радијационе динамике различитих наноемитера на бази ретких земаља са циљем да се разуме веза између њихове наноструктуре и радијационе динамике.

- D. Mara, F. Artizzu, J. Goura, M. Jayendran, **B. Bokić**, B. Kolaric, T. Verbiest and R. V. Deun, „*Molecular dysprosium complexes for white-light and near-infrared emission controlled by the coordination environment*“, Journal of Luminescence **243**, 118646, (2022).
  DOI: 10.1016/j.jlumin.2021.118646
  ISSN: 0022-2313; **IF**: 3.599;

Бојана Бокић је учествовала и у холографском проучавању дисипативних структура, које је резултирало радом објављеним у следећем часопису:

- Marina Simovic-Pavlovic, Maja C. Pagnacco, Dusan Grujić, **Bojana Bokic**, Darko Vasiljevic, Sebastien Mouchet, Thierry Verbiest, and Branko Kolaric, „*Uncovering Hidden Dynamics of Natural Photonic Structures using Holographic Imaging*“, J. Vis. Exp. (181), e63676, (2022).
  DOI: 10.3791/63676
  ISSN: 1940-087X; **IF**: 1.355;

Као и радом у часопису *Symmetry* у коме је први пут описано спонтано цепање симетрије код неравнотежне хемијске Бригз-Раушерове реакције и динамике фазног прелаза. У оба рада Бојана је активно учествовала у анализи добијених резултата са циљем да се повеже оптички одговор система са структуром и динамиком система.

- Maja C. Pagnacco, Jelena P. Maksimović, Marko Daković, **Bojana Bokic**, Sebastien R. Mouchet, Thierry Verbiest, Yves Caudano, and Branko Kolaric, „*Spontaneous Symmetry Breaking: The Case of Crazy Clock and Beyond*“, Symmetry, **14**(2), 413, (2022).
  DOI: 10.3390/sym14020413
  ISSN: 2073-8994; **IF**: 2.713;

Такође, Бојана Бокић је активно учествовала и у писању ревијалног рада из области биофотонике и оптомеханике који је објављен са циљем да се скрене пажња научне јавности на могуће примене биофотонских структура у НЕМС технологији.

- Marina Simovic-Pavlovic, **Bojana Bokić**, Darko Vasiljevic, and Branko Kolaric, „*Bioinspired NEMS-Prospective of Collaboration with Nature*“, Appl. Sci., **12**(2), 905, (2022).
  DOI: 10.3390/app12020905
  ISSN: 2076-3417; **IF**: 2.679;

4. ЕЛЕМЕНТИ ЗА КВАЛИТАТИВНУ ОЦЕНУ НАУЧНОГ ДОПРИНОСА КАНДИДАТА

4.1 Квалитет научних резултата

4.1.1 Научни ниво и значај резултата, утицај научних радова

Кандидаткиња је у досадашњој каријери објавила 11 научних радова, од чега 6 радова категорије М21, 2 рада категорије М22 и 3 рада категорије М23. Своја истраживања је представила на више конференција, и тиме остварила 1 допринос категорије М33, 6 доприноса категорије М34 и 3 доприноса категорије М64.

До сада најутицајнији радови кандидаткиње су

- Falko Diebel, **Bojana M. Bokić**, Martin Boguslawski, Aleksandra Piper, Dejan V. Timotijević, Dragana M. Jović, Cornelia Denz, „*Control of Airy-beam self-acceleration by photonic lattices*", Physical Review A **90** br. 3 (2014).
  DOI: 10.1103/PhysRevA.90.033802
  ISSN: 2469-9934; **IF**(2014) = 2.777; **SNIP**(2014) = 1.15;
- Falko Diebel, **Bojana M. Bokić**, Dejan V. Timotijević, Dragana M. Jović Savić, Cornelia Denz, "*Soliton formation by decelerating interacting Airy beams*", Optics Express **23**, br. 19, str. 24351-24361, (2015).
  DOI: 10.1364/OE.23.024351
  ISSN: 1094-4087; **IF**(2015) = 3.669; **SNIP**(2015) = 1.65;

Радови се баве изучавањем фундаменталних феномена који су повезани са простирањем дводимензионалних Еиријевих светлосних снопова у нелинеарној фоторефрактивној средини, СБН кристалу допираном церијумом.

Познато је да је контролисање особина пропагације светлости самом светлошћу кључно за реализацију напредних потпуно оптичких технологија. Постоји много начина који се могу користити како би се оне унапредиле. Један од обећавајућих приступа овом циљу који се предлаже у овим радовима јесте примена Еиријевих снопова и могућност да се модулацијом трансверзалног убрзања Еиријевих снопова контролише простирање светлости у фоторефрактивном материјалу.

Истраживање обухвата два циља: 1) проучавање динамике простирања више суперпонираних дводимензионалних Еиријевих снопова распоређених у симетричне конфигурације од два и четири снопа, са истим или различитим фазним дистрибуцијама, у линеарном и нелинеарном режиму као и 2) проучавање простирања појединачног дводимензионалног Еиријевог снопа у оптички индукованој квадратној фотонској решетци са и без оптичких дефеката.

Први циљ се заснива на формирању оптичких солитона, који представљају локализоване структуре које одржавају свој облик балансирајући између ефеката дифракције и нелинеарног самофокусирања. Идеја је да се кохерентном суперпозицијом више Еиријевих снопова модулишу њихова трансверзална убрзања тако да дође до формирања солитона или солитарних структура. За реализацију првог циља кандидат је најпре генерисао Еиријеве снопове, а затим изучавао њихову линеарну и нелинеарну пропагацију у фоторефрактивном материјалу. Кренуо је од појединачних снопова, а онда наставио са симетричном комбинацијом два и четири Еиријева снопа различите фазне дистрибуције, с циљем да пронађе ефекте интеракције више снопова и формирање солитарних структура.

Други циљ се односи на контролисање простирања Еиријевих светлосних снопова помоћу фотонских решетки. Познато је да присуство дискретних фотонских структура у фоторефрактивном материјалу драматично мења динамику пропагације светлости. Фотонске решетке су један од начина реализације фотонских кристала и представљају оптичке таласоводе са периодичном променом индекса преламања средине у којима се фотони понашају попут електрона у полупроводнику. Због својих особина погодан су оптички систем за манипулацију и контролу простирања светлости. Фотонске решетке се могу креирати модулацијом индекса преламања средине што укључује директно ласерско уписивање, оптичку литографију или технику бушења. Веома практична метода је техника оптичке индукције у фоторефрактивном материјалу коришћењем недифрагујућих зрака, која ствара трајне, реверзибилне фотонске структуре репрезентоване профилом интензитета недифрагујућег светлосног поља.

За реализацију другог циља, кандидат је техником оптичке индукције формирао квадратну решетку у фоторефрактивном материјалу помоћу дискретног недифрагујућег снопа (добијеног суперпозицијом четири раванска таласа), а након уписивања пропагирао претходно генерисани Еиријев сноп кроз уписану решетку. Кандидат је испитивао у којој мери различите јачине квадратне решетке (односно различите вредности индекса преламања у таласоводима решетке) могу да модулишу трансверзално убрзање Еиријевог снопа. Даље, помоћу технике мултиплексирања, кандидат је некохерентном суперпозицијом Беселовог снопа и недифрагујућег снопа квадратне решетке, формирао квадратну решетку са позитивним/негативним оптичким дефектом у централном таласоводу решетке. Испитивано је како локална промена индекса преламања утиче на динамику Еиријевог снопа.

Први експеримент је нешто једноставнији од другог. Светлост из ласера се шаље на просторни модулатор светлости на ком је генерисана фаза жељеног Еиријевог светлосног снопа или суперпозиције више Еиријевих снопова, који се након проласка кроз оптичке елементе шаље на кристал. Померањем камере и макроскопског објектива могуће је снимање излазне стране кристала како би се испитало да ли је зрак током простирања остао непромењен. Други експеримент је нешто комплекснији јер се паралелно уписује решетка техником оптичке индукције и ствара пробни Еиријев сноп који се простире кроз решетку.

За реализацију свих наведених циљева развијене су одговарајуће нумеричке методе као и експерименталне поставке за сваку од наведених тематика. Нумерички резултати били су од велике користи за бржу и ефикаснију реализацију експеримената, пошто су захваљујући добром нумеричком апарату пронађени услови под којима је било могуће реализовати жељене експерименте.

4.1.2 Параметри квалитета радова и часописа

Кандидаткиња је објавила 11 радова у часописима:

- 1 рад у часопису *Optics Express* (ISSN: 1094-4087), категорија M21, IF(2011) = 3.669; SNIP(2011) = 2.55;
- 1 рад у часопису *Physical Review A* (ISSN: 2469-9934), категорија M21, IF(2013) = 2.777; SNIP(2013) = 1.17;
- 1 рад у часопису *Physical Review A* (ISSN: 2469-9934), категорија M21, IF(2014) = 2.777; SNIP(2014) = 1.15;
- 1 рад у часопису *Optics Express* (ISSN: 1094-4087), категорија M21, IF(2015) = 3.669; SNIP(2015) = 1.65;
- 1 рад у часопису *Applied Surface Science* (ISSN: 0169-4332), категорија M21, IF(2015) = 6.182; SNIP(2015) = 1.27;
- 1 рад у часопису *Journal of Luminescence* (ISSN: 0022-2313), категорија M21, IF(2020) = 3.599; SNIP(2020) = 0.95;
- 1 рад у часопису *Appl. Sci.* (ISSN: 2076-3417), категорија M22, IF(2020) = 2.679; SNIP(2020) = 1.07;
- 1 рад у часопису *Symmetry* (ISSN: 2073-8994), категорија M22, IF(2020) = 2.713; SNIP(2020) = 1.10;
- 1 рад у часопису *Nuclear Technology and Radiation Protection* (ISSN: 1451-3994), категорија M23, IF(2017) = 0.429; SNIP(2017) = 0.63;
- 1 рад у часопису *Journal of Physics Communications* (ISSN: 2399-6528), категорија M23, IF(2019) = 1.13; SNIP(2019) = 0.70;
- 1 рад у часопису *J. Vis. Exp.* (ISSN: 1940-087X), категорија M23, IF(2020) = 1.355; SNIP(2020) = 0.44;

Додатни библиометријски показатељи квалитета часописа у којима је кандидаткиња објављивала радове приказани су у табели:

	ИФ	**М**	**СНИП**
Укупно	30.98	67	12.68
Усредњено по чланку	2.82	6.09	1.15
Усредњено по аутору	4.61	10.27	2

4.1.3 Цитираност научних радова кандидата

Према подацима о цитираности аутора изведених из базе *Scopus* 12.04.2022, радови чији је кандидаткиња ко-аутор цитирани су 100 пута, од чега 96 пута без аутоцитата, а Хиршов фактор је у оба случаја 5.

4.1.4 Међународна сарадња

Кандидат има међународну сарадњу. Активно сарађује od 2018. са Универзитетима KUL (Thierry Verbiest) и UNAMUR (Yves Caudano) из Белгије, као и са Ecole Central /Универзитетом у Марсеју (Thomas Durt).

4.2 Нормирање броја коауторских радова, патената и техничких решења

Сви радови кандидата су засновани на примени нумеричких прорачуна или компјутерских симулација у комбинацији са експерименталним резултатима па је приликом нормирања М бодова узимано у обзир да се нормирање врши код радова који имају више од 7 коаутора. Код радова кандидата категорије М21, 4 од 6 радова су нормирана која имају 8 или 9 коаутора. Код радова категорије М22 нормиран је 1 од 2 рада који има 8 коаутора док је код радова категорије М23 нормиран 1 од 3 рада који има више од 7 коаутора. Укупан број остварених М бодова у радовима у међународним часописима је 67, док је нормирани број остварених М бодова у овим радовима 60.72.

4.3 Учешће у пројектима, потпројектима и пројектним задацима

У оквиру пројекта ОИ171038 под називом „*Холографске методе генерисања специфичних таласних фронтова за ефикасну контролу кохерентних ефеката у интеракцији атома и ласера"* кандидат Бојана Бокић је била ангажована на истраживањима фотонских структура биолошког порекла. У оквиру истог пројекта Бојана је радила и на експерименту испитивања ефеката фемтосекундног ласерског снопа, таласне дужине из ултраљубичастог дела спектра и фреквенције 76 MHz, на два типа танких филмова на супстрату силицијума – једнослојном танком филму алуминијума, и вишеслојном танком филму који се састоји од пет алуминијум/титанијум бислојева (укупне дебљине 130 nm).

У оквиру билатералног пројекта са Немачком, под руководством др Драгане Јовић Савић, под називом „*Пропагација и локализација светлости у системима са комплексним фотоничним решеткама*" Бојана Бокић је радила на експерименту са Еиријевим сноповима. Главни циљ пројекта био је испитивање пропагације и локализације недифрагујућих снопова, креирање различитих фотонских структура са дефектима или кластерима дефеката као и различитих неуређених и квази-периодичних решетки а у циљу изучавања пропагације и локализације светлости у таквим структурама, и стварања директне везе са процесом процесуирања информација.

Радила је и на пројекту Француског министарства (STSM), који је резултат сарадње професора Бранка Коларића и професора Томаса Дурта са Универзитета у Марсеју. Назив пројекта: „*Etude expérimentale de la fluorescence émise par des quantum dots: Aspects fondamentaux et appliqués.*" / "*Experimental study of the fluorescence emission from quantum dots: Fundamental and applied aspects.*". Руководилац пројекта: Бранко Коларић; Институција координатор: Institut Fresnel, Универзитет у Марсеју.

4.4 Активност у научним и научно-стручним друштвима

4.4.1 Организација научних скупова

Кандидат Бојана Бокић учествовала је у организацији међународног онлајн симпозијума као креатор вебсајта, као члан научног одбора и један од едитора књиге апстраката (ISBN-978-86-902910-0-7 (pdf)). Међународни онлајн симпозијум под називом: ***Casimir Interaction: Where Physics Meets Chemistry and Biology,*** одржан је у Београду, 29.10.2020.

Учествовала је у организацији међународне конференције ***14th Photonics Workshop, 14-17. March 2021. Kopaonik, Serbia*** http://www.photonicsworkshop.ipb.ac.rs/14/index.php

Учествовала је и у организацији међународне конференције ***15th Photonics Workshop, 13-16. March 2022. Kopaonik, Serbia*** http://www.photonicsworkshop.ipb.ac.rs/15/index.php

4.5 Утицај научних резултата

Значај научних резултата кандидата је описан у тачки 4.1, док се њихов утицај огледа у броју цитата који су наведени у тачки 4.1.3.

4.6 Конкретан допринос кандидата у реализацији радова у научним центрима у земљи и иностранству

Кандидат је своје истраживање реализовала у Институту за физику у Београду и делом у групи за Нелинеарну фотонику на Универзитету у Минстеру приликом билатералног пројекта са Републиком Немачком. Њен допринос се огледа у извођењу математичких израза који су коришћени у компјутерским кодовима приликом симулација експеримента као и експерименталним мерењима, добијању и интерпретацији резултата у нумеричким симулацијама и експерименту, писању радова и комуникацији са рецензентима часописа.

5. ЕЛЕМЕНТИ ЗА КВАНТИТАТИВНУ ОЦЕНУ НАУЧНОГ ДОПРИНОСА КАНДИДАТА

Остварени резултати:

Категорија	М бодова по раду	Број радова	Укупно М бодова	Нормирани број М бодова
M21	8	6	48	43.05
M22	5	2	10	9.17
M23	3	3	9	8.5
M33	1	1	1	1
M34	0.5	6	3	3
M64	0.2	3	0.6	0.6
M70	6	1	6	6

Поређење са минималним квантитативним условима за избор у звање научни сарадник:

Минимални број М бодова	Неопходно	Остварено, број М бодова без нормирања	Остварено, нормирани број М бодова
Укупно	16	77.6	71.32
M10+M20+M31+M32+M33+M41+M42	10	68	61.72
M11+M12+M21+M22+M23	6	67	60.72

6. СПИСАК ОБЈАВЉЕНИХ РАДОВА

6.1 Радови у врхунским међународним часописима (М21):

- D. Pantelić, S. Ćurčić, S. Savić-Šević, A. Korać, A. Kovačević, B. Ćurčić, and **B. Bokić**, "*High angular and spectral selectivity of purple emperor (Lepidoptera: Apatura iris and A. ilia) butterfly wings*", Optics Express **19**, 5817 (2011).
  DOI: 10.1364/OE.19.005817
  ISSN: 1094-4087; **IF**(2011) = 3.669; **SNIP**(2011) = 2.55;

- Nemanja M. Lučić, **Bojana M. Bokić**, Dušan Ž. Grujić, Dejan V. Pantelić, Branislav M. Jelenković, Aleksandra Piper, Dragana M. Jović, Dejan V. Timotijević, „*Defect-guided Airy beams in optically induced waveguide arrays*", Physical Review A **88**, br. 6 (2013).
  DOI: 10.1103/PhysRevA.88.063815
  ISSN: 2469-9934; **IF**(2013) = 2.777; **SNIP**(2013) = 1.17;

- Falko Diebel, **Bojana M. Bokić**, Martin Boguslawski, Aleksandra Piper, Dejan V. Timotijević, Dragana M. Jović, Cornelia Denz, „*Control of Airy-beam self-acceleration by photonic lattices*", Physical Review A **90** br. 3 (2014).
  DOI: 10.1103/PhysRevA.90.033802
  ISSN: 2469-9934; **IF**(2014) = 2.777; **SNIP**(2014) = 1.15;

- Falko Diebel, **Bojana M. Bokić**, Dejan V. Timotijević, Dragana M. Jović Savić, Cornelia Denz, "*Soliton formation by decelerating interacting Airy beams*", Optics Express **23**, br. 19, str. 24351-24361, (2015).
  DOI: 10.1364/OE.23.024351
  ISSN: 1094-4087; **IF**(2015) = 3.669; **SNIP**(2015) = 1.65;

- Aleksander G. Kovačević, Suzana M. Petrović, **Bojana M. Bokić**, Biljana M. Gaković, Miloš T. Bokorov, Borislav Z. Vasić, Radoš B. Gajić, Milan S. Trtica, Branislav M. Jelenković, „*Surface nanopatterning of Al/Ti multilayer thin films and Al single layer by a low-fluence UV femtosecond laser beam*", Applied Surface Science **326**, str. 91-98 (2015).
  DOI: 10.1016/j.apsusc.2014.10.180
  ISSN: 0169-4332; **IF**(2015) = 6.182; **SNIP**(2015) = 1.27;

- D. Mara, F. Artizzu, J. Goura, M. Jayendran, **B. Bokić**, B. Kolaric, T. Verbiest and R. V. Deun, „*Molecular dysprosium complexes for white-light and near-infrared emission controlled by the coordination environment*", Journal of Luminescence **243**, 118646, (2022). M21
  DOI: 10.1016/j.jlumin.2021.118646
  ISSN: 0022-2313; **IF**(2020) = 3.599; **SNIP**(2020) = 0.95;

6.2 Радови у истакнутим међународним часописима (M22):

- Marina Simovic-Pavlovic, **Bojana Bokić**, Darko Vasiljevic, and Branko Kolaric, „*Bioinspired NEMS-Prospective of Collaboration with Nature*“, *Appl. Sci.*, ***12***(2), 905, (2022). M22
  DOI: 10.3390/app12020905
  ISSN: 2076-3417; **IF**(2020) = 2.679; **SNIP**(2020) = 1.07;

- Maja C. Pagnacco, Jelena P. Maksimović, Marko Daković, **Bojana Bokic**, Sebastien R. Mouchet, Thierry Verbiest, Yves Caudano, and Branko Kolaric, „*Spontaneous Symmetry Breaking: The Case of Crazy Clock and Beyond*“, Symmetry, ***14***(2), 413, (2022). M22
  DOI: 10.3390/sym14020413
  ISSN: 2073-8994; **IF**(2020) = 2.713; **SNIP**(2020) = 1.10;

6.3 Радови у међународним часописима (M23):

- Monika M. Živković, Milesa Ž. Srećković, Tomislav M. Stojić, **Bojana M. Bokić**, „*Influence of electromagnetic and nuclear radiation in medicine for therapy and diagnosis through processes, facts and statistical analysis*“, Nuclear Technology and Radiation Protection 32, br.1, pp. 91-98, (2017).
  DOI: 10.2298/NTRP1701091Z
  ISSN: 1451-3994; **IF**(2017) = 0.429; **SNIP**(2017) = 0.63;

- M. Remy, M. Cormann, W. Kubo, **B. Bokic**, Y. Caudano and B. Kolaric, “*Transmission of entangled photons studied by quantum tomography: do we need plasmonic resonances?*”, Journal of Physics Communications, **3**, 065011, (2019).
  DOI: 10.1088/2399-6528/ab292f;
  ISSN: 2399-6528: **IF**(2019) = 1.13; **SNIP**(2019) = 0.70;

- Marina Simovic-Pavlovic, Maja C. Pagnacco, Dusan Grujić, **Bojana Bokic**, Darko Vasiljevic, Sebastien Mouchet, Thierry Verbiest, and Branko Kolaric, „*Uncovering Hidden Dynamics of Natural Photonic Structures using Holographic Imaging*“, *J. Vis. Exp.* (181), e63676, (2022). M23
  DOI: 10.3791/63676
  ISSN: 1940-087X; **IF**(2020) = 1.355; **SNIP**(2020) = 0.44: ;

6.4 Саопштење са међународног скупа штампано у целини (M33):

- **Bojana M. Bokić**, Falko Diebel, Dejan V. Timotijević, Aleksandra Piper, Martin Boguslawski, Dragana M. Jović, Cornelia Denz, „*Airy beams propagation in optically induced photonic lattices*”, Nonlinear Optics And Its Applications VIII; And Quantum Optics III, vol. 9136 (SPIE), Brussels, Belgium, April 14-16, (2014).
  DOI: 10.1117/12.2052272

6.5 Саопштења са међународног скупа штампана у изводу (M34):

- M. Srećković, Ž. Tomić, Z. Fidanovski, S. Ostojić, P. Jovanić, Lj. Vulićević, A. Bugarinović, and **B. Bokić**, "*The correlation between the initial ceramic particles and final products*", 1st Conference of the Serbian Ceramic Society, Belgrade, Serbia, March 17-18. (2011).
- Nemanja M. Lučić, **Bojana M. Bokić**, Dušan Ž. Grujić, Dejan V. Pantelić, Branislav M. Jelenković, Darko M. Vasiljević, Dejan V. Timotijević, Aleksandra Piper, Dragana M. Jović, „*Defect controlled Airy beam acceleration in optically induced waveguide arrays*", PHOTONICA 2013, IV international School and Conference on Photonics, Beograd, Srbija, Avgust 26-30. (2013).
- Nemanja M. Lučić, **Bojana M. Bokić**, Dušan Ž. Grujić, Dejan V. Pantelić, Branislav M. Jelenković, Aleksandra Piper, Dragana M. Jović, Dejan V. Timotijević, „*Guiding of Airy Beams with Optically Induced Waveguide Arrays in the Nonlinear Crystal*", 16th International Conference On Transparent Optical Networks (ICTON), Graz, Austria, July 06-10. (2014).
  DOI: 10.1109/ICTON.2014.6876684
- Nemanja M. Lučić, **Bojana M. Bokić**, Dušan Z. Grujić, Dejan V. Pantelić, Branislav M. Jelenković, Aleksandra Piper, Dragana M. Jović, Dejan V. Timotijević, „*Airy beam propagation along one dimensional optically induced photonic lattice with defect* ", Oasis 5th Conference and Exhibition on Optics and Electro-Optics, MEDINANO, pp. 74-74, Izrael, March 03-04. (2015).
- M. Remy, **B. Bokić**, M. Cormann, W. Kubo, Y. Caudano, and B. Kolaric, „*Survival of quantum entanglement in transmission without plasmonic resonance*", 26th Central European Workshop on Quantum Optics, Paderborn University, Germany, June 3–7, (2019).
- Dimitrije Mara, **Bojana Bokic**, Rik Van Deun, Pete Vukusic, Thierry Verbiest, Sébastien R. Mouchet and Branko Kolaric, *Linear and Nonlinear Optical Response from Cicadas Transparent Wings*, Belgium Photonics Online Meetup - **bePOM**, 10-11 September 2020, Namur, Belgium, Virtual Poster Session, **Link:** http://hdl.handle.net/1854/LU-8674507

6.6 Саопштења са скупа националног значаја штампана у изводу (M64):

- M. Srećković, S. Polić-Radovanović, B. Timotijević, M. Timotijević, N. Borna, M. Živković, M. Dukić, and **B. Bokić**, "*Laseri, palimpsest i kulturna baština*," Fotonika 2010, Institut za fiziku (Beograd), 21-23. aprila (2010).
- S. Polić-Radovanović, M. Srećković, B. Timotijević, M. Timotijević, V. Rajković, R. Radovanović, and **B. Bokić**, "*The role of microscopy in the evaluation of the authenticity of the material of cultural heritage*," 4th Serbian Congress for Microscopy, Belgrade, Serbia, October 11-12. (2010).
- **B. Bokić**, "*Interakcija femtosekundnog laserskog impulsa sa materijalom - holografski pristup*," Četvrta radionica fotonike (2011), Kopaonik, 2-6. marta (2011).

Citation overview

Back to author details Export Print

This is an overview of citations for this author. Author *h*-index : 5 View *h*-graph

12 Cited Documents from"Bokić, Bojana M." + Add to list

Author ID:37060340500

Date range: 2011 to 2022 Exclude self citations of selected author Exclude self citations of all authors Exclude citations from books Update

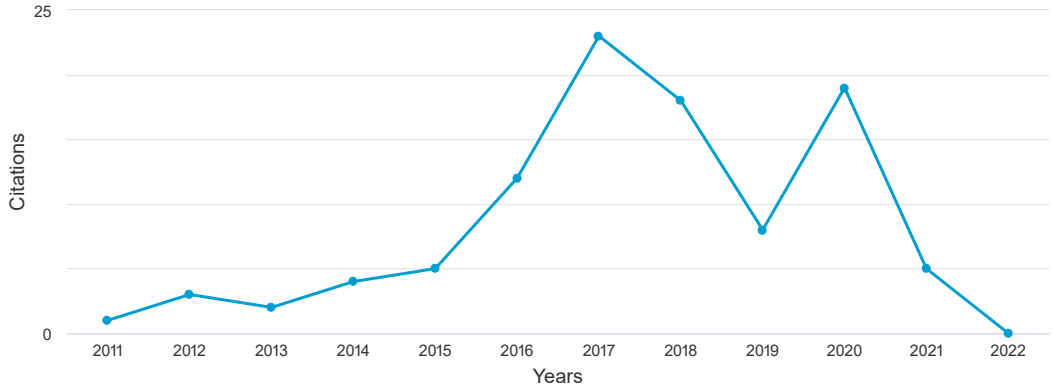

Sort on: Date (newest)

Page Remove

	Documents	Citations	<2011	2011	2012	2013	2014	2015	2016	2017	2018	2019	2020	2021	2022	Subtotal	>2022	Total
		Total	0	**1**	**3**	**2**	**4**	**5**	**12**	**23**	**18**	**8**	**19**	**5**	0	**100**	0	**100**
1	Molecular dysprosium complexes for white-light and near-infr...	2022														0		0
2	Spontaneous Symmetry Breaking: The Case of Crazy Clock and B...	2022														0		0
3	Bioinspired NEMS—Prospective of Collaboration with Nature	2022														0		0
4	Transmission of entangled photons studied by quantum tomogra...	2019														0		0
5	Influence of electromagnetic and nuclear radiation in medici...	2017									1					**1**		**1**
6	Surface nanopatterning of Al/Ti multilayer thin films and Al...	2015							2	6	2		8	2		**20**		**20**
7	Soliton formation by decelerating interacting Airy beams	2015						1	5	8	12	5	3	1		**35**		**35**
8	Control of Airy-beam self-acceleration by photonic lattices	2014						2	4	6	2	2	3	1		**20**		**20**
9	Airy beams propagation in optically induced photonic lattice...	2014														0		0
10	Guiding of Airy beams with optically induced waveguide array...	2014														0		0
11	Defect-guided Airy beams in optically induced waveguide arra...	2013					2	1	1	3			2			**9**		**9**
12	High angular and spectral selectivity of purple emperor (Lep...	2011		1	3	2	2	1			1	1	3	1		**15**		**15**

Display: 20 results per page

Citation overview

Self citations of selected authors are excluded. ×

Back to author details Export Print

This is an overview of citations for this author. Author *h*-index : 5 View *h*-graph

12 Cited Documents from"Bokić, Bojana M." + Add to list

Author ID:37060340500

Date range: 2011 to 2022 Exclude self citations of selected author Exclude self citations of all authors Exclude citations from books Update

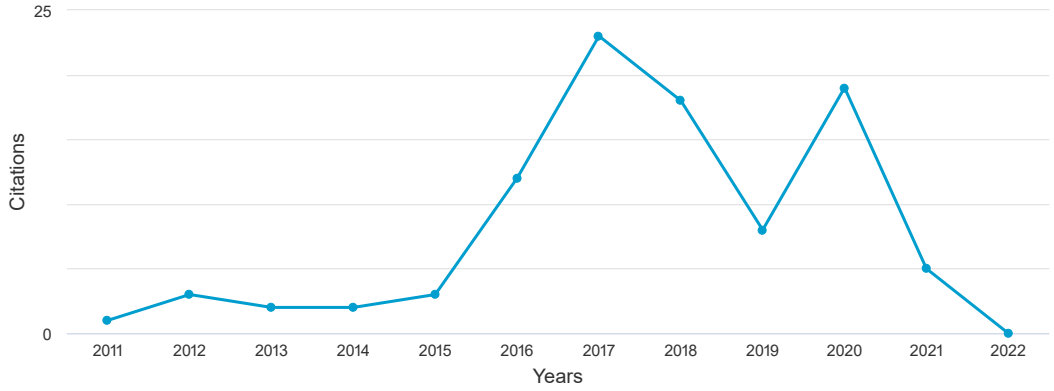

Sort on: Date (newest)

Page Remove

	Documents	Citations	<2011	2011	2012	2013	2014	2015	2016	2017	2018	2019	2020	2021	2022	Subtotal	>2022	Total
		Total	0	**1**	**3**	**2**	**2**	**3**	**12**	**23**	**18**	**8**	**19**	**5**	0	**96**	0	**96**
1	Molecular dysprosium complexes for white-light and near-infr...	2022														0		0
2	Spontaneous Symmetry Breaking: The Case of Crazy Clock and B...	2022														0		0
3	Bioinspired NEMS—Prospective of Collaboration with Nature	2022														0		0
4	Transmission of entangled photons studied by quantum tomogra...	2019														0		0
5	Influence of electromagnetic and nuclear radiation in medici...	2017									1					**1**		**1**
6	Surface nanopatterning of Al/Ti multilayer thin films and Al...	2015							2	6	2		8	2		**20**		**20**
7	Soliton formation by decelerating interacting Airy beams	2015						1	5	8	12	5	3	1		**35**		**35**
8	Control of Airy-beam self-acceleration by photonic lattices	2014						1	4	6	2	2	3	1		**19**		**19**
9	Airy beams propagation in optically induced photonic lattice...	2014														0		0
10	Guiding of Airy beams with optically induced waveguide array...	2014														0		0
11	Defect-guided Airy beams in optically induced waveguide arra...	2013							1	3			2			**6**		**6**
12	High angular and spectral selectivity of purple emperor (Lep...	2011		1	3	2	2	1			1	1	3	1		**15**		**15**

Display: 20 results per page

High angular and spectral selectivity of purple emperor (Lepidoptera: *Apatura iris* and *A. ilia*) butterfly wings

Dejan Pantelić,[1,*] Srećko Ćurčić,[2] Svetlana Savić-Šević,[1] Aleksandra Korać,[2, 3] Aleksander Kovačević,[1] Božidar Ćurčić[2] and Bojana Bokić[1]

[1]*Institute of Physics, University of Belgrade, Pregrevica 118, 11080 Zemun, Serbia*
[2]*Institute of Zoology, Faculty of Biology, University of Belgrade, Studentski Trg 16, 11000 Belgrade, Serbia*
[3]*Center for Electron Microscopy, Faculty of Biology, University of Belgrade, Studentski Trg 16, 11000 Belgrade, Serbia*
**pantelic@ipb.ac.rs*

Abstract: The iridescent features of the butterfly species *Apatura iris* (Linnaeus, 1758) and *A. ilia* (Denis & Schiffermüller, 1775) were studied. We recognized the structural color of scales only on the dorsal side of both the fore and hind wings of males of both of the aforementioned butterfly species. The scale dimensions and microstructure were analyzed by a scanning electron microscope (SEM) and transmission electron microscope (TEM). The optical properties were measured and it was found that the peak reflectivity is around 380 nm, with a spectral width (full width at half maximum) of approximately 50 nm in both species. The angular selectivity is high and a purple iridescent color is observed within the angular range of only 18 degrees in both species.

OCIS codes: (050.2770) Gratings; (050.52980) Photonic crystals; (050.6624) Subwavelength structures; (160.4760) Optical properties.

References and links

1. M. Srinivasarao, "Nano-optics in the biological world: beetles, butterflies, birds, and moths," Chem. Rev. **99**(7), 1935–1962 (1999).
2. P. Vukusic, J. R. Sambles, C. R. Lawrence, and R. J. Wootton, "Quantified interference and diffraction in single *Morpho* butterfly scales," Proc. Biol. Sci. **266**(1427), 1403–1411 (1999).
3. P. Vukusic, and J. R. Sambles, "Photonic structures in biology," Nature **424**(6950), 852–855 (2003).
4. R. O. Prum, T. Quinn, and R. H. Torres, "Anatomically diverse butterfly scales all produce structural colours by coherent scattering," J. Exp. Biol. **209**(4), 748–765 (2006).
5. P. Vukusic, "Structural colour in Lepidoptera," Curr. Biol. **16**(16), R621–R623 (2006).
6. N. L. Garrett, P. Vukusic, F. Ogrin, E. Sirotkin, C. P. Winlove, and J. Moger, "Spectroscopy on the wing: naturally inspired SERS substrates for biochemical analysis," J Biophotonics **2**(3), 157–166 (2009).
7. M. D. Shawkey, N. I. Morehouse, and P. Vukusic, "A protean palette: colour materials and mixing in birds and butterflies," J. R. Soc. Interface **6**(Suppl 2), S221–S231 (2009).
8. H. Ghiradella, "Light and color on the wing: structural colors in butterflies and moths," Appl. Opt. **30**(24), 3492–3500 (1991).
9. H. Ghiradella, "Hairs, bristles, and scales," in *Microscopic Anatomy of Invertebrates, Vol. 11A: Insecta*, F.W. Harrison and M. Locke eds. (Wiley, New York, 1988).
10. H. Ghiradella, D. Aneshansley, T. Eisner, R. E. Silberglied, and H. E. Hinton, "Ultraviolet reflection of a male butterfly: interference color caused by thin-layer elaboration of wing scales," Science **178**(4066), 1214–1217 (1972).
11. L. P. Biró, K. Kertész, Z. Vértesy, G. I. Márk, Z. Bálint, V. Lousse, and J.-P. Vigneron, "Living photonic crystals: butterfly scales – nanostructure and optical properties," Mater. Sci. Eng. C **27**(5-8), 941–946 (2007).
12. Z. Han, L. Wu, Z. Qiu, and L. Ren, "Microstructure and structural color in wing scales of butterfly *Thaumantis diores*," Chin. Sci. Bull. **54**(4), 535–540 (2009).
13. M. Imafuku, Y. Hirose, and T. Takeuchi, "Wing colors of *Chrysozephyrus* butterflies (Lepidoptera; Lycaenidae): ultraviolet reflection by males," Zoolog. Sci. **19**(2), 175–183 (2002).
14. P. Vukusic, J. R. Sambles, and C. R. Lawrence, "Structurally assisted blackness in butterfly scales," Proc. Biol. Sci. **271**(Suppl 4), S237–S239 (2004).
15. P. Vukusic, and I. Hooper, "Directionally controlled fluorescence emission in butterflies," Science **310**(5751), 1151 (2005).

#141253 - $15.00 USD Received 19 Jan 2011; revised 1 Mar 2011; accepted 1 Mar 2011; published 14 Mar 2011

16. S. M. Luke, P. Vukusic, and B. Hallam, "Measuring and modelling optical scattering and the colour quality of white pierid butterfly scales," Opt. Express **17**(17), 14729–14743 (2009).
17. K. Kertész, G. Molnár, Z. Vértesy, A. A. Koós, Z. E. Horváth, G. I. Márk, L. Tapasztó, Z. Bálint, I. Tamáska, O. Deparis, J. P. Vigneron, and L. P. Biró, "Photonic band gap materials in butterfly scales: a possible source of "blueprints"," Mater. Sci. Eng. B **149**(3), 259–265 (2008).
18. Z. Vértesy, K. Kertész, Z. Bálint, G. Molnár, M. Erős, and L. P. Biró, "SEM and TEM investigations in the scales of the European nymphalid butterfly *Apatura ilia* dark and light phenotypes," in *BioPhot Meeting Abstract Book*, Levente Tapasztó ed. (Reserach Institute for Technical Physics and Materials Science, Budapest, Hungary, 2007*)*, pp. 14–15.
19. Z. Han, L. Wu, Z. Qiu, H. Guan, and L. Ren, "Structural colour in butterfly *Apatura ilia* scales and the microstructure simulation of photonic crystal," J. Bionics Eng. **5**(Supplement 1), 14–19 (2008).
20. R. E. Silberglied, "Visual communication and sexual selection among butterflies," In *The Biology of Butterflies. Symposium of the Royal Society of London, No. 11*, R. I. Vane-Wright, and P. E. Ackery eds. (Academic Press, London. 1984) pp. 207–223.
21. R. J. C. Page, "Perching and patrolling continuum at favoured hilltop sites on a ridge: a mate location strategy by the Purple Emperor butterfly *Apatura iris*," The Entomologist's Record **122**, 61–70 (2010).
22. S. Berthier, "Photonique des Morphos," (Springer-Verlag France, Paris, 2010).
23. G. A. Blackburn, "Hyperspectral remote sensing of plant pigments," J. Exp. Bot. **58**(4), 855–867 (2006).
24. M. A. Giraldo, S. Yoshioka, and D. G. Stavenga, "Far field scattering pattern of differently structured butterfly scales," J. Comp. Physiol. A Neuroethol. Sens. Neural Behav. Physiol. **194**(3), 201–207 (2008).
25. S. Yoshioka, and S. Kinoshita, "Wavelength-selective and anisotropic light-diffusing scale on the wing of the Morpho butterfly," Proc. Biol. Sci. **271**(1539), 581–587 (2004).

1. Introduction

The diurnal active members of the order Lepidoptera (butterflies) are considered to be the most attractive insects, together with representatives of the order Coleoptera (beetles). The delicate beauty of butterfly wings is a consequence of several phenomena: selective absorption by pigments, scattering, fluorescence and iridescence. The phenomenon of bright iridescence attracted much attention [1–7] and is observed in a great number of butterfly species, mostly tropical ones. Butterflies are known as the masters of mimicry (the type of camouflage which serves to avoid predators) and aposemy (warning coloration which is usually associated with an unpleasant taste to potential predators). In some species sexual dimorphism is observed, as in the two species analyzed in this paper.

Structural coloration investigations have been very popular in the last few decades and butterfly microstructure has been thoroughly investigated [8–10]. The following aspects have been studied as well: nanostructure and optical properties of wing scales [1, 11, 12], interference and diffraction in butterflies [2], ultraviolet reflection [13], structural blackness and whiteness in butterfly scales [14], fluorescence emission [15], and coherent scattering-induced structural color of scales [4]. The optical properties of butterfly scales have been thoroughly measured and modeled [16] and their nanoscale structures could encourage further developments in artificial material manufacturing [17].

The butterfly species *Apatura iris* (Linnaeus, 1758) and *A. ilia* (Denis & Schiffermüller, 1775) (Fig. 1a and b) are distributed from Europe to Eastern Asia (China). The most obvious difference between the two species is an extra eye spot on the fore wings of *A. ilia*. The males of *Apatura* spp. possess the iridescent color on the dorsal side of their wings [18, 19]. This is probably connected with intrasexual communication between males, rather than intersexual communication and attraction [20]. The structural color of males is visible in flight when the movements of the wings are noticeable within a certain range of angles. This kind of iridescent coloration represents an excellent contrast to forest canopy – a natural habitat of *Apatura* spp. Apart from structural coloration, pigment coloration is present as well.

The flight behavior of male *Apatura iris* was recently studied and it consisted mainly of perching and patrolling flights. The daily aggregation of males at favored landmark sites from approximately midday was observed as well [21].

Here we present a detailed study of two *Apatura* species with respect to their optical properties and the relationship of these properties to the microscopic structure of the wing scales.

#141253 - $15.00 USD Received 19 Jan 2011; revised 1 Mar 2011; accepted 1 Mar 2011; published 14 Mar 2011

a) b)

Fig. 1. a) *Apatura iris*; b) *Apatura ilia*. Observe that *A. Ilia* has an extra eye spot on fore wings.

2. Materials and methods

2.1 Collecting data

Specimens of the species *Apatura iris* and *A. ilia* were used for optical investigations (Fig. 1). Both species were collected from the Balkan Peninsula: *A. iris* – Mt. Stara Planina, Southeastern Serbia (July 2009, leg. D. Stojanović), and *Apatura ilia* – Mt. Fruška Gora, Northern Serbia (July 2009, leg. D. Stojanović). The specimens were kept in the collection of the Institute of Zoology, Faculty of Biology, University of Belgrade, Serbia.

2.2 SEM procedure

The specimens of *Apatura iris* and *A. ilia* were rinsed with diethyl-ether to obtain a clear surface of the wings. The wings of the males were cut into rectangular shape (surface area of several mm^2). This was followed by dehydration in order to obtain dry samples, fixed on a test-bed and subsequently covered with gold. Prepared samples were analyzed by a scanning electron microscope (SEM) (JSM-6460LV, JEOL, Tokyo, Japan).

2.3 TEM procedure

Wings were cut into small pieces, fixed in 3% glutaraldehyde in 0.1M phosphate buffer (pH 7.2) and postfixed in 1% osmium tetroxide in the same buffer. The specimens were dehydrated with serial ethanol solutions of increasing concentration and embedded in Araldite (Fluka, Germany). For electron microscopic examination, the tissue blocks were trimmed and cut with diamond knives (Diatome, Switzerland) on an UC6 ultramicrotome (Leica, Austria). The thin sections were mounted on copper grids, stained with uranyl acetate and lead citrate (Ultrastain, Leica, Austria) and examined on a Philips CM 12 transmission electron microscope (TEM) (Eindhoven, the Netherlands) equipped with a Megaview III digital camera (Soft Imaging System, Münster, Germany).

2.4 Spectrometric measurements

A HR2000CG-UV-NIR Fiber spectrometer was used (Ocean Optics Inc., Dunedin, USA) to collect the reflection spectra of the investigated butterflies. Wing samples were positioned on a computer-controlled rotation platform and illuminated with a tungsten halogen lamp. Thus, we were able to record the reflection spectrum of the wings as a function of the angle of incidence. A MIRA titanium-sapphire laser with frequency doubler (Coherent Inc., USA) was used to investigate the spectral dependence of the wing scattering pattern in the blue and UV part of the spectrum. A diode-pumped Nd-YAG laser at 532 nm and diode laser at 630 nm were used as well. The wings were irradiated with a laser beam and the scattered radiation was photographed on the cylindrical screen by Canon EOS 50D camera. Rigorous coupled-wave analysis was used to calculate the spectral reflectivity.

#141253 - $15.00 USD Received 19 Jan 2011; revised 1 Mar 2011; accepted 1 Mar 2011; published 14 Mar 2011

3. Results

As in all butterfly species, the scales are positioned like roof tiles covering the entire dorsal and ventral sides of the wing (Fig. 2a). We recognized two types of scales on the dorsal side of both the fore and hind wings of *Apatura iris* and *A. ilia*. The cover scales are on top, while ground scales are situated below. We found that the cover scales are responsible for the blue iridescence of these two butterfly species (Fig. 2b) due to their much denser microscopic structure in comparison to the ground scales. We have found that iridescent scales are pigmented (see brownish scales in lower half of Fig. 2c).

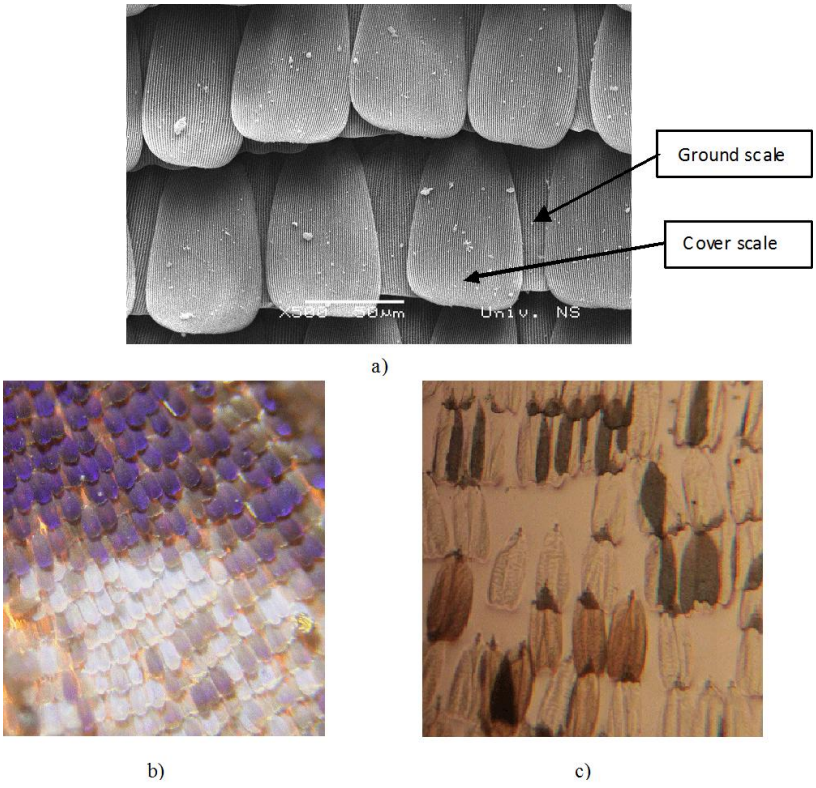

Fig. 2. *Apatura iris*: a) the cover scales on the dorsal wing side have a much denser structure in comparison to ground scales (SEM image); b) the blue iridescence of the cover scales positioned in regular rows. White scattering scales can be seen as well. The photograph is recorded in reflection; c) scattering scales have a glass-like appearance, while the iridescent scales are pigmented. Overlapping areas of glass-like scales are dark, indicating that the scattering is intensified. Microscope image is recorded in transmission.

The white areas of the dorsal wing side are also interesting. Examination of the reflective property revealed that the scales uniformly scatter light (Fig. 2b), while in transmission they look completely transparent (Fig. 2c). Scale overlapping increases the scattering, which can be seen as dark areas in upper half of Fig. 2c. We have found that there is a cumulative effect of overlapping. A single scale transmits around 90% and we measured the transmission of the overlapping scales to be about 60%.

By magnifying the iridescent butterfly scale surface of *Apatura iris* we observed long parallel ridges, each having a number of lamellas positioned one over another (see Fig. 3 for SEM images in two different views). The rows are mutually connected with orthogonally positioned cross ribs. TEM images were used to obtain the exact morphological and dimensional characteristics of each ridge and its lamellae (Fig. 4). The lamellae in cross section exhibit a multilayer structure, conifer-like, with six pairs of lateral projections which

#141253 - $15.00 USD Received 19 Jan 2011; revised 1 Mar 2011; accepted 1 Mar 2011; published 14 Mar 2011

are not widened distally and are triangularly pointed. The scale structure of *Apatura ilia* is similar, except that the ridge density is slightly higher.

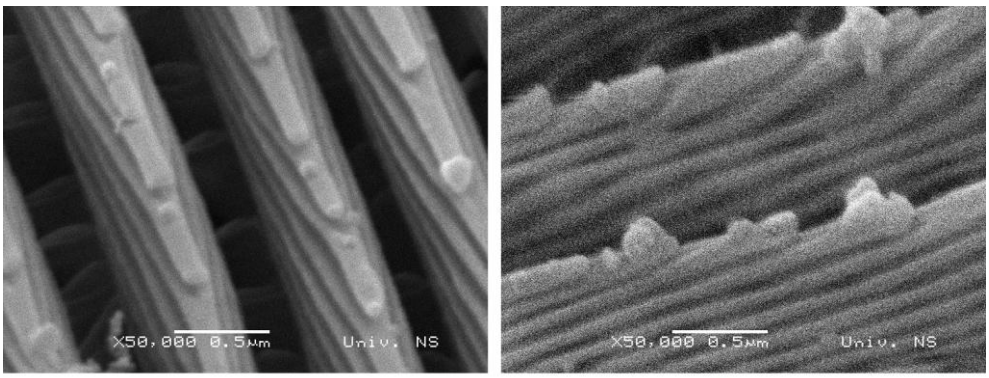

a) b)

Fig. 3. SEM of the highly-magnified structure of a) *Apatura iris* cover scale in dorsal view; b) *A. iris* cover scale in dorso-lateral view. A stacked lamellar structure is apparent.

Fig. 4. TEM image of cover scale cross section of *Apatura iris*.

Electron microscope images were used to construct a geometrical model of the structure which was further utilized for theoretical analysis of the optical properties. Characteristic dimensions can be seen in Fig. 5. Ridges form a surface relief diffraction grating, with an 820 nm period and approximately the same depth (830 nm). On the other hand, the lamellae form a volume Bragg grating, with a roughly 75 nm period, with each lamella being 40 nm thick.

Butterfly wings were studied spectroscopically in relation to the illumination and observation angles. Several spectra were recorded for different angular orientations (Fig. 6a). Maximum reflectivity is observed in the UV part of the spectrum (380 nm) and does not depend on the observation angle. Spectral width is small (50 nm FWHM) compared with more visually spectacular species, such as *Morpho* butterflies [22]. There is a slight spectral shift (in the order of 10-20 nm) as a function of the angle of illumination. All of this apparently provides an evolutionary advantage when the butterfly reflectivity spectra (with UV maximum) are compared with the canopy spectra (with almost no reflectivity in UV region, a peak at 550 nm, and a plateau in the IR region) [23]. UV reflectivity makes the butterfly very visible to its own species and considerably less visible to all other animals, especially potential predators. The intensity of reflected light at visible and IR wavelengths is much lower, making the butterfly appear dull brown from almost all directions – an excellent camouflage in forest, where *Apatura* species is living.

#141253 - $15.00 USD Received 19 Jan 2011; revised 1 Mar 2011; accepted 1 Mar 2011; published 14 Mar 2011

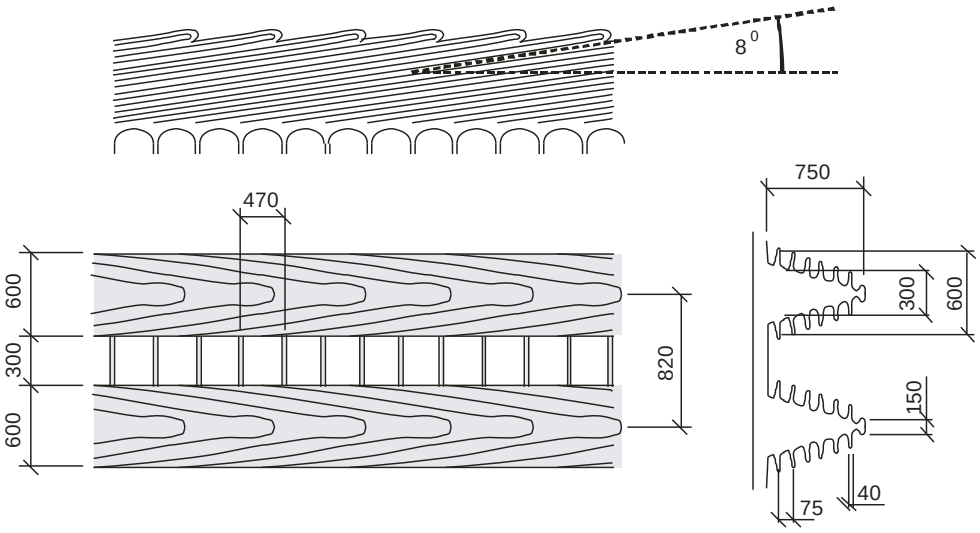

Fig. 5. Geometry of the microscopic structure of the *Apatura iris* wing scale (three orthogonal projections of the upper scale surface). All dimensions are in nanometers.

The iridescence of *Apatura iris* is observed in a rather narrow angular range (18 degrees); this is much narrower compared to other butterfly species [24]. Iridescence at 380 nm as a function of the angle of incidence is shown in Fig. 6b. Nearly identical spectral properties were observed in *Apatura ilia*.

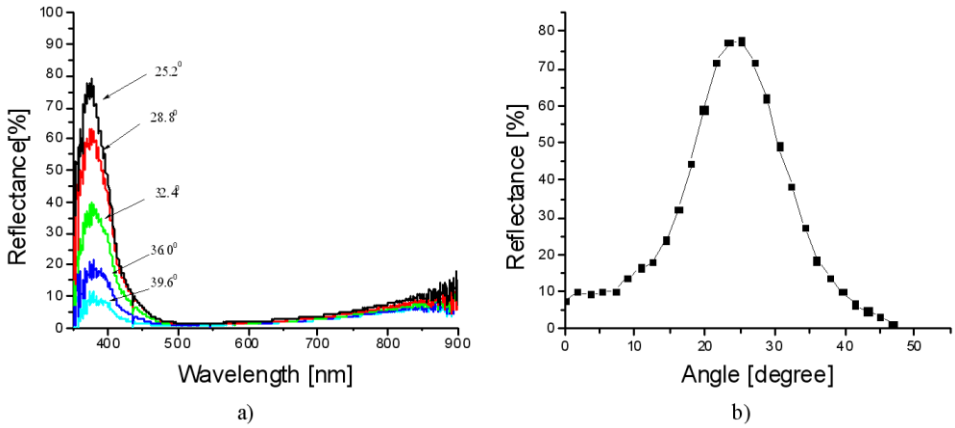

Fig. 6. a) Reflection spectra of the *Apatura iris* wing, with the angle of incidence as a parameter; b) iridescence at 380 nm as a function of the observation angle.

In order to observe the spatial distribution of iridescent light, we irradiated the butterfly wing with a laser beam from a tunable Ti-Sapphire laser coupled to frequency doubler. We were able to continuously tune the laser wavelength from 365 to 450 nm. A simple experimental setup is shown in Fig. 7a and 7b, and the typical spatial distribution of iridescence can be seen in Fig. 7c. It should be emphasized that the images were recorded by virtue of the natural fluorescence of the paper screen. In order to obtain an improved spatial distribution we applied pseudo-coloring of the recorded images.

#141253 - $15.00 USD Received 19 Jan 2011; revised 1 Mar 2011; accepted 1 Mar 2011; published 14 Mar 2011

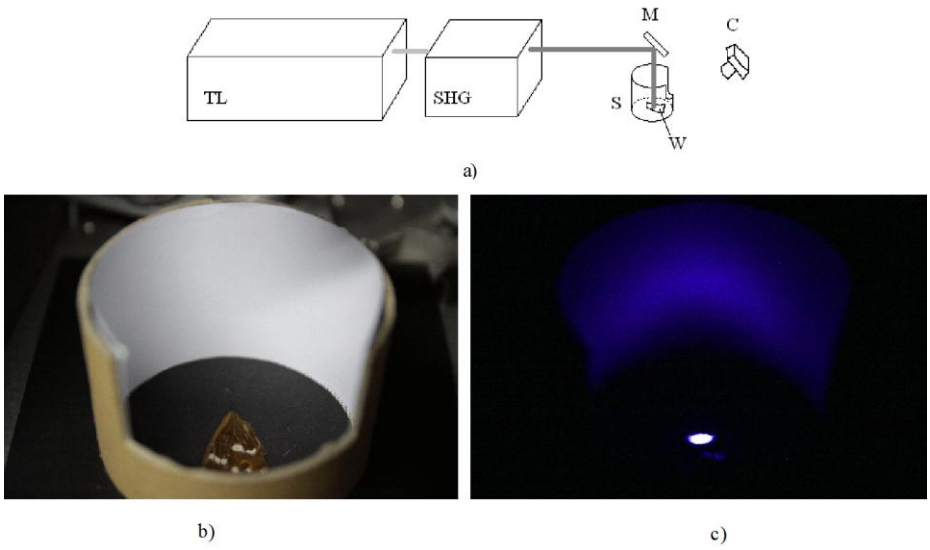

Fig. 7. a) Experimental setup used for the detection of the spatial distribution of *Apatura iris* wing iridescence (TL – titanium sapphire laser, SHG – frequency doubler, C – CCD camera, S – reflective cylinder, W – butterfly wing, M – mirror); b) a butterfly wing inside a reflective cylinder c) typical pattern of iridescence.

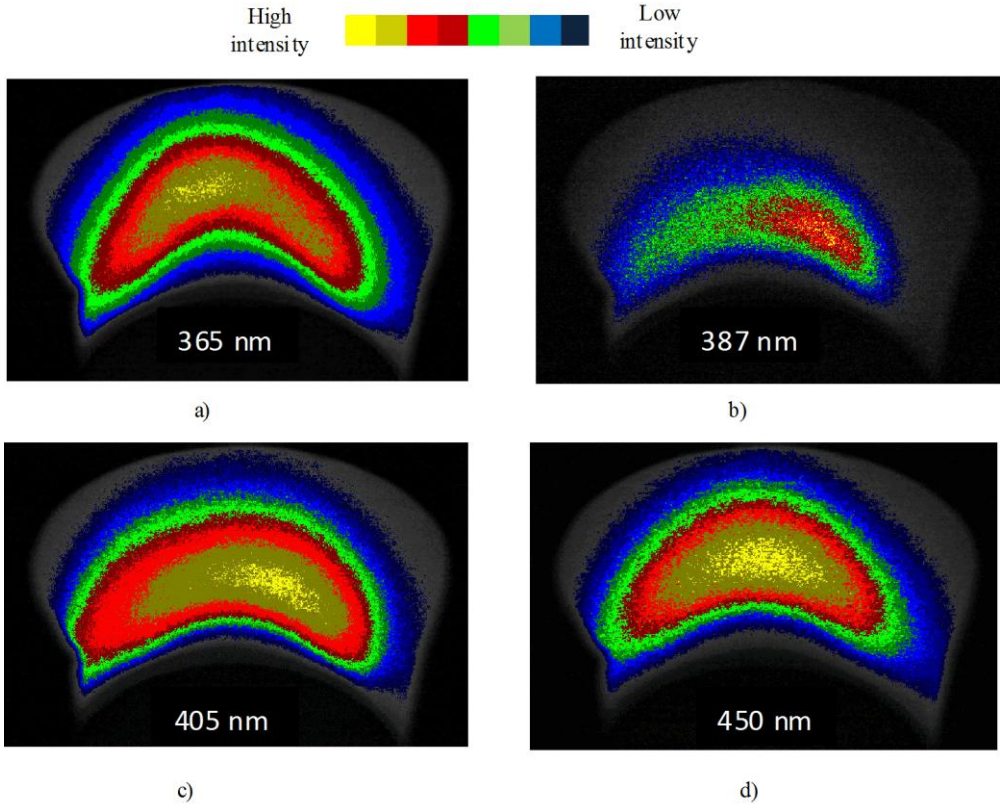

Fig. 8. Pseudo-colored images of iridescence recorded at: a) 365 nm; b) 387 nm; c) 405 nm; d) 450 nm. Patterns were recorded using a Ti-sapphire laser with frequency doubler. Light intensities are color coded according to the bar at the top of the figure.

#141253 - $15.00 USD Received 19 Jan 2011; revised 1 Mar 2011; accepted 1 Mar 2011; published 14 Mar 2011

Four images recorded at 365, 387, 405 and 450 nm are shown in Figs. 8a-8d. In comparison to other wavelengths, the spatial distribution at 387 nm is much narrower, indicating that at this particular wavelength the radiation is very directional. At 532 nm the directionality of scattered radiation is almost completely lost, as can be seen in Fig. 9, which was recorded by a diode-pumped Nd-YAG laser at 532 nm.

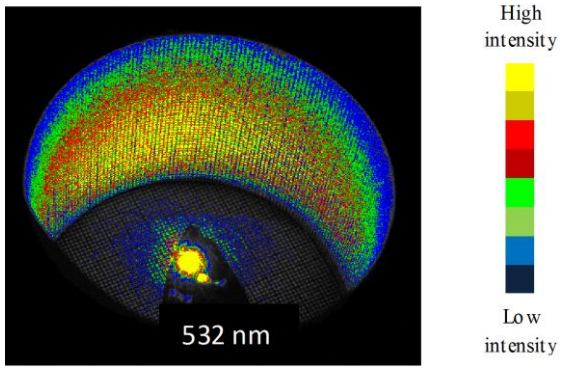

Fig. 9. Radiation at 532 nm is almost uniformly scattered at the wing of *Apatura iris*. The pattern was recorded by Nd-YAG laser. Light intensities are color coded – yellow representing the highest intensity, and blue the lowest.

4. Discussion

The results presented in this study show that the iridescence of *Apatura* spp. butterflies is spectrally and directionally constrained. With respect to the butterfly body, the radiation is directed as shown in Fig. 10 in three orthogonal projections. This particular feature is a consequence of the mutual orientations of lamellae with respect to the scale, and the scale with respect to the wing membrane (Fig. 11). There is a critical angle of incidence ($\gamma + 2\alpha + 2\beta = \pi/2$) when the radiation is Bragg-reflected along the wing surface. At a greater angle, the radiation cannot be further reflected (i.e., it is directed inside the material). In the case of *Apatura* butterflies, the angle α of the scale is large (~20°), as can be verified by the strong shadow cast by each scale in Figs. 2a and 2b.

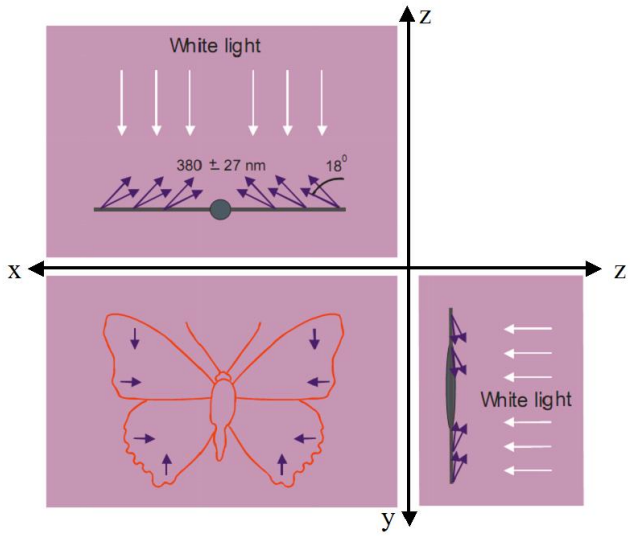

Fig. 10. Directions in which the blue iridescence can be observed (purple arrows). The butterfly is schematically presented in three orthogonal projections.

#141253 - $15.00 USD Received 19 Jan 2011; revised 1 Mar 2011; accepted 1 Mar 2011; published 14 Mar 2011

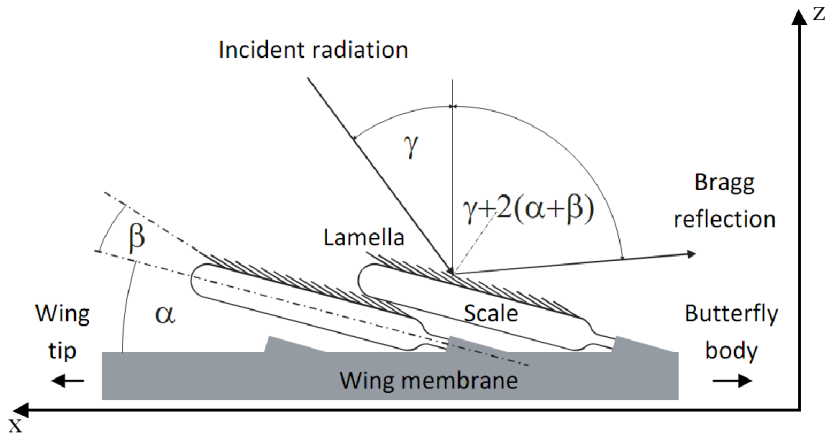

Fig. 11. Directionality of *Apatura* butterfly wing iridescence is a consequence of inclination of both lamellae (angle β) and the scale as a whole (angle α). γ is the angle of incidence of light with respect to the wing membrane. Axes x and z are in agreement with Fig. 10.

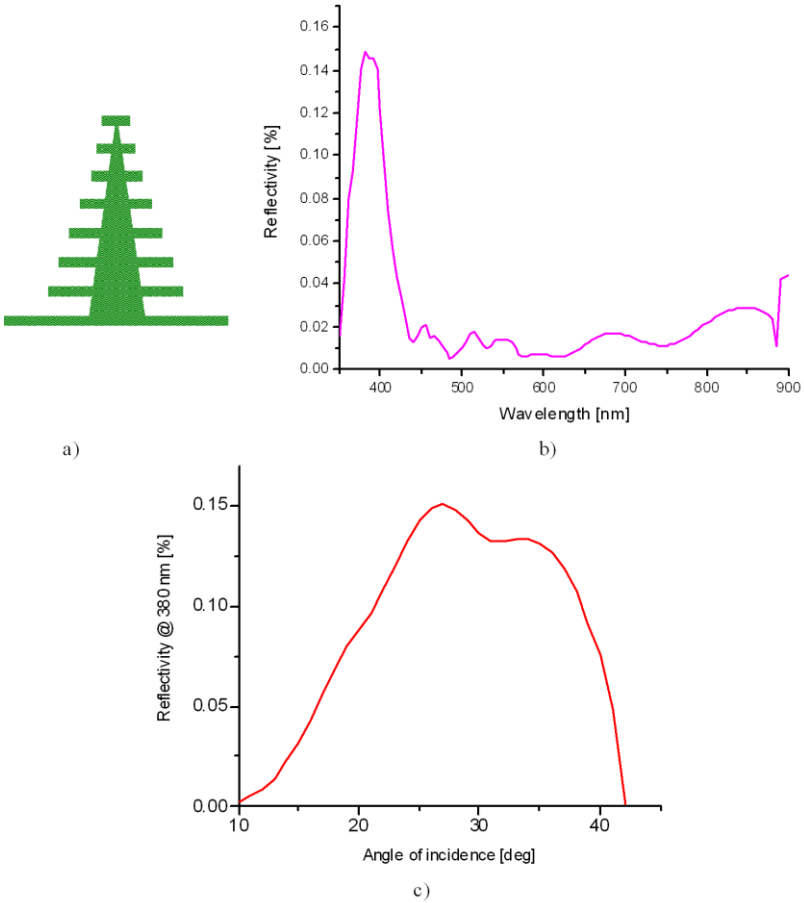

Fig. 12. a) Geometry of the butterfly cover scale in cross section, used for the calculation of the spectral reflectivity of *Apatura* spp.; b) spectral reflectivity as obtained by exact analysis using rigorous coupled-wave analysis; c) angular dependence of iridescence at 380 nm.

#141253 - $15.00 USD Received 19 Jan 2011; revised 1 Mar 2011; accepted 1 Mar 2011; published 14 Mar 2011

The spectral selectivity of the *Apatura* spp. scale was analyzed using rigorous coupled-wave analysis using simplified geometry as shown in Fig. 12a. We were able to correctly reproduce the spectral reflectivity (as shown in Fig. 12b) using dimensions presented in Fig. 5 and the refractive index of 1.56 for chitin [25]. Angular dependence of iridescence was calculated too and presented in Fig. 12c. Theoretical results slightly depart from experimental data, but this is due to idealized nature of calculation. In reality the butterfly grating is stochastically distorted, and the effect is averaged among many scales, inside illuminated wing area.

This phenomenon is in contrast with the reflection of *Morpho* butterfly wings, which direct radiation sideways and in a broad angular range. Also, the spectral maximum of iridescence shifts significantly with the angle of observation [22]. The difference between *Morpho* spp. and *Apatura* spp. is due to the different orientations of butterfly scales with respect to wing membrane. In *Morpho* butterflies the scales are almost parallel to the membrane (for example, *Morpho aega*), while in the *Apatura* species the scales are strongly inclined. On the nanoscopic level, ridges on the *Apatura* scale are not as dense as in *Morpho* butterflies. Even though the number of lamellas is almost the same in *Morpho helenor* [22] and *Apatura*, their cross sectional profile (as seen in TEM) is quite different. All these factors lead to radically different optical properties - *Apatura* iridescence is spectrally very pure, and the angular pattern is narrow.

5. Conclusions

Apatura ilia and *Apatura iris* are visually quite similar. *Apatura ilia* males have an iridescent purple color on the wings that dorsally arise from a fully ordered 3D structure, and a yellowish-brown color produced by pigments on the wings ventrally. On the other hand the males of *A. iris* have the same purple iridescent color on the dorsal side of the wings and a brownish color on the ventral side.

The photonic-type nanostructures consisting of chitin, occurring in the butterfly wing scales of the male individuals of the species *Apatura iris* and *A. ilia*, were investigated by both scanning and transmission electron microscopy and reflectance spectroscopy. A tunable laser was used to analyze the variation of spatial distribution of iridescence.

As in all butterfly species, the architecture of the scales is complex. They possess numerous alternating air and cuticle layers responsible for iridescence. From an optical point of view, both analyzed species behave similarly. Maximum reflectivity is observed in the UV region of the spectrum for both species and depends to a certain extent on the observation angle. We have found that the scale iridescence is remarkably narrow, both spectrally and angularly, in the studied butterfly species. This is the consequence of the interplay between scale structure and inclination with respect to the wing membrane. Iridescence is observed in a rather narrow angular range (18 degrees for both analyzed *Apatura* species while it is much greater in other butterfly species previously studied). The spectral width of the iridescence is small (around 50 nm FWHM for both analyzed *Apatura* species and is much greater in tropical *Morpho* butterflies).

Acknowledgments

We are grateful to Mr. Miloš Bokorov (Faculty of Science, University of Novi Sad, Novi Sad, Serbia) for helping prepare the SEM photographs. Mrs. Anita Lazarević (Center for Electron Microscopy, Faculty of Biology, University of Belgrade, Belgrade, Serbia) assisted in the production of TEM micrographs. Finally, Dejan Stojanović, M.Sc. (Fruška Gora National Park, Sremska Kamenica, Serbia) provided some butterfly specimens for the investigations. The study was financially supported by the Serbian Ministry of Science and Technological Development (projects 141003, 143053, 143050, 45016, 171038, 173038, and 173055).

#141253 - $15.00 USD Received 19 Jan 2011; revised 1 Mar 2011; accepted 1 Mar 2011; published 14 Mar 2011

Defect-guided Airy beams in optically induced waveguide arrays

N. M. Lučić,[1,2] B. M. Bokić,[2] D. Ž. Grujić,[2] D. V. Pantelić,[2] B. M. Jelenković,[2] A. Piper,[2] D. M. Jović,[2] and D. V. Timotijević[2]
[1]*Faculty of Electrical Engineering, University of Belgrade, 73 Bulevar kralja Aleksandra, 11120 Belgrade, Serbia*
[2]*Institute of Physics, University of Belgrade, P.O. Box 68, 11001 Belgrade, Serbia*
(Received 31 October 2013; published 6 December 2013)

We demonstrate both theoretically and experimentally that a finite Airy beam changes its trajectory and shape in optically induced waveguide arrays consisting of different kinds of defects. The propagation dynamics and beam acceleration are controlled with positive and negative defects, and appropriate refractive index change. An additional class of discrete beams and Airy defect modes are demonstrated.

DOI: 10.1103/PhysRevA.88.063815 PACS number(s): 42.25.Bs, 42.65.Jx, 42.82.Et

I. INTRODUCTION

Self-accelerating Airy beams were first demonstrated in quantum mechanics [1] as a dispersion-free solution of the Schrödinger equation. By means of an important link between quantum mechanics and paraxial wave optics, Airy beams have been recently transferred into an optical field [2,3]. They remain invariant along parabolic trajectories and attract a great deal of interest because of their unique properties, including transverse acceleration [4,5], nondiffraction [6,7], and self-reconstruction [8,9]. Such features make these beams useful for applications ranging from guiding and manipulation of microparticles [5] and producing curved plasma channels [10] to dynamically routing surface plasmon polaritons [11,12] and frequency generation [13].

One reason for interest in these beams is their potential application in nonlinear optics regimes: nonlinear interaction of light with some material and a study of accelerating beam dynamics inside nonlinear media. The behavior of Airy beams propagating from a nonlinear medium to a linear medium was studied in Ref. [14]. Formation of self-trapped accelerating optical beams is demonstrated with different self-focusing nonlinearities [15], ranging from Kerr and saturable to quadratic [16,17], and also with an optically induced refractive-index gradient [18]. Recent experimental realization of electron Airy beams [19] opens a novel ways of manipulating Airy beams with various magnetic or electric potentials. Although nondiffracting beams are not stationary solutions of the Schrödinger equation with introduction of uniform waveguide arrays, their modified counterparts are shown to exist and remain nondiffracting [20]. Similarly asymptotic preservation of a free accelerating property is observed [21] with Airy beam introduced in uniform waveguide arrays. This gave us motivation to study the impact of defects in waveguide arrays on uniform waveguide array counterparts of Airy beams.

In this paper, we investigate and analyze both theoretically and experimentally the active control of self-accelerating Airy beams with an optically induced waveguide array consisting of different kinds of defects. Various laser-written waveguide arrays are produced in Fe:$LiNbO_3$ crystal, with periodic refractive index change and appropriate defect guides. We consider how the positive and negative defects [22] influence the beam self-bending as well as reduction of the beam acceleration. In general, we find that with a modification of the refractive index change, Airy beam acceleration can be reduced to the discrete beams. However, close to the defect guides, the beam dynamics changes completely: the beams experience a strong repulsion from the negative defect, while in the presence of the positive defect they form simple localized waves.

II. EXPERIMENTAL REALIZATION AND THEORETICAL MODELING OF AIRY BEAM PROPAGATION IN WAVEGUIDE ARRAYS

We use an iron-doped (0.05%) Fe:$LiNbO_3$ crystal with $0.5 \times 3 \times 10$ mm^3 dimensions. Waveguides are fabricated using the laser-writing system at a laser wavelength of 473 nm, which induces an appropriate structure change in the material [see the schematic diagram in Fig. 1(a)]. By moving the sample with respect to the perpendicular laser beam, a continuous modification of the refractive index is obtained enabling light guiding. The beam is focused by the 50× microscope objective with a numerical aperture (NA) of 0.55. Our sample has waveguides of approximately 10 μm width, with spacing between the centers of the adjacent waveguides of $d = 20\,\mu$m. We fabricate various one-dimensional waveguiding systems with a refractive index change of $\Delta n \sim 1 \times 10^{-4}$, while two of the guides are fabricated with either a lower (negative defect) or higher refractive index change (positive defect), achieved by a variation of the writing velocity. Experimental setup for the investigation of Airy beam propagation in such waveguide arrays is shown in Fig. 1(b). For the creation of the Airy beam, an initial Gaussian beam from a 532 nm laser is projected through a cubic phase mask onto a spatial light modulator (SLM). The beam is then Fourier transformed and the 8 μW input Airy beam, roughly 10 μm wide in the main lobe, is launched to the front face of the crystal. The output intensity pattern, appearing at the end face of the crystal, is real time observed by means of a charge-coupled-device (CCD) camera. The intensity pattern evolution along the propagation direction (z axis) through the crystal is obtained with another CCD camera mounted above the sample, parallel to the x-z crystal plane. The camera records scattered light from the crystal, with the integration time of about 2 min.

To theoretically model Airy beam propagation in a waveguide array, along the propagation distance z, we consider the nonlinear Schrödinger equation

$$i\frac{\partial E}{\partial z} = -\frac{1}{2}\frac{\partial^2 E}{\partial x^2} - V(x)E, \tag{1}$$

where E is a slowly varying envelope, $V(x) = n_s - \Delta n \cos^2(\pi x/d)$ is the periodic refractive-index profile of the

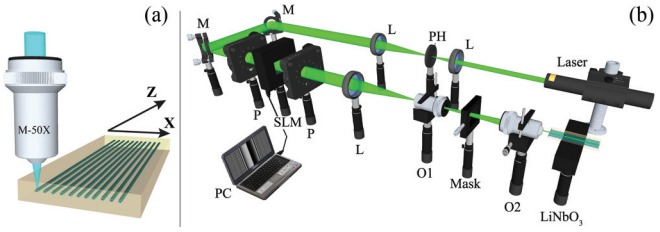

FIG. 1. (Color online) Experimental setup for an investigation of Airy beam propagation effects in waveguide arrays. (a) Scheme of the laser-writing waveguide arrays process in $LiNbO_3$ crystal. (b) Schematic of the experimental setup. Light from a 532 nm laser is expanded and phase modulated by a spatial light modulator (SLM). The beam is Fourier transformed and input into an $LiNbO_3$ crystal, and imaged into a CCD camera. L-lens, PH- pinhole, M-mirror, O-objective, PC-computer.

array with the lattice period d, n_s is a bulk material refractive index, and Δn is the optically induced refractive index change.

We investigate the propagation dynamics of Airy beams in optically induced waveguide arrays, with emphasis on the competition between the acceleration and self-bending propagation properties of Airy beams, and the trend of waveguide arrays to form discrete wave filaments. The propagation characteristics of Airy beams in waveguide arrays with and without defects are considered both theoretically and experimentally. We compare our experimental results to numerical simulations, carried out by the split-step Fourier method with the parameters of our experiment. All theoretical results are confirmed experimentally. First, to compare appropriate effects we test the Airy beam propagation in our crystal with no waveguide arrays fabricated. There is a typical Airy beam bending with a transverse displacement at the output, with no diffraction evident in the main lobe, observed both experimentally [Figs. 2(a) and 2(b)] and theoretically Fig. 2(c), after 10 mm of propagation.

Next, keeping all conditions unchanged, the Airy beam is launched in the waveguide arrays fabricated in our crystal, with the main lobe positioned in one waveguide (an incident waveguide). When refractive index change is optically induced, the Airy beam, which remains self-similar during propagation and has a ballistic trajectory, can interact with the neighboring waveguides. One can see that the bending of the main lobe of the Airy beam is weaker [Figs. 2(d)–2(f)], in comparison with the uniform case [Figs. 2(a)–2(c)]. Also, the presence of the waveguide arrays leads to a creating beam that propagates similar to the discrete waves. With appropriate refractive index change the output position of the Airy beam moves downward, indicating suppressed acceleration of the Airy beam, and it forms the various kinds of discrete structures. A series of numerical investigations are also performed to manipulate Airy beam acceleration with different refractive index change (see Sec. IV, Figs. 4 and 5).

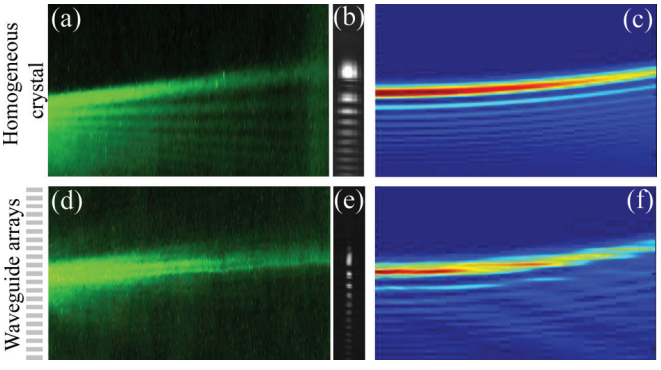

FIG. 2. (Color online) Airy beam propagation in homogeneous $LiNbO_3$ crystal (top row) and waveguide arrays optically induced in the same crystal (bottom row). Intensity plots of Airy beam structures in longitudinal direction during the propagation: (a), (d) experiment; (c), (f) theory. (b), (e) Corresponding intensity distributions at the back face of the crystal. Physical parameters: the crystal length $L =$ 10 mm, lattice constant $d = 20$ μm, width of the main Airy lobe 10 μm.

III. DEFECT-CONTROLLED AIRY BEAM ACCELERATION

We also study the influence of various defect guides on the Airy beam propagation, and active control and manipulation of the beam acceleration with such defects. We show that the balance between self-acceleration properties and defect plays an important role in the evolution of the Airy beam. Our results are shown in Fig. 3, obtained with the same Airy beam as before, but using two different classes of waveguide arrays: containing a single defect with a lower refractive index defect guide (negative defect) and with a higher refractive index defect guide (positive defect). In both cases the main Airy lobe is positioned into the defect guides, at the input. First, we consider waveguide arrays with negative defects and observe strong beam repulsion from such defects [Figs. 3(a)–3(c)]. But, shifting the main lobe position to the waveguide close to the defect channel, one can observe a typical discrete surface waves (not shown). However, the Airy beam propagation is drastically changed in the presence of a positive defect guide so the formation of simple localized waves is possible with appropriate positive defects [Figs. 3(d)–3(f)].

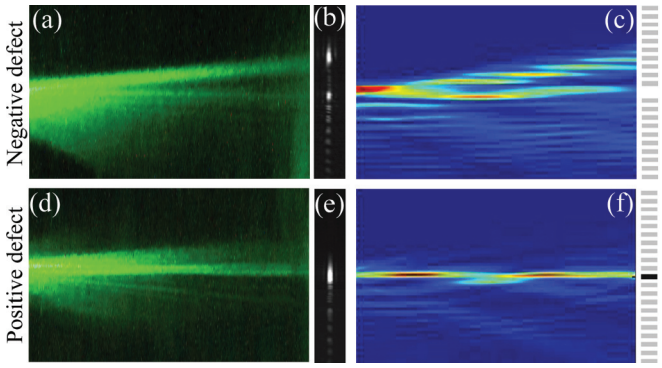

FIG. 3. (Color online) Airy beam propagation in waveguide arrays with negative (top row) and positive (bottom row) defects. Intensity plots of Airy beam structures in longitudinal direction during the propagation: (a), (d) experiment; (c), (f) theory. (b), (e) Corresponding intensity distributions at the back face of the crystal. Defect refractive index change is 0 for negative and $2\Delta n$ for positive defect. Other parameters are as in Fig. 1.

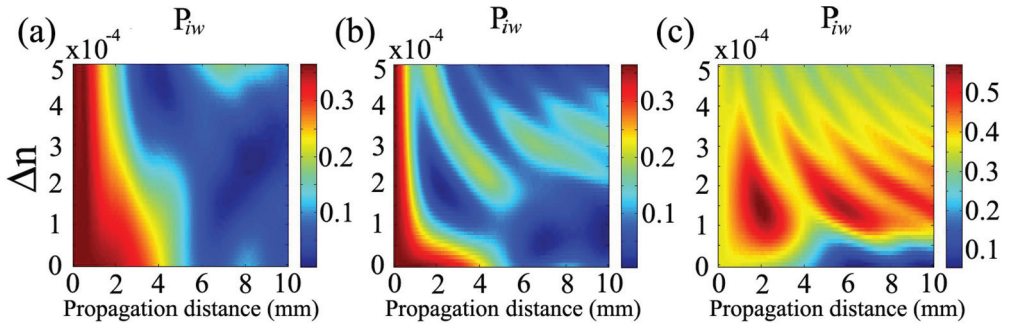

FIG. 4. (Color online) Dependence of the percentage of the Airy beam power in the incident waveguide ($P_{\rm iw}$) on refractive index change Δn and propagation distance for (a) waveguide array, (b) negative defect, and (c) positive defect. Physical parameters are as in Fig. 3.

IV. DEPENDENCE OF AIRY BEAM PROPAGATION ON THE REFRACTIVE INDEX CHANGE

Finally, we study numerically the dynamics of Airy beam propagation in waveguide arrays with various refractive index changes Δn. Again, we compare three cases with positive and negative defects and with no defects. We show that beams exhibit shape-preserving acceleration inside a low refractive index change, but discrete diffraction and formation of various discrete beams occur with an increasing refractive index change, and very rich beam dynamics and amplitude modulations are seen with further increasing of Δn. We monitor a percentage of the Airy beam power in incident waveguide ($P_{\rm iw}$), as the ratio between the power of the beam in the incident waveguide (or defect channel in the case with defect waveguides) and the total power of the Airy beam, at appropriate propagation distance. A dependence of $P_{\rm iw}$ on the refractive index change Δn and propagation distance is presented in Fig. 4 for all three cases: (a) waveguide array, (b) negative defect, and (c) positive defect. Figure 4 clearly demonstrates the impact of waveguide arrays on the formation of discrete beams [Fig. 4(a)]. Also, it demonstrates the impact of the defect inclusion on the acceleration beams, the shape-preserving nature of these beams, and the refractive index change caused with the defect inclusion [Figs. 4(b) and 4(c)]. One can see that discrete beam diffraction is more visible in the case of waveguide arrays without defects. However, an energy localization in the incident waveguide is more pronounced in the waveguide arrays with the negative defect [Fig. 4(b)], and the most with the positive defect [Fig. 4(c)].

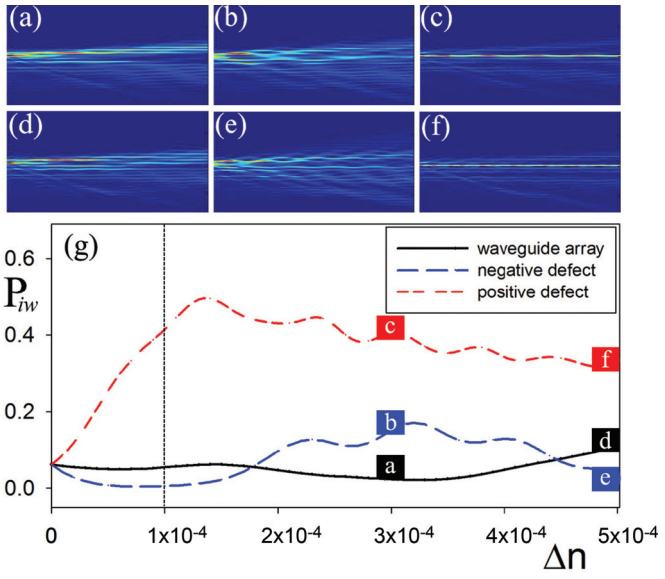

FIG. 5. (Color online) Airy beam propagation dynamics in different waveguide arrays. Typical intensity distributions of Airy beam structures in longitudinal direction during the propagation for waveguide arrays with (a), (d) no defects; (b), (e) negative defect; and (c), (f) positive defect. (a)–(c) $\Delta n = 3 \times 10^{-4}$; (d)–(f) $\Delta n = 5 \times 10^{-4}$. (g) Airy beam power in incident waveguide ($P_{\rm iw}$) at the crystal exit as a function of refractive index change Δn. A vertical dotted line shows experimental refractive index change. Physical parameters are as in Fig. 4.

Figure 5 presents some typical examples of the Airy beam propagation along the longitudinal direction for Δn higher than in our experimental sample. Intensity distributions for two values of refractive index change are shown: $\Delta n = 3 \times 10^{-4}$ (first row) and $\Delta n = 5 \times 10^{-4}$ (second row) for waveguide arrays [Figs. 5(a) and 5(d)], negative defects [Figs. 5(b) and 5(e)], and positive defects [Figs. 5(c) and 5(f)]. In the case without defects, discrete beam formation starts at shorter propagation distance while the refractive index change is increased. With the negative defect guide, increasing Δn, amplitude modulations take place, and they are more pronounced with higher Δn. The beam repulsion from defect guide is also visible. At last, inclusion of a positive defect leads to a more localized energy in the defect guide, but also with some kind of amplitude modulations for higher refractive index change. We monitor Airy beam power in the incident waveguide ($P_{\rm iw}$) at the crystal exit as a function of refractive index change Δn [Fig. 5(g)]. For waveguide arrays with no defects, $P_{\rm iw}$ after 10 mm propagation distance is slightly changed, decreases with lower, but increases with higher Δn. In the case of a negative defect, $P_{\rm iw}$ has maximal values at $\Delta n \sim 3 \times 10^{-4}$. The percentage of the Airy beam power in incident waveguide is higher for positive defect guides, and for parameters we used in our investigation it has maximum at $\Delta n \sim 1.3 \times 10^{-4}$. Also, we investigate defect guides with different refractive index change, as well as different defect size (not shown). Our analysis provides a very good tool for manipulation and controlling of Airy beam acceleration and self -ending properties, as well as appropriate conditions for the formation of discrete, surface or localized waves produced using Airy beams.

V. CONCLUSIONS

In summary, we have demonstrated the propagation dynamics of Airy beams in optically induced waveguide arrays. We have analyzed experimentally and numerically how various waveguides modify acceleration and self-bending properties of such beams, resulting in the discrete beams or Airy defect mode formation. We have demonstrated that the presence of various defect types, their sizes, as well as the refractive index change could drastically change the initial Airy beam shape. The experimental results fully agree with the theoretical analysis. A similar method can be used for control of other accelerating beams, such as parabolic beams. While we performed all our analysis in one-dimensional waveguide arrays, all our findings should also hold in two-dimensional photonic lattices.

ACKNOWLEDGMENTS

This work is supported by the Ministry of Education, Science and Technological development, Republic of Serbia (Projects OI 171036, OI 171038, III 45016).

[1] M. Berry and N. Balazs, Am. J. Phys. **47**, 264 (1979).
[2] G. A. Siviloglou and D. N. Christodoulides, Opt. Lett. **32**, 979 (2007).
[3] G. A. Siviloglou, J. Broky, A. Dogariu, and D. N. Christodoulides, Phys. Rev. Lett. **99**, 213901 (2007).
[4] G. A. Siviloglou, J. Broky, A. Dogariu, and D. N. Christodoulides, Opt. Lett. **33**, 207 (2008).
[5] J. Baumgartl, M. Mazilu, and K. Dholakia, Nat. Photon. **2**, 675 (2008).
[6] I. M. Besieris and A. M. Shaarawi, Opt. Lett. **32**, 2447 (2007).
[7] A. V. Novitsky and D. V. Novitsky, Opt. Lett. **34**, 3430 (2009).
[8] J. Broky, G. A. Siviloglou, A. Dogariu, and D. N. Christodoulides, Opt. Express **16**, 12880 (2008).
[9] H. I. Sztul and R. R. Alfano, Opt. Express **16**, 9411 (2008).
[10] P. Polynkin, M. Kolesik, J. V. Moloney, G. A. Siviloglou, and D. N. Christodoulides, Science **324**, 229 (2009).
[11] P. Zhang, S. Wang, Y. Liu, X. Yin, C. Lu, Z. Chen, and X. Zhang, Opt. Lett. **36**, 3191 (2011).
[12] A. Minovich, A. E. Klein, N. Janunts, T. Pertsch, D. N. Neshev, and Y. S. Kivshar, Phys. Rev. Lett. **107**, 116802 (2011).
[13] T. Ellenbogen, N. Voloch-Bloch, A. Ganany-Padowicz, and A. Arie, Nat. Photon. **3**, 395 (2009).
[14] Y. Hu, S. Huang, P. Zhang, C. Lou, J. Xu, and Z. Chen, Opt. Lett. **35**, 3952 (2010).
[15] I. Kaminer, M. Segev, and D. N. Christodoulides, Phys. Rev. Lett. **106**, 213903 (2011).
[16] A. Lotti, D. Faccio, A. Couairon, D. G. Papazoglou, P. Panagiotopoulos, D. Abdollahpour, and S. Tzortzakis, Phys. Rev. A **84**, 021807(R) (2011).
[17] I. Dolev, I. Kaminer, A. Shapira, M. Segev, and A. Arie, Phys. Rev. Lett. **108**, 113903 (2012).
[18] Z. Ye, S. Liu, C. Lou, P. Zhang, Y. Hu, D. Song, J. Zhao, and Z. Chen, Opt. Lett. **36**, 3230 (2011).
[19] N. Voloch-Bloch, Y. Lereah, Y. Lilach, A. Gover, and A. Arie, Nature **494**, 331 (2013).
[20] O. Manela, M. Segev, and D. N. Christodoulides, Opt. Lett. **30**, 2611 (2005).
[21] R. El-Ganainy, K. G. Makris, M. A. Miri, D. N. Christodoulides, and Z. Chen, Phys. Rev. A **84**, 023842 (2011).
[22] F. Fedele, J. Yang, and Z. Chen, Opt. Lett. **30**, 1506 (2005).

Control of Airy-beam self-acceleration by photonic lattices

Falko Diebel,[1,*] Bojana M. Bokić,[2] Martin Boguslawski,[1] Aleksandra Piper,[2] Dejan V. Timotijević,[2] Dragana M. Jović,[2] and Cornelia Denz[1]

[1]*Institut für Angewandte Physik and Center for Nonlinear Science (CeNoS), Westfälische Wilhelms-Universität Münster, 48149 Münster, Germany*

[2]*Institute of Physics, University of Belgrade, P.O. Box 68, 11001 Belgrade, Serbia*

(Received 3 June 2014; published 2 September 2014)

We demonstrate control over the acceleration of two-dimensional Airy beams propagating in optically induced photonic lattices. Depending on the lattice strength, we observe a slowing-down and suppression of the self-acceleration of Airy beams, as well as a formation of discrete lattice beams. Moreover, we explore the effects of different artificial single-side defects on the propagation and acceleration. For positive defects, the localization of the Airy beam to the defect site is further enhanced, while for negative defects most of the power is repelled from this site.

DOI: 10.1103/PhysRevA.90.033802 PACS number(s): 42.40.Jv, 42.25.Fx, 42.70.Nq

I. INTRODUCTION

Since their discovery in 1979 by Berry and Balazs [1], the fascinating class of Airy beams has attracted huge interest in different fields of physics. Originally, Airy beams were introduced as wave functions, solving the one-dimensional Schrödinger equation for free particles. Their probability density remarkably stays nonspreading under time evolution, while being transversely accelerated to follow a parabolic trajectory. Due to the formal equivalence between the Schrödinger equation in quantum mechanics and the paraxial equation of diffraction in optics, the concepts and solutions can be transferred to optics, where Airy beams can be directly observed and explored in experiments.

The first realization of optical one- and two-dimensional Airy beams [2] initiated an active field of research, leading to a number of systematic investigations of the generation, the manipulation, and the general properties of Airy beams in linear and nonlinear regimes [3–8]. The unique nonspreading and self-accelerating features of Airy beams moreover led to a huge variety of applications, including so-called autofocusing beams [9], optical snowblowers [10], and optical routers [11]. Also the influence of inhomogeneous potentials and the presence of dielectric interfaces on the propagation of Airy beams have been studied in the past [8,12–17].

Controlling the propagation behavior of light with light itself is the key requirement to realize new all-optical guiding and switching architectures. It is well known that the presence of discrete photonic lattice structures dramatically changes the propagation dynamics of light. Thus, one promising approach towards this goal is to tailor the transverse acceleration of two-dimensional optical Airy beams using photonic lattices. Recently, defect guided Airy beams in optically induced one-dimensional waveguide arrays were observed [18]. Despite the fact that Airy beams have been subject to many research activities, the propagation of such accelerated beams inside a two-dimensional optically induced photonic lattice has only been studied numerically with an isotropic refractive index potential assumed [19].

In this paper, we investigate and analyze the propagation dynamics of self-accelerating Airy beams in two-dimensional photonic lattices including defects, both theoretically and experimentally. The lattices were fabricated by optical induction [20] in photorefractive strontium barium niobate and the refractive index modulations are numerically calculated in the anisotropic model [21]. We consider how the discrete lattice changes the shape of the Airy beam and influences its self-acceleration. The propagation dynamics and beam acceleration are controlled by varying the lattice strength. We find that increasing the refractive index modulation reduces the Airy beam acceleration and leads to the formation of discrete lattice beams. Additionally, we realize different defect lattices by embedding two types of single-site defects into the regular lattice and investigate the impact onto the Airy beam. The defects remarkably change the beam dynamics. For the negative defect the beams experience a strong repulsion, while in the presence of the positive defect they form strongly localized waves or defect modes.

II. THEORETICAL BACKGROUND AND EXPERIMENTAL SETUP

To study the propagation characteristics of Airy beams in an optical system with induced photonic lattices, we consider the scaled paraxial equation of diffraction for the electric field Ψ:

$$i\frac{\partial\Psi}{\partial\zeta}+\frac{1}{2}\left(\frac{\partial^2\Psi}{\partial\chi^2}+\frac{\partial^2\Psi}{\partial\nu^2}\right)+\frac{1}{2}k_0^2w_0^2\Delta n^2(I_{\mathrm{indu}})\Psi=0. \quad (1)$$

Here, $\chi=x/\mathrm{w}_0$ and $\nu=y/\mathrm{w}_0$ are the dimensionless transverse coordinates scaled by the characteristic length w_0. $\zeta=z/k\mathrm{w}_0^2$ represents the dimensionless propagation distance with $k=2\pi n/\lambda$. The photonic lattice enters this equation in terms of an intensity-dependent refractive index modulation $\Delta n^2(I_{\mathrm{indu}})$, which is described by the full anisotropic model [21] and precisely models the optical induction process in an externally biased photorefractive crystal. Moreover, Eq. (1) is also suitable to cover nonlinear light propagation when the inducing intensity becomes a function of the field Ψ itself. In this contribution, however, we restrict ourselves to linear effects.

*Corresponding author: falko.diebel@uni-muenster.de

For the case of linear light propagation in homogenous media, where $\Delta n^2 = 0$, the wave equation (1) can always be separated into two parts, each depending only on one transverse coordinate, χ or ν, respectively. Consequently, also the solution Ψ separates and can be written as product in the following form: $\Psi(\chi,\nu,\zeta) = \psi(\chi,\zeta)\psi(\nu,\zeta)$, where ζ is the longitudinal coordinate. As first shown in Ref. [1], each part of the wave equation can be solved by a nondispersive one-dimensional Airy function $\mathrm{Ai}(X)$. Thus, the overall solution of Eq. (1) in two dimensions reads as

$$\Psi(\chi,\nu,\zeta) = \psi(\chi,\zeta)\psi(\nu,\zeta) \tag{2}$$

with

$$\psi(X,\zeta) = \mathrm{Ai}[X - (\zeta/2)^2]\exp[i(X\zeta/2) - i(\zeta^3/12)] \tag{3}$$

and $X = \{\chi,\nu\}$.

The solution $\Psi(\chi,\nu,\zeta)$ describes a nonspreading, two-dimensional optical Airy beam which is transversely accelerated while propagating along the longitudinal coordinate ζ. At first glance, the acceleration of the wave packets in homogeneous media without any index gradient seems to contradict the Ehrenfest theorem, which states that the center of mass of a wave function moves with constant speed if there is no force acting. Since Ψ is not square integrable, the center of mass cannot be defined. This also implies that the wave function contains infinite energy and extends over the whole space, both being nonphysical [6,22].

We instead have to consider a truncated solution with finite extent and energy, written as $\psi(X,0) = \mathrm{Ai}[X]\exp[a_X X]$, with the positive decay length a_X, typically $a_X \ll 1$. It has been shown that this truncated solution still solves the wave equation (1) and that the distinguished properties of two-dimensional Airy beams are mostly preserved [23]. Although the truncated intensity pattern is now nonspreading only over a limited propagation distance, this easily covers the longitudinal range which is necessary to observe sufficient transverse displacement of the Airy beam.

The characteristics of a two-dimensional optical Airy beam propagating inside a homogeneous medium are shown experimentally in Fig. 1. The transverse intensity distributions of the Airy beam at the front and the back faces of the photorefractive crystal are shown in Figs. 1(b) and 1(c), respectively. In addition, the intensity profile is recorded for a huge set of transverse planes along the crystal to demonstrate the accelerated transverse shift of the Airy beam during propagation. A cross section through this three-dimensional intensity volume along one vertical axis is shown in Fig. 1(a). This picture reveals that the experimentally realized Airy beam follows the expected accelerated trajectory and it proves that the unavoidable truncation with $a_{\chi,\nu} \neq 0$ in the experiment only negligibly affects the beam propagation compared to the ideal case of infinite beams.

A. Optically induced photonic lattices

To experimentally realize the photonic lattices for controlling the acceleration of the Airy beam we use the technique of optical induction [20], which in the past has proved its flexibility to create various types of two- and three-dimensional photonic lattices [24–26]. Moreover, this approach provides a versatile platform to study different fundamental linear and nonlinear propagation effects, such as Anderson localization [27] or discrete lattice and vortex solitons [28,29].

The optical induction method relies on the property of photorefractive materials, e.g., strontium barium niobate (SBN), to locally change their refractive index according to the intensity distribution the crystal is illuminated with [30]. For this reason the resulting refractive index structure is directly linked to the intensity of the induction beam. In all experiments presented in this contribution we require two-dimensional photonic lattices, implying that the induction beam may be conveniently realized by choosing from the wide class of nondiffracting beams [31,32].

For the realization of photonic lattices with the optical induction technique, we use nondiffracting beams characterized by optical fields whose intensity distributions are modulated in the transverse plane and stay unchanged in the longitudinal dimension. Such beams share the property that in Fourier space all contributing field components lie on an infinitely small ring with radius k_t, defining the structure size of the transverse pattern in real space. In particular, we consider a photonic square lattice which would be constituted from superimposing four tilted plane waves. The electric field E_{ndB} then reads as

$$E_{\mathrm{ndB}}(x,y,z) = \sum_{n=1}^{4} E_n e^{ik_t(x\cos\varphi_n + y\sin\varphi_n)} e^{ik_z z}, \tag{4}$$

with $\varphi_n = \pi(2n+1)/4$ and $k^2 = k_t^2 + k_z^2$. To minimize the anisotropic response of the photorefractive effect, the induction beam is rotated by 45°.

Figure 1(d) shows the recorded intensity distribution of the experimentally realized nondiffracting beam which is used to optically induce the two-dimensional square lattice. The lattice period $\Lambda = \pi/k_t \approx 25\mu\mathrm{m}$ is chosen to exactly match the distance between the main and the next neighboring lobes of the Airy beam. To realize different lattice strengths Δn, we utilize that the optically induced refractive index modulation in SBN builds up with time. By illuminating the crystal with the writing beam intensity for different times we thus are able to control the depths of the index modulation. To verify that the appropriate photonic lattice is actually induced, we illuminate the front face of the crystal with a plane wave after the writing process was completed. The initially homogeneous intensity of the plane wave is redistributed by the imprinted refractive index modulation to be locally increased at regions of higher refractive index. Thus, by recording the intensity at the back face of the crystal we can visualize the written photonic structure [Fig. 1(e)] [24].

B. Experimental setup and numerical methods

All experiments were carried out using the experimental setup sketched in Fig. 1(f). The beam from a frequency-doubled, continuous wave $\mathrm{Nd:YVO_4}$ laser emitting at a wavelength of $\lambda = 532\,\mathrm{nm}$ is divided into two separate beams, each illuminating a high-resolution, programmable phase-only spatial light modulator (SLM). The first modulator (SLM1), in combination with the following two lenses and the Fourier mask, is employed to shape the nondiffracting induction beam. We address a specially calculated phase pattern to this SLM

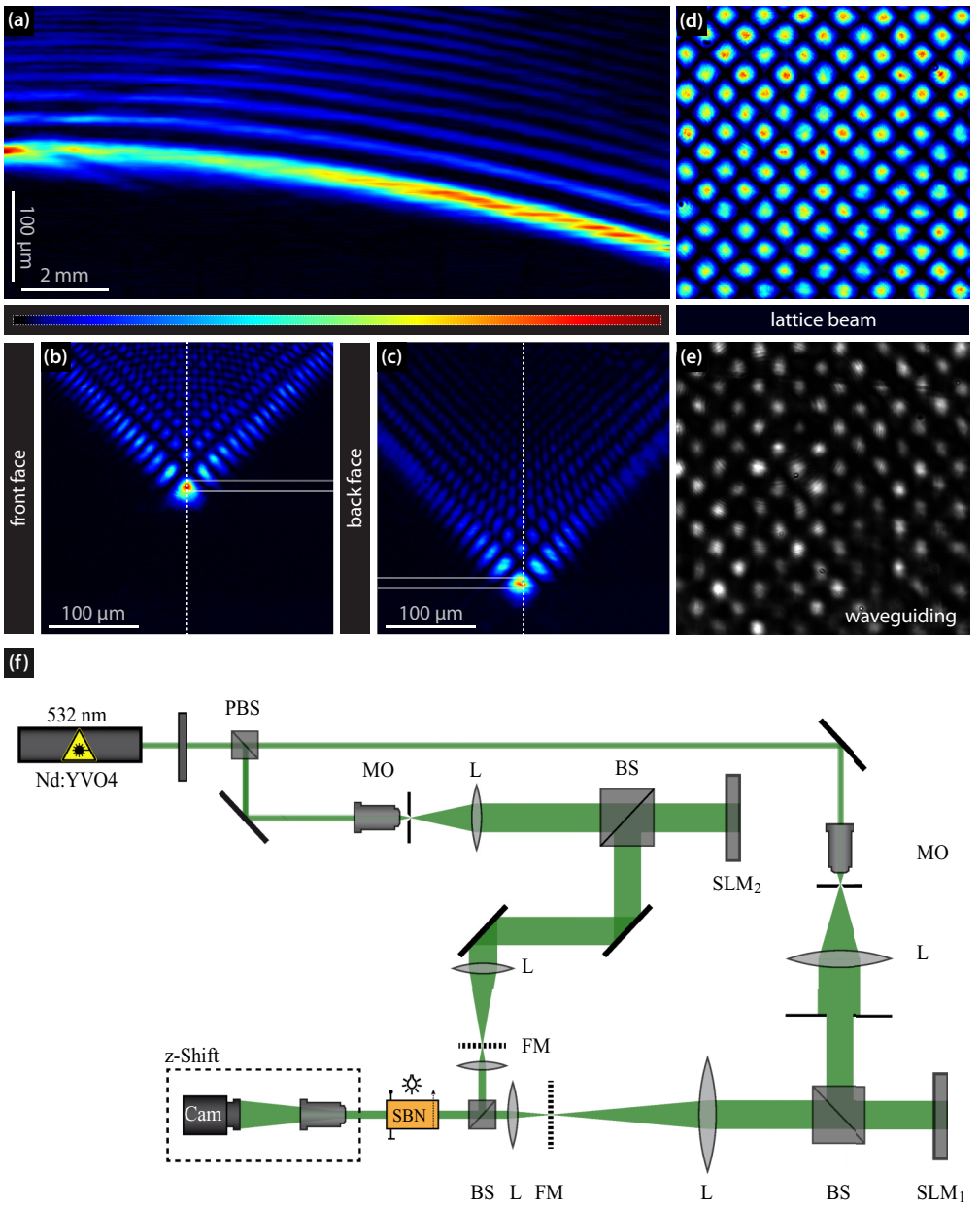

FIG. 1. (Color online) Experimental realization of two-dimensional Airy beams and photonic lattices. (a) Experimentally recorded profile during propagation, (b) intensity distribution of the Airy beam at the front face, and (c) intensity distribution at the back face. (d) Intensity pattern of the induction beam; (e) picture of the induced refractive index using wave guiding. (f) Experimental setup: (P)BS, (polarizing) beam splitter; FM, Fourier mask; L, lens; MO, microscope objective; SBN, strontium barium niobate crystal; and SLM, spatial light modulator.

which allows us to modulate the phase and the amplitude of the incident plane wave simultaneously [33]. Thereby, we obtain the complex field of the desired nondiffracting beam. Afterward, this modulated beam illuminates the 20-mm-long photorefractive $Sr_{0.60}Ba_{0.40}Nb_2O_6$ (SBN:Ce) crystal, which is externally biased with an electric dc field of $E_{ext} \approx 2000\,V/cm$ aligned along the optical c axis. To minimize the feedback of the written refractive index structure onto the induction beam itself, the induction beam is set to be ordinarily polarized with respect to the crystal's optical c axis. The high polarization anisotropy in the electro-optic coefficients of SBN:Ce [34], however, allows us to induce sufficient refractive index modulations to substantially affect the propagation of the extraordinarily polarized Airy beam. The Airy beam is realized in the same manner by directly encoding the complex field calculated in real space with Eq. (2) onto the second modulator (SLM2). To accurately overlay the two beams in the crystal, a beam splitter is placed directly in front of the SBN crystal. In addition, by illuminating the crystal homogeneously with white light, we can erase written refractive index modulations. By means of an imaging lens and a camera mounted on a translation stage we can record the intensity distribution in different transverse planes.

We support our experiments with comprehensive numerical simulations by solving the paraxial wave equation (1), which models the light propagation in media with inhomogeneous

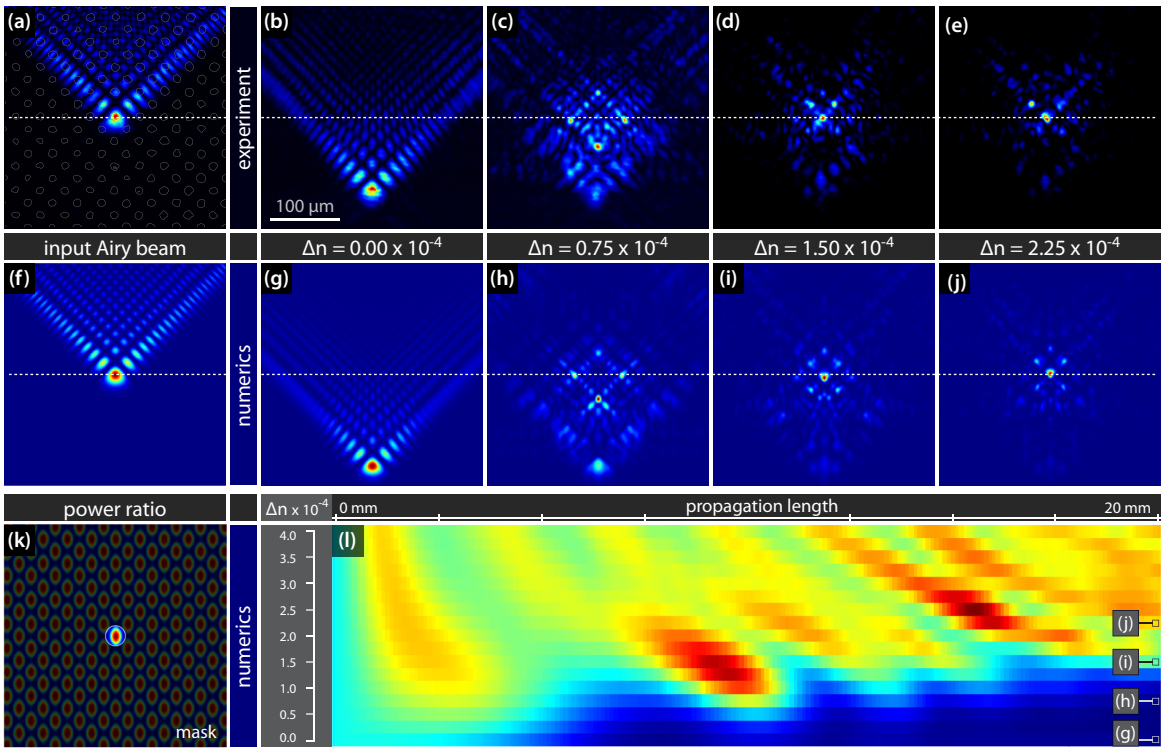

FIG. 2. (Color online) Airy beam propagation in a regular diamond lattice. (a), (f) Input Airy beams at the front crystal face in experiment and numerics [the layout of the lattice beam is indicated by open circles in panel (a)]. (b)–(e) Experimental recorded intensity distributions at the back face for different refractive index change Δn; (g)–(j) corresponding numerical results. (k) The shaded area represents the mask for the calculation of power ratio. (l) Dependance of the percentage of the Airy beam power in the incident waveguide on refractive index change Δn and propagation length z.

refractive index modulations. The resulting optically induced index modulation in the photorefractive material is represented by $\Delta n^2(I_{\mathrm{indu}})$, which can be calculated in the full anisotropic model [21] with a relaxation method. Since only linear effects are considered, the inducing intensity I_{indu} is solely given by the intensity of the nondiffracting beam, $I_{\mathrm{indu}} = |E_{\mathrm{ndB}}|^2$ [cf. Eq. (4)]. Even though the paraxial wave equation stays in the linear regime, it is not solvable analytically and we need to rely on proven beam propagation methods. The propagation equation (1) is solved numerically, using a split-step Fourier method described earlier in Ref. [35,36].

III. TWO-DIMENSIONAL AIRY BEAMS IN PHOTONIC LATTICES

In this section, we investigate the influence of an optically induced photonic lattice onto the self-acceleration of two-dimensional optical Airy beams. We set our focus on the competition between the self-bending propagation of Airy beams and the waveguiding and discrete diffraction effects of the photonic lattice. Therefore, we successively increase the strength of the induced refractive index modulation and observe the effect on the beam acceleration. While increasing the lattice strength, the Airy beam more efficiently excites different linear Bloch modes of the lattice which hinders the acceleration during propagation of the undisturbed Airy beam. This results in an effectively slowed down acceleration, which for a certain value was effectively stopped completely.

Figure 2 summarizes our results with respect to the propagation of the Airy beam inside a regular photonic lattice. The top row [Figs. 2(a)–2(e)] contains our experimental results, while the corresponding numerical simulations are shown in the second row [Figs. 2(f)–2(j)]. The first two columns recap the typical transverse displacement of the Airy beam that propagated between the front face [Figs. 2(a) and 2(f)] and the back face [Figs. 2(b) and 2(g)] of the homogenous crystal. Now, the Airy beam is launched into the induced photonic lattice with the main lobe exactly located at one lattice site. As the refractive index modulation strength growths, the interaction of the Airy beam with the lattice sites becomes stronger and consequently the bending of the Airy beam is decreased. Our experimental results [Figs. 2(c)–2(e)], as well as our numerics [Figs. 2(h)–2(j)] clearly show the frustration of the self-acceleration of the Airy beam. Depending on the different lattice strengths, various kinds of discrete structures arise until the lattice finally suppresses the acceleration of the Airy beam completely. Most of the energy then stays in the lattice site, where the main lobe of the Airy beam was initially launched.

To get a more detailed insight into the propagation dynamics, we monitor the ratio between the power guided in the central waveguide and the total power of the Airy beam as a function of the lattice strength and the propagation distance. In Fig. 2(l) the numerical results for this power ratio are shown. With this reduced representation we are able to illustrate the key signature of the complex evolution of the Airy beam during the propagation for the different lattice strengths. It illustrates,

spatially resolved, how much energy is guided in the central lattice site and thus how strong the Airy beam acceleration is frustrated by the lattice. The shaded area in Fig. 2(k) represents the mask to calculate the power in the central waveguide. This graph clearly demonstrates the impact of optically induced photonic lattice on the formation of discrete structures, as well as suppression of the acceleration and bending of the Airy beam. For certain values of Δn one can see oscillations of the beam power in the central waveguide along the propagation distance. This is due to the self-bending property of Airy beams and the influence of the central waveguide not only on the main lobe but also on other lobes that overlap with this particular waveguide along the propagation. As a result, the part of their power is monitored in the central waveguide for some propagation distances. For higher refractive index modulations Δn, one can observe the localization of most of the beam power to central waveguide as the beam leaves the crystal. Again, to experimentally control the index modulation depth we take advantage of the time-dependent buildup of the induced lattice, which grows monotonously with the writing time.

In contrast to a corresponding situation of one-dimensional Airy beams propagating in a waveguide array [18], here the localization of the two-dimensional Airy beams at the output strongly depends on the strength of the photonic lattice, which also can be seen at the right edge of Fig. 2(l). This different behavior can be explained by the fact that in two dimensions each lattice site has four next neighbors (in the one-dimensional case only two). Thus, here the interaction of the Airy beam which is launched with its main lobe exactly placed at one lattice site is more pronounced.

This dependency of the beam localization on the lattice strength, for example, can be harnessed to realize a fast switch or router for Airy beams based on their polarization. The optical induction in SBN leads to an internal space charge field that modulates the refractive index via the linear electrooptic effect. Because of the strong polarization anisotropy of the electrooptic coefficients, $r_{13} \ll r_{33}$ [34], the lattice strength experienced by the Airy beam strongly depends on the polarization. Consequently, the shape as well as center of mass of the intensity distribution that leaves the photonic lattice can be controlled solely by changing the polarization of the incoming Airy beam.

We also study the transition of the Airy beam that leaves the SBN crystal with the inscribed photonic lattice to a linear medium (e.g., air) and its further propagation. It has been shown recently that only an Airy beam initially driven by a particular self-defocusing nonlinearity experiences anomalous diffraction and can maintain its shape over a long distance after exiting the nonlinear medium [37]. In our crystal with optically induced photonic lattice we could not observe that the exiting field pattern propagates robustly with the properties characteristic for Airy beams over a long distance after the crystal.

IV. AIRY BEAM PROPAGATION IN PHOTONIC LATTICE WITH DIFFERENT DEFECTS

Besides the influence of regular photonic lattices on the behavior of two-dimensional Airy beams, we investigate the propagation effects caused by defects embedded in these lattices. In particular, we consider two-dimensional single-site defect lattices with positive or negative variable defect strengths.

To realize the different defect lattices, we use a well-localized zero-order nondiffracting Bessel beam to locally increase or decrease the refractive index modulation at one selected lattice site. It is important that the resulting defect lattice remains two-dimensional. Therefore, the lattice is induced by an effective intensity distribution resulting from an incoherent superposition of the discrete and the Bessel nondiffracting beam. This incoherent superposition is essential to get rid of the phase relation between both beams, which otherwise would lead to additional undesired intensity modulations due to interference. To avoid the coherent effects, we illuminate the crystal one after the other with the discrete and the Bessel beam, respectively. Thereby, we utilize the high dielectric response time of the SBN crystal for the used intensities that allows for switching frequencies in the order of seconds. As shown in the past, this multiplexing method is capable of fabricating a whole set of two-dimensional aperiodic structures, superlattices, and defect lattices [38–40]. In order to realize negative defects, the index modulation at one selected lattice site is decreased by switching to defocusing nonlinearity while the crystal is illuminated with the Bessel beam. This is achieved by applying the static electric field antiparallel to the optical c axis [40].

Figure 3 illustrates the basic scheme of the defect realization using multiplexed nondiffracting beams. The regular lattice is induced with the intensity distribution shown in Fig. 3(a). Simultaneously, the Bessel beam intensity shown in Fig. 3(b) increases or decreases the induced refractive index at one lattice site, depending on the direction of the applied electrical field. The resulting effective intensity distributions for the positive and negative defect lattices are shown in Figs. 3(c) and 3(d), respectively. Figures 3(e) and 3(f) show the numerically calculated refractive index modulations that result for both types of defect lattices.

Once the defect lattices are realized, we finally study how the different defects influence the Airy beam propagation and acceleration. We keep all parameters from the previous

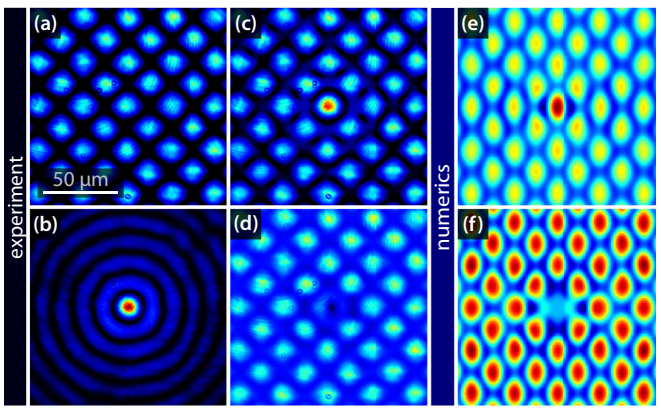

FIG. 3. (Color online) Defect generation in optically induced photonic lattice. (a) Experimental realization of the diamond lattice, (b) the Bessel beam, (c) the positive defect lattice, and (d) the negative defect lattice. Numerical realization of (e) positive and (f) negative lattice defects.

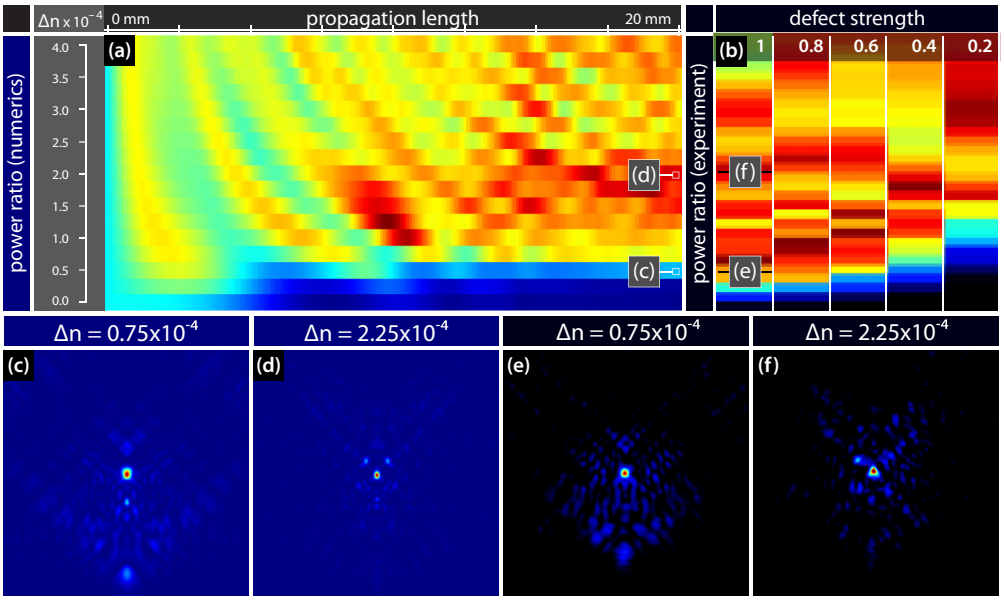

FIG. 4. (Color online) Airy beam propagation in different positive defect lattices. (a) Numerical results for the dependance of the Airy beam power propagating in defect site on refractive index change Δn and propagation length z. (b) Experimentally observed percentage of the Airy beam power propagating in the defect site as a function of the refractive index change Δn and defect strength S_{d}. (c), (d) Exemplary numerical results of Airy beam intensity distribution at the back crystal face. (e), (f) Experimentally recorded output intensity distributions. The letters in panels (a) and (b) indicate the corresponding intensity pictures.

experiments, but change the sign of the defect to both positive and negative. The Airy beam is positioned with its main lobe exactly located at the defect site. For the different defects, we record the intensity profiles of the propagated Airy beam at the back face of the crystal and monitor the percentage of the power guided in the central waveguide, as described previously.

In Figs. 4 and 5 we show our results for the positive and negative defects, respectively. The numerical results for the power ration as a function of the propagation distance ζ and the refractive index modulation Δn are presented as panels (a) in both figures. We picked two particular cases with $\Delta n = 0.75 \times 10^{-4}$ [panel (c)] and $\Delta n = 2.25 \times 10^{-4}$ [panel (d)] for representation and show the intensity profile at the back face

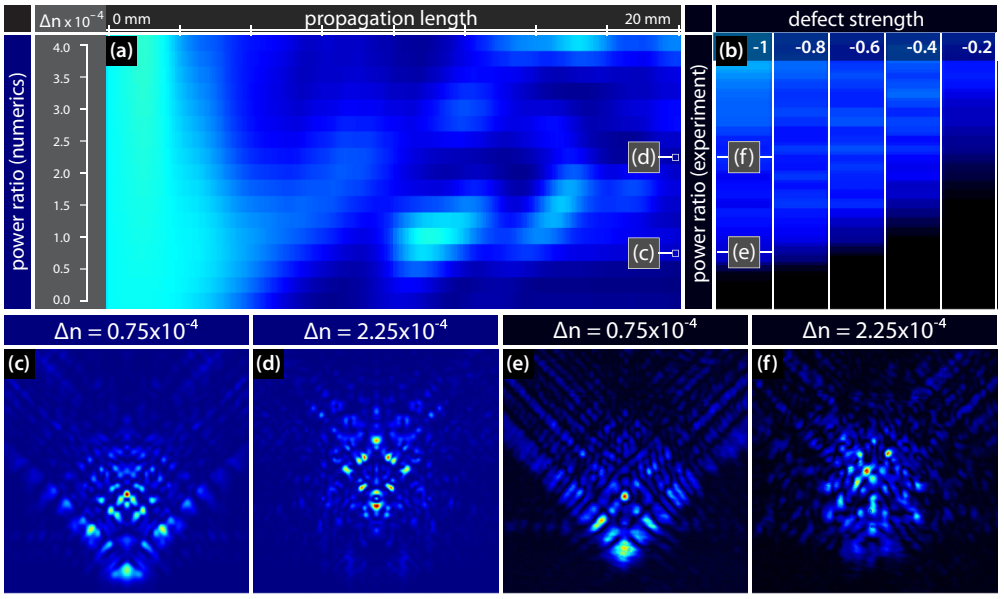

FIG. 5. (Color online) Airy beam propagation in different negative defect lattices. (a) Numerical results for the dependance of the Airy beam power propagating in defect site on refractive index change Δn and propagation length z. (b) Experimentally observed percentage of the Airy beam power propagating in the defect site as a function of the refractive index change Δn and defect strength S_{d}. (c), (d) Exemplary numerical results of Airy beam intensity distribution at the back crystal face. (e), (f) Experimentally recorded output intensity distributions. The letters in panels (a) and (b) indicate the corresponding intensity pictures.

of the crystal. The positions corresponding to these intensity profiles are indicated with the letters (c) and (d) in the power ratio plot (a).

Because in experiments it is not possible to record the intensity pattern inside an inhomogeneous crystal, we are restricted to the profiles at the back face. In Figs. 4(b) and 5(b) the experimentally measured power ratio at the back face is plotted as a function of the refractive index modulation and the defect strength. Therefore, we have repeated the experiments for five different defect strengths for both positive and negative defects and recorded the intensity profile at the back face. The modulus of the defect strength S_d is given by the ratio of the peak intensities of the discrete and the Bessel nondiffracting beam, while the sign is determined by the direction of the applied electric field. In the experiment, we also select the two representative lattice strengths Δn to show the intensity profile at the output of the crystal [panels (e) and (f)]. Again, their positions in the experimental power ratio plot (b) are indicated with the letters (e) and (f).

These results illustrate the strong dependence of the propagation and acceleration properties of the Airy beam on the lattice depths, as well as the defect strength. The positive defect [Fig. 4(a)] strongly enhances the localization of the Airy beam, while for the negative defect [Fig. 5(a)] the power guided in the defect site is significantly reduced and finally completely repelled. A similar behavior was reported earlier for one-dimensional Airy beams propagating in a waveguide array with defects [18], and it was predicted that it qualitatively agrees with the results in two dimensions.

V. CONCLUSION

In summary, we have demonstrated the control over the propagation dynamics of two-dimensional Airy beams in optically induced photonic lattices. We have shown, both theoretically and experimentally, that depending on the depths of the induced lattice, the acceleration and the bending of the Airy beam are strongly affected. For increasing refractive index contrast, different discrete patterns arise and for a certain value the acceleration of the beam is effectively stopped. Moreover, we demonstrated the influence of various single-side defects on the propagation dynamics of the Airy beam. The defect strength as well as the lattice depth dramatically change the initial Airy beam shape and its self-bending. For positive defects, the localization is remarkably increased, while for negative defects, the situation is changed to transport nearly no power along the defect site. All presented experimental results fully agree with the supporting numerical simulations. Our results can readily be generalized to other kinds of optically induced lattices and defect types, including more complex or even three-dimensional lattices. Also other classes of self-accelerated optical beams can be controlled using the presented ideas and methods.

ACKNOWLEDGMENTS

This work is partially supported by the German Academic Exchange Service (Project 56267010) and Ministry of Education, Science and Technological Development, Republic of Serbia (Project OI 171036).

[1] M. V. Berry and N. L. Balazs, Am. J. Phys. **47**, 264 (1979).
[2] G. A. Siviloglou, J. Broky, A. Dogariu, and D. N. Christodoulides, Phys. Rev. Lett. **99**, 213901 (2007).
[3] T. Ellenbogen, N. Voloch-Bloch, A. Ganany-Padowicz, and A. Arie, Nat. Photonics **3**, 395 (2009).
[4] D. Abdollahpour, S. Suntsov, D. G. Papazoglou, and S. Tzortzakis, Phys. Rev. Lett. **105**, 253901 (2010).
[5] A. Chong, W. H. Renninger, D. N. Christodoulides, and F. W. Wise, Nat. Photon. **4**, 103 (2010).
[6] G. A. Siviloglou, J. Broky, A. Dogariu, and D. N. Christodoulides, Opt. Lett. **33**, 207 (2008).
[7] Y. Hu, P. Zhang, C. Lou, S. Huang, J. Xu, and Z. Chen, Opt. Lett. **35**, 2260 (2010).
[8] W. Liu, D. N. Neshev, I. V. Shadrivov, A. E. Miroshnichenko, and Y. S. Kivshar, Opt. Lett. **36**, 1164 (2011).
[9] N. K. Efremidis and D. N. Christodoulides, Opt. Lett. **35**, 4045 (2010).
[10] J. Baumgartl, M. Mazilu, and K. Dholakia, Nat. Photon. **2**, 675 (2008).
[11] P. Rose, F. Diebel, M. Boguslawski, and C. Denz, Appl. Phys. Lett. **102**, 101101 (2013).
[12] N. K. Efremidis, Opt. Lett. **36**, 3006 (2011).
[13] Z. Ye, S. Liu, C. Lou, P. Zhang, Y. Hu, D. Song, J. Zhao, and Z. Chen, Opt. Lett. **36**, 3230 (2011).
[14] S. Chávez-Cerda, U. Ruiz, V. Arrizón, and H. M. Moya-Cessa, Opt. Express **19**, 16448 (2011).
[15] N. K. Efremidis and I. D. Chremmos, Opt. Lett. **37**, 1277 (2012).
[16] I. D. Chremmos and N. K. Efremidis, Phys. Rev. A **85**, 063830 (2012).
[17] I. D. Chremmos and N. K. Efremidis, J. Opt. Soc. Am. A **29**, 861 (2012).
[18] N. M. Lučić, B. M. Bokić, D. Ž. Grujić, D. V. Pantelić, B. M. Jelenković, A. Piper, D. M. Jović, and D. V. Timotijević, Phys. Rev. A **88**, 63815 (2013).
[19] A. Piper, D. V. Timotijević, and D. M. Jović, Phys. Scr. **T157**, 014023 (2013).
[20] N. K. Efremidis, S. Sears, D. N. Christodoulides, J. W. Fleischer, and M. Segev, Phys. Rev. E **66**, 046602 (2002).
[21] A. A. Zozulya and D. Z. Anderson, Phys. Rev. A **51**, 1520 (1995).
[22] I. M. Besieris and A. M. Shaarawi, Opt. Lett. **32**, 2447 (2007).
[23] G. A. Siviloglou and D. N. Christodoulides, Opt. Lett. **32**, 979 (2007).
[24] B. Terhalle, D. Träger, L. Tang, J. Imbrock, and C. Denz, Phys. Rev. E **74**, 057601 (2006).
[25] P. Rose, M. Boguslawski, and C. Denz, New J. Phys. **14**, 033018 (2012).
[26] J. Xavier, P. Rose, B. Terhalle, J. Joseph, and C. Denz, Opt. Lett. **34**, 2625 (2009).
[27] T. Schwartz, G. Bartal, S. Fishman, and M. Segev, Nature (London) **446**, 52 (2007).
[28] J. W. Fleischer, M. Segev, N. K. Efremidis, and D. N. Christodoulides, Nature (London) **422**, 147 (2003).

[29] B. Terhalle, T. Richter, A. S. Desyatnikov, D. N. Neshev, W. Krolikowski, F. Kaiser, C. Denz, and Y. S. Kivshar, Phys. Rev. Lett. **101**, 013903 (2008).
[30] N. V. Kukhtarev, V. B. Markov, S. G. Odulov, M. S. Soskin, and V. L. Vinetskii, Ferroelectrics **22**, 949 (1978).
[31] J. Durnin, J. J. Miceli, and J. H. Eberly, Phys. Rev. Lett. **58**, 1499 (1987).
[32] Z. Bouchal, Czechoslov. J. Phys. **53**, 537 (2003).
[33] J. A. Davis, D. M. Cottrell, J. Campos, M. J. Yzuel, and I. Moreno, Appl. Opt. **38**, 5004 (1999).
[34] U. B. Dörfler, R. Piechatzek, T. Woike, M. K. Imlau, V. Wirth, L. Bohatý, T. Volk, R. Pankrath, and M. Wöhlecke, Appl. Phys. B: Lasers Opt. **68**, 843 (1999).
[35] M. R. Belić, J. Leonardy, D. V. Timotijević, and F. Kaiser, J. Opt. Soc. Am. B **12**, 1602 (1995).
[36] M. R. Belić, M. S. Petrović, D. M. Jović, A. Strinić, D. Arsenović, K. Motzek, F. Kaiser, P. Jander, C. Denz, M. Tlidi, and P. Mandel, Opt. Express **12**, 708 (2004).
[37] Y. Hu, S. Huang, P. Zhang, C. Lou, J. Xu, and Z. Chen, Opt. Lett. **35**, 3952 (2010).
[38] F. Diebel, D. Leykam, M. Boguslawski, P. Rose, C. Denz, and A. Desyatnikov, Appl. Phys. Lett. **104**, 261111 (2014).
[39] M. Boguslawski, A. Kelberer, P. Rose, and C. Denz, Opt. Express **20**, 27331 (2012).
[40] M. Boguslawski, A. Kelberer, P. Rose, and C. Denz, Opt. Lett. **37**, 797 (2012).

Soliton formation by decelerating interacting Airy beams

Falko Diebel,[1,*] Bojana M. Bokić,[2] Dejan V. Timotijević,[2] Dragana M. Jović Savić,[2] and Cornelia Denz[1]

[1]*Institut für Angewandte Physik and Center for Nonlinear Science (CeNoS), Westfälische Wilhelms-Universität Münster, 48149 Münster, Germany*
[2]*Institute of Physics, University of Belgrade , P.O. Box 68, 11080 Belgrade, Serbia*
[*]*falko.diebel@uni-muenster.de*

Abstract: We demonstrate a new type of soliton formation arising from the interaction of multiple two-dimensional Airy beams in a nonlinear medium. While in linear regime, interference effects of two or four spatially displaced Airy beams lead to accelerated intensity structures that can be used for optical induction of novel light guiding refractive index structures, the nonlinear cross-interaction between the Airy beams decelerates their bending and enables the formation of straight propagating solitary states. Our experimental results represent an intriguing combination of two fundamental effects, accelerated optical beams and nonlinearity, together enable novel mechanisms of soliton formation that will find applications in all-optical light localization and switching architectures. Our experimental results are supported by corresponding numerical simulations.

OCIS codes: (190.4420) Nonlinear optics, transverse effects in; (190.6135) Spatial solitons; (350.5500) Propagation; (190.5330) Photorefractive optics; (140.3300) Laser beam shaping; (070.6120) Spatial light modulators

References and links

1. M. V. Berry and N. L. Balazs, "Nonspreading wave packets," Am. J. Phys. **47**, 264 (1979).
2. G. A. Siviloglou and D. N. Christodoulides, "Accelerating finite energy Airy beams," Opt. Lett. **32**, 979–981 (2007).
3. G. A. Siviloglou, J. Broky, A. Dogariu, and D. N. Christodoulides, "Observation of Accelerating Airy Beams," Phys. Rev. Lett. **99**, 213901 (2007).
4. J. Broky, G. A. Siviloglou, A. Dogariu, and D. N. Christodoulides, "Self-healing properties of optical Airy beams," Opt. Express **16**, 12880–12891 (2008).
5. J. Baumgartl, M. Mazilu, and K. Dholakia, "Optically mediated particle clearing using Airy wavepackets," Nat. Photonics **2**, 675–678 (2008).
6. M. A. Bandres, I. Kaminer, M. Mills, B. Rodríguez-Lara, E. Greenfield, M. Segev, and D. N. Christodoulides, "Accelerating Optical Beams," Opt. Photonics News **24**, 30–37 (2013).
7. A. Mathis, F. Courvoisier, L. Froehly, L. Furfaro, M. Jacquot, P. A. Lacourt, and J. M. Dudley, "Micromachining along a curve: Femtosecond laser micromachining of curved profiles in diamond and silicon using accelerating beams," Appl. Phys. Lett. **101**, 071110 (2012).
8. P. Polynkin, M. Kolesik, J. V. Moloney, G. A. Siviloglou, and D. N. Christodoulides, "Curved Plasma Channel Generation Using Ultraintense Airy Beams," Science **324**, 229–232 (2009).
9. A. Chong, W. H. Renninger, D. N. Christodoulides, and F. W. Wise, "Airy-Bessel wave packets as versatile linear light bullets," Nat. Photonics **4**, 103–106 (2010).
10. N. K. Efremidis, "Airy trajectory engineering in dynamic linear index potentials," Opt. Lett. **36**, 3006–3008 (2011).
11. N. K. Efremidis, "Accelerating beam propagation in refractive-index potentials," Phys. Rev. A **89**, 023841 (2014).

#246589 Received 23 Jul 2015; accepted 28 Jul 2015; published 8 Sep 2015

12. K. G. Makris, I. Kaminer, R. El-Ganainy, N. K. Efremidis, Z. Chen, M. Segev, and D. N. Christodoulides, "Accelerating diffraction-free beams in photonic lattices," Opt. Lett. **39**, 2129–2132 (2014).
13. S. Chávez-Cerda, U. Ruiz, V. Arrizón, and H. M. Moya-Cessa, "Generation of Airy solitary-like wave beams by acceleration control in inhomogeneous media," Opt. Express **19**, 16448–16454 (2011).
14. N. M. Lučić, B. M. Bokić, D. Z. Grujić, D. V. Pantelić, B. M. Jelenković, A. Piper, D. M. Jović, and D. V. Timotijević, "Defect-guided Airy beams in optically induced waveguide arrays," Phys. Rev. A **88**, 063815 (2013).
15. F. Diebel, B. M. Bokić, M. Boguslawski, A. Piper, D. V. Timotijević, D. M. Jović, and C. Denz, "Control of Airy-beam self-acceleration by photonic lattices," Phys. Rev. A **90**, 033802 (2014).
16. P. Rose, F. Diebel, M. Boguslawski, and C. Denz, "Airy beam induced optical routing," Appl. Phys. Lett. **102**, 101101 (2013).
17. R. Bekenstein and M. Segev, "Self-accelerating optical beams in highly nonlocal nonlinear media," Opt. Express **19**, 23706–23715 (2011).
18. Y. Hu, S. Huang, P. Zhang, C. Lou, J. Xu, and Z. Chen, "Persistence and breakdown of Airy beams driven by an initial nonlinearity," Opt. Lett. **35**, 3952–3954 (2010).
19. Y. Hu, G. A. Siviloglou, P. Zhang, N. K. Efremidis, D. N. Christodoulides, and Z. Chen, *Nonlinear Photonics and Novel Optical Phenomena*, vol. 170 of *Springer Series in Optical Sciences* (Springer New York, New York, NY, 2012).
20. R. Driben, V. V. Konotop, and T. Meier, "Coupled Airy breathers," Opt. Lett. **39**, 5523–5526 (2014).
21. Y. S. Kivshar and G. P. Agrawal, *Optical Solitons: From Fibers to Photonic Crystals* (Academic Press, San Diego, 2003).
22. C. Denz, M. Schwab, and C. Weilnau, *Transverse-Pattern Formation in Photorefractive Optics*, vol. 188 of *Springer Tracts in Modern Physics* (Springer, Berlin, 2003).
23. F. Lederer, G. I. Stegeman, D. N. Christodoulides, G. Assanto, M. Segev, and Y. Silberberg, "Discrete solitons in optics," Phys. Rep. **463**, 1–126 (2008).
24. B. Terhalle, T. Richter, A. S. Desyatnikov, D. N. Neshev, W. Królikowski, F. Kaiser, C. Denz, and Y. S. Kivshar, "Observation of Multivortex Solitons in Photonic Lattices," Phys. Rev. Lett. **101**, 013903 (2008).
25. F. Diebel, D. Leykam, M. Boguslawski, P. Rose, C. Denz, and A. S. Desyatnikov, "All-optical switching in optically induced nonlinear waveguide couplers," Appl. Phys. Lett. **104**, 261111 (2014).
26. Y. Zhang, M. R. Belić, Z. Wu, H. Zheng, K. Lu, Y. Li, and Y. Zhang, "Soliton pair generation in the interactions of Airy and nonlinear accelerating beams," Opt. Lett. **38**, 4585–4588 (2013).
27. Y. Zhang, M. R. Belić, H. Zheng, H. Chen, C. Li, Y. Li, and Y. Zhang, "Interactions of Airy beams, nonlinear accelerating beams, and induced solitons in Kerr and saturable nonlinear media," Opt. Express **22**, 7160–7171 (2014).
28. I. M. Allayarov and E. N. Tsoy, "Dynamics of Airy beams in nonlinear media," Phys. Rev. A **90**, 023852 (2014).
29. A. A. Zozulya and D. Z. Anderson, "Propagation of an optical beam in a photorefractive medium in the presence of a photogalvanic nonlinearity or an externally applied electric field," Phys. Rev. A **51**, 1520 (1995).
30. J. A. Davis, D. M. Cottrell, J. Campos, M. J. Yzuel, and I. Moreno, "Encoding Amplitude Information onto Phase-Only Filters," Appl. Opt. **38**, 5004–5013 (1999).
31. U. B. Dörfler, R. Piechatzek, T. Woike, M. K. Imlau, V. Wirth, L. Bohatý, T. Volk, R. Pankrath, and M. Wöhlecke, "A holographic method for the determination of all linear electrooptic coefficients applied to Ce-doped strontium-barium-niobate," Appl. Phys. B Lasers Opt. **68**, 843–848 (1999).
32. N. K. Efremidis and D. N. Christodoulides, "Abruptly autofocusing waves," Opt. Lett. **35**, 4045–4047 (2010).
33. D. G. Papazoglou, N. K. Efremidis, D. N. Christodoulides, and S. Tzortzakis, "Observation of abruptly autofo-cusing waves," Opt. Lett. **36**, 1842–1844 (2011).
34. W. Królikowski, C. Denz, A. Stepken, M. Saffman, and B. Luther-Davies, "Interaction of spatial photorefractive solitons," Quantum Semiclassical Opt. J. Eur. Opt. Soc. Part B **10**, 823 (1998).

1. Introduction and motivation

Airy wave packets, first predicted by Berry and Balazs [1] as free-particle solutions of the Schrödinger equation are remarkable objects within the framework of quantum mechanics. The envelope of these wave packets is described by Airy functions, centered around a parabolic trajectory. Their unique ability to freely accelerate during propagation – even in the absence of any external potential – stands out the Airy wave from any other known solution. Airy wave packets were also predicted [2], and then realized [3] in the optical domain. Their special self-healing properties – self-restoration of their canonical form after passing small obstacles – were demonstrated theoretically and experimentally [4]. The unique ballistic-like and self-accelerating properties of the Airy beam made it ideally suited for various applications ranging from particle and cell micromanipulation, optical snow-blowers [5,6], laser micromachining [7]

#246589 Received 23 Jul 2015; accepted 28 Jul 2015; published 8 Sep 2015

and self-bending plasma channels [8] to ultrafast self-accelerating pulses [9].

While the potential of tailored light fields, especially Airy beams, is well recognized in these fields, they are also of significant importance for advances in discrete and nonlinear modern photonics. On the one hand, the influence of inhomogeneous refractive index potentials on Airy beams has been investigated theoretically to design the beam caustics [10–12], on the other hand it was experimentally demonstrated that a linear refractive index gradient or a photonic lattice can be used to control and compensate the Airy beam self-acceleration [13–15]. Another inventive idea shifts the perspective and uses two-dimensional Airy beams itself to optically induce light guiding structures for optical routing and switching of signals [16].

By considering nonlinearity a new degree of freedom is added to the system which leads to interesting new effects of Airy beam propagation investigated in several theoretical and experimental studies [17–20]. One of the most fundamental effect in nonlinear systems is the existence of spatial solitons which represents localized structures that always preserve their shape by the balance between diffraction and nonlinear self-focusing. In optics, they have extensively been studies in various systems, including bulk nonlinear media or discrete systems [21–23], where fundamental solitons or even vortex solitons [24, 25] have been found. The interesting question now is if solitons or solitary structures can arise from the interaction of initially accelerated beams such as Airy beams. Very recently, first numerical studies have started to explore the interaction between two one-dimensional Airy beams in an isotropic idealized nonlinear model [26–28].

In this paper, we investigate the nonlinear interaction of two-dimensional Airy beams experimentally, as well as numerically. Therefore, we introduce advanced experimental methods to synthesize multiple accelerated Airy beams with fully controllable parameters and observe the nonlinear dynamics of this compound optical field in a photorefractive nonlinear crystal, an ideal experimental testbed for nonlinear light-matter interaction. We demonstrate that these interactions lead to solitary structures that arise from nonlinear interaction of two or four involved accelerated Airy beams. Depending on the beam intensity and on different phase configurations of the synthesized beams (in phase or out of phase), either one solitary solution or a pair is observed that propagates almost stable with small intensity modulations (breathing). Moreover, we demonstrate how the synthesized beams propagate in the linear regime, where interference leads to interesting intensity modulations, including tight-focus structures. To precisely describe all our experimental observations in a theoretical framework, we extend and generalize existing concepts to handle multiple Airy beams, as well as nonlinear propagation in the more realistic anisotropic photorefractive model.

2. Theoretical model and numerical methods

To study the propagation characteristics of Airy beams in a nonlinear optical system with intensity dependent refractive index modulations, we consider the scaled paraxial equation of diffraction for the envelope A of the optical field:

$$\mathrm{i}\frac{\partial A}{\partial \zeta}+\frac{1}{2}\left(\frac{\partial^2 A}{\partial \chi^2}+\frac{\partial^2 A}{\partial \nu^2}\right)+\frac{1}{2}k_0^2 w_0^2 \Delta n^2(I)A=0. \tag{1}$$

Here, $\chi = x/\mathrm{w}_0$ and $\nu = y/\mathrm{w}_0$ are the dimensionless transverse coordinates scaled by the characteristic length w_0. $\zeta = z/k\mathrm{w}_0^2$ represents the dimensionless propagation distance with $k = 2\pi n/\lambda$.

In this equation, the nonlinearity is given by an intensity-dependent refractive index modulation $\Delta n^2(I)$, with $I \propto |A|^2$, which is caused by the nonlinear response of a photorefractive medium. Theoretically, it is well described by the electro-optic effect combined with the band transport model, which in our case can be approximated by the full anisotropic model for the

#246589 Received 23 Jul 2015; accepted 28 Jul 2015; published 8 Sep 2015

optically induced space charge potential ϕ, [29]

$$\nabla^2\phi + \nabla\ln(1+I)\cdot\nabla\phi = E_{\text{ext}}\frac{\partial}{\partial x}\ln(1+I) + \frac{k_{\text{B}}T}{e}\left(\nabla^2\ln(1+I) + (\nabla\ln(1+I))^2\right), \quad (2)$$

where the refractive index modulation results from the electro-optic effect as $\Delta n^2 = n_0^4 r_{\text{eff}}\partial_x\phi$, and r_{reff} is the effective electro-optic coefficient.

This model precisely describes the optical induction process in a photorefractive nonlinear medium with applied electric field E_{ext} along the crystal's c-axis and accounts for the orientation anisotropy caused by the resulting directed transport of charge carriers. Moreover, this model is capable to describe the effect of charge carrier diffusion in the internal space charge field. This effects plays an important role for non-zero temperatures T and non-zero dark conductivity of the crystal, and leads to effects such as nonlinear soliton steering in bulk nonlinear media.

2.1. Two-dimensional Airy beams

In the linear regime, where $\Delta n(I) = 0$ holds, the wave equation can be solved by two-dimensional truncated Airy beam solutions that reads as

$$\psi(\chi,\nu,\zeta) = A_0\varphi(\chi,\zeta)\varphi(\nu,\zeta), \quad (3)$$

with

$$\varphi(X,\zeta) = \text{Ai}\left[X - \frac{\zeta^2}{4} + \text{i}a_X\zeta\right] \exp\left[\frac{\text{i}}{12}\left(6a_X^2\zeta - 12\text{i}a_X X + 6\text{i}a_X\zeta^2 + 6X\zeta - \zeta^3\right)\right], \text{ with } X = \{\chi,\nu\} \quad (4)$$

Here, $\text{Ai}(X)$ is the Airy function, A_0 the amplitude and a_X a positive decay length that truncates the solution to become physically relevant. In the focal plane ($\zeta = 0$) the one-dimensional Airy functions reads as $\varphi(X,0) = \text{Ai}[X]\exp[a_X X]$, where the exponential decay clearly can be seen. Without this truncations the solution will extended over the whole space and contains infinite energy. These truncated solutions still solves the wave equation (1) and the distinguished properties of Airy beams are mostly preserved [2]

2.2. Numerical methods

Due to the inhomogeneous refractive index modulation $\Delta n^2(I_{\text{indu}})$, which here is caused by the nonlocal, anisotropic photorefractive nonlinearity, the paraxial wave equation (1) cannot be solved analytically. Thus, we have implemented comprehensive numerical methods to solve this equation and model the light propagation in nonlinear media. The propagation equation (1) is evaluated numerically, using split-step Fourier methods. In the nonlinear regime, the inducing intensity $I_{\text{indu}} = |A|^2$ is given by the intensity of the propagating wave field itself (cf. equation (1)). Therefore, it is crucial to calculate the optically induced refractive index modulation for each propagation step. This index modulation, represented by $\Delta n^2(I_{\text{indu}})$, is calculated in full anisotropic model [29] using a relaxation method.

3. Experimental realization of interacting Airy beams in photorefractive media

All the experiments presented here are performed using the setup sketched in Fig. 1(a). The light from a frequency-doubled Nd:YVO_4 laser continuously emitting light at a wavelength of $\lambda = 532\,\text{nm}$ is expanded and illuminates a programmable, high-resolution phase-only spatial light modulator (SLM). The plane wave that enters the modulator experiences a spatial phase

#246589 Received 23 Jul 2015; accepted 28 Jul 2015; published 8 Sep 2015

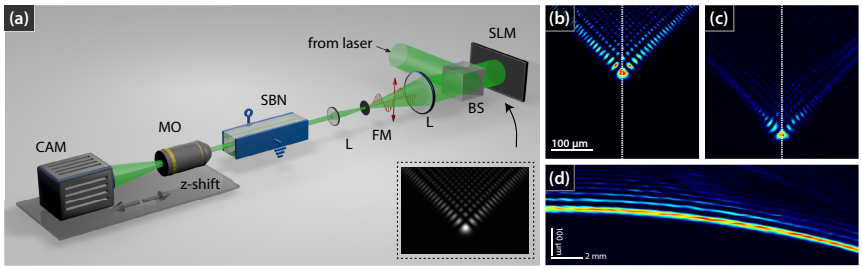

Fig. 1. Experimental setup and single Airy beam characteristics. (a) Experimental setup (SLM: Spatial light modulator, BS: beam splitter, FM: Fourier mask, SBN: strontium barium niobate crystal, MO: microscope objective). (b–d) Linear propagation of a single two-dimensional Airy beam through the homogeneous crystal. (b),(d): Intensity at the input and output face of the crystal, (c) cross-section during propagation.

modulation, which in combination with two following lenses and a Fourier filter leads to any desired complex light field at the input face of the nonlinear photorefractive medium. Therefore, we address an explicitly designed phase pattern to the SLM that allows us to modulate phase and amplitude of the light field at the same time [30]. In this way, we realize different complex light fields as combination of multiple displaced two-dimensional Airy beams, whose field distributions are calculated with equation (3).

This structured beam then illuminates the 20 mm long photorefractive $Sr_{0.60}Ba_{0.40}Nb_2O_6$ (SBN:Ce) crystal which is externally biased with an electric dc field of $E_{\text{ext}} \approx 1000\,\text{V}\,\text{cm}^{-1}$ aligned along the optical c-axis. We take care that the input face of the crystals coincides with the plan corresponding to the SLM's surface. To maximize the nonlinear self-action of the written refractive index structure onto the beam itself – in other words the nonlinearity – the beam is set to be extraordinarily polarized with respect to the crystal's optical c-axis. The high electro-optic coefficient of SBN:Ce [31] facilitates sufficient nonlinearity to substantially change the propagation of the Airy beam. By illuminating the crystal homogeneously with white light, we can erase written refractive index modulations. This reversibility make our experimental approach highly flexible to perform series of experiments using the same nonlinear material. By means of an microscope objective and a camera mounted on a translation stage we can record the intensity distribution in different transverse planes.

4. Linear propagation of multiple Airy beams

The propagation characteristics of single Airy beams have been subject to many experimental and numerical studies in the past years, considering linear and nonlinear effects, or propagation in inhomogeneous or periodically structured media. As it is well known, for linear propagation in a homogeneous environment the Airy beams follows a parabolic trajectory while propagation. This behavior can clearly be seen from the experimentally recorded intensity profile of one single Airy beam (Figs. 1(b)–1(d)) realized with the presented experimental setup (Fig. 1(a)). Although the main scope of this work is the interaction of multiple Airy beams, these basic result are presented to demonstrate that our experimental approach and setup allow to realize two-dimensional accelerated Airy beams with very high accuracy. These results serve as a good starting point for the following experimenters about multiple interacting Airy beams.

To systematically investigate the propagation and interaction of multiple two-dimensional Airy beams, we start our studies with considering the most fundamental case of two co-propagating Airy beams in the linear regime. The beams are coherently superimposed with an initial distance of $d \approx 50\,\mu\text{m}$ and are rotated by 180°, so that their accelerated trajectories

#246589 Received 23 Jul 2015; accepted 28 Jul 2015; published 8 Sep 2015

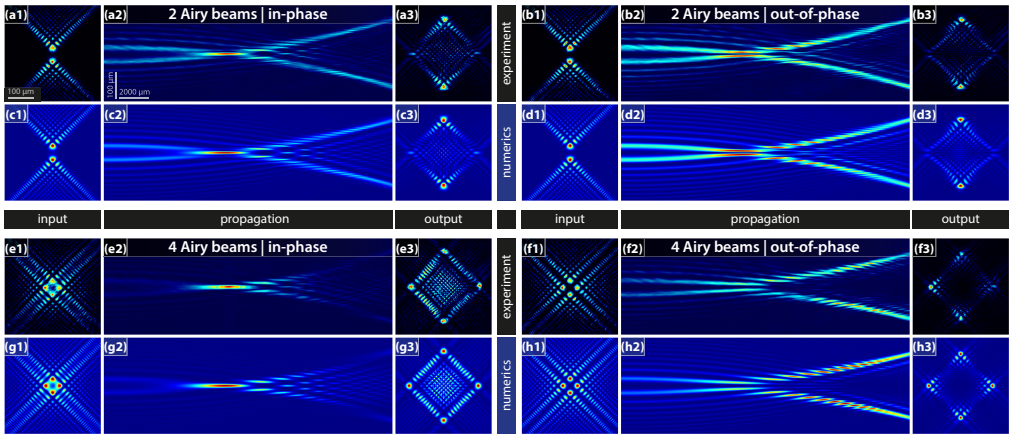

Fig. 2. Interference of multiple Airy beams in homogeneous linear medium. (a–d) Evolution of two Airy beams in experiment and numerics. (a,b) in phase, (c,d) with π phase difference. (e–h) Evolution of four Airy beams in experiment and numerics. (e,f) in phase, (g,h) with π phase difference. Each panel is normalized individually.

will intersect during propagation. The longitudinal position of this intersection point strongly depends on the curvature of the Airy beams which is determined by their size, but also depends on their initial separation. We aim to observe this defined intersection inside the volume of the 20 mm long SBN crystal. Therefore, we set the Airy beam size, measured as the distance between the main lobe and the next neighbor, to $s \approx 25\,\mu$m.

To visualize the complex evolution of the intensity distribution during propagation, we extract cross-sections through the experimentally recorded intensity volume along the coordinate in which the acceleration happens. Our experimental setup allows to retrieve this three-dimensional intensity volume by automatically recording the transverse intensity distribution in many (here 100) different planes along the crystal and stacking them. It is worth to mention that recording the intensity at planes inside the crystals is only possible if the refractive index between this plane and the camera is uniform, in other words, if the crystals in homogeneous.

The experimental results for two Airy beams are shown in Figs. 2(a) and 2(b), with the corresponding numerical simulations in Figs. 2(c) and 2(d). Thereby, we consider two cases where the beams are either in phase, or π out of phase. These different initial conditions result in distinguishable transverse intensity profiles during propagation due to interference. For the in-phase configuration, depicted in Fig. 2(a) and 2(c), a well-pronounced focus is formed by constructive interference of the beams in the intersection region of both accelerated trajectories. This feature of a very high local intensity compared to the surrounding was previously emphasized as the key advantage of so-called autofocusing beams [32,33]. For the out-of-phase case, shown in Figs. 2(b) and 2(d), the phase difference of π between the beams at the input leads to the vertical separation by a dark line of destructive interference which is preserved during the whole propagation. In both cases, the parabolic trajectories of the two superimposed Airy beams can clearly be identified. Since so far the propagation is completely linear, the complex intensity patterns results only from interference, but the beams do not interact and influence each other. Therefore, their initial general accelerated trajectories are preserved, albeit the beams trajectories intersect.

By increasing the number of the superimposed beams, the next symmetrical configuration can be constructed with four displaced Airy beams each rotated by 90°, as shown in Figs. 2(e)–2(h). In principle there are more possibilities to set the relative phases of the beams, but we

#246589 Received 23 Jul 2015; accepted 28 Jul 2015; published 8 Sep 2015

want to limit our studies to the following two cases: either all beams are in phase (Figs. 2(e) and 2(g)), or neighboring beams are π out of phase (Figs. 2(f) and 2(h)). While the transverse intensity profiles now look quite different compared to the situation where two beams are superimposed, the longitudinal cross-sections reveal a similar propagation behavior. Again, a well-pronounced high-intensity focus is formed in the region where the four in-phase Airy beams interfere constructively, while the dark line of destructive interference always separates the beams in the out-of-phase case. Due to the fact that now four beams are interfering, the relative strength of the focus for constructive interference is much higher than for two beams. The number of interfering Airy beams could be further increased while the contrast between the focal intensity and the background continuously grows to the limit achieved by radially distributed Airy beams [32].

All presented experimental results are supported by corresponding numerical simulations. For the propagation of multiple Airy beams in the linear regime the numerical results perfectly fits to the experimental measurements. Although the wave equation (1) for homogenous media ($\Delta n(I) = 0$) has analytical solution in form of truncated Airy beams which can be explicitly calculated for any distance z, we already here employ the numerical beam propagation method to prove and emphasize that the simulation methods we developed precisely describe the real experimental conditions.

5. Nonlinear interaction of multiple two-dimensional Airy beams

From the above presented results we see, that during linear propagation of multiple Airy beams interference alone already leads to interesting intensity distributions, even as the beams do not interact and influence each other. If such an interdependency mediated by a nonlinear light matter interaction is included into the theoretical models and experiments, interesting novel effects can be expected, as for example soliton formation as predicted numerically in [26, 27].

In the following, we will investigate and analyze the nonlinear propagation and interaction of multiple Airy beams experimentally in photorefractive SBN. As introduced above, the refractive index of the nonlinear crystal depends non-locally on the incident intensity distribution and leads to a self-focusing, saturable nonlinearity. This complex nonlinearity completely changes the propagation dynamics of the Airy beams and leads to fascinating new types of beam evolution that depends amongst others on the number of superimposed beams, their relative phase and intensity. The experimental and numerical results for two and four superimposed Airy beams are presented in the following sections.

5.1. Interaction of two Airy beams

We start our investigations about the nonlinear interaction with the most fundamental configuration of two displaced Airy beams. We use the same beam parameters as described above for the linear case (cf. Fig. 2). At the input, the two beams that are separated by $d \approx 50\,\mu$m and are orientated to accelerate towards each other. Thereby, the trajectories of the undisturbed Airy beams would intersect and the beams strongly interact. In contrast to the linear experiment, we now increase the beam power, as well as the writing time to gain sufficient nonlinearity. To observe the intensity dependency of the propagation dynamics we set four different probe beam powers: $P_{\text{in}} \approx \{237,\ 475,\ 950,\ 1.425\}\,$nW and perform the experiment for each value, while keeping all other parameters such as external field, induction time, and background illumination unchanged.

The experimental results for the in-phase beams are shown in Fig. 3(a). While increasing the probe beam power we can see the transition from the almost linear interference pattern Fig. 3(a1) to a well-localizes, solitary output state for higher nonlinearities Figs. 3(a3) and 3(a4). This localized state origins at the intersection point of the beam trajectories, where

#246589 Received 23 Jul 2015; accepted 28 Jul 2015; published 8 Sep 2015

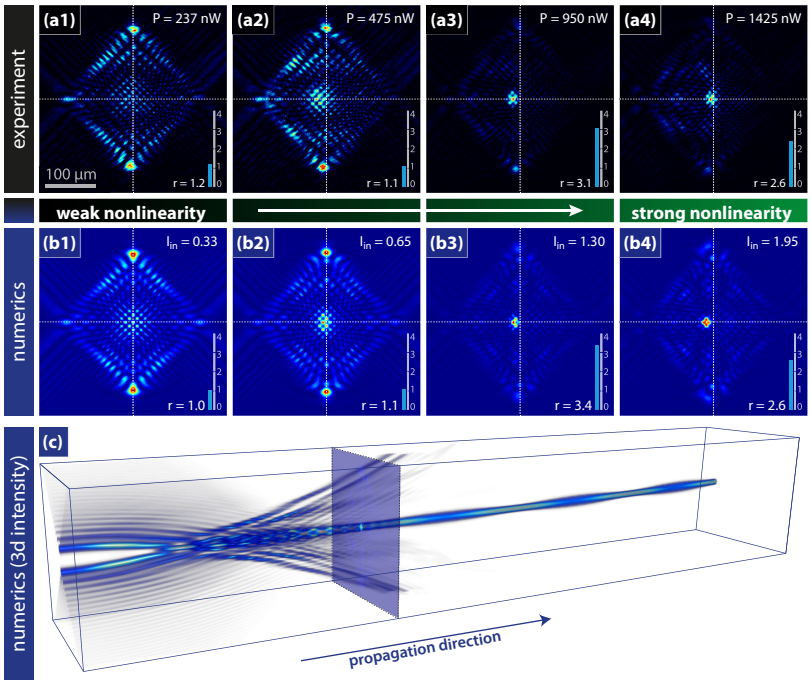

Fig. 3. Formation of solitary states from the interaction of two in-phase Airy beams. (a) Experimental results for different probe beam power. Each panel shows the intensity pattern at the output face of the SBN crystal (individually normalized). (b) Results from corresponding numerical simulations. (c) Volumetric plot of the numerically calculated three-dimensional intensity distribution (three times longer crystal) for strong nonlinearity. The position of the marked plane corresponds to the length of the used SBN crystal, $L = 20\,\mathrm{mm}$ and to Figs. (a4),(b4).

the constructive interference of the in-phase Airy beams leads to a strongly increased local intensity. Afterward, it propagates almost unchanged, except small breathing, due to the compensation of the diffraction by nonlinear self-focusing. The merged localized state further propagates straight obviously without any transverse momentum remaining from initial accelerated beams. The nonlinearity allows for this complex interaction between the two beams that in consequence compensates the acceleration. The peak intensity of the resulting state at the output of course is higher than the peak intensity at the input where the individual beams do not noticeably overlap. The factor $r = I_{\mathrm{max,out}}/I_{\mathrm{max,in}}$ (see insets in Fig. 3) represents the ratio between the maximal intensity at the output and the input, respectively. Due to the principal limitation that direct imaging through a non-homogeneous medium is not possible, only the output face of the SBN crystal is accessible for all nonlinear experiments throughout this paper. The factor r helps to compare experiments and numerics also quantitatively.

The comparison between the experimental results Fig. 3(a) and the numerical simulation presented in Figs. 3(b) and 3(c) shows a very good overall agreement. According to the different probe beam powers in the experiment, we simulated the nonlinear propagation for different corresponding input intensities $I_{\mathrm{in}} \approx \{0.33, 0.65, 1.30, 1.95\}$. The output profiles, as well as the intensity factor r perfectly matches the real observations in experiment. This verifies that our implemented numerical methods exactly describe the real situation and justify to employ numerical simulations to get a detailed impression what dynamics happens during nonlinear

#246589 Received 23 Jul 2015; accepted 28 Jul 2015; published 8 Sep 2015

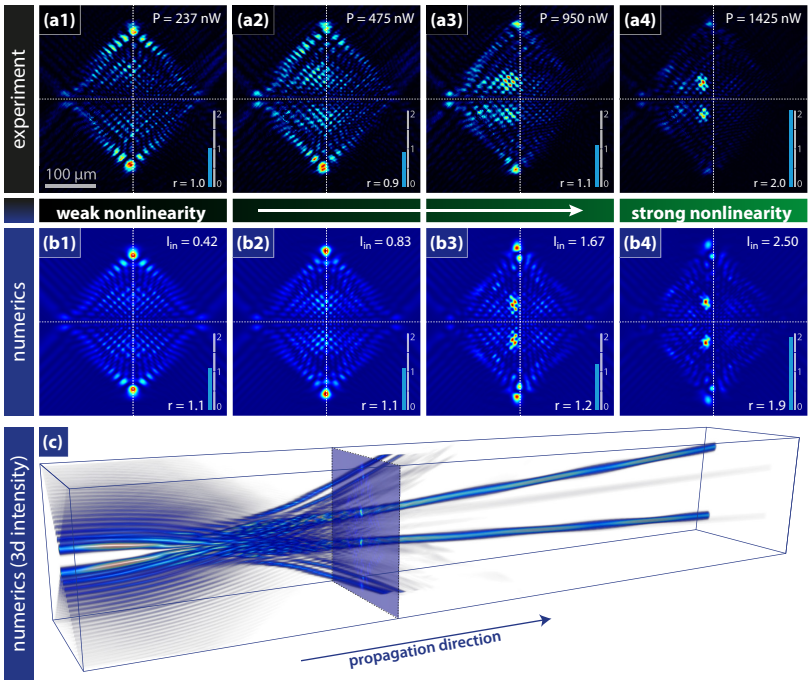

Fig. 4. Formation of solitary states from the interaction of two out-of-phase Airy beams. (a) Experimental results for different probe beam power. Each panel shows the intensity pattern at the output face of the SBN crystal (individually normalized). (b) Results from corresponding numerical simulations. (c) Volumetric plot of the numerically calculated three-dimensional intensity distribution (three times longer crystal) for strong nonlinearity. The position of the marked plane corresponds to the length of the used SBN crystal, $L = 20\,\mathrm{mm}$ and to Figs. (a4),(b4).

propagation in the SBN crystal. As mentioned above, in the experiment these data are not accessible due to principle physical reasons.

Figure 3(c) shows a volumetric rendering of the numerically retrieved intensity distribution during nonlinear propagation. The formation of the solitary state is clearly visible. While during the build-up process noticeable modulations in the shape and the intensity of the solitary state occurs (i.a. due to the passing of the remaining side lobes of the initial Airy beams), after some propagation distance the situation stabilizes and the solitary state propagates almost unchanged, except small breathing. The marked plane in Fig. 3(c) corresponds to the length of the SBN crystal and the pictures shown in Figs. 3(a) and 3(b).

A similar localization behavior was also found numerically for simpler idealized isotropic Kerr, and saturable Kerr nonlinearities [27]. For the presented experimental and numerical results in a realistic photorefractive SBN crystal, the situation is much more complicated, due to the anisotropic, saturable and drift-dominated nonlinearity. The slight shift of the intensity peaks in horizontal direction can be explained by additionally taking into account diffusion effects in the numerical model.

In the opposite case where the two Airy beams are π out of phase, the situation is completely changed, as can be seen from the results shown in Fig. 4. The two main lobes do not merge (c.f. Figs. 2(b) and 2(d)) due to the separating line of destructive interference in the middle between the beams. As a consequence, two localized solitary spots build up and stably propagate as a

#246589 Received 23 Jul 2015; accepted 28 Jul 2015; published 8 Sep 2015

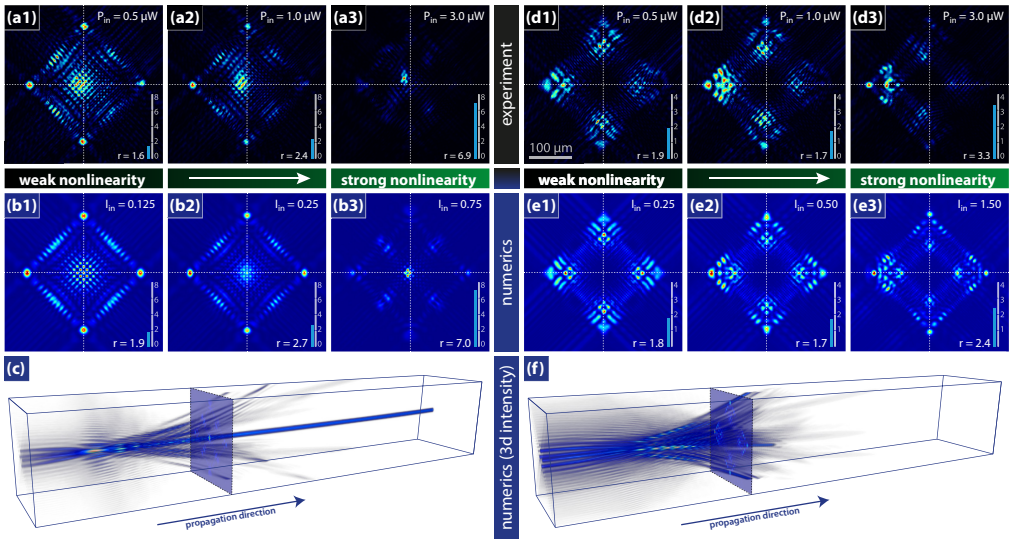

Fig. 5. Interaction of four Airy beams. (left) Formation of solitary state for the case where the beams are in phase. (right) Nonlinear propagation for π phase difference. (a),(d) Experimental results for different probe beam power. Each panel shows the intensity pattern at the output face of the SBN crystal (individually normalized). (b,e) Results from corresponding numerical simulations. (c,f) Volumetric plot of the three-dimensional intensity distribution (from numerics) for strong nonlinearity.

pair over large distances. Again, the build-up process is accompanied by intensity modulations, but after a certain distance only small breathing remains. Introduced by the initial phase difference, these two solitons also have a phase difference of π and hence repel each other, as reported for fundamental solitons [34]. Therefore, they propagate on straight lines but with a small divergence, as can bee seen in Fig. 4(c). The remaining side lobes of the initially launched Airy beams further follows their parabolic trajectory and quickly depart out of the volume.

5.2. *Interaction of four Airy beams*

After investigating the nonlinear processes for the fundamental case of two interacting Airy beams, we now turn towards the more advanced case where four beams are synthesized. The four Airy beams are combined in the way that their trajectories will intersect, as described above (c.f. Fig. 2). In general, four beams allow more than two different phase configuration with integer values in units of π, nevertheless we restrict ourselves to the two cases: either all beams are in phase, or with π phase difference between neighboring beams. These two cases leads to completely different results.

For the case where all beam are in phase, the results are shown in Fig. 5 (left). Although the transverse intensity structure at the input face of the crystal looks different since now four beams are superimposed, the general nonlinear behavior is similar to the case where two Airy beams were launched in phase (c.f. Fig. 3). With increasing nonlinearity, the intensity localizes in the middle and forms a stable solitary state that emerges from the constructive interference of the beams in the region where their trajectories intersect. The experimental results for three different beam intensities $P_{\text{in}} \approx \{0.5, 1.0, 3.0\}\,\mu\text{W}$ (Fig. 5(a)) clearly show the described formation of the solitary state as the transition from the four separated Airy main lobes (see Fig. 5(a1)) to the high-intensity localized state (see Fig. 5(a3)). Here, the ratio r between the maximal intensity at the input and the peak intensity of the built-up solitary state is much higher compared to

#246589 Received 23 Jul 2015; accepted 28 Jul 2015; published 8 Sep 2015

the two-beam case, which is understandable because four beams are merging.

The situation is completely changed for the configuration with a phase difference of π between neighboring beams. The corresponding results are shown in Fig. 5 (right). In contrast to all other presented cases, here neither a straight soliton nor a soliton-pair or cluster is forming. Owed to the phase differences, no pronounced high-intensity spot arises from interference at the intersection of the beam trajectories that could develop into a soliton. Moreover, the remaining side lobes of the four Airy beams prevent the build-up of a solitary states or clusters, like it was observed in the previous case for two beams (Fig. 4). For higher intensities, the intensity tends to localize predominantly on one side (cf. Fig. 5(d3)) and keeps traveling away from the center.

Comparing all results of the nonlinear interaction of two and four Airy beams, we could identity three different types of nonlinear dynamic. First, in all cases where the synthesized beams are in phase, the interaction leads to the formation of one single stable spatial solitary state initiated by the high intensity resulting from constructive interference of the main lobes. The second type, the formation of a solitary pair, could be observed if two beams are superimposed with a phase difference of π. For these two types the acceleration of the initial Airy beams is exactly compensated, leading to straight propagating solutions. Interestingly, there is a third type where no solitary structures appears, even for the same intensities and nonlinearities. This could be observed if four Airy beams are superimposed with π phase difference, as it was done in the last example. For this configuration the nonlinear dynamic shows symmetry-breaking behavior that depends critically on small perturbations and asymmetries in the system. The directed diffusion of charge carriers inside the photorefractive SBN crystals causes such an asymmetry, that is also responsible for the horizontal shift of the other solitary solutions, as reported above.

Conclusion

In summary, we have presented the first experimental and numerical study about nonlinear interaction of multiple two-dimensional Airy beams. As the most important result, we could demonstrate the build-up of solitary structures from the nonlinear interaction of multiple accelerated beams. By investigating the nonlinear dynamic of the superimposed Airy beams for different configurations (numbers of beams, phase relations), we could demonstrate the intensity-dependent formation of straight propagating solitary states or pairs. These fundamental results could be achieved using a highly-developed experimental platform to perform nonlinear experiments which allows us to precisely shape the input beam as requested and reproducibly control all relevant parameters, such as input beam power, external electric field, and illumination time. Our experimental results and methods enable further investigations about the interaction of other types of tailored optical beams (e.g. nondiffracting beams) and moreover could find applications in modern optical information processing architectures as a basis for light guiding and switching approaches.

Acknowledgments

This work is partially supported by the German Academic Exchange Service (Project 56267010) and Ministry of Education, Science and Technological Development, Republic of Serbia (Project OI 171036).

#246589 Received 23 Jul 2015; accepted 28 Jul 2015; published 8 Sep 2015

Applied Surface Science 326 (2015) 91–98

Contents lists available at ScienceDirect

Applied Surface Science

journal homepage: www.elsevier.com/locate/apsusc

Surface nanopatterning of Al/Ti multilayer thin films and Al single layer by a low-fluence UV femtosecond laser beam

Aleksander G. Kovačević[a,*], Suzana Petrović[b], Bojana Bokić[a], Biljana Gaković[b], Miloš T. Bokorov[c], Borislav Vasić[a], Radoš Gajić[a], Milan Trtica[b], Branislav M. Jelenković[a]

[a] Institute of Physics, University of Belgrade, Pregrevica 118, 11080 Beograd, Serbia
[b] Institute of Nuclear Sciences "Vinča", University of Belgrade, PO Box 522, 11001 Belgrade, Serbia
[c] Center for Electron Microscopy, University of Novi Sad, Trg Dositeja Obradovića 2, 21000 Novi Sad, Serbia

ARTICLE INFO

Article history:
Received 8 July 2014
Received in revised form 25 October 2014
Accepted 31 October 2014
Available online 22 November 2014

Keywords:
Periodic surface structures
Femtosecond beam
Multilayered thin film
Surface modification

ABSTRACT

The effects of UV femtosecond laser beam with 76 MHz repetition rate on two types of thin films on Si substrate – the Al single layer thin film, and the multilayered thin film consisted of five Al/Ti bilayers (total thickness 130 nm) – were studied. The surface modification of the target was done by low fluences and different irradiation times, not exceeding ~300 s. Nanopatterns in the form of femtosecond-laser induced periodic surface structures (fs-LIPSS) with periodicity of <315 nm and height of ~45 nm were registered upon irradiation of the thin films. It was shown that: (i) the fs-LIPSS evolve from ruffles similar to high spatial frequency LIPSS (HSFL) into a low spatial frequency LIPSS (LSFL) if a certain threshold of the fluence is met, (ii) the number of LSFL increases with the exposition time and (iii) the LSFL remain stable even after long exposure times. We achieved high-quality highly-controllable fabrication of periodic structures on the surface of nanosized multilayer films with high-repetition-rate low-fluence femtosecond laser pulses. Compared to the Al single layer, the presence of the Ti underlayer in the Al/Ti multilayer thin film enabled more efficient heat transmittance through the Al/Ti interface away from the interaction zone which caused the reduction of the ablation effects leading to the formation of more regular LIPSS. The different outcomes of interactions with multi and single layer thin films lead to the conclusion that the behavior of the LIPSS is due to thin film structure.

1. Introduction

The occurrence of periodic structures on material surfaces induced by pulsed laser irradiation (LIPSS) has been attracting attention due to potential and interesting applications [1–10]. Various materials have been used, ranging from metals and semiconductors to dielectrics and compounds, as well as from bulk to thin films. Moreover, lasers with different operation modes and beam parameters have been used [1,2,4,11–14]. Two types of periodic structures generally occur, high spatial frequency LIPSS (HSFL) and low spatial frequency LIPSS (LSFL) [15,16].

In the femtosecond range, near infrared (NIR) irradiation (around 800 nm) with fluences >100 mJ/cm^2 is commonly used with the tendency that produced periodic structures disintegrate after a great number of pulses [4,7,9]. For many metals, the absorption for normal incidence is low in the infrared (IR) and NIR, rising in the visible (VIS) and being high in the ultraviolet (UV) part of the spectrum. However, by showing low absorption (high reflectivity) in the UV, Al surpasses all the others, posing challenging difficulties for laser-induced surface modifications [17–20]. Using UV beams would in return lead to the formation of periodic structures of lower spatial period [16], which gives more opportunity for finer nanopattening. The interaction of femtosecond laser beam with surfaces leads to the adsorption of the oxygen and nitrogen from the atmosphere, which changes the surface properties [21].

Formation of periodic nanostructures influences the tribological properties of the surfaces [22]. Aluminum-titanium (Al/Ti) multilayer thin films have been attractive for structural coatings in mechanical applications, due to their extraordinary wearing behavior and corrosion resistance. Adding a Ti to Al alloy can lead to the formation of a fine scale, equiaxed grain structure, which reduces hot tearing, increases feeding to eliminate shrinkage porosity and thus improves the mechanical properties [23]. The fs-beam nanostructuring of Al surface has been present in

* Corresponding author. Tel.: +381 11 3713 008; fax: +381 11 3162 190.
E-mail address: Aleksander.Kovacevic@ipb.ac.rs (A.G. Kovačević).

http://dx.doi.org/10.1016/j.apsusc.2014.10.180
0169-4332/

the literature [24–27]. The interaction of femtosecond laser beam with Al/Ti multilayer structures on silicon has not been sufficiently described in literature, especially for low laser intensities, below the ablation threshold. Therefore, it is expected that exposing the Al/Ti multilayer to fs beam would change the tribological and chemical properties of the surface. We have irradiated the Al/Ti multilayer and Al single layer thin films with femtosecond UV (390 nm) laser pulses of low single pulse fluence (<100 mJ/cm^2) and demonstrated the emergence of femtosecond-laser induced periodic surface structures (fs-LIPSS) on the top surface of the multilayered structure. The evolution of initial nanoroughness to the LSFL has been interpreted and the causes of the LSFL formation have been suggested. The difference in surface modifications after fs laser interactions with Al/Ti multilayered and Al single layered thin films has been demonstrated.

2. Experimental setup

We have irradiated two types of targets. The target/specimen of the first type was comprised of the silicon (1 0 0) wafer on which five Al/Ti bilayers were deposited reaching the total thickness of ~130 nm (each layer of ~13 nm). The second type was Al single layer of ~130 nm of thickness on the wafer of same type. The depositions were performed by the Balzers Sputron II apparatus using 1.3 keV argon ions and with 99.9% of Al and Ti targets purity.

The irradiations were performed in air with focused femtosecond laser beam under normal incidence at the top layer (Al). The beam was generated by the Coherent Mira 900 Ti:Sapphire system, frequency-doubled by the Inrad 5-050 ultrafast harmonic generation system (as a second-harmonic generator, SHG), and its wavelength monitored with the Ocean Optics HR2000CG-UV-NIR fiber-optic spectrometer (Fig. 1). The beam properties at the target were: wavelength 390 nm, pulse duration ~150 fs, repetition rate 76 MHz (corresponding to ~13 ns of interpulse time), power of 160–260 mW, linear polarization in the horizontal plane, Gaussian-like elliptic profile. The exposition times were between 1 and 300 s.

The results have been analyzed by scanning electron microscopy (SEM): the JEOL JSM 6560 LV system with the Oxford Instruments EDS analyzer (typical spatial resolution ~2 μm^3) and atomic force microscopy (AFM) by the NT-MDT NTEGRA Prima system in the tapping mode with NSG01 probes (tip curvature radius 6 nm).

3. Results and discussion

Selected results of the surface changes after laser irradiation (SEM micrographs) are presented in Figs. 2–5. Changing the beam power resulted in the single pulse fluence range between 8.6 and 14 mJ/cm^2. The irradiation time was between 1 and 300 s.

In Fig. 2(a), the illuminated area (IA) on Al/Ti multilayer thin film sample generated by the beam of single pulse fluence14 mJ/cm^2 during 1 s of exposition time is shown. This corresponds to effective delivered power per spot of 1.06 MW/cm^2. The time between two consecutive pulses (the interpulse time) was ~13 ns for all cases of irradiation. The elliptically-shaped modified area (MA) of dimensions 2.07 μm × 3.40 μm stands out from the surroundings by its ruffles (the form of regrouping of the surface material), i.e. a noise in which a certain periodicity can be recognized similar to high HSFL [16]. For the same single pulse fluence but longer exposition

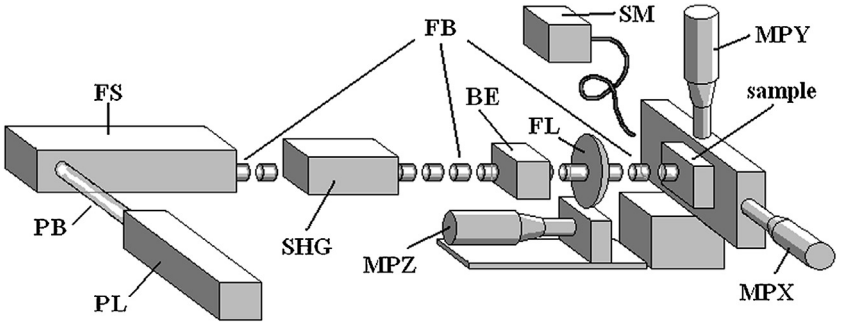

Fig. 1. Experimental setup; PL – pump laser, PB – pump beam, FS – femtosecond laser, FB – femtosecond beam, SHG – second-harmonic generator, FL – focusing lens (f = 5 mm), MPX, MPY, MPZ – micropositioners, SM – spectrometer.

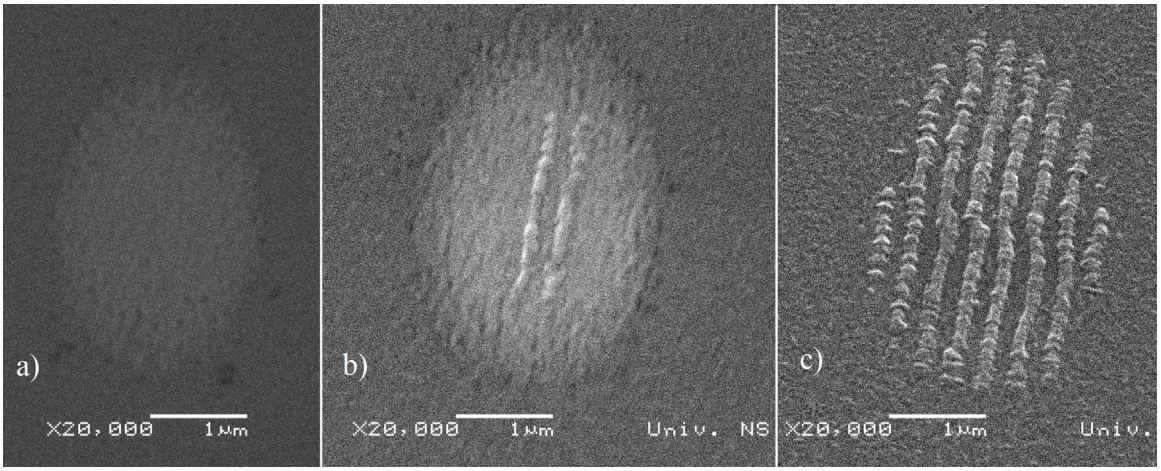

Fig. 2. SEM micrograph of the spots generated on the Al/Ti sample by the beam of: (a) 14 mJ/cm^2 single pulse fluence and 1 s exposition time (effective delivered power per spot 1.06 MW/cm^2); (b) 14 mJ/cm^2 and 2 s (1.06 MW/cm^2); (c) 13.6 mJ/cm^2 and 10 s exposition time (1.03 MW/cm^2). White bar represents 1 μm.

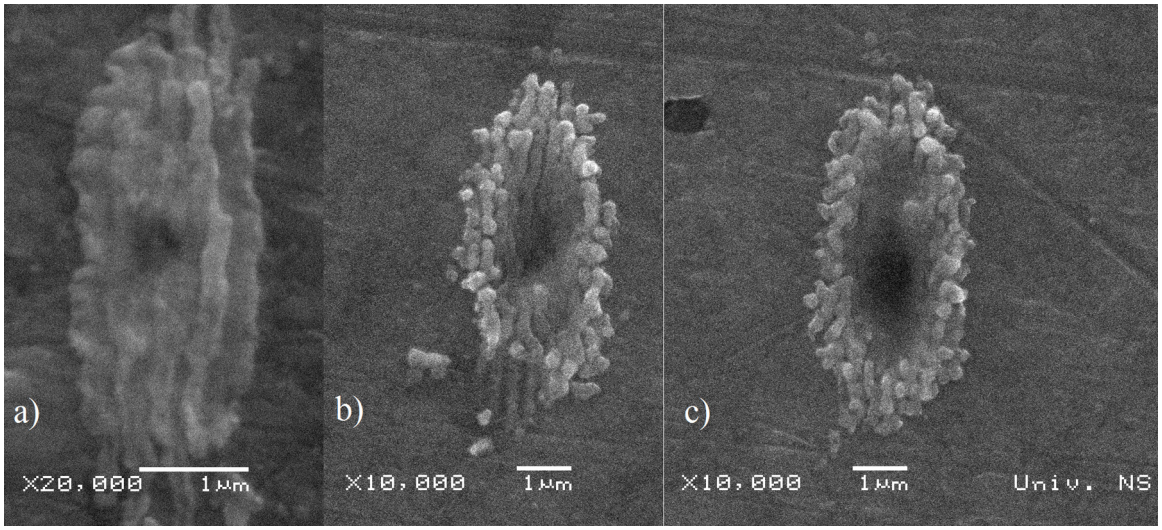

Fig. 3. SEM micrograph of the spot on the Al thin film specimen, generated by the beam of 8.6 mJ/cm^2 single pulse fluence (effective delivered power per spot 654 kW/cm^2): (a) exposition time 1 s; (b) exposition time 4 s; (c) exposition time 10 s. White bar represents 1 μm.

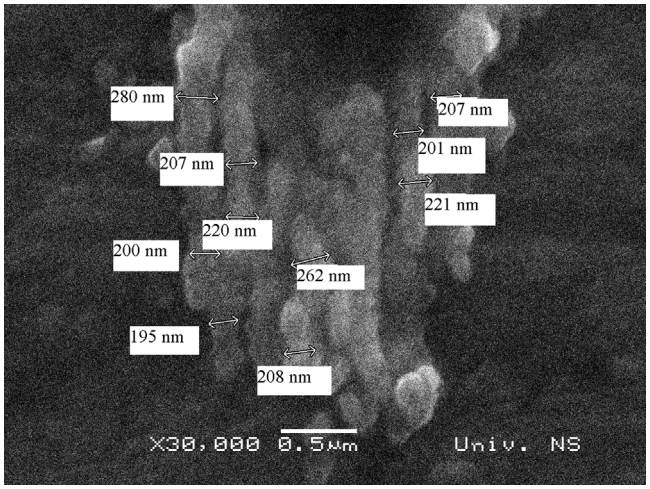

Fig. 4. SEM micrograph of the spot on the Al thin film specimen, generated by the beam of 8.6 mJ/cm^2 single pulse fluence and exposition time of 2 s (effective delivered power per spot 654 kW/cm^2). Detailed view with the dimensions of ripples. White bar represents 1 μm.

time, besides ruffles two prominent ripples were formed in the MA, as seen in Fig. 2(b). The ripples, having the shape of a string of nanoparticles, were 130 nm wide, 2 μm long and perpendicular to the direction of the beam polarization. For even longer exposition times, greater number of ripples was formed; however, the ripples remained limited inside the MA, Fig. 2(c). The periodicities of the LSFL have been determined from the extracted profile of the pixel brightness and are given in Table 1.

Having the spatial period ~320 nm close to the incident wavelength (390 nm), the ripples are the LSFL. Comparing the LSFL formed for different expositions, Fig. 2(b) and (c), both shape and

Table 1
LSFL periodicities over number of samples.

Sample	Fig.	Number of pulses	Number of LSFL stripes	Periodicity
AlTi	2(b)	152×10^6	2	(~310 ± 20) nm
AlTi	2(c)	760×10^6	8	(314 ± 20) nm
AlTi	5(a)	~23×10^9 and scanning	68–70	(320 ± 20) nm
Al	5(b)	Scanning	>50	(~350 ± 20) nm
Al	3(a)	76×10^6	5–6	(~260 ± 20) nm
Al	3(b)	304×10^6	7–8	(~262 ± 20) nm
Al	3(c)	760×10^6	6–7	(~314 ± 20) nm

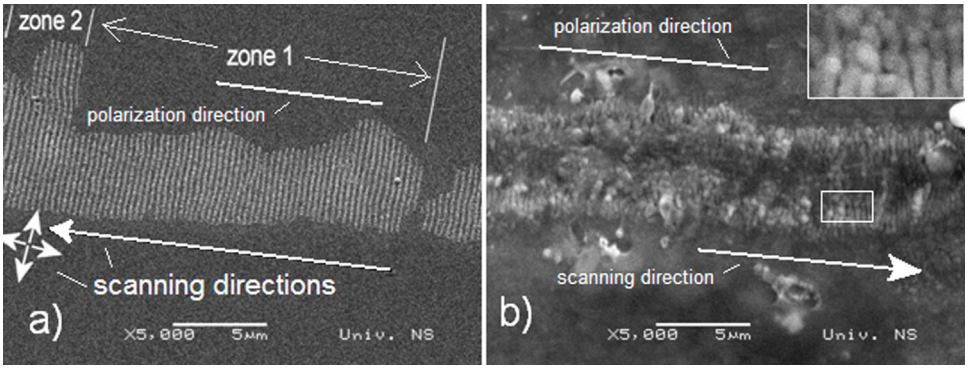

Fig. 5. SEM micrograph of irradiated areas, white bar represents 5 μm, the samples were translated during the irradiation (arrows indicate the direction of beam traversing over the sample), exposition time ~300 s: (a) Al/Ti specimen, single pulse fluence14 mJ/cm^2 (corresponding to 1.06 MW/cm^2); (b) Al thin film sample, 8.6 mJ/cm^2 (654 kW/cm^2). Inset in (b) shows enlarged part.

width of the LSFL seems to remain unchanged with exposition time. The ruffles are the precursor to the formation of the ripples – the strings of nanoparticles.

The specimen of the second type, the Al single layer thin film, was exposed to 8.6 mJ/cm^2 of the single pulse fluence and the same exposition times (for (a), (b) and (c), respectively) and the results are presented in Fig. 3. For 1 s of irradiation, Fig. 3(a), the material in the MA regrouped in the form of ripples. For longer exposition times, Fig. 3(b) and (c), ablation took part in the central part of the MA (dark spot) and ablated material accumulated around in the form of ripples (LSFL). The width of the ripples could be determined to ~200–220 nm and approximate spatial period to ~260–314 nm (Fig. 4). The ripples, with the direction perpendicular to the polarization direction of the beam, show lower regularity compared to the ones of the Al/Ti samples.

In order to see whether the relative movement between the laser beam and the samples influences the occurrence of the LSFL, the samples were slowly translated with estimated speed between 1 and 4 μm/s while exposed; the irradiation lasted ~300 s.

For 14 mJ/cm^2 of the single pulse fluence (corresponding to 1.06 MW/cm^2), the Al/Ti sample was translated in parallel (Fig. 5(a), zone 1 arrow) and both perpendicular and parallel (Fig. 5(a), zone 2 arrows) directions in respect to the beam polarization direction. It is apparent that the arrangement of the LSFL is independent on the sample translation. This suggests that the interaction between the incident laser beam and induced surface wave [8,9], the surface plasmon polariton (SPP), together with dewetting [28,29] plays an important role in the formation of the LSFL. It should also be noted that, in spite of the long exposition times (~300 s while scanning), the disintegration of the LSFL has not occurred for the Al/Ti sample. From the extracted profile of the pixel brightness in Fig. 5(a), the spatial period of the LSFL has been determined to be (315 ± 20) nm. The sample was moved in such manner that the laser beam, after being switched on, first traversed over the sample in the direction to the left and stopped. The rightmost group of the stripes represents the position where the laser beam was shut off. Next movement of the sample positioned the beam for next ~2 μm to the left, where the sample stopped and the beam was switched on for ~300 s. While the laser beam still being switched on, the next movement with the speed of ~1–2 μm/s led the beam for next 10 μm (the long white arrow pointing to the left, Fig. 5(a)), along the polarization direction, where the sample stopped and the laser beam was left on for ~300 s. Without switching the laser beam off, the beam traversed (by sample movement) to the left (the long white arrow pointing to the left) with speed ~3–4 μm/s for next 10 μm, entered the zone 2, stopped and left for ~300 s. The discrepancies in the thickness of the ripple trace might come for the reasons of the speed instability of the sample movement. Then the beam traversed with ~2 μm/s in the direction of the small up-pointing arrow for 5 μm, then back down for ~5 μm, then to the left ~5 μm and in the end back to the right and stopped, remaining in the zone 2 for ~300 s. In all cases of the movement, the polarization direction was as shown in the Fig. 5(a), i.e. horizontal.

The implementation of the low single pulse fluences (~14 mJ/cm^2, corresponding to 1.06 MW/cm^2) enables the generation of permanent high-quality LSFL tracks (ripple trace) on the multilayer film for the length of ~20 μm, indicating the potential of LSFL fabrication, covering of large surface areas without loss of quality. This is in contrast to the case of the Al single layer sample, where obtained LSFL structure is loose and contains bifurcations (Fig. 5(b)). The sample was translated along the polarization direction (arrow in the Fig. 5(b), with the scanning speed of 5 μm/s). The LSFL are less prominent, but still noticeable – see inset in Fig. 5(b). Fig. 5 demonstrates that the regularity of LSFL is highly improved with using the multilayer configuration.

Table 2
EDS analysis (in weight %) of non-irradiated area and modified area (MA) irradiated with single pulse fluence of 14 mJ/cm^2.

Element (%)	Non-irradiated area	MA during 1 s	MA during 300 s
Si	88.6	70.72	51.33
Al	3.58	3.05	2.17
Ti	8.36	6.52	4.53
N	0	19.70	31.25
O	0	0	10.72

The influence of the femtosecond laser beam irradiation to the chemical modification of the surface has been investigated. The adsorption of N into Al surface under the irradiation of femtosecond laser pulses has been reported [21]. In Table 2, the EDS results obtained from three spots of the Al/Ti sample are presented: (1) from non-irradiated area (unmodified surface), (2) from MA irradiated with 14 mJ/cm^2 single pulse fluence during 1 s (corresponding to 1.06 MW/cm^2) – where only the HSFL-like noise appeared, and (3) from MA irradiated with 14 mJ/cm^2 single pulse fluence during 300 s (corresponding to 1.06 MW/cm^2) – where the LSFL appeared. The results after short exposures show the appearance of N, but not of O in the MA. The results of longer exposition, where the LSFL occurred, show the increased content of N and the occurrence of O in the MA. The adsorption of N is likely to occur for shorter exposition times (smaller accumulated energies), while additional oxides appear for longer expositon times (greater accumulated energies). Due to the constraints of the EDS (spatial resolution, i.e. great volume from which the information is obtained, and the detection from the deep of the interaction volume) neither oxygen nor nitrogen has been detected in non-irradiated spots. Their common presence (particularly of natural oxides) is of much lower contribution compared to irradiated spots.

The profile of structures developed on irradiated multilayer 5× (Al/Ti)/Si sample, together with 2D FFT (see Fig. 2), is shown as the AFM images in Fig. 6. The irradiation by 14 mJ/cm^2 during 2 s (corresponding to 1.06 MW/cm^2) changes the surface RMS roughness from 0.5 nm (in non-irradiated area, mirror-like surface) [23] to 6.8 nm (HSFL). The existence of the periodicity could be determined from the 2D FFT image, Fig. 6(c), where the orders are linked to periodicities of LSFL (1st order) and also to HSFL-like ruffles (2nd order), which approximate value of ~130 nm could be estimated from Fig. 6(b). Moreover, in the central part, the height of the LSFL reached a value of about (45 ± 0.5) nm above the mean. On the other hand, the irradiation during 10 s produced a clearly regular periodic topography of eight ripples (Fig. 2(c), AFM images with 2D FFT and profile in Fig. 7). The average ripple height given by the AFM in Fig. 7 is 45 nm above the mean, which is similar to the height after 2 s of irradiation (Fig. 6). This may lead to the conclusion that the height of the LSFL is not influenced by the exposition time; increasing time of laser irradiation only increases the number of the LSFL inside the MA. The SEM and AFM images indicate that each ripple has a fine granular structure (the average granule size is about 130 nm), which could be attributed to the formation and self-arranging of nanoparticles. The growth of the LSFL could also be explained by considerable nitriding and oxidation of the sample material [28,30–34] with possible forming of intermetallic mixture of Al and Ti [35].

The penetration depth, l_α, for the 390 nm laser beam in Al is about 3 nm, and in Ti is about 9.3 nm, calculated by using the formula [3] $l_\alpha = 1/\alpha = \lambda/4\pi\kappa$, for picosecond pulses [23,35,36], where λ is a laser beam wavelength, α is an absorption coefficient and κ is an extinction coefficient.

There are various explanations of the occurrence of nanostructures (ripples) on the surfaces irradiated by laser beam depending on the laser type, beam characteristics (repetition rate, wavelength, power ...) and the target material. The generation and evolution

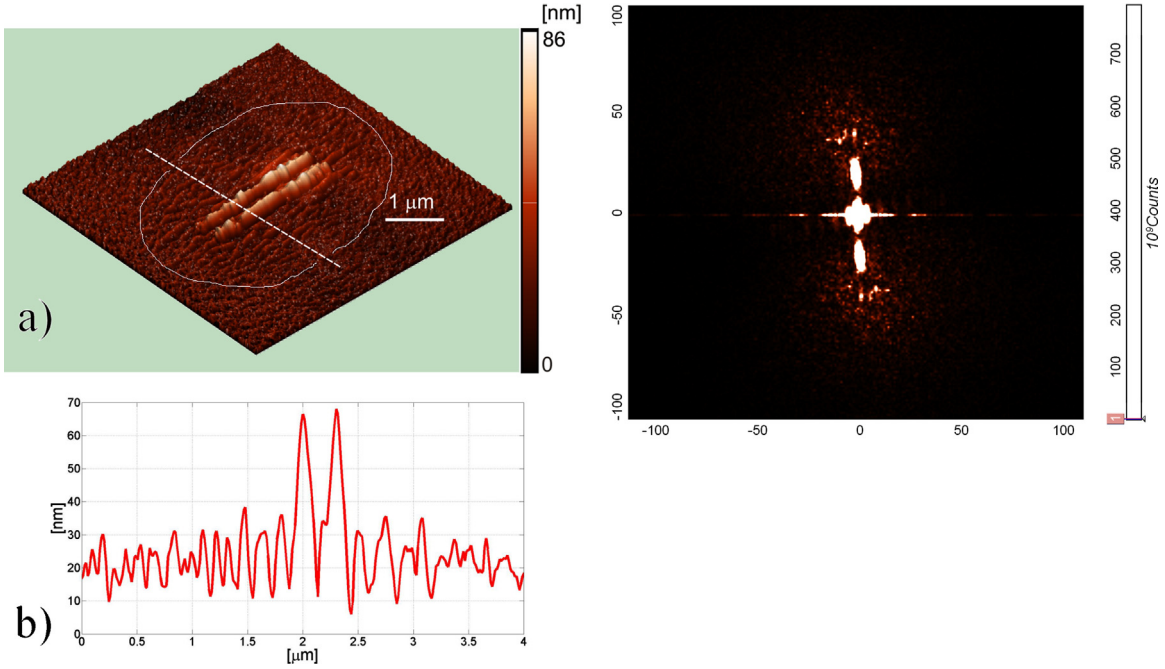

Fig. 6. (a) AFM micrograph of the irradiated spot (SEM presented in Fig. 2(b)): single pulse fluence14 mJ/cm^2, exposition time 2 s (corresponding to 1.06 MW/cm^2); (b) profile along the dashed line, captured by AFM; (c) 2D FFT of the area shown in (a).

of the LSFL as surface ripples on metals (Pt, Ag, Au, Cu, W) under the irradiation of femtosecond beam of 160–480 mJ/cm^2 fluences and small repetition rates (1 kHz) have been reported in Refs. [7–9], showing that the incident wavelength influences the periodicity of the LSFL and that the LSFL gradually disappear in the central area of the spot for further increase of the number of shots. Our SEM analysis has shown that the beam of ~10.3 mJ/cm^2 single pulse fluence (corresponding to 783 kW/cm^2) induced the occurrence of small-amplitude ruffles, the HSFL-like noise, on the Al/Ti samples. The beams of both 13.6 and 14 mJ/cm^2 (1.03 and 1.06 MW/cm^2, respectively) induced the occurrence of the HSFL-like noise for shorter exposition times and the LSFL for longer exposition times. It could be concluded from Fig. 7(b) that the number of the LSFL (ripples) increased with the increase of the exposition time while their width and height did not change. The damage threshold of the Al topmost layer is increased and the surface electron temperature is decreased due to the presence of the Ti underlayer. The lattice temperature is formed through the interplay between two competing mechanisms: electron–phonon (which induces heat localization) and carrier transport linked to the electron heat conductivity (which transfers heat away from the laser-exited region) [37]. The difference in electron–phonon coupling between the two materials leads to the steep change of the lattice temperature inside the inner (Ti) layer. Top layer electrons can quickly transfer energy to the next inner layer (Ti). In this way thermal energy is transmitted through the Al/Ti interface, it is then coupled to the lattice and transferred away from the interaction zone [38]. On the other hand, when the ratio between the interpulse time (~13 ns in our case) and pulse duration (~150 fs in our case) is more than five, more energy from the surface is available to be transferred towards the lattice before it dissipates to the bulk through transport mechanisms. For even greater ratio, mass removal and phase transition are less pronounced. This could be one of the possible causes of the material regrouping in the form of ruffles/ripples on the surface of Al/Ti system without ablation [39].

For the Al samples, the LSFL also occurred with similar spatial period close to the irradiation wavelength. However, the LSFL show much better regularity in Al/Ti samples compared to the single Al films, that is most probably linked to the presence of the Ti layers in the target. Ablated material re-deposited around the ablation zone in the form of ripples (LSFL). For longer expositions, Fig. 3(c), total accumulated energy prevented the regular formation of the ripples. If compared to the Al/Ti case, the absence of the underlayer (Ti) in the single Al layer case has the result that the temperature of the top layer lattice is not reduced and in that way the damage threshold is not increased [38].

Single pulse ablation threshold for various materials at applied wavelength depends on the surface reflectivity, which in turn depends on the number of accumulated pulses. Also, substantial heat accumulation should take place for very high repetition rate, providing decrease of the ablation/melting threshold. For the mirror-like surface the ablation threshold should be slightly higher. Following our results, the evolution of the surface morphology could be explained. The laser beam changes the initial random-ruffle state of the surface in the way that initial ruffles evolve into the HSFL-like noise. For higher fluences the HSFL amplitude is higher. If the fluence is above the threshold of ~13 mJ/cm^2, corresponding to 988 kW/cm^2, the primary condition for the occurrence of the LSFL is met. The exposition time is the secondary condition for the LSFL generation. Thus, for the values above the threshold, the exposition time of ~2 s (corresponding to ~150 million pulses) is required for the generation of the LSFL (in the form of the strings of nanoparticles), which is the cumulative effect. Possible explanation is that there is a fluence threshold for the LSFL formation and – moreover – that there exists the threshold in the number of pulses, effective if the fluence threshold is reached.

Our results show that the beam induces the formation of nanoparticles and their clusters, which regroup or redeposit on the surface in the shape of the string of nanoparticles (the LSFL). The possible driving mechanism in multilayer system may be dewetting upon melting [28,29]. Also, dewetting possibly may occur only in external Al layer, and continue to lower layers. Due to heat accumulation effect, the ablation occurred in single layer configuration. Absence of the ablation in the multilayer sample could be possibly caused by dewetting. According to the measurements (Fig. 6), the LSFL are grown well above the initial surface that can be explained

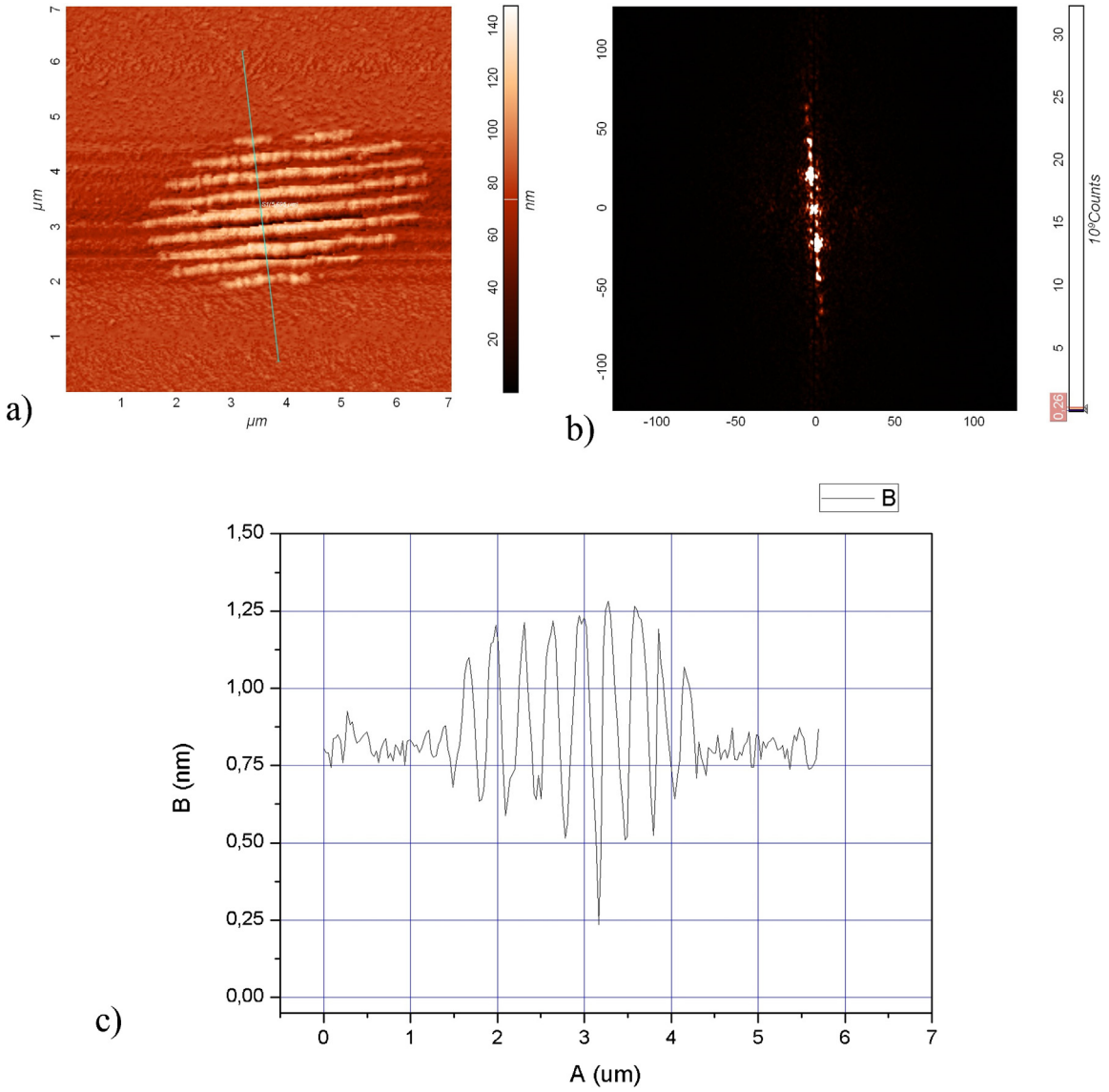

Fig. 7. (a) AFM micrograph of the irradiated spot (SEM presented in Fig. 2(c)): single pulse fluence13.6 mJ/cm^2 and 10 s exposition time (1.03 MW/cm^2); (b) profile along the dashed line, captured by AFM; (c) 2D FFT of the area shown in (a).

by considerable nitriding and oxidation of the material in the irradiated zone (consuming material not only from the sample depth but also from atmosphere) [28]. However, dewetting is not pronounced for single Al layer system of thickness >100 nm.

The dimensions of the individual nanoparticles were in the interval from ~50 to ~150 nm. In the periphery of the MA, that is, in the boundaries of the Gaussian laser beam profile, lower fluence on the Al/Ti target generates nanoparticles of smaller dimension. In the Al single layer sample, Fig. 3(a), the nanoparticles disintegrated (due to melting) and the LSFL formed. In both the Al/Ti and Al single layer samples, the LSFL were most probably caused by the surface plasmon polariton (SPP).

The subwavelength spatial period of the LSFL seems to be dependent on the implemented wavelength. The period of 280 nm was obtained for the laser light at 400 nm, and of 542 nm for the 800 nm laser light [9]. Taking into consideration the previous investigations of the generation, evolution and disintegration of the LSFL under high fluences, low repetition rates and specific wavelengths, one could see different explanations for their occurrence, pointing to various causes, but the most probable is the interaction between the incoming beam and induced surface wave [9,12,40–41]. In spite of using low fluences, our results are consistent with [9], which suggests similar causes of the LSFL generation. It is possible with low-fluence beam – with high repetition rates – to generate HSFL on the irradiated surface, and to induce and control their evolution to the LSFL (subwavelength fs-LIPSS). Moreover, the implementation of low fluence will preserve the LSFL from disintegration even after the great number of pulses, Fig. 5(a). The dielectric constant variation leads to the increase of the optical penetration depth [16,37]. Compared to the Al/Ti multilayer case, the optical penetration depth in the single Al layer case is lower, having higher values of heat accumulation (and absorbed energy) as a consequence. Melting and ablation is induced and more pronounced, and the ruffle/ripple structure is formed. On the other hand, in the Al/Ti multilayer case, the dielectric constant of Ti leads to different values of optical penetration depth and absorbed energy, which means that the mechanism of ruffle/ripple formation is different due to the presence of the Ti layer. Also, due to higher concentration of the laser-induced carriers in single Al layer case, the ripple structure periodicity is lower compared to the Al/Ti case. In the Al/Ti case, the observed monotonicity of the ripple period could be attributed to the constant value of the laser-induced carrier concentration [16].

Moreover, two competing forces (recoil and surface tension) would squeeze the originally produced profile and therefore decrease the period [39]. The presence of Ti underlayer would affect the squeezing, resulting in different values of the periodicity for the two cases (single layer Al and multilayer Al/Ti).

4. Conclusion

The study of surface modifications induced at two types of thin films – five (Al/Ti) bilayers (total thickness of 130 nm) on Si as well as Al single layer (130 nm thickness) on Si – by femtosecond laser beam at 390 nm and repetition rate of 76 MHz (~13 ns of interpulse time), is presented. Morphological changes of the surface were induced with single pulse fluences of 10.3–14 mJ/cm^2 in Al/Ti multilayer samples and with 8.6 mJ/cm^2 in Al single layer samples. We have shown that the fs-LIPSS occur as periodic strings of both nanoparticles and nanoparticle clusers (LSFL) and can be generated on the surface if both the fluence and the exposition time are above certain thresholds. For Al/Ti multilayered thin film, the threshold single pulse fluence is 13 mJ/cm^2 and the exposition time should be $\geq$2 s. While – at this relatively low-fluence regime – shape, height and width of the strings show no dependence on the exposition time, the number of strings of this permanent grating strictly depends on it. We can generate different numbers of lines of this permanent grating by varying the exposition time. We achieved high-quality highly-controllable production of surface periodic structures on nanosized multilayer films with high-repetition-rate low-fluence femtosecond laser pulses.

The LSFL formation could be explained by regrouping of the material under the influence of the SPP. The subwavelength spacing (periodicity) is different for the two cases, the Al single layer and the Al/Ti multilayer, due to the presence of the Ti underlayer. For Al thin film samples, the ablation occurred in the central part of the irradiation area and the material deposited around in the form of the LSFL. The regularity of the ripples (LSFL) is higher at the surface of the Al/Ti multilayer samples due to the presence of the Ti underlayer. The LSFL occurring in laser-based nanopatterning processes could be of interest – for example – in medical, tribological, photovoltaic or decorative applications.

Acknowledgments

The work was supported by the Ministry of Education and Science of the Republic of Serbia under No. III45016 and OI171005. The authors would like to thank to U. Ralević and Dr. S. Savić from the Institute of Physics (University of Belgrade) as well as to Prof. M. Srećković from the Faculty of Electrical Engineering (University of Belgrade) for valuable discussions and help. Kind suggestions and comments from Prof. K. Itoh from Graduate School of Engineering (Osaka University) are also greatly appreciated.

References

[1] H.M. van Driel, J.E. Sipe, J.F. Young, Laser-induced periodic surface structure on solids: a universal phenomenon, Phys. Rev. Lett. 49 (1982) 1955–1958.
[2] J.E. Sipe, J.F. Young, J.S. Preston, H.M. van Driel, Laser-induced periodic surface structure. I. Theory, Phys. Rev. B 27 (1983) 1141–1154.
[3] D. Bauerle, Laser Processing and Chemistry, Springer, Berlin, 2000.
[4] J.F. Young, J.E. Sipe, H.M. van Driel, Laser-induced periodic surface structure. III. Fluence regimes, the role of feedback, and details of the induced topography in germanium, Phys. Rev. B 30 (1984) 2001–2015.
[5] I. Ursu, I.N. Mihăilescu, A.M. Prokhorov, V.I. Konov, V.N. Tokarev, On the role of the periodical structures induced by powerful laser irradiation of metallic surfaces in the energy coupling process, Physica B + C 132 (1985) 395–402.
[6] W. Kautek, P. Rudolph, G. Daminelli, J. Krüger, Physico-chemical aspects of femtosecond-pulse-laser-induced surface nanostructures, Appl. Phys. A 81 (2005) 65–70.
[7] J. Wang, C. Guo, Ultrafast dynamics of femtosecond laser-induced periodic surface pattern formation on metals, Appl. Phys. Lett. 87 (2005) 251914(3).
[8] A.Y. Vorobyev, V.S. Makin, C. Guo, Periodic ordering of random surface nanostructures induced by femtosecond laser pulses on metals, J. Appl. Phys. 101 (2007) 034903(4).
[9] A.Y. Vorobyev, C. Guo, Femtosecond laser-induced periodic surface structure formation on tungsten, J. Appl. Phys. 104 (2008) 063523(3).
[10] M.S. Trtica, B.B. Radak, B.M. Gakovic, D.S. Milovanovic, D. Batani, T. Desai, Surface modifications of Ti6Al4V by a picosecond Nd:YAG laser, Laser Part. Beams 27 (2009) 85–90.
[11] D. von der Linde, K. Sokolowski-Tinten, J. Bialkowski, Laser–solid interaction in the femtosecond time regime, Appl. Surf. Sci. 109–110 (1997) 1–10.
[12] J. Bonse, A. Rosenfeld, J. Krüger, Implications of transient changes of optical and surface properties of solids during femtosecond laser pulse irradiation to the formation of laser-induced periodic surface structures, Appl. Surf. Sci. 257 (2011) 5420–5423.
[13] H. Mochizuki, W. Watanabe, Y. Ozeki, K. Itoh, K. Matsuda, S. Hirono, Fabrication of diffractive optical elements inside polymers by femtosecond laser irradiation, Thin Solid Films 518 (2009) 714–718.
[14] B. Gakovic, C. Radu, M. Zamfirescu, B. Radak, M. Trtica, S. Petrovic, P. Panjan, F. Zupanic, C. Ristoscu, I.N. Mihailescu, Femtosecond laser modification of multilayered TiAlN/TiN coating, Surf. Coat. Tech. 206 (2011) 411.
[15] J. Bonse, J. Krüger, Pulse number dependence of laser-induced periodic surface structures for femtosecond laser irradiation of silicon, J. Appl. Phys. 108 (2010) 034903(5).
[16] J. Bonse, J. Krüger, S. Höhm, A. Rosenfeld, Femtosecond laser-induced periodic surface structures, J. Laser Appl. 24 (2012), 042006 (7pp).
[17] McPherson, Inc. http://www.mcphersoninc.com/reflectivity.htm.(Accessed October 1, 2014).
[18] M. Bass (Ed.), Handbook of Optics, vol. 2, second ed., McGraw-Hill, NY, 1995.
[19] J.F. Young, J.S. Preston, H.M. van Driel, J.E. Sipe, Laser-induced periodic surface structure. II. Experiments on Ge, Si, Al and brass, Phys. Rev. B 27 (1983) 1155.
[20] Alumatter, by European Aluminium Association and MATTER Project at the University of Liverpool, UK, http://aluminium.matter.org.uk/content/html/eng/default.asp?catid=197&pageid=2144416839 (Accessed: October 1, 2014).
[21] X. Li, C. Yuan, H. Yang, J. Li, W. Huang, D. Tan, Q. Hu, Morphology and composition on Al surface irradiated by femtosecond laser pulses, Appl. Surf. Sci. 256 (2010) 4344–4349.
[22] N. Yasumaru, K. Miyazaki, J. Kiuchi, Control of tribological properties of diamond-like carbon films with femtosecond-laser-induced nanostructuring, Appl. Surf. Sci. 254 (2008) 2364–2368.
[23] S.M. Petrović, D. Peruško, B. Salatić, I. Bogdanović-Radović, P. Panjan, B. Gaković, D. Pantelić, M. Trtica, B. Jelenković, Laser induced damage/ablation morphology on the 8(Al/Ti)/Si system in different ambient conditions, Opt. Laser Technol. 54 (2013) 22–29.
[24] Sh. Bashir, M.Sh. Rafique, W. Husinsky, Femtosecond laser-induced subwavelength ripples on Al, Si, CaF_2 and CR-39, Nucl. Instrum. Meth. B 275 (2012) 1–6.
[25] E.V. Golosov, V.I. Emel'yanov, A.A. Ionin, Yu.R. Kolobov, S.I. Kudryashov, A.E. Ligachev, Yu.N. Novoselov, L.V. Seleznev, D.V. Sinitsyn, Femtosecond laser writing of subwave one_dimensional quasiperiodic nanostructures on a titanium surface, JETP Lett. 90 (2009) 107–110.
[26] E.V. Golosov, A.A. Ionin, Yu.R. Kolobov, S.I. Kudryashov, A.E. Ligachev, S.V. Makarov, Yu.N. Novoselov, L.V. Seleznev, D.V. Sinitsyn, Formation of periodic nanostructures on aluminum surface by femtosecond laser pulses, Nanotechnol. Russ. 6 (2011) 237–243.
[27] A.Y. Vorobyev, C. Guo, Colorizing metals with femtosecond laser pulses, Appl. Phys. Lett. 92 (2008), 041914 (5pp).
[28] A. Sharma, R. Khanna, Pattern formating in unstable liquid films, Phys. Rev. Lett. 86 (1998) 3463–3466.
[29] A. Herz, D. Wang, Th. Kups, P. Schaaf, Solid-state dewetting of Au/Ni bilayers: the effect of alloying on morphology evolution, J. Appl. Phys. 116 (2014), 044307 (7pp).
[30] B.E. Deal, A.S. Grove, General relationship for the thermal oxidation of silicon, J. Appl. Phys. 36 (1965) 3770–3778.
[31] E. Sicard, C. Boulmer-Leborgne, T. Sauvage, Excimer laser induced surface nitriding of aluminium alloy, Appl. Surf. Sci. 127–129 (1998) 726–730.
[32] T. Aubert, M.B. Assouar, O. Legrani, O. Elmazria, C. Tiusan, S. Robert, Highly textured growth of AlN films on sapphire by magnetron sputtering for high temperature surface acoustic wave applications, J. Vac. Sci. Technol. A 29 (2011), 021010 (6pp).
[33] A.Gh. Bhuiyan, A. Hashimoto, A. Yamamoto, Indium nitride (InN): a review on growth, characterization, and properties, J. Appl. Phys. 94 (2003) 2779–2808.
[34] P. Schaaf, M. Han, K.-P. Lieb, E. Carpene, Laser nitriding of iron with laser pulses from femtosecond to nanosecond pulse duration, Appl. Phys. Lett. 80 (2002) 1091–1093.
[35] D. Peruško, S. Petrović, J. Kovač, Z. Stojanović, M. Panjan, M. Obradović, M. Milosavljević, Laser-induced formation of intermetallics in multi-layered Al/Ti nano-structures, J. Mater. Sci. 47 (2012) 4488–4495.
[36] D. Peruško, M. Čizmović, S. Petrović, Z. Siketić, M. Mitrić, P. Pelicon, G. Dražić, J. Kovač, V. Milinović, M. Milosavljević, Laser irradiation of nano-metric Al/Ti multilayers, Laser Phys. 23 (2013), 036005 (7pp).
[37] G. Tsibidis, Thermal response of double-layered metal films after ultrashort pulsed laser irradiation: the role of nonthermal electron dynamics, Appl. Phys. Lett. 104 (2014) 051603.

[38] A.M. Chen, H.F. Xu, Y.F. Jiang, L.Z. Sui, D.J. Ding, H. Liu, M.X. Jin, Modeling of femtosecond laser damage threshold on the two-layer metal films, Appl. Surf. Sci. 257 (2010) 1678–1683, and references therein.
[39] M. Barberoglou, G.D. Tsibidis, D. Gray, E. Magoulakis, C. Fotakis, E. Stratakis, P.A. Loukakos, The influence of ultra-fast temporal energy regulationon the morphology of Si surfaces through femtosecond doublepulse laser irradiation, Appl. Phys. A 113 (2013) 273–283.
[40] S. Sakabe, M. Hashida, S. Tokida, S. Namba, K. Okamuro, Mechanism for self-formation of periodic grating structures on a metal surface by a femtosecond laser pulse, Phys. Rev. B 79 (2009), 033409 (4pp).
[41] J. Bonse, A. Rosenfeld, J. Krüger, On the role of surface plasmonpolaritons in the formation of laser-induced periodic surface structures upon irradiation of silicon by femtosecond laser pulses, J. Appl. Phys. 106 (2009), 104910 (5pp).

Journal of Luminescence 243 (2022) 118646

Contents lists available at ScienceDirect

Journal of Luminescence

journal homepage: www.elsevier.com/locate/jlumin

Molecular dysprosium complexes for white-light and near-infrared emission controlled by the coordination environment

Dimitrije Mara [a,*], Flavia Artizzu [b,c], Joydeb Goura [b], Manjari Jayendran [b], Bojana Bokić [d], Branko Kolaric [d,e], Thierry Verbiest [a], Rik Van Deun [b,**]

[a] Molecular Imaging and Photonics, Department of Chemistry, KU Leuven, Celestijnenlaan 200 D, box 2425, B-3001, Leuven, Belgium
[b] L^3 – Luminescent Lanthanide Lab, Department of Chemistry, Ghent University, Krijgslaan 281 – S3, B-9000, Ghent, Belgium
[c] Department of Sciences and Technological Innovation, University of Eastern Piedmont "Amedeo Avogadro", Viale Teresa Michel 11, 15112, Alessandria, Italy
[d] Photonics Center, Institute of Physics, University of Belgrade, Pregrevica 118, 11080, Belgrade, Serbia
[e] Micro- and Nano-photonics Materials Group, University of Mons, Avenue Maistriau 19, B-7000, Mons, Belgium

ARTICLE INFO

Keywords:
White-light emission
Lanthanide complexes
Luminescence
NIR emission

ABSTRACT

A series of single-molecule dysprosium (Dy^{3+}) complexes consisting of β-diketonate ligands, L_1 = 4,4,4-trifluoro-1-phenyl-1,3-butadionate and L_2 = 4,4,4-trifluoro-1-(4-chlorophenyl)-1,3-butadionate, as water-containing complexes, and the auxiliary triphenylphosphine oxide (tppo) ligand as water-free complexes were investigated as potential white-light emitters. The coordination environment and choice of the ligands play an important role in the behavior of the yellow/blue emission of the Dy^{3+} complexes (Y: $^4F_{9/2} \rightarrow {}^6H_{13/2}$ – yellow, and B: $^4F_{9/2} \rightarrow {}^6H_{15/2}$ and ligand phosphorescence – blue) based on the sensitization efficiency of the Dy^{3+} ion by the ligands. By introducing the auxiliary tppo ligand in the complex, the relative intensity of the Dy^{3+} emission increases due to a more efficient sensitization of the Dy^{3+} ion. The CIE (Commission International d'Eclairage) coordination at room temperature for water-containing, **DyL_1H_2O** (0.340, 0.333), and **DyL_2H_2O** (0.270, 0.249), and for water-free complexes, **DyL_1tppo** (0.364,0.391) and **DyL_2tppo** (0.316, 0.331), are close to the coordinates of 'ideal' white light (0.333, 0.333). The CCT (Correlated Color Temperature) values at room temperature for **DyL_1H_2O** (5129 K), **DyL_2H_2O** (18,173 K), and **DyL_2tppo** (6319 K) correspond to 'cold-white-light' emitters, while the **DyL_1tppo** (4537 K) matches a 'warm-white-light' emitter. Beside emitting in the visible (Vis) region, the Dy^{3+} complexes also show emission in the near-infrared (NIR) part of spectrum, which has been studied in detail.

1. Introduction

The growth of the global energy consumption has accelerated development and usage of energy-saving smart devices and energy-efficient solid-state lighting (SSL). Solid-state white-light-emitting materials posses exceptional properties such as energy saving and long operational lifetime, which has already led to their widespread application covering large-panel displays to ambient lighting [1–3]. First, the SSL sources can be subdivided based on the materials, from which they are made of, either inorganic phosphors (LED) or organic molecule semiconductors (OLDE). From another perspective, the SSLs are subdivided in two categories based on the way they are stimulated to emit light, that is, by UV excitation (LEDs) or by electrical excitation (OLEDs). SSLs are much more efficient compared to the classical incandescent lamps, or environmentally friendly as compared to fluorescent and mercury lamps [4–6].

In general, there are two different approaches to obtain white-light emission (WLE): using dichromatic emitters (blue and yellow (B/Y) or blue and red (B/R)), or by using trichromatic emitters which combine the three primary colors (red, green, and blue (RGB)) [1,7–19]. White light is obtained by using separate dopants or multiple phase matrices such as organic compounds, metal complexes, nanomaterials, hybrid organic-inorganic materials or inorganic phosphors. All these types of materials have some unique characteristics to exploit their advantages in obtaining white light, but sometimes it is necessary to mix different types of materials to achieve the intended goal. On the other hand,

* Corresponding author.
** Corresponding author.
E-mail addresses: dimitrije.mara@kuleuven.be (D. Mara), rik.vandeun@ugent.be (R. Van Deun).

https://doi.org/10.1016/j.jlumin.2021.118646
Received 23 August 2021; Received in revised form 19 November 2021; Accepted 25 November 2021
Available online 27 November 2021

white-light emission (WLE) from single molecules can also be achieved, spanning the whole visible (Vis) spectrum [20–25]. The advantage of such systems is that they consist of a single phase single emitter, and this simplifies the production of lighter and thinner materials, which is highly favorable for the implementation of optical devices [26].

Additionally, because of the unique properties of the lanthanide (Ln^{3+}) ions, lanthanide complexes, are interesting platforms for applications in lighting technologies. The Ln^{3+} luminescence arises from 4f – 4f transitions, which correspond to characteristic colors (wavelengths) from the ultra-violet (UV) across the Vis to the near-infrared (NIR) spectral region. Unfortunately, the 4f – 4f transitions are difficult to excite directly according to Laporte's rule and a way to overcome this disadvantage is by using organic chromophores which act as antenna to sensitize the Ln^{3+} ions [27]. β-Diketonate complexes are well known in lanthanide coordination chemistry and have been studied in extent [28,29]. Their ability to excite virtually every spectroscopically active Ln^{3+} ion to obtain the pure Ln^{3+} luminescence colors, as well as their processability into more complex matrices creates the opportunity for a wide range of applications, such as lighting, ion sensing, temperature sensing, telecommunications, etc. [30–33] The organic chromophores in this case should be designed or chosen to act as antennas for the Ln^{3+}, but at the same time they should be able to emit by themselves to yield the blue component necessary to obtain white light. The design of such WLE Ln^{3+} complexes is in fact typically based on the combination of an organic chromophore which emits in the blue region, with a Ln^{3+} ion that emits in the yellow (Dy^{3+}) or in the red (Eu^{3+}) region [34–50].

Here, we present a series of single-molecule WLE tris Dy^{3+} β-diketonate complexes of two different β-diketonate ligands (4,4,4-trifluoro-1-phenyl-1,3-butadionate and 4,4,4-trifluoro-1-(4-chlorophenyl)-1,3-butadionate), with either coordinated water molecules or triphenylphosphine oxide (tppo) as co-ligand, which can be excited at 365 nm [50,51]. Simultaneous emission from the ligand and Dy^{3+} has been observed, giving rise to WLE, which by modifying the coordination environment, could be altered from deep cold (blue) to warm (yellow) white light. In addition to white emission in the Vis region, the series of Dy^{3+} complexes also showed emission in the NIR spectral region.

2. Experimental Section

2.1. Materials

$DyCl_3$•$6H_2O$ (99.9%), 4,4,4-trifluoro-1-phenyl-1,3-butadione (Hbfa) 99% and triphenylphosphine oxide 98% were purchased from Sigma Aldrich. The 4,4,4-trifluoro-1-(4-chlorophenyl)-1,3-butadione 98% was purchased from TCI Europe. Methanol (laboratory grade, 100%) and NaOH were purchased from Fisher Scientific. All chemicals were used without further purification. All reaction were carried out under atmospheric conditions.

2.2. Synthesis of $[Dy(L_{1(2)})_3(H_2O)_2]$ and $[Dy(L_{1(2)})_3(tppo)_2]$ complexes

The synthesis procedure has been previously reported in detailed and will be only discussed in short [51]. The synthesis of $[Dy(L_{1(2)})_3(H_2O)_2]$ was done in methanol by first dissolving an appropriate amount of ligand L_1 and L_2 (0.9 mmol), which were then deprotonated with an equimolar amount of NaOH prior to the addition of methanol solution of $DyCl_3$•$6H_2O$ (0.3 mmol). The obtained crystals were recrystallized from methanol solution and used for further analysis. The synthesis of $[Dy(L_{1(2)})_3(tppo)_2]$ was done in methanol, by addition of a methanol solution of $[Dy(L_{1(2)})_3(H_2O)_2]$ (0.1 mmol) to dissolve triphenylphosphine oxide (tppo) (0.2 mmol) and the complexes were used without any additional purification. No crystals suitable for single crystal X-ray diffraction could be obtained due to the formation of twinned crystals during crystallization.

$[Dy(L_1)_3(H_2O)_2]$ **DyL_1H_2O**: Elemental analysis (%) calculated for $C_{30}H_{22}F_9O_8Dy$ (847.00): C 42.54, H 2.98, found: C 42.45, H 2.93. FT-IR (KBr) ν_{max} (cm^{-1})): 3657 (s; νst O–H, free), 3449 (w; νst O–H, H-bonded), 3083, 2774, 2601, 2525 (w; νst C–H and Fermi resonance), 2482, 2381, 2321, 2273, 2229, 2137 (w; aromatic overtone), 2085 2044, 1985, 1908, 1863, 1820, 1775 (w; comb, aromatic), 1667 (w; νst C═O, keto form), 1628, 1571, 1532, 1493, 1467 (w; νst ar C–C), 1379, 1288 (w; νst C–F, CF3), 1249, 1197, 1144 (w; νst C–F, CF3 and δip ar C–H), 1096 (w), 1027 (s; δip ar C–H), 996 (s; δoop C–H), 817 (w; γ ar C–C and νst C–Cl), 773, 721 (w; δ C–F, CF3, δoop C–H and γ ar C–C and νst C–Cl). ESI-MS (negative mod, -), *m/z*: 868.00 $[M + Na–2H]^-$, 1023.97 $[M+2Br + H]^-$ Isotope used for calculation is ^{164}Dy.

$[Dy(L_2)_3(H_2O)_2]$ **DyL_2H_2O**: Elemental analysis (%) calculated for $C_{30}H_{19}Cl_3F_9O_8Dy$ (950.33): C 37.92, H 2.33; found: C 37.88, H 2.25. FT-IR (KBr) ν_{max} (cm^{-1}): 3657 (s; ν_{st} O–H, free), 3434 (s; ν_{st} O–H, H-bonded), 3072, 2779, 2677, 2591 (w; ν_{st} C–H and Fermi resonance), 2508, 2434, 2389, 2327, 2286, 2232, 2133 (w; aromatic overtone), 2096, 2051, 1911, 1796 (w; comb, aromatic), 1681 (w; ν_{st} C═O, keto form), 1627, 1574, 1536, 1487, 1463 (w; ν_{st} ar C–C), 1401, 1359, 1294 (w; ν_{st} C–F, CF_3), 1248, 1191, 1146 (w; ν_{st} C–F, CF_3 and δ_{ip} ar C–H), 1096 (w), 1014 (s; δ_{ip} ar C–H), 944 (s; δ_{oop} C–H), 849 (w; γ ar C–C and ν_{st} C–Cl), 799, 738, 705, 664 (w; δ C–F, CF_3, δ_{oop} C–H and γ ar C–C and ν_{st} C–Cl). ESI-MS (negative mod, -), *m/z*: 972.00 $[M + Na–2H]^-$, 1159.00 $[M+2Br + H]^-$. Isotope used for calculation is ^{164}Dy.

$[Dy(L_1)_3(tppo)_2]$ **DyL_1tppo**: Elemental analysis (%) calculated for $C_{66}H_{48}F_9O_8P_2Dy$ (1367.54): C 57.97, H 3.76; found: C 57.88, H 3.70. FT-IR (KBr) ν_{max} (cm^{-1}): 3267, 3147 (w; νst C–O, enol beyond the range), 3061 (s; νst ar C–H), 2965, 2913, 2771, 2710, 2599 (w; νst C–H and Fermi resonance), 2520, 2471, 2434, 2381, 2323, 2278, 2129 (w; aromatic overtone), 2088, 2030, 1969, 1895, 1820 (w; comb, aromatic), 1776, 1713 (w; νst C═O, keto form), 1656, 1577, 1535, 1491, 1442 (w; νst ar C–C), 1376, 1323 (w; νst C–F, CF3), 1290 (w; νst P═O), 1244, 1199, 1146 (w; νst C–F, CF3, δip ar C–H and νst R3P═O), 1094, 1075, 1026 (s; δip ar C–H and νst R3P═O), 997, 972 (w; νst R3P═O), 943 (s; δoop C–H and νst R3P═O), 848, 807, 795 (w; γ ar C–C and νst P–C), 758, 725, 635 (w; δ C–F, CF3, δoop C–H and γ ar C–C). ESI-MS (positive mode +), *m/z*: 1428.00 $[M + Na + ACN]^+$, 1150.00 $[M\text{-}tppo + Na + ACN]^+$, 870.00 $[M\text{-}2tppo + Na]^+$. Isotope used for calculation is ^{164}Dy.

$[Dy(L_2)_3(tppo)_2]$ **DyL_2tppo**: Elemental analysis (%) calculated for $C_{66}H_{45}Cl_3F_9O_8P_2Dy$ (1470.87): C 53.89, H 3.29; found: C 53.80, H 3.25. FT-IR (KBr) ν_{max} (cm^{-1}): 3265, 3146 (w; νst C–O, enol beyond the range), 3060 (s; νst ar C–H), 2961, 2920, 2829, 2768, 2714, 2586 (w; νst C–H and Fermi resonance), 2467, 2380, 2327, 2286, 2249, 2129 (w; aromatic overtone), 2088, 2039, 1964, 1898, 1820 (w; comb, aromatic), 1776 (w; νst C═O, keto form), 1627, 1594, 1533, 1483, 1438 (w; νst ar C–C), 1380, 1318 (w; νst C–F, CF3), 1288 (w; νst P═O), 1240, 1187, 1141 (w; νst C–F, CF3, δip ar C–H and νst R3P═O), 1088, 1067, 1030 (s; δip ar C–H and νst R3P═O), 1014, 972 (w; νst R3P═O), 930 (s; δoop C–H and νst R3P═O), 849, 783 (w; γ ar C–C and νst P–C), 725, 693, 660 (w; δ C–F, CF3, δoop C–H and γ ar C–C). ESI-MS (positive mode +), *m/z*: 1497.87 $[M + Na + ACN]^+$, 1218.87 $[M\text{-}tppo + Na + ACN]^+$, 980.00 $[M\text{-}2tppo + Na]^+$. Isotope used for calculation is ^{164}Dy.

2.3. Characterization

Luminescence measurements were performed on an Edinburgh Instruments FLSP920 UV–Vis–NIR spectrometer setup. A 450 W Xe lamp was used as steady-state excitation source. Time-resolved measurements were recorded using a 60 W Xe lamp operating at frequency of 100 Hz. A Hamamatsu R928P photomultiplier tube was used to detect emission signal in the visible region. A Hamamatsu R5509-72 multiplier tube was used to detect emission in the NIR region. The absolute quantum yield (QY) of the complex was determined using an integrating sphere coated with BENFLEC (provided by Edinburgh Instruments) and calculated using Equation (1):

$$\eta = \frac{\int L_{emission} d\lambda}{\int E_{blank} d\lambda - \int E_{sample} d\lambda} \quad (1)$$

Where $L_{emission}$ is the integrated area under the emission spectrum (dλ = 400–700 nm), E_{blank} is the integrated area under the "excitation" band of the blank, and E_{sample} is the integrated area under the excitation band of the sample (as the samples absorbs part of the light, this area will be smaller than E_{blank}). All luminescent measurements were recorded at room temperature. Crystals were put between quartz plates (Starna cuvettes for powder samples, type 20/C/Q/0.2). The time-resolved data were fitted with a biexponential function where the short component (in the range from 1.4 to 1.9 μs) is attributed to the Xe lamp signal, while the longer component is associated to the emission signal of the Dy^{3+} complexes and are presented in Tables 1 and 2. Only for the samples DyL_1tppo and DyL_2tppo the emission signal at ~995 nm, with a significantly longer decay time, was fitted with a monoexponential function.

Fourier Transform Infrared (FTIR) spectra were acquired in the region of 400–4000 cm^{-1} with a Thermo Scientific Nicolet 6700 FT-IR spectrometer equipped with a nitrogen-cooled Mercury Cadmium Telluride (MCT) detector and KBr beam splitter; samples were measured in KBr pellets. Elemental analysis (C, H, N) was performed on a Thermo Fisher 2000 elemental analyzer, using V_2O_5 as catalyst. ESI-MS was performed on an Agilent 6230 time-of-flight mass spectrometer (TOF-MS) equipped with Jetstream ESI source and positive and negative ionization modes were used.

3. Results and discussion

3.1. Synthesis and characterization of Dy^{3+} complexes

The complexes were synthesized using mild reaction conditions, where the β-diketonate ligand was deprotonated with an equimolar amount of sodium hydroxide and reacted with the Dy^{3+} ion in a stoichiometric ratio in methanol. The high reactivity of the β-diketonate ligand toward coordination to Dy^{3+} ions prevents the formation of highly insoluble lanthanide hydroxides, which could be formed under basic conditions. The complexes with formula $[Dy(L_1)_3(H_2O)_2]$ (L_1 = 4,4,4-trifluoro-1-phenyl-1,3-butadionate) and $[Dy(L_2)_3(H_2O)_2]$ (L_2 = 4,4,4-trifluoro-1-(4-chlorophenyl)-1,3-butadionate) were isolated. The synthesis of water-free complexes was performed by introducing tppo in methanol solution in a stochiometric ratio to the $[Dy(L_{1(2)})_3(H_2O)_2]$ complex to form and isolate the water-free complexes with formula $[Dy(L_1)_3(tppo)_2]$ and $[Dy(L_2)_3(tppo)_2]$. These complexes have been characterized by FT-IR, ESI-MS (see SI Figs. S1-S8) and elemental analysis which confirmed that all the complexes have the same composition as the previously reported analogs [51,52].

3.2. Steady-state and time-resolved photoluminescence (PL) studies

3.2.1. Steady-state and time-resolved PL of Dy^{3+} complexes in the visible region

Upon excitation into the β-diketonate ligand absorption band (see SI Figs. S9-S12) with UV light all studied Dy^{3+} complexes showed emission in the Vis and NIR spectral range displaying the characteristic Dy^{3+} peaks. In Fig. 1, the PL emission spectra of **DyL_1H_2O**, **DyL_1tppo** (a), **DyL_2H_2O** and **DyL_2tppo** (c) are presented. The Dy^{3+} $^4F_{9/2} \rightarrow {}^6H_{15/2}$ transition appearing at 480 nm, the $^4F_{9/2} \rightarrow {}^6H_{13/2}$ transition at 575 nm and the $^4F_{9/2} \rightarrow {}^6H_{11/2}$ transition at 660 nm are clearly observed. Besides the emission peaks of the Dy^{3+} ion, a broad band (400–450 nm) with a peak maximum at ~ 430 nm is observed, which is assigned to ligand-centered emission. In water-free complexes the relative intensity of this broad band is lower as compared to its intensity in water-containing complexes. The advantage of the introduction of the tppo ligand into the water-containing complexes brings two benefits: first, the exclusion of water molecules from the first coordination sphere around the Dy^{3+} ion

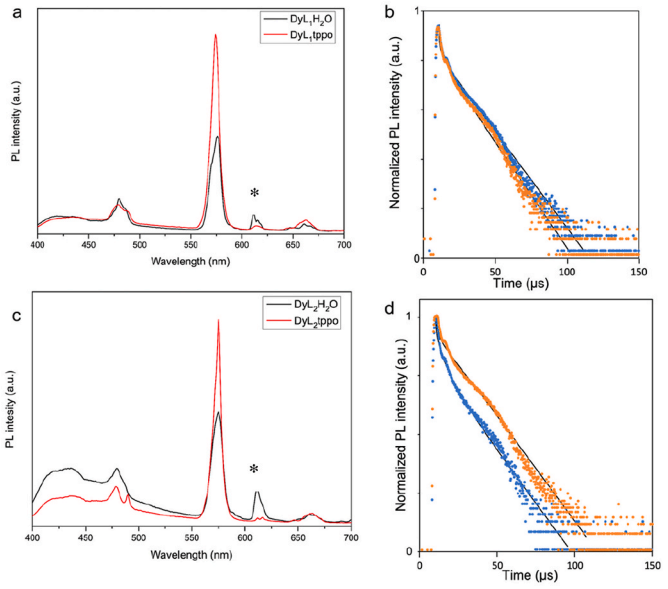

Fig. 1. (a) PL emission spectra of DyL_1H_2O and DyL_1tppo, excited at 365 nm and measured at RT; (b) decay profile of DyL_1H_2O (blue) and DyL_1tppo (orange) observed at 575 nm; (c) PL emission spectra of DyL_2H_2O and DyL_2tppo, excited at 365 nm and measured at RT; (d) decay profile of DyL_2H_2O (blue) and DyL_2tppo (orange) observed at 575 nm * Contamination of the $DyCl_3 \cdot 6H_2O$ salt with europium salts not influencing the photophysics of Dy^{3+}. (For interpretation of the references to color in this figure legend, the reader is referred to the Web version of this article.)

(reducing quenching) and second, a more efficient energy transfer from the tppo ligand to Dy^{3+}, increasing the relative intensity of the metal peaks in the emission spectra in comparison to the ligand band (Fig. 1 a and c).

Time-resolved measurements (Fig. 1 and Table 1) show that the decay dynamics of the Dy^{3+} $^4F_{9/2}$ level is monoexponential and that the water-free complexes have slightly longer luminescent lifetimes compared to the water-containing complexes, likely because of the reduced quenching efficiency by high-energy oscillators related to the water molecules in the first coordination sphere. The sensitization efficiency of the Dy^{3+} ion in the water-free complexes is estimated to be slightly higher as well, because of the possible contribution of the tppo co-ligand to the process. In fact, to realize an efficient energy transfer (ET), the difference between the energy donor, being the triplet state (T_1) of the ligand, and the acceptor, being the emitting level of the Ln^{3+} ion, should be ideally between 2500 and 3500 cm^{-1}. While an energy match between the donor and acceptor states is key to an efficient ET, a small energy gap, which could easily be overcome in molecular complexes by a vibrationally assisted ET, is also desirable to prevent collateral back energy transfer (BET) which could reduce the efficiency of the metal-to-ligand sensitization process (Fig. 2) [53]. This issue is

Table 1
Luminescence lifetimes and absolute quantum yields in the visible range for the Dy^{3+} complexes.

Compound	τ (μs)	R^2	QY [%]
DyL_1H_2O	9.85	0.996	4.94
DyL_1tppo	11.41	0.996	5.32
DyL_2H_2O	9.38	0.995	3.00
DyL_2tppo	10.49	0.996	3.58

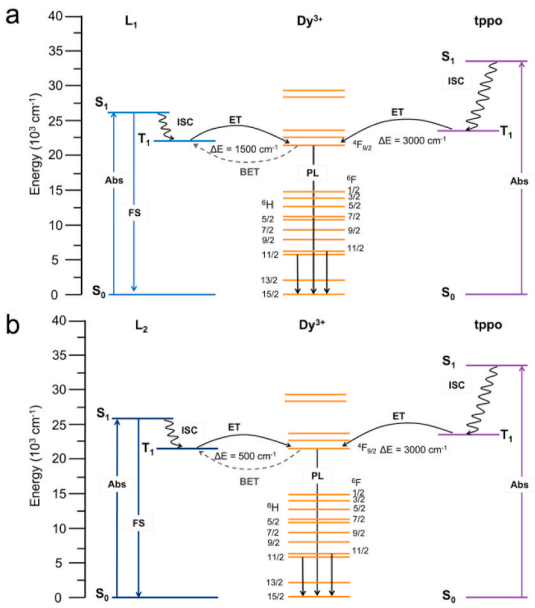

Fig. 2. Jablonski diagram for the Dy^{3+} complexes with the ligand L_1 (a) and with the ligand L_2 (b). S_0 – singlet ground state, S_1 – singlet excited state, T_1 – triplet state, ISC – inter system crossing, ET – energy transfer, BET – back energy transfer, Abs – absorbance, FS – fluorescence, PL – photoluminescence.

particularly relevant in Dy^{3+} compounds where the long-lived main emitting $^4F_{9/2}$ level is placed at ~21,000 cm^{-1}, an energy that is relatively high with respect to the triplet energy level of most organic ligands. In the water-free compounds, the tppo co-ligand has a higher triplet state (T_1 = 23,800 cm^{-1}) compared to the triplet states of ligands L_1 (T_1 = 22,500 cm^{-1}) and L_2 (T_1 = 21,500 cm^{-1}) and is expected to be a more effective antenna towards Dy^{3+} [54,55]. These observations explain the increased relative intensity of the ligand-centered emission in the derivatives with ligand L_2, particularly with coordinated water, indicating a less effective ligand-to metal sensitization (Fig. 1).

3.2.2. *Steady-state and time-resolved PL of Dy^{3+} complexes in the NIR region*

When exciting into the absorption bands of the ligands, the investigated complexes, **DyL_1H_2O** and **DyL_1tppo** (Fig. 3a and b), **DyL_2H_2O** and **DyL_2tppo** (Fig. S13a and 13b in SI), show NIR luminescence. The PL spectrum in the range 800–1650 nm is dominated by the characteristic emission peaks of Dy^{3+} corresponding to the following transitions: $^4F_{9/2} \rightarrow {}^6H_{7/2} + {}^6F_{9/2}$ (846 nm), $^6H_{5/2} + {}^6F_{7/2} \rightarrow {}^6H_{15/2}$ (~ 994 nm), $^6F_{3/2} \rightarrow {}^6H_{13/2}$ (1066 nm), $^4F_{9/2} \rightarrow {}^6F_{5/2}$ (~ 1170 nm), $^6F_{11/2} \rightarrow {}^6H_{15/2}$ and $^6H_{9/2} \rightarrow {}^6H_{15/2}$ (~ 1320 nm), $^4F_{9/2} \rightarrow {}^6F_{1/2}$ (1404 nm) and $^6F_{5/2} \rightarrow {}^6H_{11/2}$ (~ 1500 nm) [56]. However, the **DyL_2H_2O** complex (Fig. S13a) only shows a clear emission peak at 1317 nm while the other peaks in this region are not visible. This is likely ascribable to a significant quenching effect on the Ln^{3+} ion to NIR-emission by high-strength oscillators such as C–H (ν C–H at 1650 nm and 3ν C–H 1130 nm) and O–H (2ν O–H at 1400 nm), especially for water molecules directly bonded to the emitter [50].

The luminescence decay traces of the Dy^{3+} complexes in the NIR have been recorded at 994 nm and ~ 1320 nm corresponding to the $^6H_{5/2} + {}^6F_{7/2}$ and $^6H_{9/2} + {}^6F_{11/2}$ levels, respectively. All decay traces are well fitted with a monoexponential function (see Experimental Section for details), pointing to the existence of one population of emitters and confirming the purity of the samples.

As expectable, for both series of complexes with ligands L_1 and L_2, the emission signal can be only barely detected in water-containing complexes (Fig. 3c and S13c). This effect can be attributed to vibrational quenching through the third harmonic of the OH stretching, as was previously observed in analogous Yb^{3+} complexes [51].

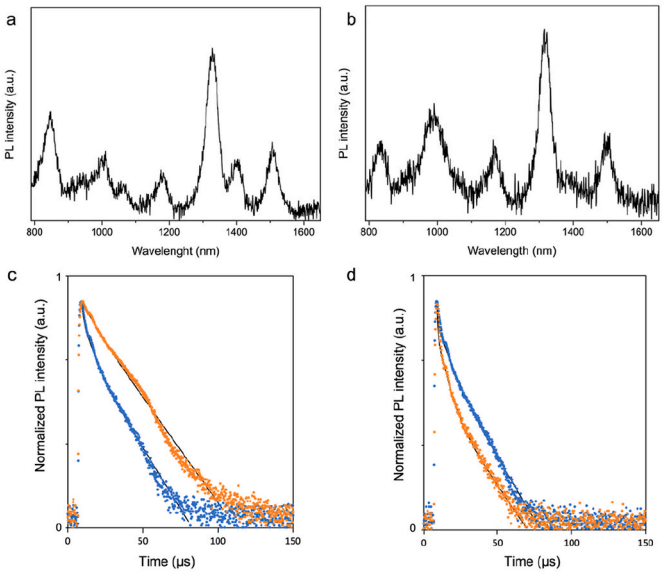

Fig. 3. NIR PL emission spectra of DyL_1H_2O (a) and DyL_1tppo (b), excited at 365 nm and measured at RT; (c) decay profile of DyL_1H_2O (blue) observed at 846 nm, DyL_1tppo (orange) observed at 994 nm; (d) decay profile of DyL_1H_2O (blue) and DyL_1tppo (orange) observed at 1320 nm. (For interpretation of the references to color in this figure legend, the reader is referred to the Web version of this article.)

Table 2
Observed luminescence decay time constants and corresponding Dy^{3+} transitions.

Compound	λ (nm)	Transition	τ (μs)	R^2
DyL_1H_2O	846	$^4F_{9/2} \rightarrow {}^6H_{7/2} + {}^6F_{9/2}$	10.82	0.998
	1320	$^6F_{11/2} \rightarrow {}^6H_{15/2}$ $^6H_{9/2} \rightarrow {}^6H_{15/2}$	10.34	0.997
DyL_1tppo	994	$^6F_{7/2} \rightarrow {}^6H_{15/2}$ $^6H_{5/2} \rightarrow {}^6H_{15/2}$	15.07	0.997
	1320	$^6F_{11/2} \rightarrow {}^6H_{15/2}$ $^6H_{9/2} \rightarrow {}^6H_{15/2}$	10.71	0.998
DyL_2H_2O	1320	$^6F_{11/2} \rightarrow {}^6H_{15/2}$ $^6H_{9/2} \rightarrow {}^6H_{15/2}$	10.73	0.996
DyL_2tppo	994	$^4F_{9/2} \rightarrow {}^6F_{7/2}$	16.33	0.998
	1320	$^6F_{11/2} \rightarrow {}^6H_{15/2}$ $^6H_{9/2} \rightarrow {}^6H_{15/2}$	10.34	0.997

Interestingly, the decay dynamics of the $^6F_{11/2} + {}^6H_{9/2} \rightarrow {}^6H_{15/2}$ transition at 1320 nm is very similar for the water-containing complexes and the tppo derivates of the same ligands. This finding seems apparently in contrast with the expected shortening of the lifetimes in the presence of bound water molecules and with observation made for the relaxation of the $^4F_{9/2}$ level. However, the change of the coordination environment, following the replacement of water molecules by tppo ligands, is likely to induce a significant variation of the oscillator strength of the transition, possibly leading to a decrease of the radiative lifetime in the water-free compounds [51,57]. This could therefore explain the similar observed lifetimes despite the envisaged quenching effect by water molecules. It should be also noted that the discrepancy of the observed lifetime values between the complexes with ligands L_1 and L_2 (Table 2), despite the similar amount of quenching sites, is attributed to a difference in the radiative lifetime dynamics induced by the subtle differences in the ligand structure, further highlighting the relevant role of the coordination environment of the emission properties of these compounds.

3.3. *White-light emission (WLE) of Dy^{3+} complexes*

The CIE chromaticity diagram (Fig. 4) shows that the Dy^{3+}

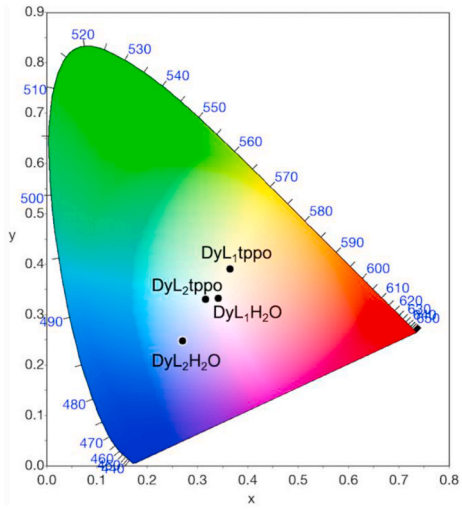

Fig. 4. The CIE chromaticity diagram with the color coordinates of the Dy^{3+} complexes excited at 365 nm. (For interpretation of the references to color in this figure legend, the reader is referred to the Web version of this article.)

Table 3
CIE color coordinates (x,y) and CCT for the Dy^{3+} complexes in the solid state.

Compound	x	y	CCT (K)
DyL_1H_2O	0.340	0.333	5129
DyL_1tppo	0.364	0.391	4537
DyL_2H_2O	0.270	0.249	18,173
DyL_2tppo	0.316	0.331	6319

complexes with both ligands, L_1 and L_2, are emitting in the region from cold to warm white light upon excitation with UV light (365 nm). Exciting by different wavelengths in the ligand absorption bands did not result in significant emission differences. According to the CIE coordinates (Table 3) obtained for the **DyL_1H_2O** and **DyL_2tppo** complexes, the emitted white light is close to the pure white light (CIE 1931 chromaticity x = 0.333, y = 0.333) with Correlated Color Temperatures (CCT) of 5470 K. Instead, the CIE coordinates for the **DyL_1tppo** complex are more situated toward the warm white light region leaning toward yellow-white light and the **DyL_2H_2O** complex shows emission in the cold-white light region, corresponding to blueish-white light. As it can be seen in the CIE diagram, color tunability was achieved by changing the coordination environment by introducing the auxiliary tppo ligand. This resulted in tuning the color for the complexes with ligand L_2 from blue to white light, while for the complexes with ligand L_1 the color was tuned from white to yellow-white light. The observed tunability is in accordance with the decrease of the intensity of the residual blue emission from the β-diketonate ligand upon introduction of the tppo co-ligand, as previously discussed.

4. Conclusions

A series of water-containing and water-free Dy^{3+} β-diketonate complexes were prepared with two ligands, L_1 and L_2, with similar chemical properties but with a slight structural difference. In the ligand L_2 the H-atom of the phenyl ring in *para*-position to the β-diketonate group was substituted with a Cl-atom. The water-free complexes have been prepared with a neutral tppo co-ligand that excludes water molecules from the first coordination sphere of the Dy^{3+} ion and acts as an additional sensitizer for energy transfer to the nearby Dy^{3+} ion. All the complexes showed emission with characteristic transitions in both Vis and NIR region. The proximity of the energies of the triplet (T_1) states of ligands L_1 and L_2 to the emitting level of Dy^{3+} ($^4F_{9/2}$) led to a partial depopulation of the ligand excites states and resulted in the observation of ligand emission in the visible blue in addition to the emission of the Dy^{3+} ion in the yellow-green region. This was exploited to obtain white-light emission. The observed WLE of **DyL_1H_2O** (x = 0.340, y = 0.333) and **DyL_2tppo** (0.316, 0.331) is close to ideal white light with CCT in the cold white-light region. Interestingly, the complexes also yield the rarely observed Dy^{3+} - centered NIR emission with a peak at 1320 nm falling in the O-band region of interest in optical telecommunications. The careful design of a ligand that would promote the emission in the NIR region, without enhancing the quenching of Dy^{3+} emission in this region, could introduce Dy^{3+} as an alternative to the commonly used NIR-emitting lanthanide ions, such as Er^{3+} and Nd^{3+}, that are currently exploited for optical telecommunications. Also the possibility of wider use such as multifunctional molecular materials such as optical applications (lighting) and molecular magnets can be interesting for further design.

Author statement

Dimitrije Mara: Conceptualization, Methodology, Formal analysis, Investigation, Data curation, Writing – original draft. Flavia Artizzu: Formal analysis, Validation, Writing – review & editing. Joydeb Goura: Validation, Writing – review & editing. Manjari Jayerdran: Writing – review & editing. Bojana Bokic: Formal analysis, Writing – review & editing. Brako Kolaric: Formal analysis, Validation, Writing – review & editing. Thierry Verbiest: Supervision, Writing – review & editing. Rik Van Deun: Supervision, Resources, Writing – review & editing.

Declaration of competing interest

There are no conflicts to declare.

Acknowledgments

DM and TV acknowledge KU Leuven Postdoctoral Mandate Internal Funds (PDM) for a postdoctoral fellowship (PDM/20/092). BK and BB acknowledge financial support of The Ministry of Education, Science and Technological Development of The Republic of Serbia. BK also acknowledge support from F R S-FNRS.

Appendix A. Supplementary data

Supplementary data to this article can be found online at https://doi.org/10.1016/j.jlumin.2021.118646.

References

[1] E.F. Schobert, J.K. Kim, Sciences 308 (2005) 1274–1278.
[2] C. Feldmann, T. Jüstel, C.R. Ronda, P.J. Schmidt, Adv. Funct. Mater. 13 (2003) 511–516.
[3] T. Jüstel, H. Nikol, C. Ronda, Angew. Chem. Int. Ed. 37 (1998) 3084–3103.
[4] A. De Almeida, B. Santos, B. Paolo, M. Quicheron, Renew. Sustain. Energy Rev. 34 (2014) 30–48.
[5] H.A. Höppe, Angew. Chem. Int. Ed. 48 (2009) 3572–3582.
[6] N.T. Kalyani, S.J. Dhoble, Renew. Sustain. Energy Rev. 16 (2016) 2696–2723.
[7] J. Leng, H. Li, P. Chen, W. Sun, T. Gao, P. Yan, Dalton Trnas 43 (2014) 12228–12235.
[8] E. Ravindra, S.J. Anathakrisahnan, E. Varanthan, V. Subramanian, N. Somanathan, J. Mater. Chem. C 3 (2015) 4359–4371.
[9] A.H. Shelton, I.V. Sazanovich, J.A. Weinstein, M.D. Ward, Chem. Commun. 48 (2012) 2749–2751.
[10] S. Kamal, K.P. Bera, M. Usman, B. Sainbileg, S. Mendiratta, A. Pathak, A. I. Inamdar, C.-H. Hung, M. Hayashi, Y.-F. Chen, K.-L. Lu, ACS Appl. Nano Mater. 4 (2021) 2395–2403.
[11] J. Qui, C. Yu, X. Wang, Y. Xie, A.M. Kirillov, W. Huang, J. Li, P. Gao, T. Wu, Q. Nie, D. Wu, Inorg. Chem. 58 (2019) 4524–4533.
[12] T.S. Mahapatra, H. Singh, A. Maity, A. Dey, S.K. Prananik, E. Suresh, A. Das, J. Mater. Chem. C 6 (2018) 9756–9766.
[13] Z. Zhang, Y. Chen, H. Chang, Y. Wang, X. Li, X. Zhu, J. Mater. Chem. C 8 (2020) 2205–2210.
[14] Y. Yang, L. Chen, F. Jiang, M. Yu, X. Wan, B. Zhang, M. Hong, J. Mater. Chem. C 5 (2017) 1981–1989.
[15] S. Reineke, F. Lindner, G. Schwartz, N. Seidler, K. Walzer, B. Lüssem, K. Leo, Nature 459 (2009) 234–238.

[16] J. Xue, X. Xu, Y. Zhu, D. Yang, J. Mater. Chem. C 8 (2020) 3380–3385.
[17] Q. Zhu, L. Zhang, K. Van Vilet, A. Miserez, N., ACS Appl. Mater. Interfaces 10 (2018) 10409–10418.
[18] L. Xu, Y. Li, Q. Pan, D. Wang, S. Li, G. Wang, Y. Chen, P. Zhu, W. Qin, ACS Appl. Mater. Interfaces 12 (2020) 18934–18943.
[19] M. Zhang, J. Xue, Y. Zhu, C. Yao, D. Yang, ACS Appl. Mater. Interfaces 12 (2020) 22191–22199.
[20] Z. Chen, C.-L. Ho, L. Wang, W.Y. Wong, Adv. Funct. Mater. 32 (2020) 1903269.
[21] Z. Xie, Q. Huang, T. Yu, L. Wang, Z. Mao, W. Li, Z. Yang, Y. Zhang, S. Liu, J. Xu, Z. Chi, M.P. Aldred, Adv. Funct. Mater. 27 (2017) 1703918.
[22] J. Chen, J. Wang, X. Xu, J. Li, J. Song, S. Lan, S. Liu, B. Cai, B. Han, J.T. Precht, D. Ginger, H. Zeng, Nat. Photonics 15 (2021) 238–244.
[23] M. Chen, Y. Zhao, L. Yan, S. Yang, Y. Zhu, I. Murtaza, G. He, H. Meng, W. Huang, Angew. Chem. Int. Ed. 56 (2017) 722–727.
[24] J. Manzur, R.C. De Santana, L.J.Q. Maia, A. Vega, E. Spodine, Inorg. Chem. 58 (2019) 10012–10018.
[25] R. Bouddula, K. Singh, S. Giri, S. Vaidyanathan, Inorg. Chem. 56 (2017) 10127–10130.
[26] G.-L. Law, K.-L. Wong, H.-L. Tam, K.-W. Cheah, W.-T. Wong, Inorg. Chem. 48 (2009) 10492–10494.
[27] S.I. Weissman, J. Chem. Phys. 10 (1942) 214–217.
[28] K. Binnemans, in: A.K. Gschneider Jr., J.-C.G. Bünzli, K.V. Pecharsky (Eds.), Handbook on Physics and Chemistry of Rare Earths, vol. 35, Elsevier B. V., Amsterdam, 2005, pp. 107–272.
[29] D.J. Bray, J.K. Cleeg, L.F. Lindoy, D. Schilter, Adv. Inorg. Chem. 59 (2006) 1–37.
[30] S.V. Eliseeva, J.-C.G. Bünzli, New J. Chem. 35 (2011) 1165–1176.
[31] K. Binnemans, Chem. Rev. 109 (2009) 4283–4374.
[32] D. Mara, F. Artizzu, B. Laforce, L. Vincze, K. Van Hecke, R. Van Deun, A. M. Kaczmarek, J. Lumin. 213 (2019) 343–355.
[33] Y. Yang, P. Wang, L. Lu, Y. Fan, C. Sun, L. Fan, C. Xu, A.M. El-Toni, M. Alhoshan, F. Zhang, Anal. Chem. 40 (2018) 7946–7952.
[34] S.V. Eliseeva, E.V. Salerno, B.A. Lopez Bermudez, S. Petoud, V.L. Pecoraro, J. Am. Chem. Soc. 142 (2020) 16173–16176.
[35] R. Devi, K. Singh, S. Vaidyanathan, J. Mater. Chem. C 8 (2020) 8643–8653.
[36] L. Zhong, W.-B. Chen, Z.-J. OuYang, M. Yang, Y.-Q. Zhang, S. Gao, M. Schulze, W. Wernsdofer, W. Dong, Chem. Commun. 56 (2020) 2590–2593.
[37] W.A. Dar, Z. Ahmed, K. Iftikhar, J. Photochem. Photobiol. Chem. 356 (2018) 502–511.
[38] J. Wang, S. Chorazy, K. Nakabayashi, B. Sieklucka, S.-i. Ohkosi, J. Mater. Chem. C 6 (2018) 473–481.
[39] Q.-Y. Yang, K. Wu, J.-J. Jiang, C.-W. Hsu, M. Pan, J.-M. Lehn, C.-Y. Su, Chem. Commun. 50 (2014) 7702–7704.
[40] Z.-F. Li, L. Zhou, J.-B. Yu, H.-J. Zhang, R.-P. Deng, Z.-P. Peng, Z.-Y. Guo, J. Phys. Chem. C 111 (2007) 2295–2300.
[41] P.-H. Guo, J.-L. Liu, J.-H. Jia, J. Wang, F.-S. Guo, Y.-C. Chen, W.-Q. Lin, J.-D. Leng, D.-H. Bao, Z.-D. Zhang, J.-H. Luo, M.-L. Tong, Chem. Eur J. 19 (2013) 8769–8773.
[42] L. Zhong, W.-B. Chem, X.-H. Li, Z.-J. OuYang, M. Yang, Y.-Q. Zhang, S. Gao, W. Dong, Inorg. Chem. 59 (2020) 4414–4423.
[43] J. Chen, Z. Xie, L. Meng, Z. Hu, X. Kuang, Y. Xie, C.-Z. Lu, Inorg. Chem. 59 (2020) 6963–6977.
[44] Z. Wang, H. Yang, P. He, Y. He, J. Zhao, H. Tang, Dalton Trans. 45 (2016) 2839–2844.
[45] Y. Wei, Q. Li, R. Sa, K. Wu, Chem. Commun. 50 (2014) 1820–1823.
[46] Y.-H. Zhang, X. Li, S. Song, Chem. Commun. 49 (2013) 10397–10399.
[47] Y.S.L.V. Narayana, S. Basak, M. Baumgarten, K. Müllen, R. Chandrasekar, Adv. Funct. Mater. 23 (2013) 5875–5880.
[48] D. Sykes, I.S. Tidmarsh, A. Barbieri, I.V. Sanzanovich, J.A. Weinstein, M.D. Ward, Inorg. Chem. 50 (2011) 11323–11339.
[49] P. Coppo, M. Duati, V.N. Kozhevnikov, J.W. Hofstraat, L. De Cola, Angew. Chem. Int. Ed. 44 (2005) 1806–1810.
[50] D. Mara, L. Pilia, M. Van de Steen, I. Miletto, M. Zeng, K. Van Hecke, A. Serpe, P. Deplano, R. Van Deun, F. Artizzu, J. Mater. Chem. C. 9 (2021) 15641–15648.
[51] D. Mara, F. Artizzu, P.F. Smet, A.M. Kaczmarek, K. Van Hecke, R. Van Deun, Chem. Eur J. 25 (2019) 15944–15956.
[52] D. Mara, A.M. Kaczmarek, F. Artizzu, A. Abalymov, A.G. Skirtach, K. Van Hecke, R. Van Deun, Chem. Eur J. 27 (2021) 6479–6488.
[53] M. Latva, H. Takalo, V.-M. Mukkala, C. Matachescu, J.C. Rodrígez-Ubis, J. Kankare, J. Lumin. 75 (1997) 149–169.
[54] M. Pietraszkiewicz, O. Pietraszkiewicz, J. Karpiuk, A. Majka, G. Kutkiewicz, T. Borowiak, A.M. Kaczmarek, R. Van Deun, J. Lumin. 170 (2016) 411–419.
[55] A. Zhang, J. Zhang, Q. Pan, S. Wang, H. Jia, B. Xu, J. Lumin. 132 (2012) 965–971.
[56] W.T. Carnall, P.R. Fields, K. Rajnak, J. Chem. Phys. 49 (1968) 4424–4442.
[57] J. Liu, P. Geiregat, L. Pilia, R. Van Deun, F. Artizzu, Adv. Optical Mater. 9 (2021) 2001678.

applied sciences

MDPI

Perspective

Bioinspired NEMS—Prospective of Collaboration with Nature

Marina Simovic-Pavlovic [1,2,*], Bojana Bokic [1], Darko Vasiljevic [1] and Branko Kolaric [1,3,*]

[1] Photonics Center, Institute of Physics, University of Belgrade, Pregrevica 118, 11000 Belgrade, Serbia; bojana@ipb.ac.rs (B.B.); darko@ipb.ac.rs (D.V.)
[2] Faculty of Mechanical Engineering, University of Belgrade, Kraljice Marije 16, 11000 Belgrade, Serbia
[3] Micro- and Nanophotonic Material Group, Department of Physics, University of Mons, Place du Parc 20, 7000 Mons, Belgium
* Correspondence: simovicmarina99@gmail.com (M.S.-P.); branko.kolaric@umons.ac.be (B.K.); Tel.: +381-604273777 (M.S.-P.)

Abstract: The fields of micro- and nanomechanics are strongly interconnected with the development of micro-electro-mechanical (MEMS) and nano-electro-mechanical (NEMS) devices, their fabrication and applications. This article highlights the biomimetic concept of designing new nanodevices for advanced materials and sensing applications.

Keywords: NEMS; bio photonics; biomimetics; bioinspiration; nanotechnology

1. Introduction

Nowadays, technology of any kind is faced with the constant need to minimalize gauges as an imperative for lowering the energy consumption and reduction in materials utilization. The most contributing aspect in this technological revolution is science. By emulating nature's patterns, science seeks sustainable solutions for everyday human challenges. It is vital to harness biomimetic concepts to develop advanced bio-inspired devices for various applications. This article describes the potentials of biomimetic concepts for the design of future nanodevices, especially NEMS, which could have a plethora of potential applications. A practical representation of the order of magnitude of nano devices is given in Figure 1.

After a short introduction, we discuss the state-of-the-art bioinspired NEMS from a fundamental and design perspective, especially highlighting bio-oriented applications. We hope that this article will increase the awareness of the engineering community for biomimetics and highlight biomimetic-inspired concepts and solutions.

check for updates

Citation: Simovic-Pavlovic, M.; Bokic, B.; Vasiljevic, D.; Kolaric, B. Bioinspired NEMS—Prospective of Collaboration with Nature. *Appl. Sci.* **2022**, *12*, 905. https://doi.org/10.3390/app12020905

Academic Editor: Chih-Ching Huang

Received: 13 November 2021
Accepted: 7 January 2022
Published: 17 January 2022

Publisher's Note: MDPI stays neutral with regard to jurisdictional claims in published maps and institutional affiliations.

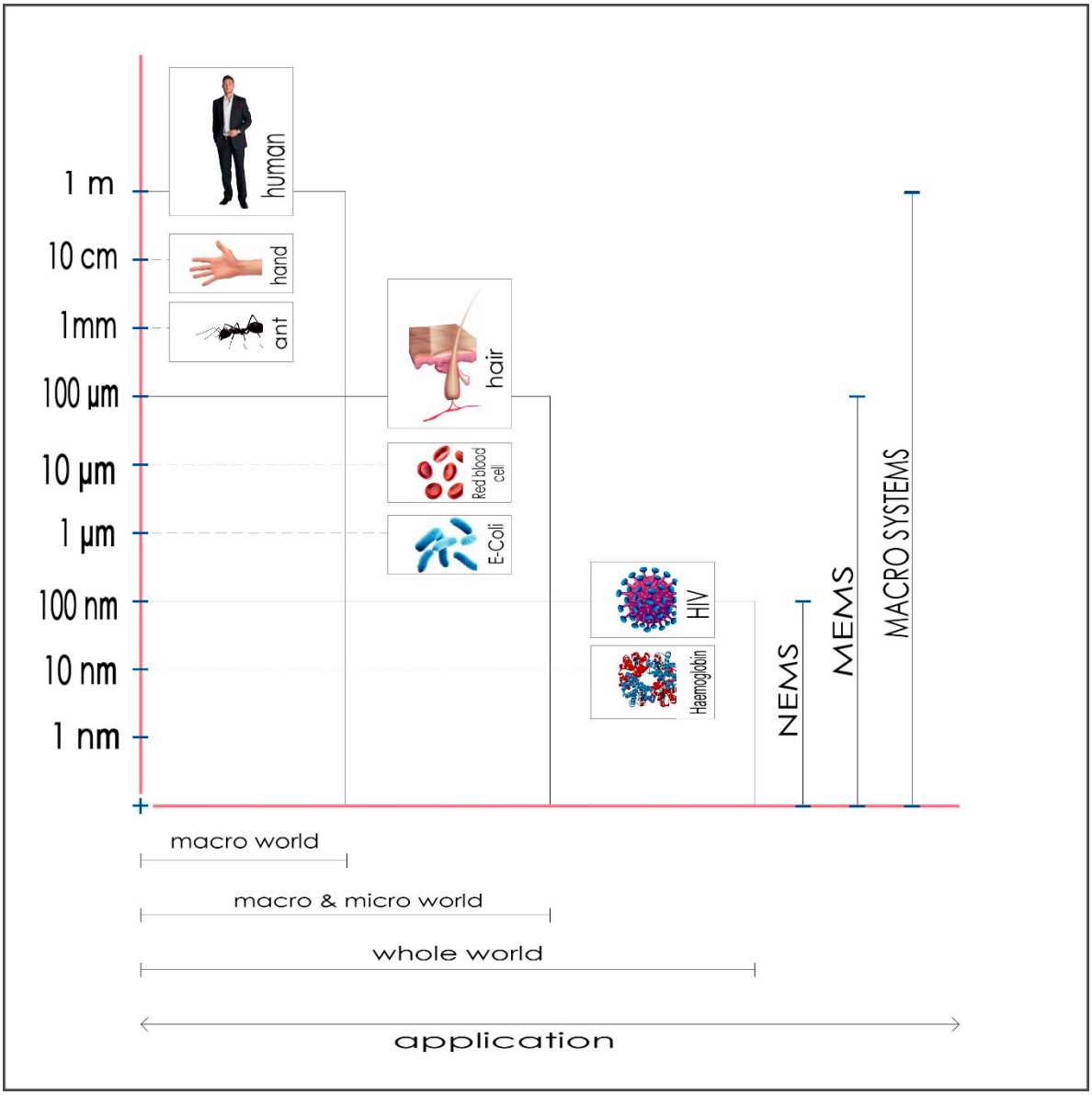

Figure 1. Different scales in nature.

2. The Emergence of Bioinspired NEMS

Bioinspired devices are nanodevices with structure and functions designed to mimic examples from the natural world. Biomimetics is based on mimicking biological principals and patterns as a recipe for creating new materials and structures and integrating them into functional devices. The functionality of these devices also relies on the combined power of optics and nanoengineering. Figure 2 shows the synergy between nanoengineering, optics and biomimetics, which creates the new field of bioinspired NEMS.

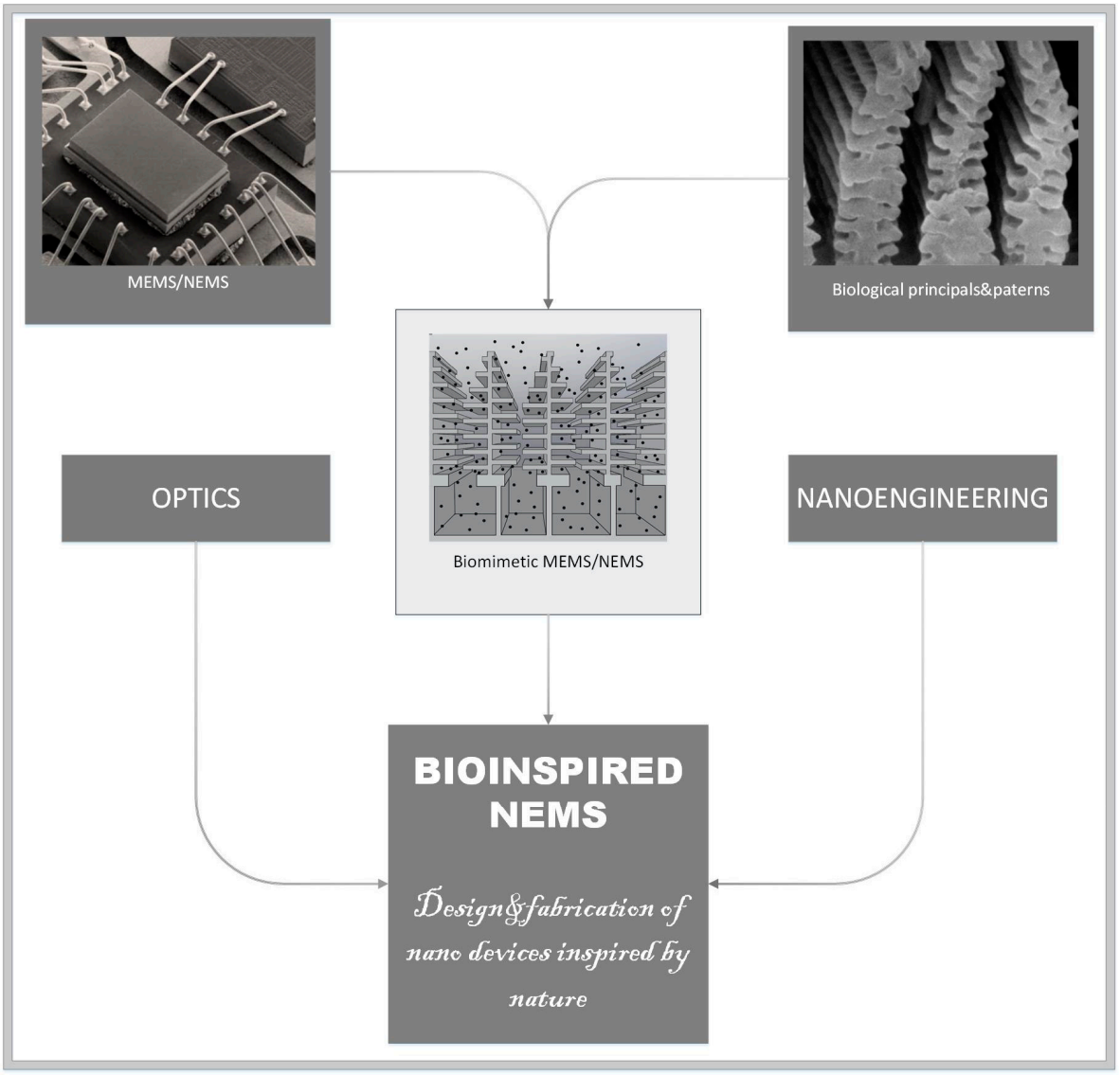

Figure 2. NEMS–Synergy of different technical approaches.

Devices inspired by nature can be classified into two categories: (1) devices that incorporate natural biological structures within their systems and (2) biomimetic (bioinspired) devices that mimic structures and functions from the natural world.

The primary aim of this paper is to attract the interest of the broad material science community towards the bioinspired NEMS concept, which could be used to open new horizons in physical and material research. The authors of this article are confident that soon, in order to reach a cellular economy-driven society, we must develop technology that will be able to harness perfect engineering solutions designed by billions of years of evolution. For this approach to succeed, we must understand the complexity of the biological functions and patterns and their interconnections.

Biomimetics, to begin with [1–3], has a great potential for solving human problems by imitating the natural environment or learning from it. For example, an extensive review of bioinspired triboelectric nanogenerators includes a comparative analysis of structures and materials that draw inspiration from nature [4]. Additionally, a comprehensive review of nanomembranes and their application can be found in MDPI papers [5].

3. Fabrication of Bioinspired NEMS

Most of techniques for the fabrication of bioinspired NEMS use the lithographic method (Figure 3), which proved very suitable for processing nanoelements [6].

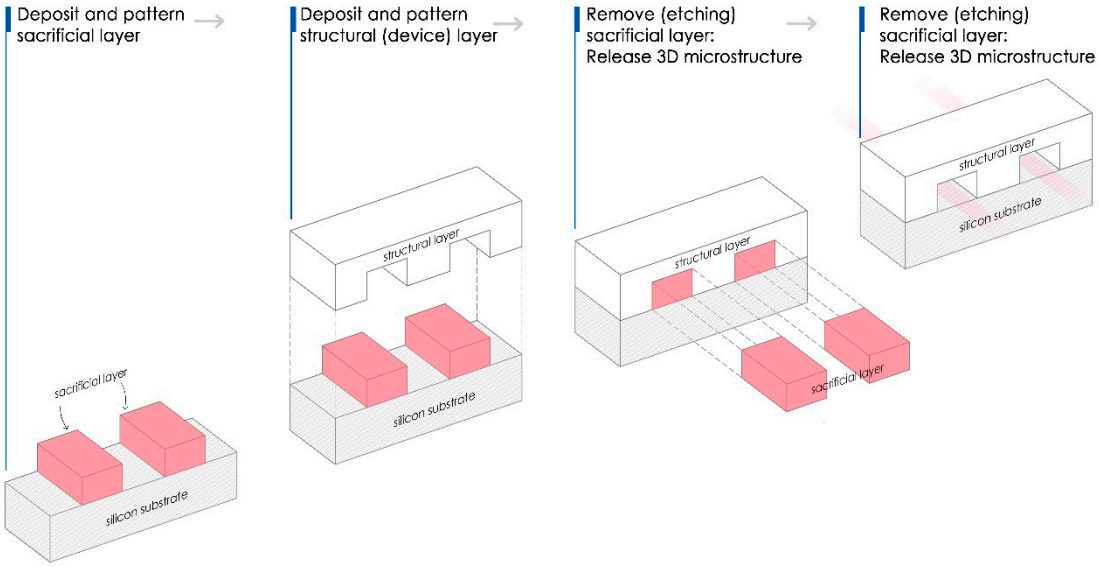

Figure 3. Simplified scheme of a lithography process.

Fabrication of Bioinspired Nano-Structures

Recently, the additive engineering, i.e., 3D printing [7], is used for NEMS fabrication [8].

The future of bioNEMS technology is strongly connected with the development of new fabrication techniques (3D printing, self-assembly, etc.) and opens up many possibilities for potential applications in various fields, such as photonics, biomedicine, nanoelectronics, and sensing.

Micro molding is one of the most widely used techniques. The fabrication of replicas that perfectly match biostructure geometry is an enormous challenge for NEMS fabrication. The most straightforward technique used for replication consists of two-step process.

The development of a negative mold from a biopattern is the first step, and the second is making the positive replica. Kumar et al. [9] presents a precise micro-replication technique, as shown in Figure 4, to transfer surface microstructures of plant leaves onto a highly transparent, soft polymer material to design smooth surfaces with specific nano-corrugation. Structuring surfaces is beneficial for designing materials with controllable properties such as wetting, heat transfer, fluid flow, optical effects, etc.

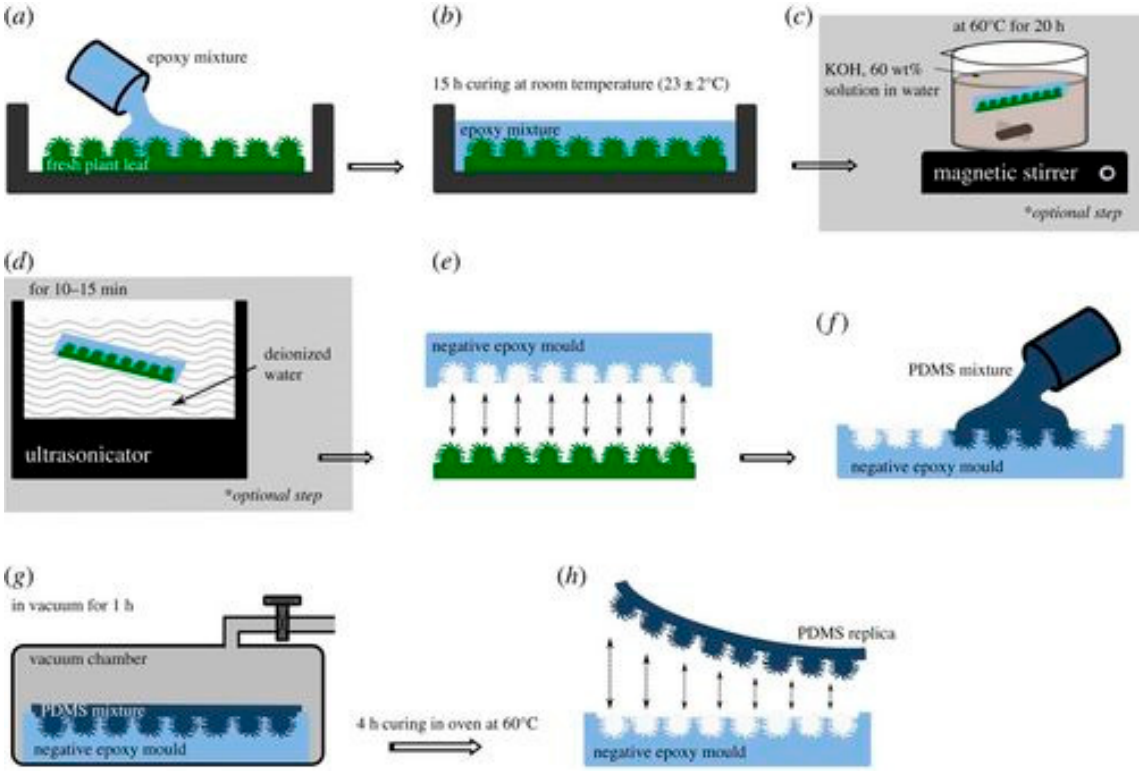

Figure 4. Schematic sketch of the two-step replication process: (**a**) Fresh plant leaf glued on a plastic Petri dish, filled up with epoxy resin. (**b**) Curing of epoxy mixture for 15 h to produce negative epoxy mould. (**c**) Epoxy sample (which adhered with leaf surface) is kept for chemical treatment in potassium hydroxide solution on magnetic stirrer (at 60 ± 3 °C for 20 h). (**d**) Chemically treated sample washed in deionized water using an ultrasonicator. (**e**) Negative epoxy mould separated from the leaf surface. (**f**) Negative epoxy mould filled up with PDMS mixture. (**g**) Degassed in vacuum chamber to remove air trapped at the interface. (**h**) PDMS-positive replica peeled off from the epoxy mould. Reproduced with permission [9].

The unification of biostructures and nanosystems requires simple but reliable tools and techniques. The limited knowledge regarding materials leave us with just a few types of micro- and nanodevices. Modern technologies such as nanopatterning provide an excellent potential to obtain a new class of customized energetic materials for MEMS/NEMS application [10]. These materials allow advances in the processing of microscopic systems that are energy-demanding and may be even more important for bioinspired NEMS. An even more fascinating proposal is based on the utilization of so-called Pavlovian materials [11]. These materials are specially adapted to respond to certain stimuli, and they are proposed for application in integrated devices. As far as materials science is concerned, the inevitable dominance of bioinspired materials in technological applications will happen soon [12].

Recently, Shanker et al. designed melanin nanoparticles for new printable inks with a high boiling point to manage stable jetting and a high-printing efficiency [13]. The advantages of inkjet printing are mainly the reduction in processing times and materials requirement. An even more interesting example of nanofabrication is presented through the method of roll-to-plate (R2P) ultraviolet nanoimprint lithography (UV-NIL). This method uses the combined power of Nickel mold and transparent polycarbonate substrates [14]. The operation simplicity, high efficiency and low-cost fabrication make this antireflection technique promising. The imprint of nanostructures is also described elsewhere [15].

4. Bioinspired NEMS—The State of the Art

Here, we present a few exciting applications based on mimics of natural structures.

4.1. Hair-like Structures

Structures that resemble the hair are widespread in the living world. In biology, organisms often use these body parts to communicate with the environment [16]. Regarding the relatively simple shape of the hair, functional devices that mimic hair structures are constructed with the capability to mold mechanical responses as a function of the slightest changes in their environment. Inspired by the clavate hair-based sensory system used by crickets to sense gravitational acceleration and obtain information on their orientation, a one-axis-biomimetic accelerometer was developed and fabricated using different micro-machining processes [17,18]. Clavate hair is a receptor that is most sensitive to positional changes, while in practical terms, it can be seen as a pendulum subjected to external influences or accelerations from the environment. Staring at the halters of flies that serve to maintain balance based on Coriolis forces, a biomimetic gyroscope was made with the help of MEMS technology [19]. These are tiny organs by which flies sense the rotation of the body, practically opposing the orientation of wings during flight. The oblong extensions that are an integral part of most hair cells receive an external impulse and generate displacement to neurons as a mechanical response. The remarkable abilities of the fish and many sophisticated functions of their organs have led to the development of micro-biomimetic sensors made of artificial materials that resemble hair cells in shape and dimensions [20]. Practically, and in the physiological sense, sensory units are distributed throughout the body of the fish. These units receive flow rate information and convert it to electrical signals that pass through the innervated fibers directly to the brain for further processing. In the end, there are plenty of attractive models from nature to mimic, that could be used for the design of new functional devices.

4.2. BioMEMS: Medical Perspective

A significant subset of MEMS/NEMS devices is biomedical MEMS/NEMS or bioMEMS /bioNEMS. BioMEMS/BioNEMS refers to devices developed for biomedical and medical applications [21]. The potential for the applications of MEMS/NEMS in medicine is practically unlimited [22–24]. Scuor et al. [22] described a new appliance as MEMS-based in-plane biaxial cell stretcher used to study the influences of biaxial stresses on an individual living cell. By exploiting stretchable tools of the described device, the authors [22] recorded a displacement of several micrometers. Using this MEMS approach, it is possible at the same time to actuate and sense at a length scale comparable with single cells. In combination with biological microscopy techniques such as fluorescence, it is possible to visualize the effect of the stress. Parallel with Scuor research, Wang et al. [23] described the new micro-fabrication method for designing micro and nanosize artificial biocompatible capillaries.

Additionally, Tsuda et al. [24] observed a large multi-nuclear, single-cellular organism with no nervous system. The objective of his research was to make an integrated local sensor system that relies on intercellular information exchange. In search of an alternative to control and monitor the functioning of autonomous robots, Tsuda developed a system that works for an extended period without a power supply. This bio-hybrid creation is based on circuitry from amoeboid plasmodia of the slime mold, Physarum polycephalum. The circuits are connected to a hexapod robot that drives the system and exchanges information with the environment.

Soft robotics is an example of a field that has great potential for applications in medicine. Recently Kim et al. [25] developed an artificial micro-muscle fiber crafted from coiled shape–memory alloy (NiTi) springs.

4.3. The Last Decade—an Age of Great Promise

Ten years ago, an exciting moment occurred in materials science. The ability of all complex biological organisms to self-repair minor damages [26] was described, as well as the prospect of mimicking this feature in nanodevices.

"We continually learn things and borrow ideas from nature, but we design devices beyond nature" [27]. This beautiful, harmonious quote as well as the whole book by Di

Zhang [27] represents a useful and exciting introduction to biomimetics. During this period, one gets the impression that thinking begins with a look at biomimetics; biomimetics finally gains its true meaning and becomes officially recognized.

Bioinspired NEMS can play a crucial role in curing or preventing disease. There are currently many NEMS applications in biology and biomedicine, and thus many articles in this field [28,29].

An example of such an application is a silicon micro-channel, used to provide an improved blood plasma separation from whole blood by acoustophoresis. Karthick et al. [30] harnessed the theory of acoustophoresis of dense suspension to understand the acoustic focusing of cells within blood capillaries. Such works are not only inspiring but also have promising applications.

A new lab-on-a-chip (LOC) technology is a kind of bioinspired nano system, recently described elsewhere [31–33]. It is a device that integrates one or several laboratory functions on a single integrated circuit. LOC can be defined as a subset of complex MEMS/NEMS devices. LOC is designed as a sensor capable of detecting different chemicals in bodily fluids and providing information about the current health condition. Currently, many MEMS are customized and programmed within LOC devices for various sensing applications. However, the ultimate goal is to detect any health issue without using expensive techniques and to stop the disease before it progresses. The potential uses of LOC in medicine and health application are unlimited. Recently, the *New York Post* highlighted LOC technology for non-specialists [33].

An exceptional example is a prototype of a 3D-printed artificial lung [34]. In brief, lungs are a mechanical sensor that reacts to the external effects, which is analogous to microsystems. Potkay [34] foresaw this product for short- and long-term respiratory support. In the beginning, it was used as a temporary measure while waiting for transplantation or another healing process, but it could become a permanent solution in the future. Although it does not look like an original organ overall, the structure is perfectly imitated. Thanks to the flexibility enabled by 3D printing, the variation in dimensions and shape is a huge advantage and a step towards new possibilities. Biomimicry is a constant inspiration to researchers and engineers, and now with new 3D technology, better production possibilities are affordable.

The successful replication of organ functions by natural materials, or biocompatible materials, represents the future of medical technology [35]. The possibility of replacing the lung is mind-blowing, with the potential to drastically change many patients' lives.

Aside from that, You et al. [28] studied a self-organization of sessile bacteria within a controlled and closed environment. The ability of bacteria to sense the environment and its gradients and to adjust their movements to them, in combination with the hydrodynamic properties, has a significant impact on the bacterial colonization and management of nutrient resources [29] and could have a substantial impact on understanding complex ecological interactions.

Finally, the MEMS/NEMS applications reach the realm of pharmacy. The main challenge in pharmaceutical analytics is to find a fast and accurate test for sensing in the nano domain at a single-molecule or -particle level. Recently the PMTA method (Particle Mechanical Thermal Analyses) [36] was developed and uses a single particle as a resonator to determine changes in their mechanical properties. The PMTA opens the possibility of the characterization of materials at the single-particle level, which is crucial for developing future nano medicine devices. This achievement represents a remarkable advancement in pharmaceutical science. In recent years, various nanosystems targeting the drug delivery of different anticancer drugs were proposed and based on biomimetic approaches [37].

5. Biomimetics Meets Photonics and Nanomechanics

Recently, Pris et al. [38] and Zhang et al. [39] showed an interesting usage of biostructures. In their papers, the unique example of the management of thermal radiation by biophotonic structures of a *Morpho* butterfly is described. Additionally, the research described

by Grujic et al. [40], pointed out the exciting mechanisms of thermophoresis/photophoresis within biophotonic structures, which could be harnessed for thermal radiation detection. Grujic et al. shows that, in the case of the *Morpho* butterfly, nature exploited natural photonic structures and their optical properties to develop IR detectors much more advanced than currently fabricated ones. Grujic et al.'s [40] experiment revealed a complex functional relationship between biological patterns and their functions. By imitating butterfly wing scales by polymer or composite materials, the thermophoretic effect can be further amplified for different sensing applications and the large-scale production of sensing devices. Polymers are particularly promising materials for infrared sensing applications because of their high IR absorption due to their organic bonds' vibrational resonance modes and their high thermal expansion coefficient compared to metals and semiconductors [41]. Figure 5 shows a portion of a circular section of a sample, the microscopic image, and a holographic image of the investigated butterfly's wing, accompanied with holographic reconstruction.

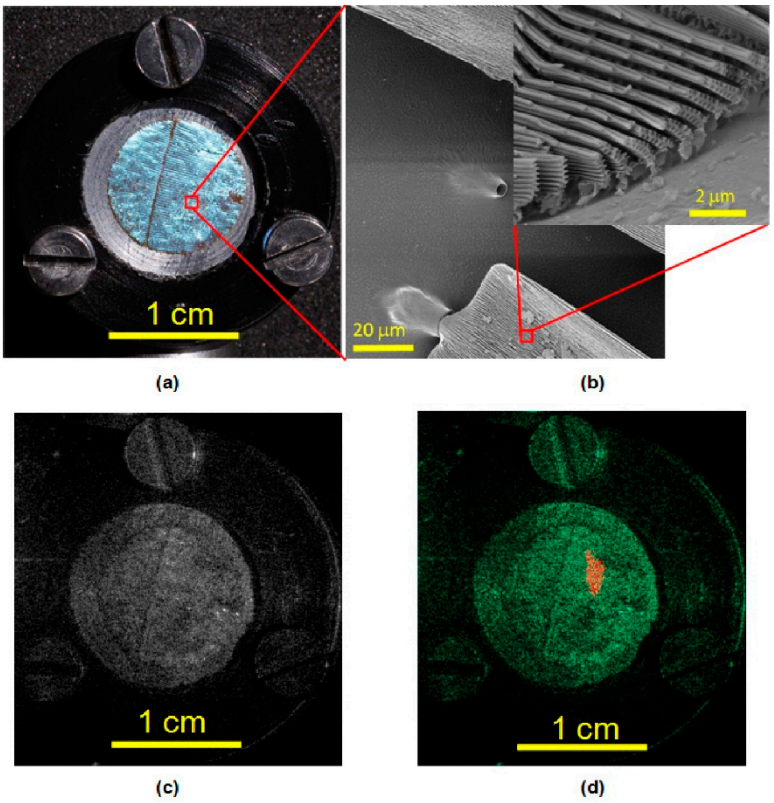

Figure 5. Circular section of a butterfly's wing: (**a**) A photograph, (**b**) a microscope image, (**c**) a hologram reconstruction and (**d**) a holographic image. Reproduced with permission [40].

In the end, to advance in nanoscience and biomimetics, it is imperative to understand the physics of the studied systems. When the microscale is reached, for example, when the distance between two structures or surfaces corresponds to the molecule-free path, thermal forces can occur [42]. Due to the temperature gradient, the surrounding gas causes the formation of a force that creates mechanical displacement at the microscale level. This phenomenon is called thermophoresis. These forces are mechanical forces that scale almost linearly with pressure and temperature. In their paper, Passian et al. [43] described the study of the pressure dependence of Knudsen forces by exploiting MEMS devices.

Moreover, when downscaling from the MEMS to NEMS level, forces between system elements cannot be described by using a classical physics framework. The quantum effect must be considered and controlled, which is one of the most challenging tasks for the development and applications of future NEMS. Figure 6 shows the cartoon image of "strangeness" of quantum mechanics [44].

Figure 6. Cartoon sketch of the limitations of classical physics and "strangeness" of quantum mechanics.

6. Conclusions

The possibility of harnessing biomimetics for the design of advanced NEMS devices is highlighted in this account. The topic discussed here is interesting from a fundamental perspective, with practically unlimited applications in the areas of photonics, sensing, and biomedicine. Even though, at the moment, bioinspired NEMS is still in its infant stage of development, the primary aim of this article is to attract the interest of the broad material and photonics science community for the biomimetic concept, which could open new horizons in material research.

Author Contributions: This study was conducted in partial fulfillment of the requirements for the PhD degree of Marina Simović Pavlović at the University of Belgrade, Faculty of Mechanical Engineering. Conceptualization: M.S.-P. and B.K.; Writing—original draft preparation: M.S.-P.; Writing—review and editing: M.S.-P., B.B., D.V. and B.K.; Visualization: B.B.; Supervision: B.K.; Administration: D.V. All authors have read and agreed to the published version of the manuscript.

Funding: This research was funded by NATO SPS (NATO Science for Peace and Security) 2019–2022, and by the Ministry of Science, Republic of Serbia grant number [Grant III 45016].

Institutional Review Board Statement: Not applicable.

Informed Consent Statement: Not applicable.

Acknowledgments: M.S.-P., D.V. and B.K. acknowledge support of the biological and bioinspired structures for multispectral surveillance, funded by NATO SPS (NATO Science for Peace and Security) 2019–2022. B.K., D.V. and B.B. acknowledge financial support of the Ministry of Science, Republic of Serbia (Grant III 45016). B.K. acknowledges support from FRS–FNRS. Authors warmly acknowledge the architects, Stevan Simovic and Tina Urosevic, for their assistance in creating the images for publication.

Conflicts of Interest: All authors confirmed that there is no conflict of interest among authors.

References

1. Driessen-Mol, A. Biomimetics: A Molecular Perspective. *Green Processing Synth.* **2013**, *2*, 527. [CrossRef]
2. Zheng, X.; Kamot, A.M.; Cao, M.; Kottapalli, A.G.P. Creating underwater vision through wavy whiskers: A review of the flow-sensing mechanisms and biomimetic potential of seal whiskers. *J. R. Soc. Interface* **2021**, *18*, 20210629. [CrossRef]
3. Stenvinkel, P.; Painer, J.; Johnson, R.J.; Natterson-Horowitz, B. Biomimetics—Nature's roadmap to insights and solutions for burden of lifestyle diseases. *Rev. Simp.* **2020**, *287*, 238–251. [CrossRef]
4. Li, W.; Pei, Y.; Zhang, C.; Kottapalli, A.G.P. Bioinspired designs and biomimetic applications of triboelectric nanogenerators. *Nano Energy* **2021**, *84*, 105865. [CrossRef]

5. Jakšić, Z.; Jakšić, O. Biomimetic nanomembranes: An overview. *Biomimetics* **2020**, *5*, 24. [CrossRef] [PubMed]
6. Liu, L.; Sun, L.; Qi, L.; Guo, R.; Li, K.; Yin, Z.; Wu, D.; Zou, H. A low-cost fabrication method of nanostructures by ultraviolet proximity exposing lithography. *AIP Adv.* **2020**, *10*, 045221. [CrossRef]
7. Duda, T.; Raghavan, L.V. 3D Metal Printing Technology. *IFAC-PapersOnLine* **2016**, *49*, 103–110. [CrossRef]
8. Chen, Y.P.; Yang, M.D. Micro-Scale Manufacture of 3D Printing. *Appl. Mech. Mater.* **2014**, *670*, 936–941. [CrossRef]
9. Kumar, C.; Le Houerou, V.; Speck, T.; Bohn, H.F. Straightforward and precise approach to replicate complex hierarchical structures from plant surfaces onto soft matter polymer. *R. Soc. Open Sci.* **2018**, *5*, 172132. [CrossRef]
10. Rossi, C.; Zhang, K.; Esteve, D.; Alphonse, P.; Tailhades, P.; Vahlas, C. Nanoenergetic materials for MEMS: A review. *J. Microelectromech. Syst.* **2007**, *16*, 919–931. [CrossRef]
11. Zhang, H.; Zeng, H.; Priimagi, A.; Ikkala, O. Pavlovian materials—Functional biomimetics inspired by classical conditioning. *Adv. Mater.* **2020**, *32*, 1906619. [CrossRef] [PubMed]
12. Wang, Y.; Naleway, S.E.; Wang, B. Biological and bioinspired materials: Structure leading to functional and mechanical performance. *Bioact. Mater.* **2020**, *5*, 745–757. [CrossRef] [PubMed]
13. Shanker, R.; Sardar, S.; Chen, S.; Gamage, S.; Rossi, S.; Jonsson, M.P. Noniridescent biomimetic photonic microdoms by inkjet printing. *Nano Lett.* **2020**, *20*, 7243–7250. [CrossRef]
14. Sun, J.; Wang, X.; Wu, J.; Jiang, C.; Shen, J.; Cooper, M.A.; Wu, D. Biomimetic moth-eye nanofabrication: Enhanced antireflection with superior self-cleaning characteristic. *Sci. Rep.* **2018**, *8*, 1–10. [CrossRef]
15. Chou, S.Y.; Krauss, P.R.; Renstrom, P.J. Imprint of sub-25 nm vias and trenches in polymers. *Appl. Phys. Lett.* **1995**, *67*, 3114–3116. [CrossRef]
16. Seale, M.; Cummins, C.; Viola, I.M.; Mastropaolo, E.; Nakayama, N. Design principles of hair-like structures as biological machines. *J. R. Soc. Interface* **2018**, *15*, 20180206. [CrossRef]
17. Droogendijk, H.; De Boer, M.J.; Sanders, R.G.P.; Krijnen, G.J.M. A biomimetic accelerometer inspired by the cricket's calvate hair. *J. R. Soc. Interface* **2014**, *11*, 20140438. [CrossRef]
18. Sakaguchi, D.S.; Murphy, R.K. The equilibrium detecting system of the cricket: Physiology and morphology of an identified interneuron. *J. Comp. Physiol.* **1983**, *150*, 141–152. [CrossRef]
19. Droogendijk, H.; Brookhuis, R.A.; De Boer, M.J.; Sanders, R.G.P.; Krijnen, G.J.M. Towards a biomimetic gyroscope inspired by the fly's haltere using microelectromechanical systems technology. *J. R. Soc. Interface* **2014**, *11*, 20140573. [CrossRef]
20. Asadnia, M.; Kottapalli, A.G.P.; Miao, J.; Warkiani, M.E.; Triantafyllou, M.S. Artificial fish skin of self-powered micro-electromechanical systems hair cells for sensing hydrodynamic flow phenomena. *J. R. Soc. Interface* **2015**, *12*, 20150322. [CrossRef]
21. Folch, A. *Introduction to bioMEMS*; CRC Press: Boca Raton, FL, USA, 2016.
22. Scuor, N.; Gallina, P.; Panchawagh, H.V.; Mahajan, R.L.; Sbaizero, O.; Sergo, V. Design of a novel MEMS platform for the biaxial stimulation of living cells. *Biomed. Microdevices* **2006**, *8*, 239–246. [CrossRef]
23. Wang, G.J.; Chen, C.L.; Hsu, S.H.; Chiang, Y.L. Bio-MEMS fabricated artificial capillaries for tissue engineering. *Microsyst. Technol.* **2005**, *12*, 120–127. [CrossRef]
24. Tsuda, S.; Zauner, K.P.; Gunji, Y.P. Robot control with biological cells. *Biosystems* **2007**, *87*, 215–223. [CrossRef]
25. Kim, S.; Hawkes, E.; Choy, K.; Joldaz, M.; Foleyz, J.; Wood, R. Micro Artificial Muscle Fiber Using NiTi Spring for Soft Robotics. In Proceedings of the International Conference on Intelligent Robots and Systems, St. Louis, MO, USA, 10–15 October 2009; pp. 2228–2234.
26. Nosonovsky, M.; Rohatgi, P.K. *Biomimetics in Materials Science: Self-Healing, Self-Lubricating, and Self-Cleaning Materials*; Springer Science & Business Media: Berlin/Heidelberg, Germany, 2011; Volume 152.
27. Zhang, D. *Morphology Genetic Materials Templated from Nature Species*; Springer Science & Business Media: Berlin/Heidelberg, Germany, 2014.
28. You, Z.; Pearce, D.J.G.; Sengupta, A.; Giomi, L. Geometry and mechanics of microdomains in growing bacterial colonies. *Phys. Rev. X* **2018**, *8*, 031065. [CrossRef]
29. Desai, N.; Ardekani, A.M. Combined influence of hydrodynamics and chemotaxis in the distribution of microorganisms around spherical nutrient sources. *Phys. Rev. E* **2018**, *98*, 012419. [CrossRef] [PubMed]
30. Karthick, S.; Sen, A.K. Improved understanding of acoustophoresis and development of an acoustofluidic device for blood plasma separation. *Phys. Rev. Appl.* **2018**, *10*, 034–037. [CrossRef]
31. Zhang, J.M.; Ji, Q.; Liu, Y.; Huang, J.; Duan, H. An integrated micro-milli fluidic processing system. *Lab Chip* **2018**, *18*, 3393–3404. [CrossRef]
32. Shuler, M.L. Advances in Organ-, body-, and Disease-on-a-chip Systems. *Lab Chip* **2019**, *19*, 9–10. [CrossRef] [PubMed]
33. Tousignant, L. This Miracle Medical Chip Could One Day Heal almost Anything. *New York Post*, 8 August 2017.
34. Richman, M. *Breathing Easier*; U.S. Department of Veterans Affairs: Washington, DC, USA, 2018.
35. Tan, G.Z.; Zhou, Y. Electrospinning of biomimetic fibrous scaffolds for tissue engineering: A review. *Int. J. Polym. Mater. Polym. Biomater.* **2020**, *69*, 947–960. [CrossRef]
36. Okeyo, P.O.; Larsen, P.E.; Kissi, E.O.; Ajalloueian, F.; Rades, T.; Rantanen, J.; Boisen, A. Single particles as resonators for thermomechanical analysis. *Nat. Commun.* **2020**, *11*, 1–11. [CrossRef]

37. Li, A.; Zhao, Y.; Li, Y.; Jiang, L.; Gu, Y.; Liu, J. Cell-derived biomimetic nanocarriers for targeted cancer therapy: Cell membranes and extracellular vesicles. *Drug Deliv.* **2021**, *28*, 1237–1255. [CrossRef] [PubMed]
38. Pris, A.D.; Utturkar, Y.; Surman, C.; Morris, W.G.; Vert, A.; Zalyubovskiy, S.J.; Deng, T.; Ghiradella, H.T.; Potyrailo, R.A. Towards high-speed imaging of infrared photons with bio-inspired nanoarchitecture. *Nat. Photonics* **2012**, *6*, 195–200. [CrossRef]
39. Zhang, F.; Shen, Q.; Shi, X.; Li, S.; Wang, W.; Luo, Z.; He, G.; Zhang, P.; Tao, P.; Song, C.; et al. Infrared detection based on localized modification of Morpho butterfly wings. *Adv. Matter.* **2015**, *27*, 1077–1082. [CrossRef]
40. Grujic, D.; Vasiljevic, D.; Pantelic, D.; Tomic, L.J.; Stamenkovic, Z.; Jelenkovic, B. Infrared camera on the butterfly's wing. *Opt. Express* **2018**, *26*, 14143–14158. [CrossRef] [PubMed]
41. Mueller, M.T. Biomimetic, Polymer-Based Microcantilever Infrared Sensors. Ph.D. Dissertation, University of California, Berkeley, CA, USA, 2007.
42. Passian, A.; Wig, A.; Meriaudeau, F.; Ferrell, T.L.; Thundat, T. Knudsen forces on microcantilevers. *J. Appl. Phys.* **2002**, *92*, 6326–6333. [CrossRef]
43. Passian, A.; Warmack, R.J.; Ferrel, T.L.; Thundat, T. Thermal transpiration at the microscale: A Crookes cantilever. *Phys. Rev. Lett.* **2003**, *90*, 124503. [CrossRef] [PubMed]
44. Verstraete, C.; Mouchet, S.R.; Verbiest, T.; Kolarić, B. Linear and nonlinear optical effects in biophotonic structures using classical and nonclassical light. *J. Biophotonics* **2019**, *12*, e201800262. [CrossRef]

symmetry

MDPI

Article

Spontaneous Symmetry Breaking: The Case of Crazy Clock and Beyond

Maja C. Pagnacco [1,*], Jelena P. Maksimović [2], Marko Daković [2], Bojana Bokic [3], Sébastien R. Mouchet [4,5], Thierry Verbiest [6], Yves Caudano [7] and Branko Kolaric [3,8,*]

1 Center for Catalysis and Chemical Engineering, Institute of Chemistry, Technology and Metallurgy, University of Belgrade, Njegoševa 12, 11000 Belgrade, Serbia
2 Faculty of Physical Chemistry, University of Belgrade, Studentski Trg 12, 11158 Belgrade, Serbia; jelena.maksimovic@ffh.bg.ac.rs (J.P.M.); marko@ffh.bg.ac.rs (M.D.)
3 Center for Photonics, Institute of Physics, University of Belgrade, Pregrevica 118, 11080 Belgrade, Serbia; bojana@ipb.ac.rs
4 Department of Physics & Namur Institute of Structured Matter (NISM), University of Namur, Rue de Bruxelles 61, 5000 Namur, Belgium; sebastien.mouchet@unamur.be
5 School of Physics, University of Exeter, Stocker Road, Exeter EX4 4QL, UK
6 Department of Chemistry, Molecular Imaging and Photonics, KU Leuven, 3001 Heverlee, Belgium; thierry.verbiest@fys.kuleuven.be
7 Department of Physics & Namur Institute of Structured Matter (NISM) & Namur Institute for Complex Systems (naXys), University of Namur, Rue de Bruxelles 61, 5000 Namur, Belgium; yves.caudano@unamur.be
8 Micro- and Nanophotonic Materials Group, University of Mons, Place du Parc 20, 7000 Mons, Belgium
* Correspondence: maja.pagnacco@nanosys.ihtm.bg.ac.rs (M.C.P.); branko.kolaric@umons.ac.be (B.K.)

Abstract: In this work, we describe the crazy-clock phenomenon involving the state I (low iodide and iodine concentration) to state II (high iodide and iodine concentration with new iodine phase) transition after a Briggs–Rauscher (BR) oscillatory process. While the BR crazy-clock phenomenon is known, this is the first time that crazy-clock behavior is linked and explained with the symmetry-breaking phenomenon, highlighting the entire process in a novel way. The presented phenomenon has been thoroughly investigated by running more than 60 experiments, and evaluated by using statistical cluster K-means analysis. The mixing rate, as well as the magnetic bar shape and dimensions, have a strong influence on the transition appearance. Although the transition for both mixing and no-mixing conditions are taking place completely randomly, by using statistical cluster analysis we obtain different numbers of clusters (showing the time-domains where the transition is more likely to occur). In the case of stirring, clusters are more compact and separated, revealed new hidden details regarding the chemical dynamics of nonlinear processes. The significance of the presented results is beyond oscillatory reaction kinetics since the described example belongs to the small class of chemical systems that shows intrinsic randomness in their response and it might be considered as a real example of a classical liquid random number generator.

Keywords: crazy clock; Briggs–Rauscher reaction; state I to state II transition; symmetry breaking; iodine; K-means analysis; random number generator

Citation: Pagnacco, M.C.; Maksimović, J.P.; Daković, M.; Bokic, B.; Mouchet, S.R.; Verbiest, T.; Caudano, Y.; Kolaric, B. Spontaneous Symmetry Breaking: The Case of Crazy Clock and Beyond. *Symmetry* **2022**, *14*, 413. https://doi.org/10.3390/sym14020413

Academic Editor: Stefano Profumo

Received: 10 January 2022
Accepted: 14 February 2022
Published: 19 February 2022

1. Introduction

The presence of symmetry around us inspired many scientists to search for beauty, harmony, order, and regularity in nature and her fundamental laws [1,2]. Additionally, phase transitions with and without spontaneously broken symmetries are widespread concepts through different areas of physics and physical chemistry. The applications of spontaneously broken symmetries cover a wide range of condensed matter science topics, such as superconductivity, super-fluidity, Bose–Einstein condensation, nucleation physics, self-assembly processes, morphogenesis, and chemical kinetics. In this account, we describe spontaneous symmetry breaking in the case of the nonlinear Briggs–Rauscher reaction. We

highlight the importance of symmetry breaking, in non-equilibrium and pattern formation processes, which is of vital meaning to the understanding of the morphogenesis process and for applications in several areas of biomimetics and nanoscience.

The Briggs–Rauscher (BR) [3] reaction is a hybrid oscillating reaction formed by coupling two chemical oscillators, Bray–Liebhafsky [4,5] and Belousov–Zhabotinskii [6]. Since its discovery in 1973, the Briggs–Rauscher oscillating reaction has been one of the most investigated oscillatory systems. It is probably due to its simplicity and exciting colour alternation caused by changes in reaction kinetics (when starch is used as an indicator) [7].

BR reaction typically occurs within mixtures of H_2O_2, H_2SO_4, and KIO_3. Additionally, Mn(II) ions are added as a metal catalyst and malonic acid (H_2MA) as an organic substrate. Substitutions of chemicals are possible; different acids, organic substrates, and ions, such as Ce(III) instead of Mn(II) catalyst, can be used to generate BR oscillations [7–10]. However, the oscillatory behavior is not the only one that attracted the attention of non-linear scientists in the Briggs–Rauscher reaction [11–15].

Indeed, as described elsewhere [16], after the well-controlled initial oscillatory behavior, the reaction becomes chaotic. Depending on the initial conditions, particularly on the ratio $[H_2MA]_0/[IO_3^-]_0$ [16,17], the reaction exhibits a sudden and unpredictable phase transition. This transition, from state I (low concentration of iodide and iodine) to state II (high concentration of iodide and iodine), happens randomly in practice, as the time spent by the system in the state I is irreproducible (see Figure 1). The transition is characterized by a "sharp and sudden" increase of iodine and iodide concentration, followed by the formation of solid iodine. The observed stochastic feature, called a crazy clock (due to the unpredictable time needed to provoke the transition), is linked to imperfect mixing that affects convection and diffusion dynamics. The imperfect mixing results in extremely complicated phenomena, which occur on multiple length and time scales [18]. Possible kinetical consequences are the appearance of bifurcation, chaos, intermittent behavior, and symmetry-breaking [18,19]. In the experiments of our previous paper [16], the mixing was stopped after an intensive homogenization (stirring at 900 rpm) of the Briggs–Rauscher solution in the oscillatory period. Herein, the experiments carried out with or without specific mixing were maintained all the time. Additionally, we apply the statistical cluster K-means analysis for the first time, by processing more than 60 experiments. Therefore, this paper further studies the mixing effects in connection to the crazy-clock phenomenon in the Briggs–Rauscher oscillatory reaction. It compares and processes statistically more than #60 experiments obtained under identical initial concentrations of all reactants. Although the BR crazy-clock phenomenon was previously detected [16], this behavior is linked for the first time to symmetry-breaking, highlighting the entire process in a novel way. Furthermore, the investigated crazy clock exhibits a truly random behavior that might be considered as an example of a classical, liquid random number generator. Additionally, the investigated system also belongs to the particular class of classical systems that shows intrinsic randomness in their response (as also observed in colloid particles placed on an oscillating surface) [20,21].

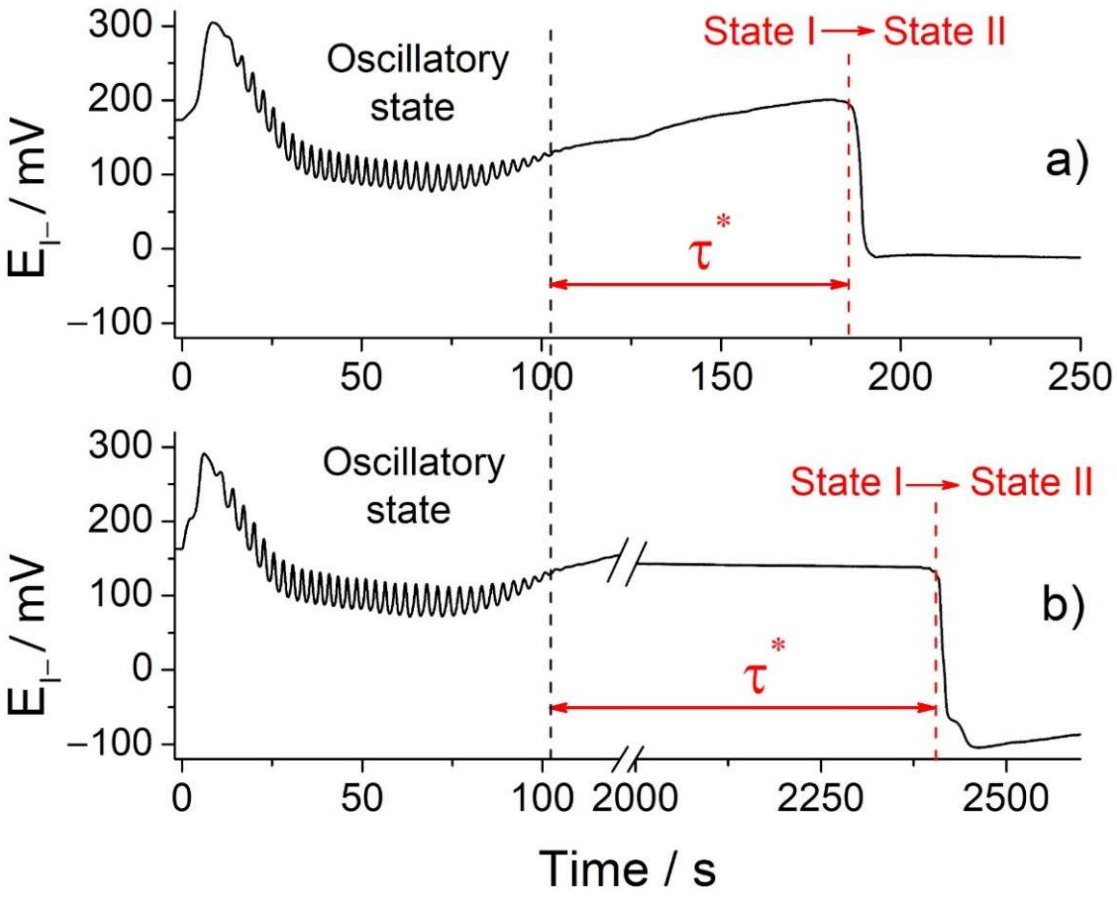

Figure 1. Two independent measurements (**a**,**b**) of iodide potential vs. time obtained for BR reaction under experimental conditions: $[H_2MA]_0$ = 0.0789 mol/dm^3, $[MnSO_4]_0$ = 0.00752 mol/dm^3, $[HClO_4]_0$ = 0.03 mol/dm^3, $[KIO_3]_0$ = 0.0752 mol/dm^3, $[H_2O_2]_0$ = 1.176 mol/dm^3, T = 37.0 °C. The experiments were performed without stirring and without protection from light. τ^* denotes the time from the end of the oscillatory mode to the occurrence of state I→state II transition.

2. Materials and Methods

2.1. Briggs–Rauscher Experimental Setup

Since the time of the transition between state I and II is unpredictable, great attention must be paid to the experimental procedure. Only analytically graded reagents without further purification were used for preparing the solutions. Malonic acid was obtained from Acrōs Organics (Geel, Belgium), manganese sulphate from Fluka (Buchs, Switzerland), perchloric acid, potassium iodate, and hydrogen peroxide from Merck (Darmstadt, Germany). The solutions were prepared in deionized water with specific resistance 18 MΩ/cm (Milli-Q, Millipore, Bedford, MA, USA).

All experiments were done in a container not protected from light. Reactions were monitored electrochemically (unless specified in the text). An I-ion-sensitive electrode (Metrohm 6.0502.160) was used as the working electrode and an Ag/AgCl electrode (Metrohm 6.0726.100), as the reference. During the experiments, the temperature of the reaction container was regulated by a circulating thermostat (JULABO GmbH, Seelbach, Germany) and maintained constant at 37 °C. The reaction mixture was stirred by magnetic stirrer (Ingenieurbüro, M. Zipperrer GmbH, Cat-ECM5, Staufen, Denmark).

Five independent series of measurements were carried (they differed in stirring bar size and shape, as well as mixing rate) with the identical solution composition $[H_2MA]_0$ = 0.0789 mol/dm^3, $[MnSO_4]_0$ = 0.00752 mol/dm^3, $[HClO_4]_0$ = 0.03 mol/dm^3, $[KIO_3]_0$ = 0.0752 mol/dm^3 and $[H_2O_2]_0$ = 1.176 mol/dm^3 in 25 mL volume:

(1) without mixing (number of conducted experiments #30);
(2) with mixing 100 rpm using cylindrical stirring bar 10 mm length, 4 mm diameter (BRAND magnetic stirring bar, PTFE-coated cylindrical), (number of conducted experiments #30);
(3) with mixing 300 rpm using cylindrical stirring bar 10 mm length, 4 mm diameter (BRAND magnetic stirring bar, PTFE-coated cylindrical), (in triplicate);
(4) with mixing 100 rpm using cylindrical stirring bar 20 mm length, 6 mm diameter (BRAND magnetic stirring bar, PTFE-coated cylindrical) (in triplicate);
(5) with mixing 100 rpm using triangular stirring bar 12 mm length, 6 mm diameter (BRAND magnetic stirring bar, PTFE-coated triangular) (in triplicate).

2.2. Statistical Processing and Cluster Analysis

The obtained experimental results were analyzed in the open-source statistic software "R" using "hclust" algorithm for the hierarchical cluster analysis (HCA) [22,23].

3. Results and Discussion

3.1. Effects of the Stirring Bar Shape and Dimensions on the State I→State II Transition

The BR oscillatory period is strongly reproducible, while the transition from state I to state II occurred practically randomly (Figure 1), as previously reported by our research group [16].

It is imperative to emphasize that in our measurements (Figure 1), unlike in other crazy-clock reactions found in the literature [18,19,24], large time fluctuations (the order of magnitude could be more than two hours) occur after a highly reproducible oscillatory period. Two independent measurements and consequently obtained BR oscillograms exhibit identical trends in oscillation amplitude and time between two neighboring oscillation maxima $\tau_{n-(n-1)} = t_n - t_{n-1}$, as it can be observed in Figures 1 and 2a,b. Conversion from higher to lower potential of iodine electrode (or from low to high iodide concentration) marks the transition from state I to state II (state I→state II). Furthermore, the choice of the working electrode affects only the transition shape. However, the transition itself is very noticeable due to the intense color change of the system from colorless to yellow accompanied by solid iodine formation. This allows monitoring the state I→state II transition with the naked eye.

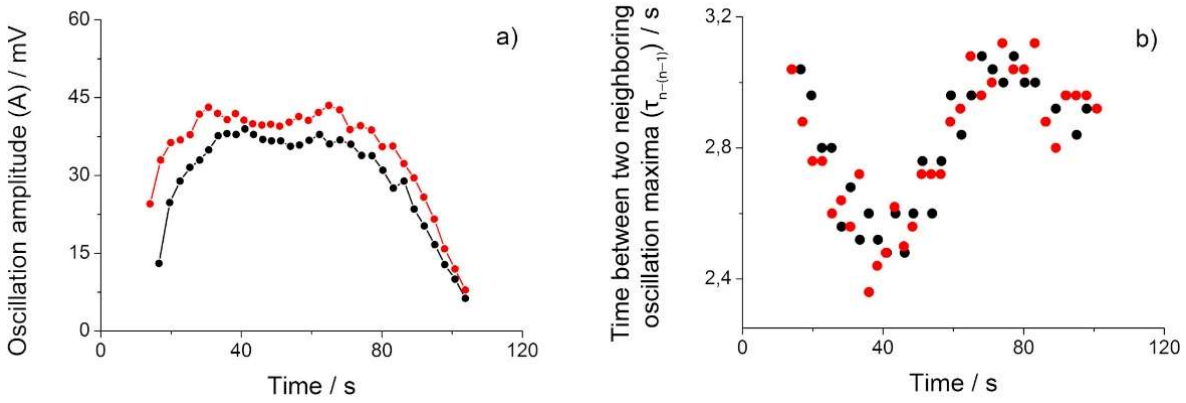

Figure 2. Briggs–Rauscher oscillation amplitude (**a**) and time between two neighboring oscillation maxima $\tau_{n-(n-1)} = t_n - t_{n-1}$ (**b**) in the two independent measurements presented at Figure 1. The resulting BR oscillograms have the same number of oscillations (N_{osc} = 33) and identical oscillation period, however the time of state I→state II transition differs more than 10 times (as shown at Figure 1).

The cause of this unexpected transition is still unknown. Previous work highlighted the significance of mixing conditions for the appearance of state I→state II transition and crazy-clock behavior [13,16]. Therefore, we want to reveal in detail the effect of mixing on

the transition, by using stirring bars of different sizes and shapes and applying various mixing rates (Figure 3).

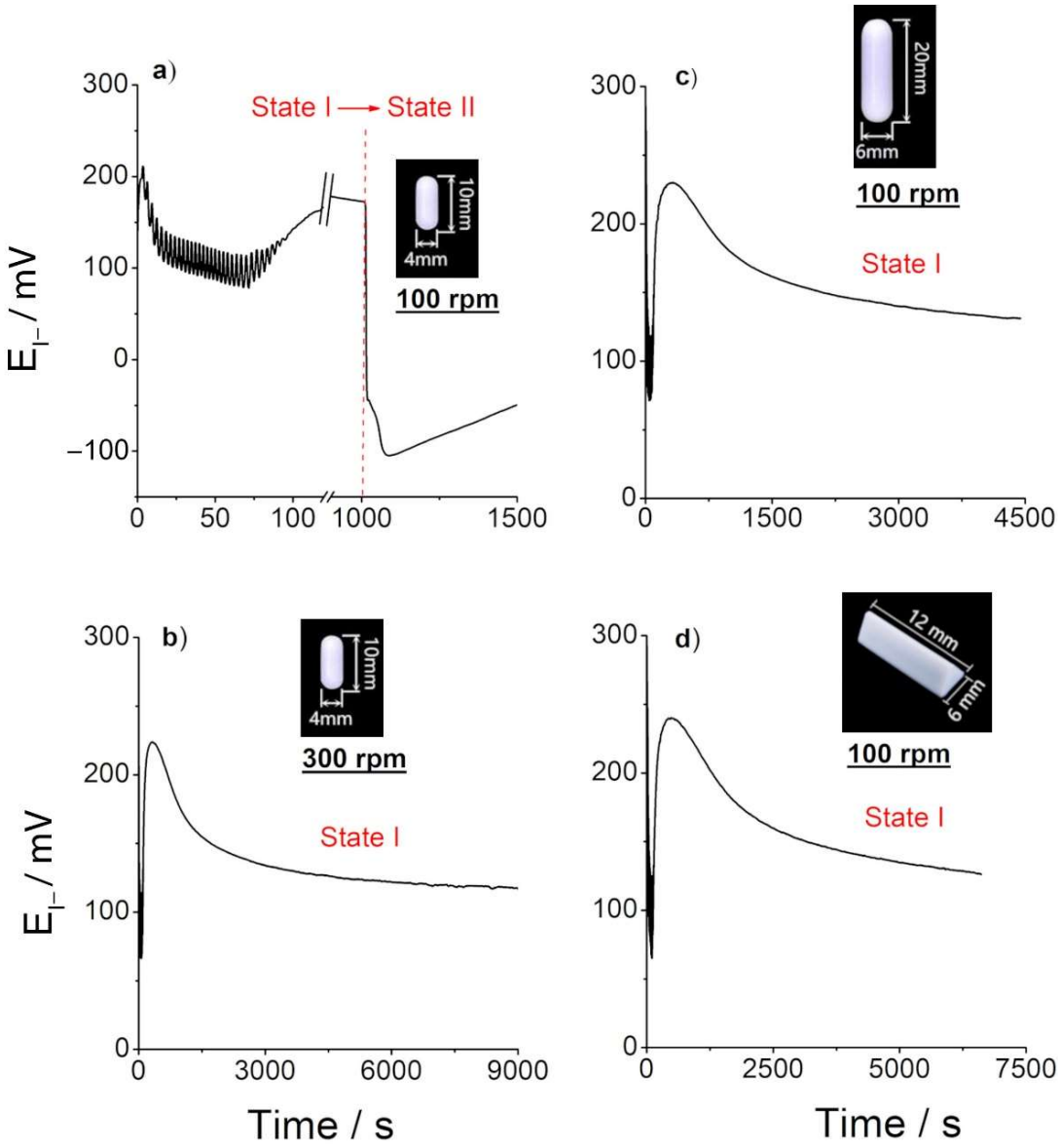

Figure 3. Typical measurements with iodide-sensing and reference electrodes with different mixing rates and different shapes of magnetic bar: (**a**) 100 rpm with magnetic stirring bar, PTFE-coated cylindrical, 10 mm length, 4 mm diameter (in inset), (**b**) 300 rpm with magnetic stirring bar, PTFE-coated cylindrical, 10 mm length, 4 mm diameter (in inset), (**c**) 100 rpm with magnetic stirring bar, PTFE-coated cylindrical, 20 mm length, 6 mm diameter (in inset), and (**d**) 100 rpm with magnetic stirring bar, PTFE-coated triangular, 12 mm length, 6 mm diameter (in inset). The reactant concentrations are identical as in Figure 1.

The transition from the state I to state II occurs only with a low stirring rate and a stirring bar of small dimensions (namely, 100 rpm and a magnetic stirring bar made of PTFE-coated cylindrical with a length of 10 mm and a diameter of 4 mm, Figure 3a). The results also underline the importance of the particular magnetic bar shape and mixing rate that was used (Figure 3a–d). Even with a low stirring rate (100 rpm), the transition does not occur with a bar exhibiting a triangular section (bar 12 mm length, 6 mm diameter) (Figure 3d). This result implies that the transition is strongly connected a particular diffusion conditions

and vortex type behavior created by using specific stirring rods. Furthermore, we perform a detailed statistical analysis to reveal the connection between the state I→state II transition and the mixing rate (using the 10-mm long and 4-mm large cylindrical stirring bar). A set of 60 experiments were performed without stirring and with stirring at a 100-rpm mixing rate (30 experiments, each). The results (τ_{osc} and τ^*) are tabulated (Tables S1 and S2) and presented in Supplementary Materials. The τ^* mean value with 95% confidence limit is for no-mixing $\tau^*_{no\ mix}$ = (12 ± 4) min and for mixing conditions, τ^*_{mix} = (17 ± 5) min.

3.2. Statistical Analysis of Experimental Results and Evidence of Clustering

Is there a connection between the time that the system spends in the oscillatory regime (τ_{osc}) and the time when the state I to state II transition occurs (τ^*)? Or, in other words, are the minor differences in oscillatory period duration responsible for a significant deviation in transition appearance? The detailed exploration of the relation between BR oscillatory time, τ_{osc}, and the time τ^* of the occurrence of the state I→state II transition (Figure 1), with and without stirring of the solutions, was performed by statistical cluster analysis (CA). Cluster analysis performs subdivision of datasets based on the relationships among their members (in our case datasets of τ_{osc} and τ^*). The application of CA allows the separation of data in clusters (namely, in groups) based on mutual distances, which reflect a degree of similarity among data [25]. The greater the similarity in the cluster, the higher the distance between the clusters, and hence the better the clustering. Our results combine a total of 60 experiments, obtained with no-mixing conditions (30 experiments) and with a mixing rate of 100 rpm (30 experiments). They were analyzed in the open-source statistic software "R" using "hclust" algorithm for the hierarchical cluster analysis (HCA) [22,23]. The HCA divided the ratios τ_{osc}/τ^* into three clusters for both mixing and no-mixing measurements (Figure 4a,b). It can be noticed that the number of members of a particular cluster slightly changes upon alteration of experimental conditions (Table 1).

It appears that the stirring effect causes an increase in the members of Cluster 1 and Cluster 3, as well as decreasing in members in Cluster 2. The increase of members in Cluster 3 suggested that stirring has prolonged time for the state I→state II transition taking place (Figure 4b.). It can be also seen from the τ* mean value for no-mixing $\tau^*_{no\ mix}$ = (12 ± 4) min and mixing conditions, τ^*_{mix} = (17 ± 5) min. Furthermore, all clusters are more compact and separated, in the case of stirring (if compared with those obtained without stirring).

The results presented in Table 1 clearly indicate that the investigated crazy-clock exhibits a truly random behavior. The shift (Figure 4a,b, Table 1) in the position of the cluster centroids towards higher τ^* values (i.e., a delaying time to transition to happen) can be observed for the case of applied stirring conditions. Due to a small number of members, the centroid of Cluster 3, in both cases, was not calculated. Furthermore, there is no significant change in the cluster's centroid position regarding τ_{osc} oscillatory coordinate for clusters. That leads to the conclusion that the transition from state I to state II is independent of oscillatory time duration or, in other words, that the minor differences in oscillatory period duration are not responsible for a significant deviation in transition appearance. Therefore, we calculated the optimal number of clusters by a one parameter (by parameter τ^*) K-means analysis, for no-mixing and mixing conditions (Figure 5a,b, respectively). The determination of optimal numbers of clusters was performed using gap method in fviz_nbclust alghoritm [26]. In brief, the gap statistic compares the total within intra-cluster variation for different values of k with their expected values under null reference distribution of the data. The estimate of the optimal clusters will be value that maximizes the gap statistic (i.e., that yields the largest gap statistic) [27].

As it can be seen from the Figure 5 the optimal number of clusters obtained by using one parameter K-means analysis is changed. The BR system which is not stirred has one cluster (Figure 5a), while the stirring induces differentiation of two clusters (see Figures 5b and 6). The dimensions refer to the first two components. The fitviz_cluster function has been used to analyze the main components, after which the cluster is represented in the dimensions of the first two Principal Component Analysis (PCA) components.

The clusters are well separated. This indicates that mixing introduced additional effects responsible for a significant cluster separation revealing the existence of time domains where the state I to state II transition is more likely to occur.

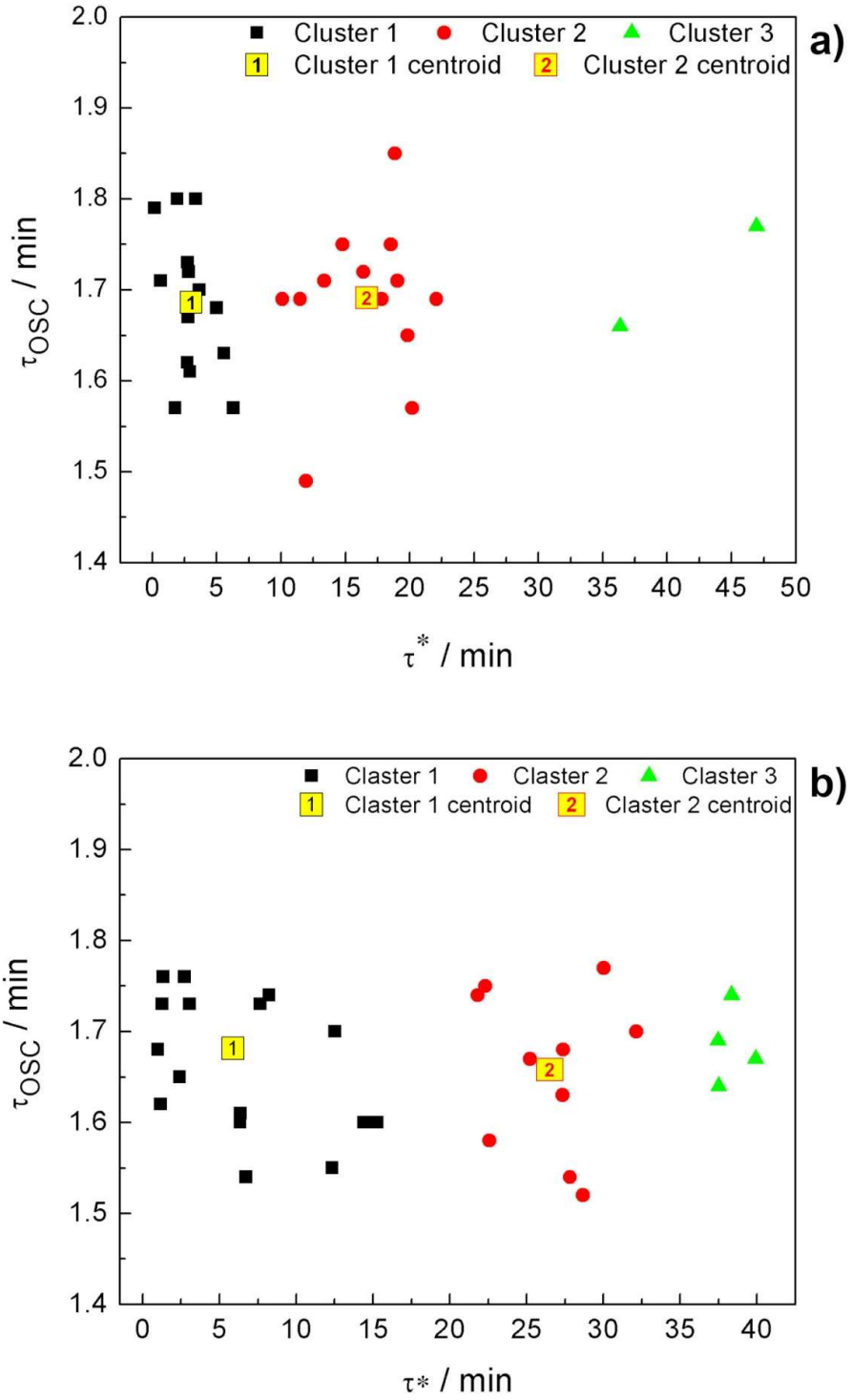

Figure 4. Clusters obtained for thirty experiments run without stirring of the reaction mixture (**a**) and clusters obtained for thirty experiments run with stirring of reaction mixture in the vessel, stirring rate was 100 rpm (**b**). τ_{osc} is the BR oscillatory time, while τ^* denotes the time from the end of the oscillatory mode to the occurrence of state I→state II transition (see Figure 1).

Table 1. Clusters and Cluster centroids.

Exp. Condition	Cluster	Number of Cluster Members	Cluster Centroids in Minute	
			τ_{osc}	τ^*
without stirring	1	15	1.686	3.036
	2	13	1.691	16.672
	3	2	/	/
with stirring	1	16	1.681	5.893
	2	10	1.658	26.536
	3	4	/	/

3.3. The State I→State II Phenomenon and Its Relation to (Spontaneous) Symmetry Breaking

The appearance of clusters indicates the existence of time domains where the state I to state II transition is more likely to occur. The stirring of the reaction mixture has a strong indirect influence on the state I→state II transition, delaying the crazy-clock behavior, shifting cluster centroids toward higher τ^* values, and increasing the cluster separation (i.e., time domain separation), as well. The existence of clusters could be connected to different nucleation and growth mechanisms of iodine crystals in the case of mixing [28], and further examination of solid iodine products would be the subject of future work.

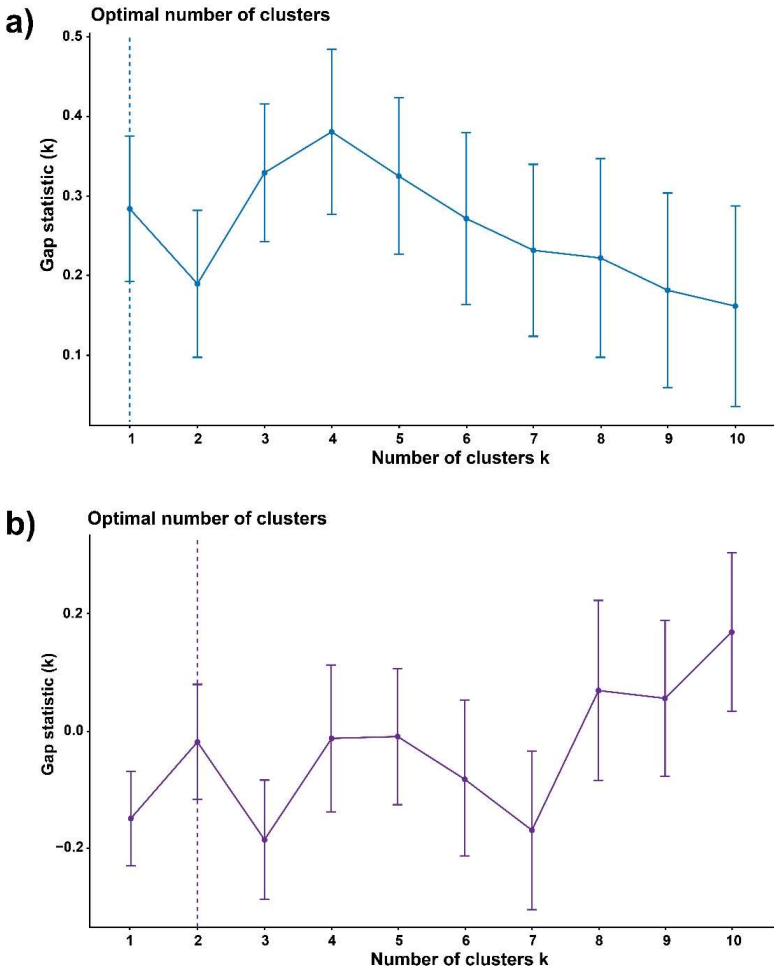

Figure 5. The optimal number of clusters for one parameter analysis by parameter τ^* (time when state I to state II transition occurs) for non-mixing conditions (**a**) and mixing conditions 100 rpm (**b**).

However, if we assumed that state I (low iodide and iodine concentration) is the symmetric state, which under some conditions becomes absolutely unstable, then, reaching the state II (high iodide and iodine concentration, with a new I_2 solid phase) could be considered as spontaneous symmetry breaking [29], see Figure 7. Such an observation of state I to state II transition could also explain the persistence of the BR system "indefinitely" in the state I, as obtained for strong mixing condition (see Figure 3).

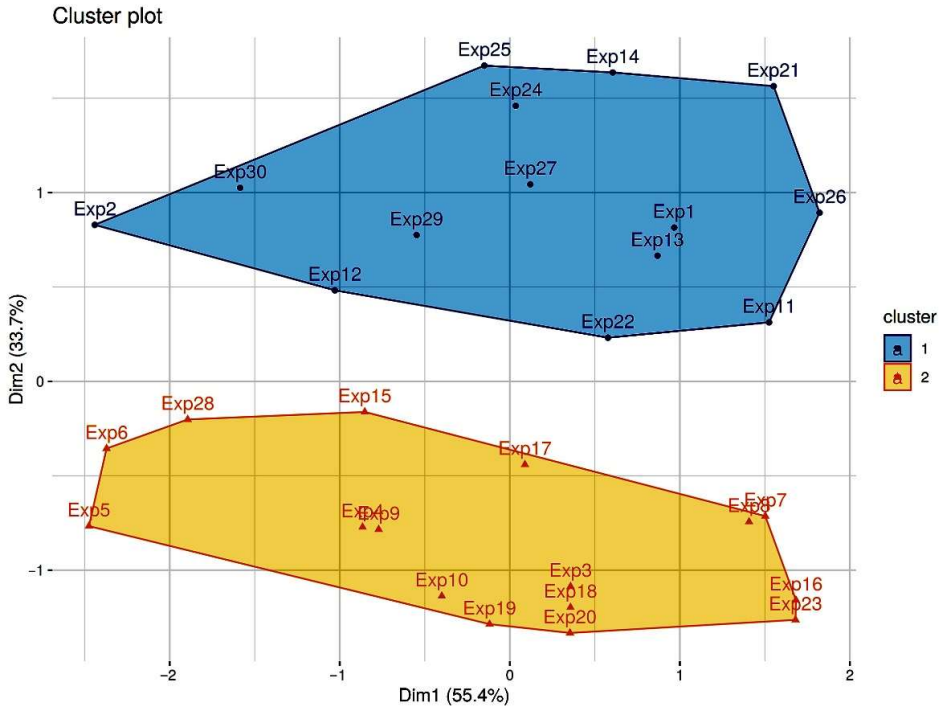

Figure 6. The evidence of two clusters for state I→state II transition obtained for mixing condition in BR system. Clusters are plotted in two dimensions (Dim1 and Dim2).

Namely, in the case of the symmetry-breaking process, the system must overcome a sufficiently large energy barrier (as shown in Figure 7). Therefore, the system's state (state I, low iodide and iodine concentration) will remain unchanged until a sufficiently large perturbation throws it over the energy barrier, ΔV, which separates the states. We assume that ΔV corresponds to the energy threshold of the formation of solid iodine from chemical reactions that principally occur in the BR solution after the oscillatory period. It is well-known that the post-oscillatory period could be excitable [30,31], meaning that a nonlinear system can be shifted (perturbed) from one state to another. It is usually achieved by the addition of some stable intermediate or reactants, playing the role of an external perturbation, to the reaction mixture [32]. Since, in our case, there is no external perturbants/stimulus (all experiments are conducted under identical conditions, and the system remained under constant temperature), the BR system should find an internal stimulus to overcome the energy barrier. The mixing itself should not influence activation energies of chemical reactions responsible for state I to state II transition. In other words, the energy threshold (ΔV) should be identical for mixing and no-mixing condition. However, the system has behaved differently, and the state I to state II transition strongly depends on the mixing conditions. Therefore, some phenomena related to mixing are accountable for the obtained behavior. Figure 7 is a cartoon view that links thermodynamics (far from equilibrium) with kinetic processes driven by the gradient of diffusion/concentration. The changes in time of these local gradients are probably a source of fluctuations. When fluctuations reach a certain threshold (such as a critical number of interacted dissipative structures), a new order/phase spontaneously appears. Cluster analysis (Figures 4–6) allows us to group different dissipation architectures as a function of time.

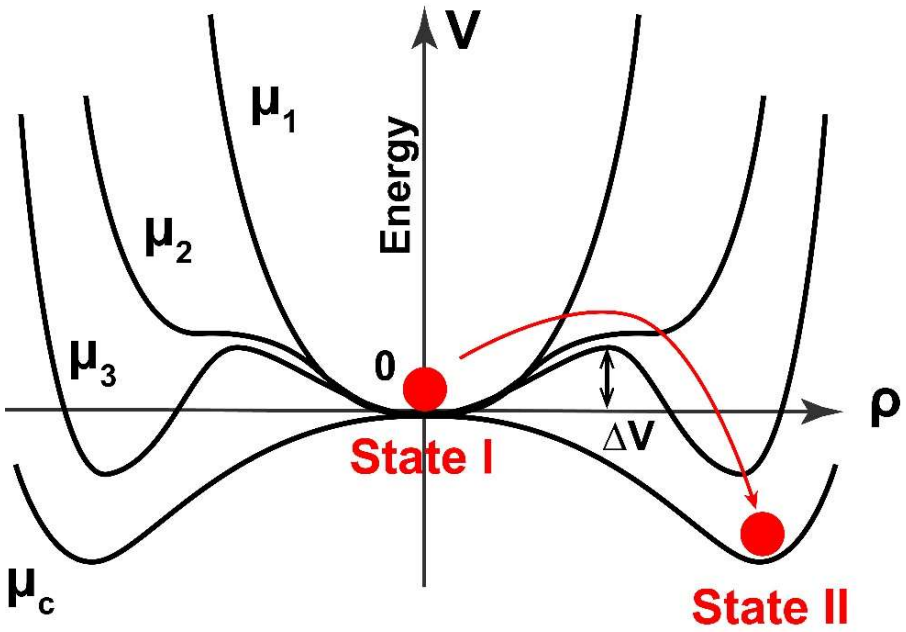

Figure 7. Possible symmetry breaking during the transition from the state I (low iodide and iodine concentration) to state II (high iodide and iodine, with segregation of solid iodine) in Briggs–Rauscher oscillatory reaction after an oscillatory period. Energetic consideration and symmetry breaking depending on control parameter, μ and ordering parameter, ρ. ΔV corresponds to the energy threshold of the formation of solid iodine from chemical reactions that occur in the BR solution after oscillatory period.

The diffusion-driven instability combined with nonlinear chemical reactions (with autocatalytic steps and radical reactions) is a broad concept and it could be responsible for the "internal stimulus" necessary for passing the energy barrier. The diffusion-driven instability is intensified by gaseous oxygen and carbon dioxide/carbon monoxide, which are released in the BR solution during the oscillatory period [33]. Additionally, the possible energetic coupling between physical and chemical processes, such as the nucleation of gaseous phase (O_2 and/or CO_2), nucleation of solid iodine and particular chemical reactions, could also be considered as an "internal stimulus" necessary for overcoming the energy barrier and breaking symmetry [34–36].

This proposal is actually a reformulated original idea of Turing [37], where the interplay of chemical reactions and diffusion are responsible for pattern formation in living systems. As suggested by Prigogine, the spontaneous appearance of a spatial organization via diffusion-driven instability can be considered as a spontaneous symmetry-breaking transition [38]. In the presented work, we deal with a bulk solution and there is no visible spatial organization, but the spatial organization (spatiotemporal patterns) of the identical process (state I→state II transition in Briggs–Rauscher reaction) in a thin layer, is very recently found by Li and coworkers [15]. Therefore, this work indirectly links spontaneous symmetry breaking and crazy-clock behavior (stochastic nature) in the bulk. The stochastic nature of state I to state II transition and its relation to symmetry breaking (and pattern formation), introduced a new approach in the investigation of crazy-clock behavior. On the other hand, the investigation of chemical systems with stochastic nature and symmetry breaking could improve our understanding of more complex phenomena in living organisms, such as morphogenesis.

Additionally, this paper nominates state I→state II transition as an easily available chemical system for intrinsic random number generator and thus, expands the potential application of this crazy-clock reaction.

4. Conclusions

In this work, we further investigated the crazy-clock phenomenon (state I to state II transition) which occurs after a strongly reproducible Briggs–Rauscher oscillatory reaction. The mixing rate, as well as the magnetic bar shape and dimensions, have a strong influence on the transition appearance. In order to better understand the stochasticity of the mentioned process, we ran more than 60 experiments (30 experiments with mixing and 30 experiments with no-mixing conditions), and we applied the statistical cluster K-means analysis. Although the transition for both mixing and no-mixing conditions are taking place completely randomly, by using statistical cluster analysis, we obtained different number of clusters pointing to different time-domains where the transition is more likely to occur. Two-parameter analysis (by oscillatory time duration, τ_{osc} and by the moment when the transition occurs, τ^*) suggests that the state I→state II is independent of the oscillatory time duration. Therefore, we performed a one parameter analysis (by τ^*). In the case of no-mixing, we found one cluster, while the statistical analysis of the results for mixing conditions revealed two compact and well-separated clusters. The clustering method reveals new hidden details regarding the chemical dynamics of nonlinear processes. The state I to state II transition could be explained through a symmetry breaking approach, and the necessity of the BR system to overcome a sufficiently large energy barrier. This is the first link of the crazy-clock behavior to the symmetry breaking phenomenon. The investigation of chemical systems with stochastic nature and symmetry breaking could improve our understanding of more complex phenomena in living organisms and therefore the scope of the presented results goes beyond oscillatory reaction kinetics. Furthermore, the described example belongs to the small class of chemical systems that shows intrinsic randomness in their response and it might be considered as a real example of a classical liquid random number generator.

Supplementary Materials: The following supporting information can be downloaded at: https://www.mdpi.com/article/10.3390/sym14020413/s1, Table S1: The Briggs-Rauscher oscillogram duration (τ_{osc}), the numbers of oscillations, and state I to state II transition time (τ^*) when no-mixing conditions is applied: [Malonic acid]0 = 0.0789 M, [MnSO4]0 = 0.00752 M, [HClO4]0 = 0.03 M, [KIO3]0 = 0.0752 M, [H2O2]0 = 1.176 M, T= 37.0 °C, reaction volume 25 mL, Table S2: The Briggs-Rauscher oscillogram duration (τ_{osc}), the numbers of oscillations, and state I to state II transition time (τ^*) when 100 rpm mixing conditions is applied: $[\text{Malonic acid}]_0$ = 0.0789 M, $[MnSO_4]_0$ = 0.00752 M, $[HClO_4]_0$ = 0.03 M, $[KIO_3]_0$ = 0.0752 M, $[H_2O_2]_0$ = 1.176 M, T= 37.0 °C, reaction volume 25 mL.

Author Contributions: Conceptualization, M.C.P. and B.K.; methodology, M.C.P., J.P.M., Y.C., and B.K.; statistical K-means analysis M.D.; investigation, M.C.P. and J.P.M.; writing—original draft preparation, M.C.P. and B.K.; writing—review and editing, M.C.P., B.K., Y.C., S.R.M. and T.V.; visualization, J.P.M. and B.B. All authors have read and agreed to the published version of the manuscript.

Funding: This research was funded by the Ministry of Education, Science and Technological Development of the Republic of Serbia, Contract numbers: 451-03-68/2022-14/200026 and 451-03-68/2022-14/200146; BEWARE Fellowship of the Walloon Region (Convention n°2110034); the Fund for Scientific Research F.R.S.-FNRS; the Ministry of Education, Science and Technological Development of the Republic of Serbia (grant III 45016); the Office of Naval Research Global (Research Grant N62902-22-1-2024).

Institutional Review Board Statement: Not applicable.

Informed Consent Statement: Not applicable.

Data Availability Statement: Data underlying the results presented in this paper are not publicly available at this time but may be obtained from the authors upon reasonable request. Please contact for this corresponding authors.

Acknowledgments: This work was supported by the Ministry of Education, Science and Technological Development of the Republic of Serbia Contract numbers: 451-03-68/2022-14/200026 and 451-03-68/2022-14/200146. S.R.M. was supported by a BEWARE Fellowship of the Walloon Region (Convention n°2110034), as a postdoctoral researcher. Y.C. is a research associate of the Fund for

Scientific Research F.R.S.-FNRS. B.K. and B.B. acknowledge financial support of the Ministry of Education, Science and Technological Development of the Republic of Serbia (grant III 45016). Additionally, B.K. acknowledges support from F.R.S.-FNRS. M.P., B.B., and B.K. acknowledge the support of the Office of Naval Research Global through the Research Grant N62902-22-1-2024.

Conflicts of Interest: The authors declare no conflict of interest.

References

1. Gross, D.J. The role of symmetry in fundamental physics. *Proc. Natl. Acad. Sci. USA* **1996**, *93*, 14256–14259. [CrossRef] [PubMed]
2. Smits, J.; Stoof, H.T.C.; Straten, P.V.D. Spontaneous symmetry breaking in a driven-dissipative system. *Phys. Rev. A* **2021**, *104*, 023318. [CrossRef]
3. Briggs, T.S.; Rauscher, W.C. An oscillating iodine clock. *J. Chem. Educ.* **1973**, *50*, 496. [CrossRef]
4. Bray, W.C. A periodic reaction in homogeneous solution and its relation to catalysis. *J. Am. Chem. Soc.* **1921**, *43*, 1262–1267. [CrossRef]
5. Bray, W.C.; Liebhafsky, H.A. Reaction involving hydrogen peroxide, iodine and iodate ion. *I. Introd. J. Am. Chem. Soc.* **1931**, *53*, 38–43. [CrossRef]
6. Belousov, B.P. A periodic reaction and its mechanism, in collection of short papers on radiation medicine for 1958. *Medgiz* **1959**, 145–147.
7. Furrow, S.D. A modified recipe and variations for the briggs–rauscher oscillating reaction. *J. Chem. Educ.* **2012**, *89*, 1421–1424. [CrossRef]
8. Furrow, S.D.; Noyes, R.M. The oscillatory Briggs-Rauscher reaction. 1. Examination of subsystems. *J. Am. Chem. Soc.* **1982**, *104*, 38–42. [CrossRef]
9. Noyes, R.M.; Furrow, S.D. The oscillatory Briggs-Rauscher reaction. 3. A skeleton mechanism for oscillations. *J. Am. Chem. Soc.* **1982**, *104*, 45–48. [CrossRef]
10. Schmitz, G.; Furrow, S. Kinetics of the iodate reduction by hydrogen peroxide and relation with the Briggs–Rauscher and Bray–Liebhafsky oscillating reactions. *Phys. Chem. Chem. Phys.* **2012**, *14*, 5711–5717. [CrossRef]
11. Furrow, S.D.; Cervellati, R.; Greco, E. A study of the cerium-catalyzed briggs-rauscher oscillating reaction. *Z. Nat. B* **2012**, *67*, 89–97.
12. Vanag, V.K.; Alfimov, M.V. Light-induced nonequilibrium phase transition between quasistationary states of the Briggs-Rauscher reaction under batch conditions. *J. Phys. Chem.* **1993**, *97*, 1878–1883. [CrossRef]
13. Vanag, V.K.; Alfimov, M.V. Effects of stirring on photoinduced phase transition in a batch-mode Briggs-Rauscher reaction. *J. Phys. Chem.* **1993**, *97*, 1884–1890. [CrossRef]
14. Pagnacco, M.C.; Mojović, M.D.; Popović-Bijelić, A.D.; Horváth, A.K. Investigation of the halogenate–hydrogen peroxide reactions using the electron paramagnetic resonance spin trapping technique. *J. Phys. Chem. A* **2017**, *121*, 3207–3212. [CrossRef] [PubMed]
15. Li, Z.; Yuan, L.; Liu, M.; Cheng, Z.; Zheng, J.; Epstein, I.R.; Gao, Q. The briggs–rauscher reaction: A demonstration of sequential spatiotemporal patterns. *J. Chem. Educ.* **2021**, *98*, 665–668. [CrossRef]
16. Pagnacco, M.C.; Maksimović, J.P.; Potkonjak, N.I.; Božić, B.; Horváth, A.K. The transition from low to high iodide and iodine concentration state in the briggs rauscher reaction-evidence on crazy clock behavior. *J. Phys. Chem. A* **2018**, *122*, 482–491. [CrossRef]
17. Furrow, S.D.; Cervellati, R.; Greco, E. Study of the transition to higher iodide in the malonic acid Briggs–Rauscher oscillator. *React. Kinet. Mech. Catal.* **2015**, *118*, 59–71. [CrossRef]
18. Epstein, I.R. The consequences of imperfect mixing in autocatalytic chemical and biological systems. *Nature* **1995**, *374*, 321–327. [CrossRef]
19. Valkai, L.; Cseko, G.; Horvath, A.K. Initial Inhomogeneity-induced crazy-clock behavior in the iodate-arsenous acid reaction in a buffered medium under stirred batch conditions. *Phys. Chem. Chem. Phys.* **2015**, *17*, 22187–22194. [CrossRef]
20. Andersen, A.; Madsen, J.; Reichelt, C.; Ahl, S.R.; Lautrup, B.; Ellegaard, C.; Levinsen, M.T.; Bohr, T. Double-slit experiment with single wave-driven particles and its relation to quantum mechanics. *Phys. Rev. E* **2015**, *92*, 013006. [CrossRef]
21. Ellegaard, C.; Levinsen, M.T. Interaction of wave-driven particles with slit structures. *Phys. Rev. E* **2020**, *102*, 023115. [CrossRef] [PubMed]
22. Murtagh, F. *Multidimensional Clustering Algorithms in COMPSTAT Lectures 4*; Physica-Verlag: Wuerzburg, Germany, 1985.
23. R Core Team. *R: A Language and Environment for Statistical Computing*; R Foundation for Statistical Computing: Vienna, Austria, 2018. Available online: https://www.R-project.org/ (accessed on 20 November 2021).
24. Horváth, A.K.; Nagypál, I. Classification of Clock Reactions. *ChemPhysChem* **2014**, *16*, 588–594. [CrossRef] [PubMed]
25. Kaufman, L.; Rousseeuw, P.J. *Finding Groups in Data: An Introduction to Cluster Analysis*; John Wiley & Sons: New York, NY, USA, 2009.
26. Available online: https://cran.r-project.org/web/packages/factoextra/factoextra.pdf (accessed on 20 November 2021).
27. Tibshirani, R.; Walther, G.; Hastiee, T. Estimating the number of clusters in a data set via the gap statistic. *J. R. Stat. Soc. Ser. B (Stat. Methodol.)* **2001**, *63*, 411–423. [CrossRef]

28. Pagnacco, M.C.; Maksimovic, J.P.; Jankovic, B.Z. Analysis of transition from low to high iodide and iodine state in the briggs–rauscher oscillatory reaction containing malonic acid using kolmogorov–johnson–mehl–avrami (kjma) theory. *React. Kinet. Mech. Catal.* **2018**, *123*, 61–80. [CrossRef]
29. Genz, H. Symmetry and symmetry breaking in nature. *Interdiscip. Sci. Rev.* **1999**, *24*, 129–138. [CrossRef]
30. Ruoff, P. Excitability in a closed stirred Belousov—Zhabotinskii system. *Chem. Phys. Lett.* **1982**, *90*, 76–80. [CrossRef]
31. Rouff, P. Excitability created by oxygen inhibition in the stirred malonic acid belousov-zabotinskii system. *Chem. Phys. Lett.* **1982**, *92*, 239–244. [CrossRef]
32. Vukojevic, V.; Anic, S.; Kolar-Anic, L. Investigation of dynamic behavior of the bray–liebhafsky reaction in the CSTR. Properties of the system examined by pulsed perturbations with I^-. *Phys. Chem. Chem. Phys.* **2002**, *4*, 1276–1283. [CrossRef]
33. Muntean, N.; Szabo, G.; Wittmann, M.; Lawson, T.; Fulop, J.; Noszticzius, Z.; Onel, L. Reaction routes leading to CO_2 and CO in the briggs−rauscher oscillator: Analogies between the oscillatory br and bz reactions. *J. Phys. Chem. A* **2009**, *113*, 9102–9108. [CrossRef]
34. Bowers, P.G.; Noyes, R.M. Chemical oscillations and instabilities. 51. Gas evolution oscillators. 1. Some new experimental examples. *J. Am. Chem. Soc.* **1983**, *105*, 2572–2574. [CrossRef]
35. Sevcik, P.; Kissimonova, K.; Adamcikova, L. Oxygen Production in the oscillatory bray−liebhafsky reaction. *J. Phys. Chem. A* **2000**, *104*, 3958–3963. [CrossRef]
36. Stevanovic, K.Z.; Bubanja, I.N.M.; Stanisavljev, D.R. Is iodine oxidation with hydrogen peroxide coupled with nucleation processes? *J. Phys. Chem. C* **2019**, *123*, 16671–16680. [CrossRef]
37. Turing, A.M. The chemical basis of morphogenesis. *Philos. Trans. R. Soc. B Biol. Sci.* **1952**, *237*, 37–72.
38. Prigogine, I.; Nicolis, G. On symmetry-breaking instabilities in dissipative systems. *J. Chem. Phys.* **1967**, *46*, 3542–3550. [CrossRef]

INFLUENCE OF ELECTROMAGNETIC AND NUCLEAR RADIATION IN MEDICINE FOR THERAPY AND DIAGNOSIS THROUGH PROCESSES, FACTS AND STATISTICAL ANALYSIS

by

Monika M. ŽIVKOVIĆ [1,2]***, Milesa Ž. SREĆKOVIĆ*** [3]***,***
Tomislav M. STOJIĆ [4]***, and Bojana M. BOKIĆ*** [5, 6*]

[1]Clinical Hospital Centre, Zemun, Belgrade, Serbia
[2] Medical Faculty, University of Belgrade, Belgrade, Serbia
[3] Faculty of Electrical Engineering, University of Belgrade, Belgrade, Serbia
[4] Faculty of Mechanical Engineering, University of Belgrade, Belgrade, Serbia
[5] Institute of Physics, University of Belgrade, Belgrade, Serbia
[6] Faculty of Physics, University of Belgrade, Belgrade, Serbia

Scientific paper
http://doi.org/10.2298/NTRP1701091Z

Contemporary medicine (biomedicine) cannot be imagined without diagnostics and therapeutic methods based on nuclear, laser, acoustical and other processes. The application of these methods is linked to common computer support, signal processing, measuring monitoring techniques, high degree of automatization, and image analyses. The paper analysed contemporary technical issues related to neonatology, ophthalmology, based on the influence of nuclear radiation and laser beams. Some statistical processing and presentations of results obtained in the IGA KCS Hospital, Belgrade, Serbia, in curing vision of prenatal type newborns with a different degree of pathological state of retinopathy of prematurity are presented. The general conclusion is that, in spite of the good results, a multidisciplinary approach is needed for a deeper understanding of the role of lasers and laser techniques in medicine as well as possible couplings. Potential new applications of lasers important for the fields of neonatology and ophthalmology were also considered.

Key words: retinopathy of prematurity, neonatology, laser, nuclear radiation, damage, dosimetry

INTRODUCTION

Among diagnostic and therapeutic applications of electromagnetic (EM) and nuclear radiations in medicine, the basics are the mechanisms of beam interactions with material. Techniques of magnetic resonance (MR), tomography (nuclear and optical), holography with non-linear systems are the areas where the answers should be found. Not involving the mechanisms of nuclear magnetic resonance (NMR), the obtained signals and signal processing deserve specific attention, as well as the signal/noise (S/N) ratio, image generation, reconstruction, and selective excitation. Pulse sequences, the influence of microcentres moving, correction of moving through the image series, imaging flow, MR spectroscopy and system design are also of interest, too [1]. An approach to the new energy resources combines lasers and nuclear physics and techniques, as well as biology. This applies to therapy, diagnostics, for power sources through plants, bioconversion and biological sensors, as well as optical recording through bacteria. World catastrophes such as Chernobyl, accidents, Three Miles Island, Fukushima, provoke discussions about doses, caused biological effects of radiation and genetics (early and late effects). Unfortunately, new facts are provided through accidents in nuclear and laser technologies [2-14]. In tab. 1 the levels of radiobiological processes [9-13] are presented. Biological entities and hardness of organic/inorganic materials and systems are connected with doses with appropriate definition, measurements, uncertainties, as well as biological radiation effects [2-17]. Many theoretical models on various organization levels are developed. From the position of a systematic approach to the processes and modelling principles, concepts of biophysical models on molecular, genetic and cell levels are derived. Models should be compared and some investigations are in [13] regarding boundary conditions, applications and disadvantages. The probability estimation through many criteria should follow the analysis for their inves-

* Corresponding author; e-mail: bojana@ipb.ac.rs

Table 1. Levels of processes in biology caused by radiation

Level	Existence time on level [s]	Processes on the presented level; possible modifications
Physical	10^{-18}-10^{-8}	Excitation, ionisation, elastic collisions-thermalization and formation of high reactivity radicals of macromolecules and short lived free radicals of water and organic molecules; no modification
Chemical	10^{-14}-10^{-4}	Reactions of free radicals mutually, with organelles – forming primary damage (DNA damages, dimerizations); modification by protector, oxygen, temperature
Biochemical (subcell)	10^{-4}-10^{5}	Reparation, interactions of damaged microcenters (mutation, aberration, modification by temperature and other agents)
Biological (cellular)	10^{3}-10^{7}	Division of cells and molecular chains, exchange of performances as a result of mutations

tigation and experimental assessment. Theoretical approaches and results based on appropriate formalisms are of importance in the field of radiation protection and dosimetry, which are constantly competing due to new sources in radiology. Molecular biology (for structure, DNA functioning and repair processes), uses only the simplest biological effects (inactivations of phages, viruses, and gene-mutations). The explanation through complex biological processes and behaviour could rather remain without results. The cell inactivation model based on physical considerations, and later models as radiobiological ones (on the genetic level without the existence of repair processes and chromosome structures) are developed. Self-repair, interactions of damages, dynamics of the processes, stochastic energy transfer to the cells are also important topics. Micro dosimetry, the structure of the cell traces, stochastics, classification and conceptual analyses appeared as typical. Characteristics of physical models, the theory of dual effect, and modifications are compared. They include the radiobiological effects to DNA and model of cell /systems inactivation. It is important to implement physical doses, target theories and modifications. The two-component dual effect model of probability on molecular and genetic levels (*E. coli* mutations and mammals) deals with various effects (lymphocytes irradiated by neutrons). Table 1, figs. 1-2 based on results [13] show some trends in modelling and experimental irradiations of different cells and aberrations. Figure 3 presents the qualitative behaviour of different beams and radiation on plants.

Sensitivity of mammal cells to the irradiation of heavy ions depending on the viability level (or survival) of the human and animal cells, (lymphocytes, diploid fibroblasts, and kidney cells) are studied [13]. The defined threshold for survival as well as energy loss per range of ions are parameters of interest.

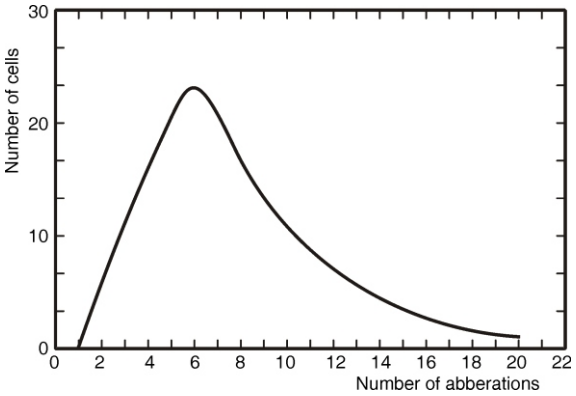

Figure 1. Chromosome aberration for lymphocytes irradiated: moderate neutrons (0.35 MeV; 3.3 Gr)

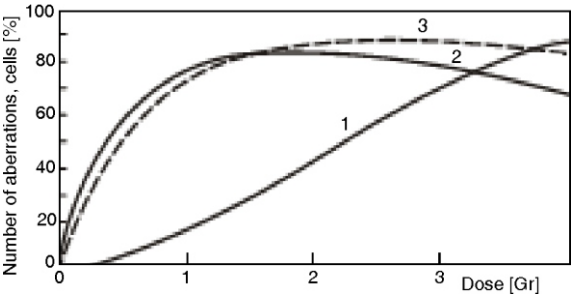

Figure 2. Aberrations of cells *vs.* the neutron dose (0.35 MeV (1), 0.85 MeV (2), and for γ radiations of ^{60}Co (3)

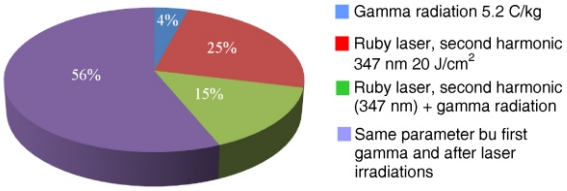

Figure 3. Frequency of changed barley seeds (type Nadya) in the case of combined radiation of gamma rays and frequency doubled ruby laser (347 nm)

The same goes for sensitivity of the mammalian cells to the irradiation of ions, induced number of structural changes after X-ray irradiation of the tumour cell *vs.* dose. Models of: inactivation, Karposs and Foloty, repaired and unrepaired damages include/(do not include) saturation processes, viability of prokaryotes, sensibility of *E. coli* to neutrons, eukaryotes, and fatal damages. Thermal damage and critical temperatures, threshold for effects and concentration limits are important. Couplings between the nuclear power engineering, laser technique and medicine are multiple (some are connected by the laser excitations in the nuclear reactions and pumping neutrons, protons, α and β radiations). Modern problems include gamma and X-rasers (X-ray Amplification by Stimulated Emission of Radiation), or preionizations to decrease the lasing threshold, but also for disposal of various waste.

The biological damage threshold is studied for various cell types and systems. An epidemiological study and variation of estimated doses and the real damage are the subjects of a wide investigation in the theory of microdosimetric cellular radiobiological action, lymphocytes and stochastic/astochastic effects.

Considering vision, in the sense of colour prejudice in various problems, it should start from the primary eye functions and its mechanisms. Medically speaking, there are numerous links between ophthalmology, neonatology and lasers techniques. Diagnostic techniques and operatives, including biostimulative treatments with lasers penetrated into many branches of medicine and could be applied for many tissues and organs. There are two phenomena where we have to stay in one of the natural organs which is the eye: structure complexity and simple functioning, describe modern problems for techniques-medicine-protection couplings and tasks. Since the first application of lasers in medicine, the area of application has significantly expanded, in eye surgery and diagnostics. Medical terminology and diagnostics are expressed through quantitative indicators for biomaterial and generalized processes. Modern methods of coherent, linear and nonlinear optics, have to be involved in the world of medical diagnostics and monitoring. The dynamics of human and animal cells, protoplazmatic and blood circulation, tissue pathology, could be observed due to the development of photon beating and Laser Doppler Anemometry (LDA) techniques.

The paper intends to show the role of lasers in diagnostics, gynaecology and ophthalmology. Vision problems incurred in neonatal infants, require a complete diagnosis and medical history. Similar types of lasers are used both in diagnostic and operative treatments. The treatments differ in accessories, but essentially, models of interaction and diagnosis are associated with many of the general applications, where optical beams have the role of a knife (scalpel), therapy or diagnosis. Sources are beams of coherent radiation in the visible, infra red (IR), far infra red (FIR) or ultra violet (UV) portion of the EM spectra. The study of the ocular performances has come a long way from the first images of muscle tissue and Helmholtz's assumption up to the present, with computer diagnostics, polarizing microscope, Stokes parameters and Mueller matrices [12].

Besides many diagnostic techniques in ophthalmology, some of the relevant laser techniques of interest to several branches of medicine are analysed. One of them is used for the early diagnosis of glaucoma. The solutions appeared based on methods: (a) Laser Induced Fluorescence (LIF) and (b) monitoring of the Stokes parameters through ellipsometric measurement [7, 12]. Fluorescence methods were not new in medicine, however, Raman, IR and UV spectroscopies and new areas of nonlinear laser spectroscopies with tunable lasers, made precise application possible. Measurements of turbidity belong to the category of reliable, but less accurate measurements. Harmonics of the Nd^{3+}: YAG (yttrium aluminium garnet) laser are favourable for biosamples in the picosecond (ps)-region (in mastitis tissue diagnosis).

The eye system is well studied in the linear region. There is data available on absorption of the eye and its constituents, spectral sensitivity curves relative spectral brightness and eye adaptation to the light vision (photopic and scotopic). However, the variety of eye-damages existed even before the use of lasers. Damages occurred in the process of welding, by the focused radiation of the sun and sources in other portions of the EM spectrum. Nowadays most of the relevant data concerning laser (laser era) damage originate from accidents. With the first giant laser pulses, it was possible to organize the study of nonlinear effects. The first ophthalmic devices applied on to rabbits appear as new experimental material. The people working in space and next to the terrestrial accelerator devices are experiencing sparkles of light due to the environment of cosmic and gamma rays. Absorption of the photopigments in human eye receptors (cones and rods), versus different wavelengths was studied. Saturation effects were likewise found [18]. Data of the normalized absorbance of the photoreceptors, or photopigment molecules, are obtained through microphotometry methods, and further investigations explained the human feeling for colours. Main data comparison between the physics, metrics of colours, and psychological concepts can be a subject of discussion.

RETINOPATHY OF PREMATURITY INCIDENCE IN THE IGA KCS HOSPITAL

Important topics in the field of neonatology are retinopathy of prematurity (ROP) and risk factors. In the light of new methods for treating ROP, comprehensive theoretical and experimental support is needed and it requires a multidisciplinary approach. Optical methods in diagnosis and treatment, light influence on the eye systems, damage threshold, scattering and absorption processes are of interest. Lasers and fiberoptics are also unavoidable topics in ophthalmology. Laser surgery is rivalled by the cryo-surgery technique, but for the moment it seems that lasers have more advantages. The institutional procedure with questionnaires for parents before the intervention in cases of ROP can be found on the internet. Many questions exist concerning ROP progress, laser treatments, complications and measures of protection.

Laser methods and hazards

Laser surgery for cases of ROP is actually causing partial damage to the ischemic retina. We will not describe the processes on a microscopic level con-

nected to ribonucleic acid (RNA), process of peripheral retinal vascularization and other important factors. Destruction of ischemic retina can be performed with various laser types: Ar^+: ion (488-515 nm; 200 mW, in the appropriate regime) or semiconductor laser (IR range, 810 nm). The binocular microscope – ophthalmoscope, is the second necessary component, and the systems for beam positioning and shaping with the low power He-Ne laser. Various reference data confirms the positive outcome with the different laser types and details about advantages and disadvantages of the ROP laser treatment [19-24]. Reduced vascularisation can be observed 7 days after the intervention (photocoagulation). A detailed database should be made for both lasers and cryogenics, which is necessary for decision making and analysing the laser ROP treatment compared to other techniques. Perhaps it is important to note that for now the χ^2 test gives no significant difference method.

Regulations, ecology and laser (eye and skin damage)

The application of lasers in everyday life, biology, ecology, medicine, pharmacy and military is related to many administrative regulations worldwide that vary in different countries. In particular, principal parameters and protections are defined. Nominal Ocular Hazard Distance (NOHD) was one of the first regulated definitions. The classification of lasers varies from one state to another, however most countries share the same regulation. The lasers are classified into four groups, assuming that both the III class as well the IV class would lead to laser induced damage. Therefore many investigations of laser influence on animal eyes and plants were performed including the investigation of the impact of various environmental conditions (fog, smoke, and fume), using different chemical products. The threshold for laser damage depends on the different parameters of investigated bio-objects, (biomaterials, biotargets) and pupil size; quantitative presentation of those investigations is connected to protection and regulation for selected lasers and working regimes. Therefore relevant data of transparent, absorptive, parts of the ocular performances are needed. Absorption of EM radiation in the eye deals with four principal bands: (a) Microwaves and γ rays. (b) Far UV and FIR, (c) Near (N) UV, (d) Visible and NIR regions.

There are four categories of laser (equipment) interactions with tissue: (a) optical radiation hazards to the eye and skin, (b) chemical, (c) electrical, and (d) casual hazards [4]. Most of the Nd^{3+}: YAG laser beam energy is absorbed inside the optical structure of the eye (cornea, lens and vitreous). Note that this laser type is also used in everyday applications in ophthalmology and other branches of medicine. The retinal effects are expected in the visible and close IR-A case (400-1400 nm). Minimal sizes of the image on the retina depend on wavelength and are limited by diffraction. Radiation in the UV or FIR portion of the spectra is absorbed in the inner part of the eye. High levels of exposure can permanently damage the cornea or lens. Medium levels of the UV beams cause serious damage, which is severe but temporary (analogue to industrial welder flash, *i. e*. photokeratitis). Description of the biological effects of radiation, according to the International Commission on Illumination (CIE), is performed in 7 spectral bands 4].

Skin damage is far less likely to occur, except in cases of high-power lasers. The skin is usually not injured by common lasers, *i. e*. low and medium power lasers. Levels of skin injuries visible and IR areas require at least a few Wcm^{-2}, and depend on the skin's surface characteristics [4]; exposure conditions are presented by dosimetry (a laser can be viewed as a thermal damage source). Radiation (200-300 nm) causes burns, the same as those caused by the sun (cancer, erythema). Electrical hazards will not be described in detail, however a source of high voltage present in lasers, can provoke electric shock resulting in electro-cauterisation. Therefore appropriate electrical and electronic standards have to be applied. Considering standards and regulations in chemistry, many highly volatile or even explosive or highly toxic materials are used in laser laboratories. During laser processing of a material (welding/cutting) much chemical evaporation is created. Standards for industrial manufacturing require adequate ventilation during the laser operation. Items connected to retina treatment risks (injuries) are: blue/UV light, retinal image, retinal burns, intensity and spectral characteristics of coherent sources.

ROP is the subject of research in many clinics worldwide, as well as in Serbia. For this type of study, trained teams, originating from various branches of expertise (beside experts in gynaecology and ophthalmology) are needed. As ROP presents a disorder of retinal blood vessel development in prematurely born infants, it can be interrupted by laser beam interactions with tissue. The process can affect the vitreous body and lead to detachment of the retina. In the most severe ROP forms, it leads to partial retinal detachment. This can cause blindness in childhood and is considered to be one of the main causes. We will consider some of the important approaches in ROP diagnostics and treatment. ROP was mentioned for the first time in 1942, and has been regularly mentioned to this day. Various methods of operation have been attempted during almost three quarters of a century. It was identified as a fibrous state process of the retina and vitreous body (retrolental fibroplasia). The correlation between these processes and prematurity of childbirth was established. The name ROP (1952.) was first mentioned in the middle of the last century. The study of

pathogenesis was enhanced through development of the animal models. The International Classification of Retinopathy Prematurity – ICROP has been formed over time. It represents an important and unifying criterion for the diagnosis and treatment of active forms of ROP. Screening, monitoring and treatment of ROP are implemented in several countries. In Serbia, since May 2003, many cases of ROP, as an active disease, have been diagnosed. In Belgrade, Serbia, the IGA KCS hospital initiated systematic ophthalmological examinations. The method of using an indirect ophthalmoscope, provided an early diagnosis of disease, and monitoring of severe forms of active retinopathy.

Parameters and stages of ROP

Various stages of the disease are described [20, 22, 25-29]. The zone of interest is divided into the central area of growth in the retina, which encompasses the macula, the highest ROP and the last area of growth. Different descriptions and classifications of the main parameters of ICROP exist. Most of them agree that the most important parameters are: severity (pathological mutation) with different stages, localization with 3 characteristic zones, prevalence – number of hours, tab. 2, and fig. 4.

RESULTS OF ANALYSIS

The results of the study of ROP should in principle be related to the frequency of prevalence and the appropriate time of observation in order to obtain the data that have sufficient statistical importance. In the analysis, several factors are included: prematurity time, birth weight (small weight at birth), hyperoxia and oxygeno therapy duration, sepsis, respiratory diseases, coherent/incoherent EM irradiation. Figure 5 represents the percentage display of the data on the numbers of births and treatments applied. Percentage data are related to several hundreds of prematurely

Table 2. Stages of retinopathy

1 stage	Normal but incomplete growth
2 stage	Medium abnormal growth
3 stage	Very abnormal growth
4 stage	Partially detached retina
5 stage	Retina with entirely detached retina

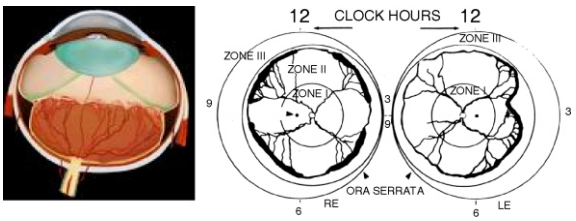

Figure 4. Typical stages of ROP and eye anatomy [30]

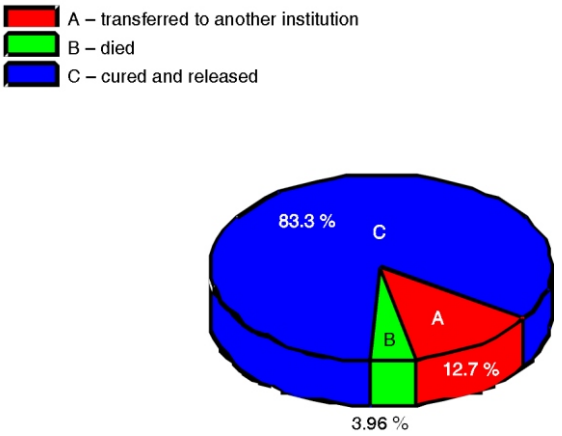

Figure 5. Percentage display of early childbirth with different final outcomes – transferred to another institution, fatal and treated in the maternity hospital and allowed to go home

Table 3. Incidence of ROP related to weight at birth in 2004

Incidence of ROP	Number [%]
<999 g	3 newborns [0.52 %]
1000-1499 g	13 newborns [2.2 %]
1500-1999 g	7 newborns [1.19 %]

born infants; therefrom, the cases of ROP are present in a few percents (~4 %). Table 3 covers the number of data with respect to the weight. In figs. 6-10 the results of the study are graphically presented.

Prematurely born infants or infants with low body weight are the most indicated groups for ROP, however only a small percentage of them end up with a severe form of the disorder.

Ophthalmologic results of the examined children despite the risk for retrolental fibroplasia, were within normal limits, with no statistically significant differences compared to the reference values, $-p > > 0.05$ (DF = 67, $t = 0.2371$), [21].

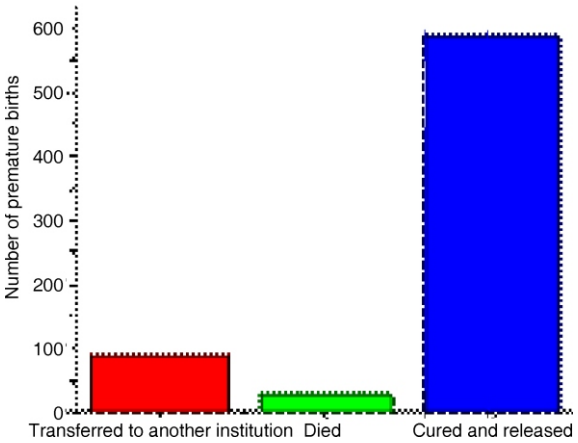

Figure 6. Number of premature births with different outcomes – transferred to another institution, fatal and treated at the maternity hospital and released home

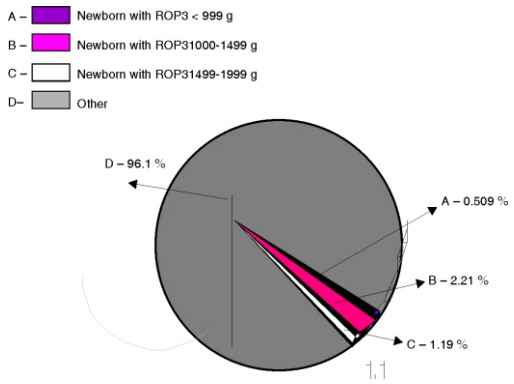

Figure 7. Premature births treated at the maternity hospital and discharged afterwards – percentage of patients' cases according to weight

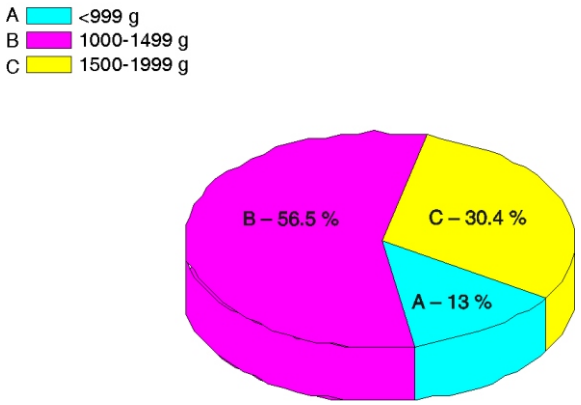

Figure 8. Incidence of ROP with respect to body weight (2004)

Table 3 and fig. 9 represent the cases of ROP developed in children who have not been exposed to an elevated concentration of O_2. They contain information on the ROP and sanitation.

Usually, the shortest O_2 therapy lasts 3 days and the maximum lasts 86 days. The average duration of therapy is 23 days.

According to the data analysis, a large number of newborns with ROP has been successfully treated. From the statistical data regarding ROP, the largest number of detected ROP cases occurred with newborns weighting between 1000 g and 1499 g. In tab. 4 it can be seen that most cases are diagnosed with asphyxia prenatal and RDS. The number of perinatal infections and pneumonia is somewhat smaller. It would be of great interest to collect data and create a database for diagnosis and laser treatment of ROP in Belgrade, Serbia.

CONCLUSIONS

Discussions about the correlation between the oxygen therapy and ROP occurrence are still present. ROP is considered to be a serious disease and here are the results of the study from the IGA KCS Hospital in

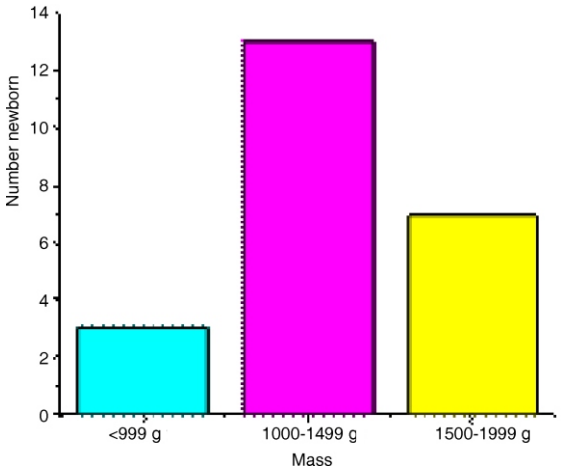

Figure 9. Number of ROP incidence depending on body weight (2004)

Table 4. Pathology and oxygen therapy for children with ROP

Pathology	Number of newborns
Asphyxia prenatal	48 children
RDS	47 children
Perinatal infections: sepsis	32 children
Candida	4 children
Pneumonia	21 children
Haemorrhagia pulm	3 children
BPD	8 children
IVH I and II	41 children
IVH III and IV	13 children
Hydrocephalus post-haem	4 children
Ventriculodilatatio	3 children

Belgrade, Serbia. One of the methods for ROP treatment are laser techniques (semiconductor lasers are also favourable).

Besides the ROP treatment, there are other laser applications in gynaecology, neonatology and ophthalmology. One of the very important applications is the analysis of milk quality for newborns. There are different methods to control the quality of milk through the measurement of turbidity (He Ne laser or with Nd^{3+}:YAG and its harmonics in the ps-region). Measurements of turbidity belong to the category of reliable, but not highly accurate. Adjusted selection with the excitation wavelength and the fluorescence method with pulse lasers, present for a long time is a more precise method for mastitis diagnosis. From the references it could be seen that the distinction could be made in the quality of milk (whether it is pathogenic or healthy). Another application of laser treatment is the rehabilitation of the mastitis affected tissue.

AUTHORS' CONTRIBUTIONS

The idea and results for the presented research were initiated and performed by M. Živković at the IG

KCS Hospital. The data processing and graphic presentation *i*. *e*. manuscript preparation were carried out by M. Ž. Srećković, T. M. Stojić, and B. M. Bokić. The manuscript was written by M. Živković and M. Ž. Srećković and all the authors participated in the discussion of the results presented in the final version of the paper.

REFERENCES

[1] ***, Advanced Signal Processing Handbook, Theory and Implementation for Radar, Sonar and Medical Imaging Real-Time Systems (Ed. S. Stergiopoulos), CRC Press, Boca Raton, Fla., USA, 2001
[2] Marjanović, N., *et al*., Simulated Exposure of Titanium Dioxide Memristors to Ions Beams, *Nucl Technol Radiat, 25* (2010), 2, pp. 120-125
[3] ***, LESON Learned from Accidents in Industrial Irradiation, IAEAQ, Vienna, 1996
[4] Sliney, D. H., Wolbarsht, M. I., Safety with Lasers and Other Optical Sources, Plenum Press, New York, 1980
[5] Chadwick, K. H., Leenhouts, H. P., The Molecular Theory of Radiation Biology, Springer, Berlin, 1961
[6] Biological Effects of Low-Level Radiation, International Atomic Energy Agency, Vienna, 1983
[7] Srećković, M., *et al.*, Laser in Medicine (in Serbian), Institute of Physics for Technical Faculties, Belgrade, 2010
[8] Obaturov, G. M., Biophysical Models of Radiobiological Effects (in Russian), Moskva, Energoatom, 1987
[9] Ullmaier, H., Schilling, W., Radiation Damage in Metallic Reactor Materials, pp. 301-in Physics of Modern Materials, Vol. 1, International Atomic Energy Agency, Vienna, 1980
[10] Stanković, K., *et al*., Influence of Tube Volume on Measurement Uncertainty of GM Counters, *Nucl Technol Radiat, 25* (2010),1, pp. 46-50
[11] Overbeek, F., *et al.*, Carcinogenic Risk in Diagnostic Nuclear Medicine : Biolo Gical and epidemiological Considerations, *Eur. J. of Nucl. Med., 21* (1994), 9, pp. 997-1012
[12] Srećković, M., *et al.*, Laser Influence and Application to Biosystems, Organisms and Cells, Lasers 2001, Proc. Lasers 2001, Mc Lean, SoQue, STS Press, 2002, pp. 323-330
[13] Srećković, M., *et al*., Photoinduced Processes, Radiation Interaction with Material and Damages – Material Hardness, *Nucl Technol Radiat, 30* (2015), 1, pp. 23-34
[14] Praskalo, Ž., *et al*., A Survey of Short-Term and Long-Term Stability of Tube Parameters in a Mammography Unit, *Nucl Technol Radiat, 29* (2014), 4, pp. 321-325
[15] Dolićanin, Ć. B., *et al*., Statistical Treatment of Nuclear Counting Results, *Nucl Technol Radiat, 26* (2011), 2, pp. 164-170
[16] Djekić, S., *et al*., Conditions of the Applicability of the Geometrical Similarity Law to Impulse Breakdown in Gases, *IEEE Trans. on Dielectrics and Electric Insulation, 17* (2010), 4, 10.1109/tdei.2010.5539689
[17] Vujisić, M., *et al*., A Statistical Analysis of Measurement Results Obtained from Nonlinear Physical Laws, *Appl. Matemat. Modelling, 35* (2011) , July, pp. 3128-3135
[18] Bowmaker, J. K., Dartnall, H. J. A., Visual Pigments of Rods and Cones in a Human Retina, *J. Physiol., 298* (1980), pp. 501-511
[19] Naseri, A., Patel, N. P., Vision Loss as a Complication of Gamma Knife Radio Surgery for Trigeminal Neuralgia, *Br. J. Ophthalmol. 88* (2004), 9, pp. 1225-1226
[20] Dunjić, Z. B., Infection and Risk Factors for retinopathy Prematurity; Incidenca ROP in IGA KCS, 2006
[21] Živković, M., Longitudinal Follow Up of Growth and Development of Children from Most Severe Cases of RH(D) Alloimmune Pregnancies After Application of intrauterine Intravascular Transfusion, Ph.D. Thesis, Faculty of Medicine, University of Belgrade, 2012
[22] Oros, A., Premature Retinopathy (in Serbian), Andrejević Foundatin, Belgrade, 2003
[23] Abramson, D. H., Schefler, A. C., Transpupillary Thermotherapy as Initial Treatment for Small Intraocular Retinoblastoma, Technique and Predict of Success, *Ophtalmology, 111* (2004), 5, pp. 984-991
[24] Langston, D. H., Manual of Ocular Diagnosis and Therapy, Ed. Boston, Littel, Brown and Comp., 1996, pp. 159-167
[25] ***, Conference, Premature Retinopathy and Blindness Preservation at Neonatal Born, 2007
[26] Harley, R. D., *et al*., Eds. Harley's Paediatric Ophthalmology, Lippincourt, Wiliams and Ewilkins, Md., 2005
[27] Fankhauser, F., Kawasniewska, S., Laser in Ophthalmology, Eds. Kugler, The Hague, 2003
[28] Biglan, A. W., *et al.*, Retinopathy of Prematurity, Amsterdam, Ugler, 1995
[29] Lorenz, B., Moore, A. T., Paediatric Ophthalmology, Neuro-Ophthalmology, Genetics, Berlin, Springer, 2006
[30] ***, Cryotherapy for Retinopathy of Prematurity Cooperative Group, Multicenter Trial of Cryotherapy for Retinopathy of Prematurity Preliminary Results, *Arch Ophthalmol, 106* (1988), 4, pp. 471-479

Received on October 27, 2016
Accepted on March 23, 2017

**Моника М. ЖИВКОВИЋ, Милеса Ж. СРЕЋКОВИЋ,
Томислав М. СТОЈИЋ, Бојана М. БОКИЋ**

УТИЦАЈ ЕЛЕКТРОМАГНЕТНОГ И НУКЛЕАРНОГ ЗРАЧЕЊА У МЕДИЦИНИ ЗА ТЕРАПИЈУ И ДИЈАГНОЗУ – ПРОЦЕСИ, ЧИЊЕНИЦЕ И СТАТИСТИЧКА АНАЛИЗА

Савремена медицина (биомедицина) не може да се замисли без дијагностике и терапеутских метода базираних на нуклеарној, ласерској, акустичкој техници и процесима заснованим на њима. Примена ових метода је везана са рачунарском подршком, обрадом сигнала, мерним-контролним техникама, високим степеном аутоматизације и анализом слике. У раду се анализирају савремени проблеми техничке природе који се односе на неонатологију и офталмологију, а заснивају се на дејству нуклеарног зрачења и ласерских снопова. Овде су представљене статистичке обраде резултата из Института за гинекологију и акушерство Клиничког центра Србије, Београд, у вези побољшања вида новорођенчади пренаталног типа са различитим степенима патолошког стања ретинопатије. Упркос добрим резултатима, закључује се да је мултидисциплинарни приступ потребан за боље разумевање улоге ласера и ласерских техника у медицини, као и могућности спрезања. Размотрене су и нове потенцијалне примене ласера од интереса за неонатологију и офталмологију.

Кључне речи: ретинопатија код новорођенчади, неонатологија, ласер, нуклеарно зрачење, оштећење, дозиметрија

Transmission of entangled photons studied by quantum tomography: do we need plasmonic resonances?

Journal of Physics Communications

PAPER

Transmission of entangled photons studied by quantum tomography: do we need plasmonic resonances?

Mathilde Remy[1], **Bojana Bokic**[2], **Mirko Cormann**[1], **Wakana Kubo**[3], **Yves Caudano**[1,5] and **Branko Kolaric**[2,4,5]

[1] Department of Physics, University of Namur, Rue de Bruxelles 61, 5000 Namur, Belgium
[2] Institute of Physics, University of Belgrade, Pregrevica 118, 11080 Belgrade, Serbia
[3] Department of Electrical and Electronic Engineering, Tokyo University of Agriculture and Technology, 2-24-16 Naka-cho, Koganei-shi, Tokyo 184-8588, Japan
[4] Micro- and Nanophotonic Materials Group, University of Mons, Place du Parc 20, 7000 Mons, Belgium
[5] Authors to whom any correspondence should be addressed.

E-mail: yves.caudano@unamur.be **and** branko.kolaric@umons.ac.be

Keywords: quantum entanglement, quantum tomography, plasmonic, nanoscale optics

OPEN ACCESS

RECEIVED
23 April 2019

REVISED
24 May 2019

ACCEPTED FOR PUBLICATION
12 June 2019

PUBLISHED
26 June 2019

Abstract

We performed quantum tomography to reveal the robustness of quantum correlations of photons entangled in polarisation after their interaction with plasmonic and nonplasmonic environments at normal incidence. The experimental findings clearly show that the visibility of quantum correlations survives the interaction, and that the presence of plasmonic resonances has not any significant influence on the survival of polarisation correlations for transmitted photon pairs. The results indicate that quantum states can be encoded into the multiple motions of a many-body electronic system without demolishing their quantum nature. The plasmonic structures and their resonances only enhance the overall transmission. Thus, they could benefit the pair detection rate, that is the number of coincidences per unit of time, but they do not affect the visibility of quantum correlations. We also performed quantum tomography of the entangled pairs after interaction with the continuous planar gold film as a function of the incidence angle. The latter illustrates the loss of polarization correlations that arises from the partially polarizing properties of the isotropic sample out of normal incidence. Our work shows that plasmonic structures are not needed to exploit quantum entanglement if the rate of coincidence counting is sufficient.

1. Introduction

Recently a few articles [1–3] described and thoroughly discussed the importance of polaritonic structures and plasmonic resonances for the survival of quantum entanglement in polarization or energy (frequency bin entanglement). Surface plasmon polaritons (SPPs) are quasi-particles created by the coupling of light with collective oscillations of the conduction electrons at a metal-dielectric interface. SPPs exhibit an evanescent field in the direction perpendicular to their propagation. Therefore, they strongly confine light at the interface. Metallic nanostructures can convert photons into SPPs, which tunnel through the structure before reradiating as photons [4, 538]. This photon-plasmon-photon conversion process has been investigated with polarisation [1, 39] (see also the theoretical analysis of [6]), time-bin [2, 7] and orbital-angular-momentum [8] entanglement. It has been shown that plasmons maintain nonclassical photon statistics, and preserve entanglement, encoding entangled photons in multi-electronic systems.

The work of Olislager *et al.* [2] reviewed different quantum experiments with plasmons, such as Young's double-slit experiment [9], evidence of quantum superpositions of single plasmons [10–14], and the generation of plasmonic squeezed states [15], as well as two-particle experiments [16–21]. The studies mentioned above proved the quantum bosonic nature of plasmonic excitations. It has also been shown that the spin–orbit coupling of incident light allows the post-selection of the final state in a quantum weak measurement of the light

chirality [22]. The polarisation entanglement of photon pairs [1], as well as energy-time entanglement, are preserved [2] in cascading photon to SPP and subsequently to photon conversions, with preservation of temporal coherence that is larger than the SPP lifetime [7]. Besides, both the quasi-particle and wave nature of SPP are highlighted in experiments similar to those attesting the wave-particle duality of photons when they interact with beam splitters [12].

For these reasons, the advantages of quantum plasmonics have gained much visibility in the physical community [1–3, 23], since plasmons and SPPs or localized surface plasmon resonances (LPSRs) offer the unique possibility to control and manipulate nonclassical states of light. Integrated quantum technologies that allow scalability and miniaturization, as well as coherent coupling to single emitters [3, 4, 24] harnessing plasmonic resonances, offer a great potential for multiple applications in quantum information and technology, such as design and fabrication of single-photon sources, transistors, and ultra-compact circuitry, with potential applications for secure communication and advanced computing [25–27].

Here, we go further into the characterization of the entanglement preservation properties of thin metallic structures. We study not only the visibility of the coincidence detections but the full quantum state and correlations after transmission, i.e. after interaction with corrugated and noncorrugated metallic films. In this particular study, we use photons entangled in polarisation at a near-infrared wavelength (818 nm) and investigate the interaction of the photons with an entirely different metallic structure, a continuous planar gold film, in order to reveal by quantum tomography the robustness of quantum correlations in the absence of plasmonic resonance.

2. Experimental part

A planar and continuous metallic film with thickness of 10 nm (3 nm Cr + and 7 nm Au) was deposited by thermal sputtering on a glass substrate. The precise thicknesses of the deposited Cr and Au layers were determined using the Rutherford Back Scattering method (RBS) after deposition.

The anisotropic, chiral plasmonic structures were fabricated by electron beam lithography [28] and lift-off process. They were drawn on a resist thin film (Zeon Corporation, ZEP-520a) on a transparent substrate. Chromium and gold films of 5 and 20 nm (total thickness of 25 nm) were deposited on the patterned resist film by thermal deposition technique. After the lift-off process, the anisotropic, chiral plasmonic arrays were obtained. The geometry of the array and a high resolution image of the plasmonic units are presented in figure 1.

3. Quantum optical setup

Initially, a half-wave plate and a polarising beam splitter prepare the polarisation of the pump laser beam at 45° with a central wavelength at 409 nm (see figure 2). Photon pairs with a double central wavelength are produced via spontaneous parametric downconversion within two orthogonal and superimposed BBO-crystals of type I [29]. Nonlinear crystals are oriented such that horizontal and vertical polarisations participate in the downconversion within the first and the second crystal, respectively. A third BBO-crystal is placed in front of the source to compensate the group velocity mismatch. This configuration allows us to prepare a maximally entangled Bell State $|\phi_+\rangle = \frac{1}{\sqrt{2}}(|HH\rangle + |VV\rangle)$.

In the second part of the setup, a half-wave plate, a quarter-wave plate and a polarising beam splitter are placed along each optical path of photon pairs. Photons are detected with four single-photon-counting modules (SPCM) and a field-programmable gate array (FPGA) coincidence counter. Count and coincidence counting are used to make polarisation measurements. This means that single-photon detection event resulting from losses along one optical path (due for example to reflection, absorption, or scattering) are not considered for quantum tomography, as only photon correlations are taken into account. (Technically: we only probe the two-photon subspace of the Hilbert space.) Different basis are adjusted with the combined orientations of wave plates. Iris and low-pass filters select the desired superposed emission cones and reduce noise. Complementary information on the optical and detection setup can be found in [30].

4. Results and discussion

4.1. Transmission spectrum of the planar and nanostructured metallic film

The transmission (T) spectra of the gold films were measured at normal incidence with the UV–Vis Cary spectroscope on circular areas of 0.5 cm diameter. The spectrum of the noncorrugated gold film (see figure 3, upper) exhibits the well-known spectrum of a semi-transparent film, as it is rather opaque in the visible range [31]. The optical spectrum of the plasmonic nanostructures is also presented (see figure 3, lower). The optical

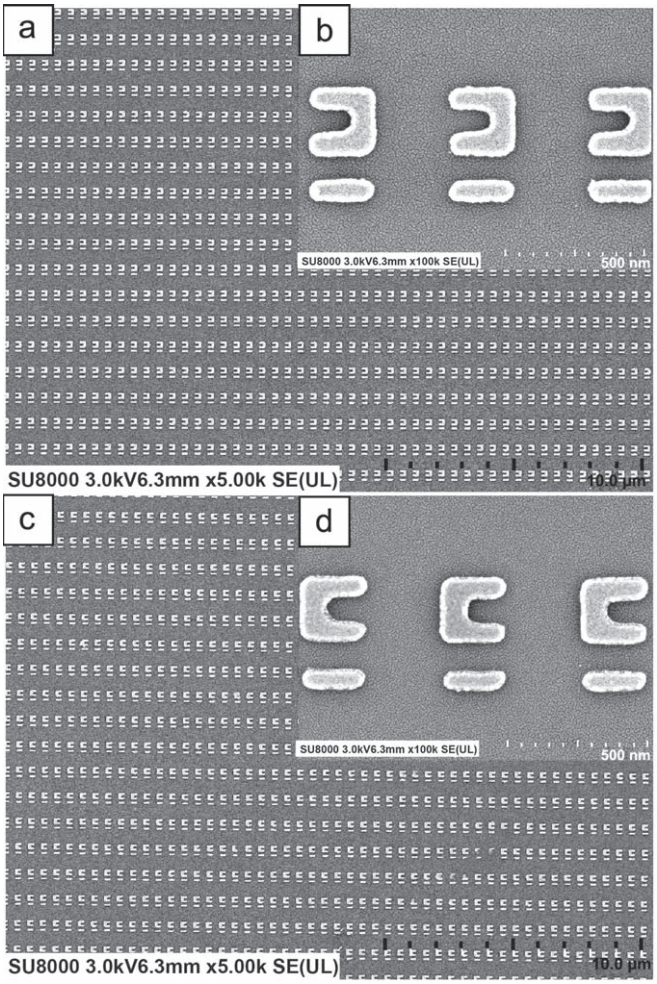

Figure 1. SEM image of the anisotropic chiral plasmonic nanostructures (upper-a: left handed; lower-c: right handed). The insets are large magnification images of the left-handed (upper-b) and right-handed (lower-d) chiral plasmonic structures. The scale bars in the insets are 500 nm. The distance between the structures as well as the height and the broadest width of the C-like structures are approximately 250 nm. The length of the rods is also approximately 250 nm while the corresponding width is about 84 nm. The different structures were deposited on the same substrate near each other using lithography method (see Experimental Part).

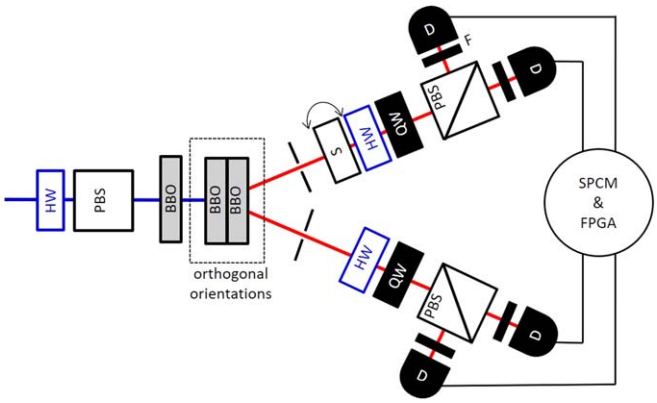

Figure 2. Experimental setup. Red lines represent the optical path of frequency-degenerate photon pairs. HW (half-wave plate), PBS (polarising beam splitter), BBO (BBO-crystal of type I), QW (quarter-wave plate), F (low-pass filter), D (lens and fibre coupler to SPCM) and sample (S). The sample is put in one of the two, otherwise equivalent, optical paths. It can rotate around an axis perpendicular to the optical table to change the angle of incidence.

properties of metallic particles are influenced by the particle size and orientation. The optical spectrum of plasmonic nanostructures is significantly structured. Due to the anisotropy and chirality of the array, a small difference in transmission (on different parts of the array) can be observed using different polarizations of the

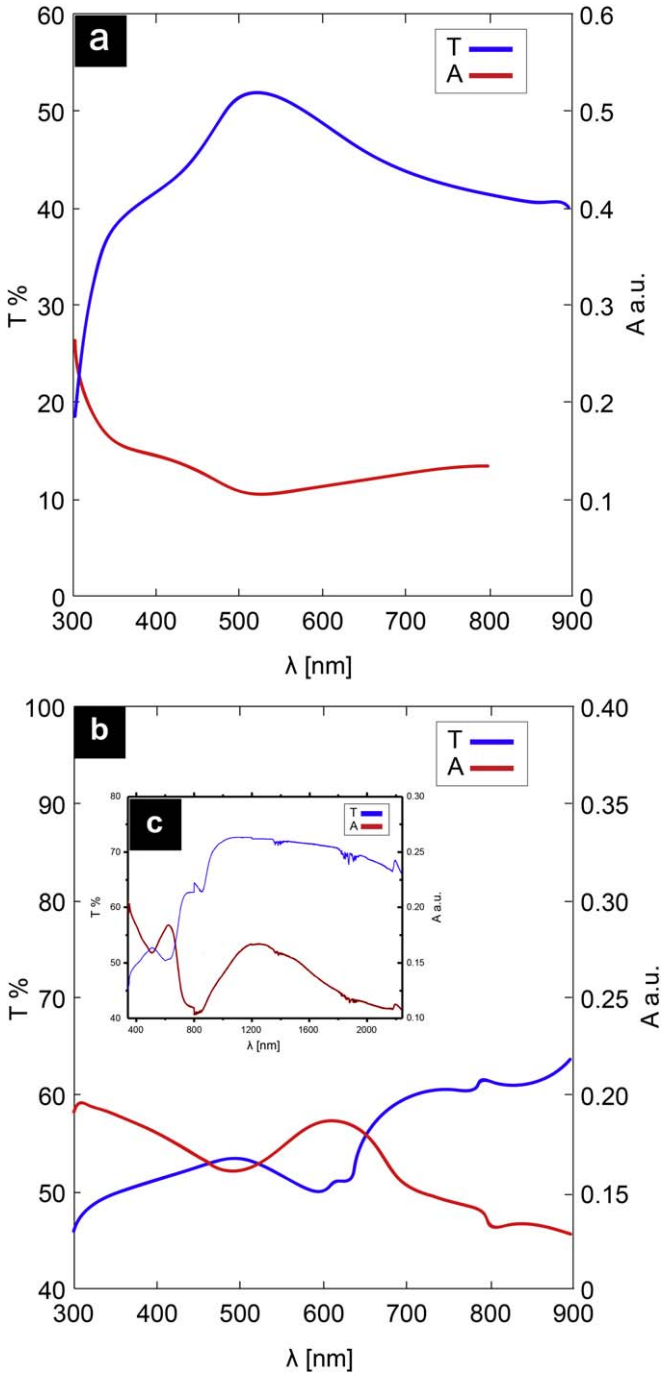

Figure 3. Optical Spectra of planar (upper-a) and nanostructured (lower-b) metallic films. Transmission curves are in blue while absorbance curves are in red. The inset (c) shows the optical spectra of the nanostructured sample over a wavelength range exhibiting also near-IR plasmonic resonances.

incident light (results not shown). In our experimental results depicted in figure 3, transmission and absorption of both the continuous and structured metallic films were measured using nonpolarized light and through a large spot, so that it was not possible to observe the small difference in transmission related to the anisotropy and chirality of the array. Thanks to the plasmonic resonances, the overall transmission of the nanostructured film increases, and becomes larger than the continuous planar film (see figure 3), even though the nanostructured film is thicker than the continuous film (25 versus 10 nm). It exhibits resonances with an asymmetric peak, which resembles very much the one previously reported for extraordinary transmission of different metallic subwavelength nanostructures [2, 31, 32]. In the case of the structured film, the peak in the absorption probably arises from the excitation of dipolar mode of the plasmonic array.

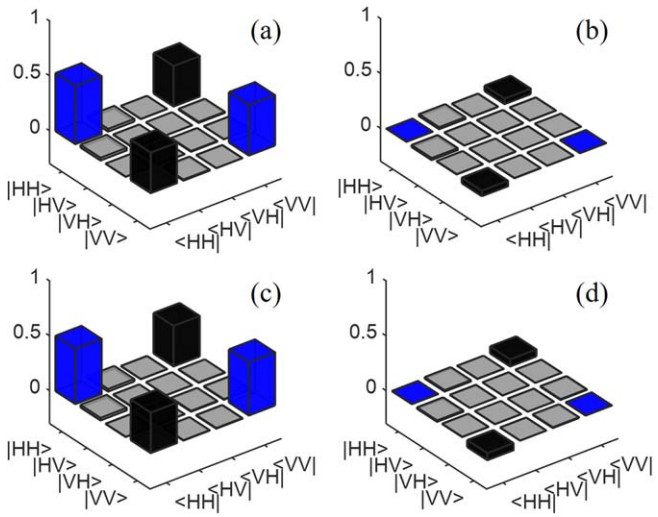

Figure 4. Graph of the real (left) and imaginary (right) parts of the density matrix. Graphs (a) and (b) represent the density matrix $\hat{\sigma}$ of the biphoton state after transmission through the structured plasmonic film. Graphs (c) and (d) represent the density matrix $\hat{\rho}$ of the initial biphoton state. Blue rods and black rods represent diagonal and off-diagonal terms of the density matrix, respectively.

4.2. Quantum tomography with the nanostructured metallic film at normal incidence

We start by evaluating the effect of the plasmonic nanostructures on polarisation-entanglement, in transmission. We realise a quantum tomography to reconstruct the density matrix of the system of the initial biphoton state $\hat{\rho}$ obtained without the sample and the state $\hat{\sigma}$ obtained after transmission through the sample with the plasmonic nanostructures and at normal incidence. We realise quantum tomography of a system of two qubits with two detectors per qubit. In this case, 9 different measurement bases are sufficient to realise the quantum tomography [33]. Although using 36 different analysis settings can improve the measurement precision, in order to minimise the total time of tomography and increase the stability during the complete course of measurements, quantum tomography is performed with 9 different bases. Each basis measurement without and with the nanostructured sample is realised within a time total of 60 s and with a time window of 16 ns for coincidence counting. All results are treated with the code developed by Paul Kwiat's quantum information group to determine the maximum likelihood estimation of each state, the metrics describing the features of the quantum state and its uncertainties [33, 34]. The fidelity $F(\hat{\rho}_1, \hat{\rho}_2) = (Tr[\sqrt{\sqrt{\hat{\rho}_1}\ \hat{\rho}_2\ \sqrt{\hat{\rho}_1}}])^2$ is a measurement of similarity between the two states $\hat{\rho}_1$ and $\hat{\rho}_2$ and can take value in the interval [0,1]. In our experiment, $F(\hat{\rho}, \hat{\sigma}) = 0.9966 \pm 0.0012$ is very close to one. Furthermore the computed fidelities with the Bell state $|\phi_+\rangle$, $F(|\phi_+\rangle, \hat{\rho}) = 0.8630 \pm 0.0018$ and $F(|\phi_+\rangle, \hat{\sigma}) = 0.8627 \pm 0.0012$ are nearly identical. These show that the initial and final states are nearly identical. We conclude that, at normal incidence, the nanostructured sample does not change significantly the polarisation, the polarisation correlations, and the entanglement of the transmitted photon pairs. This is confirmed by the similarity between the graphical representations of these states (see figure 4). These results are in line with previous observations, which indicate that plasmonic nanostructures are able to preserve entanglement [1, 2].

4.3. Quantum tomography with the continuous metallic film at normal incidence and as a function of the incidence angle

In order to assess the effect of plasmonic resonances on preserving quantum correlations, we performed a detailed quantum tomography study on the planar structure without plasmonic resonances. For classical waves, our continuous, planar film does not affect the polarisation at normal incidence. Transmittance is the same for all polarisations as it is isotropic in the surface plane. For non-normal incidence, the transmittance becomes a function of the polarisation. We investigate the effect of introducing the sample with different angles of incidence on the entangled polarisation state produced by the quantum source, as described below.

Firstly we measure both the initial biphoton state $\hat{\rho}$ obtained without the sample and the state $\hat{\sigma}$ obtained after transmission through the continuous metallic film at normal incidence. We realise a quantum tomography to reconstruct the density matrix of the system. Polarisation measurements are made in 36 different bases. Each measurement without (with) the planar sample is realised within a time total of 30 s (60 s) and with a time window of 16 ns (16 ns) for coincidence counting. The graphical representations of these states are also very similar (see figure 5).

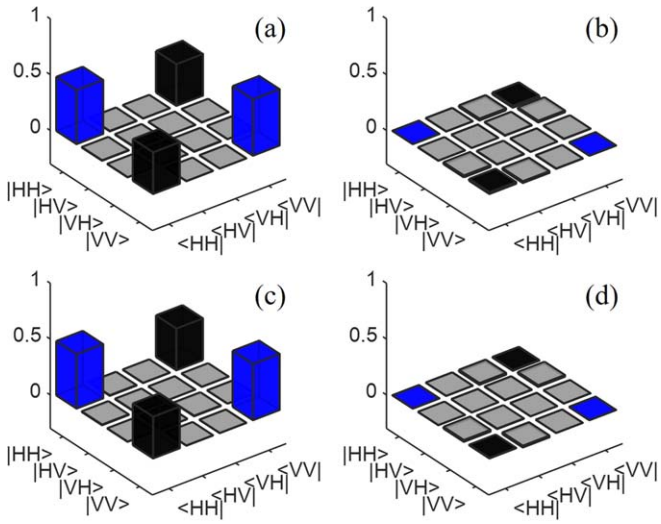

Figure 5. Graphical representation of the density matrix estimated by quantum tomography. The value of the real (a) and imaginary (b) parts of the density matrix $\hat{\sigma}$ of the biphoton state after transmission through the continuous metallic film and the value of the real (c) and imaginary (d) parts of the density matrix $\hat{\rho}$ of the initial biphoton state. Blue rods and black rods represent diagonal and off-diagonal terms of the density matrix, respectively.

The fidelity between the two states $F(\hat{\rho}, \hat{\sigma}) = 0.9989 \pm 0.0003$ is very close to one. In other words, the two-photon states before and after the sample at normal incidence are closely similar. Furthermore, the computed fidelities with the Bell state $|\phi_+\rangle$, $F(|\phi_+\rangle, \hat{\rho}) = 0.8683 \pm 0.0008$ and $F(|\phi_+\rangle, \hat{\sigma}) = 0.8673 \pm 0.0006$ are nearly identical and lead to the same conclusion. At normal incidence the thin, continuous, metallic film does not change significantly the polarisation of the transmitted photon pairs. Consequently, polarisation entanglement is completely preserved within the experimental uncertainties.

Secondly, we compare the initial, unperturbed state $\hat{\rho}_0$ and the states obtained after the sample with 4 different orientations: at normal incidence ($\hat{\sigma}_0$), 20° ($\hat{\sigma}_1$), 35° ($\hat{\sigma}_2$) and 50° ($\hat{\sigma}_3$) with respect to the surface normal. In order to maximise the stability of the experiment throughout the measurements, quantum tomography is performed with 9 different bases with a total time of 60 s for each basis measurement and a coincidence time window of 16 ns. To compare the measured quantum state to the expected state produced by each sample rotation (0°, 20°, 35° and 50°), we calculate the theoretical renormalized state of the system after the sample:

$$\hat{\sigma}_t = \frac{(\hat{M}\hat{\rho}_0\hat{M}^\dagger)}{Tr\,(\hat{M}\hat{\rho}_0\hat{M}^\dagger)} \text{ with } \hat{M} = \hat{I} \otimes (t_H\hat{P}_H + t_V\,\hat{P}_V),$$

which we evaluate using the theoretical complex transmission coefficients through the metallic film sample of $p(t_H)$ and $s(t_V)$ polarisations and the projectors $\hat{P}_H$ and $\hat{P}_V$ on the horizontal and vertical polarisation states, respectively. As the transmission coefficients are complex numbers, the impact of phase differences between the transmitted *s* and *p* polarisations is taken into account in our evaluation of the transmitted two-photon state and in our calculations of the fidelities to the initial state. The transmission coefficients are obtained numerically with the matrix transfer method applied to flat multilayers of Au/Cr/glass, with thickness of 7 nm/3 nm/1 mm respectively. We use the complex refractive index at wavelength $\lambda = 818$ nm for the gold $n_{Au} = 0,15905 + 5,0572\,i$ [35], chromium $n_{Cr} = 3,1945 + 3,4772\,i$ [36] and glass N-BK7 (SHOTT) $n_{glass} = 1,5104 + 9,3260.10^{-9}\,i$ obtained from [37]. Rapid oscillations of small amplitude of the wavelength-dependent transmission coefficients were averaged out. These arise from multiple reflections between the optical interfaces. They are not observed experimentally due to the finite coherence time and beam size.

The entanglement of formation $E_f(\hat{\sigma})$ is a measurement of entanglement for a state $\hat{\sigma}$. For a system of two qubits, $E_f(\hat{\sigma}) = -x\log_2(x) - (1-x)\log_2(1-x)$ with $x = \frac{1+\sqrt{1-C^2}}{2}$ and the concurrence $C = \max(\lambda_4 - \lambda_3 - \lambda_2 - \lambda_1, 0)$ where λ_i with $i = 1,2,3,4$ are the square roots of the eigenvalues of $\hat{\rho}(\hat{\sigma}_y \otimes \hat{\sigma}_y)\,\hat{\rho}^*(\hat{\sigma}_y \otimes \hat{\sigma}_y)$ in increasing order. We measure the entanglement of formation $E_f(\hat{\sigma}_i)$ and the experimental state fidelity with respect to the state without the sample $F(\hat{\rho}_0, \hat{\sigma}_i)$, and with respect to the maximally entangled Bell state theoretically produced $F(|\phi_+\rangle, \hat{\sigma}_i)$. These properties quantify the influence of the planar film on the entanglement and polarisation state of the transmitted photon pairs. As our aim is to quantify the preservation of quantum entanglement in transmission through the sample, we first measure and compute the entanglement of

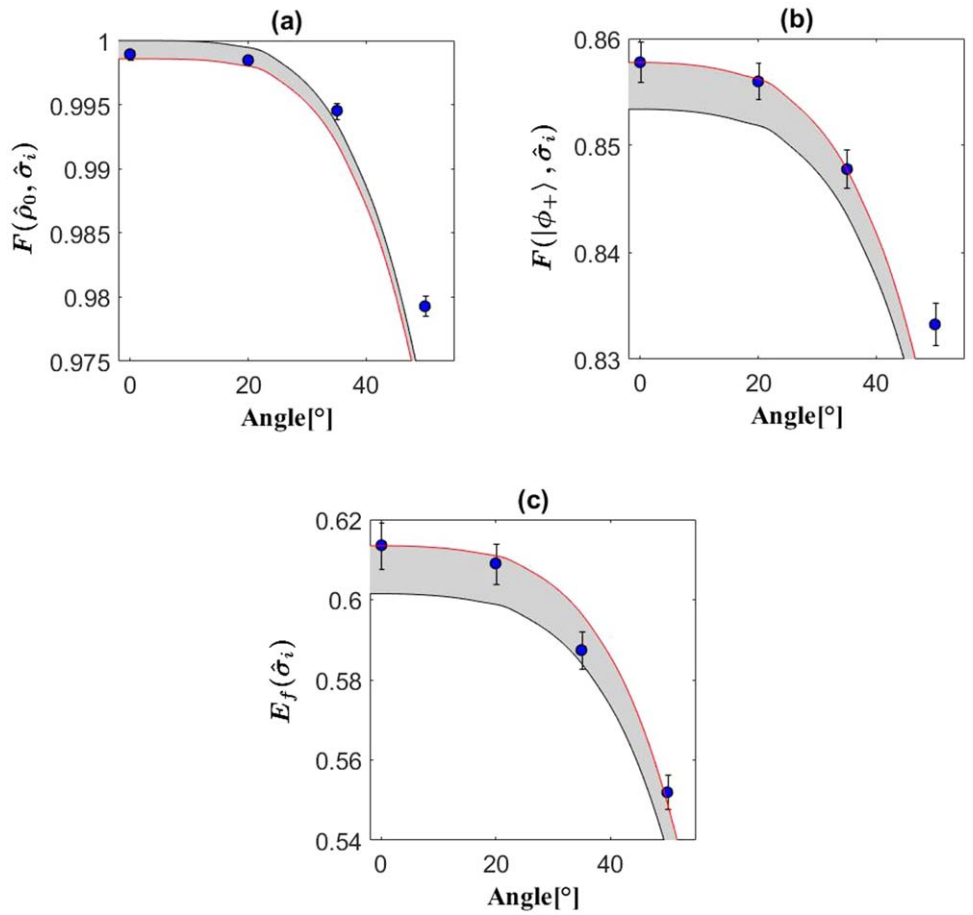

Figure 6. (a) Graph of the fidelity $F(\hat{\rho}_0, \hat{\sigma}_i)$ between the polarisation state with the continuous metallic film $\hat{\sigma}_i$ and without the sample $\hat{\rho}_0$ in function of the angle of incidence, i.e. of the rotation of the sample; (b) Graph of the fidelity $F(|\phi_+\rangle, \hat{\sigma}_i)$ with respect to the maximally entangled Bell state; (c) Graph of the measure of entanglement of formation $E_f(\hat{\sigma}_i)$ of the polarisation state with the sample $\hat{\sigma}_i$ in function of the angle of incidence. (a)–(c) Error bars represent the statistical error evaluated with a Monte Carlo method. Theoretical curves are calculated with the theoretical renormalized state $\hat{\sigma}_t$. For each graphic, there are two theoretical curves, calculated with respect to the two reference states $\hat{\rho}_0$ (in black) and $\hat{\sigma}_0$ (in red). We use two curves because theoretically the density matrix of the state with and without the sample at normal incidence should be the same, as confirmed experimentally (fidelity between them nearly equal to 1). The area between the two theoretical curves is filled in grey.

formation. However, the degree of entanglement can be left unchanged by transmission while the state is transformed to another (equally) entangled state. For this reason, it is also important to quantify the closeness between the states before and after transmission through the sample, which we do by calculating the fidelity. In theory, the state of the photon pairs transmitted through the planar sample at normal incidence $\hat{\sigma}_0$ should be the same as in the configuration without the sample $\hat{\rho}_0$. This is confirmed experimentally with the measure of the fidelity $F(\hat{\rho}_0, \hat{\sigma}_0)$, which is nearly equal to one. This is an immediate consequence of the equality between the transmission coefficients for *s* and *p* polarisations. For this reason, we use both $\hat{\rho}_0$ and $\hat{\sigma}_0$ as a reference to calculate the theoretical fidelity with respect to the initial state as a function of the incidence angle (see figure 6). We use these two references to provide a bound on experimental uncertainties due to the global stability of the system over long acquisition times. The theoretical curves associated with these two references are really close to each other, as shown by the *Y*-axis scales. The experimental entanglement of formation $E_f(\hat{\sigma}_i)$ and the fidelities $F(|\phi_+\rangle, \hat{\sigma}_i)$ and $F(\hat{\rho}_0, \hat{\sigma}_i)$ decrease slowly with the angle of incidence (see figure 6) and are in agreement with the theoretical predictions.

For each state $\hat{\sigma}_i$ with $i \in \{0, 1, 2, 3\}$, quantum tomography reveals that the probability of measuring a final polarisation $|HH\rangle$ ($|VV\rangle$) after the planar, continuous, metallic film increases (decreases) with the angle of rotation of the sample (see figure 7). The asymmetry between the coloured diagonal rods (blue or red) increases with the angle. This is explained by the fact that, out of normal incidence, the transmission coefficient of *p* polarisation is larger than the transmission coefficient of *s* polarisation. We quantify this behaviour experimentally and we compare it with theory (see figure 8). We represent the probabilities of measuring a final

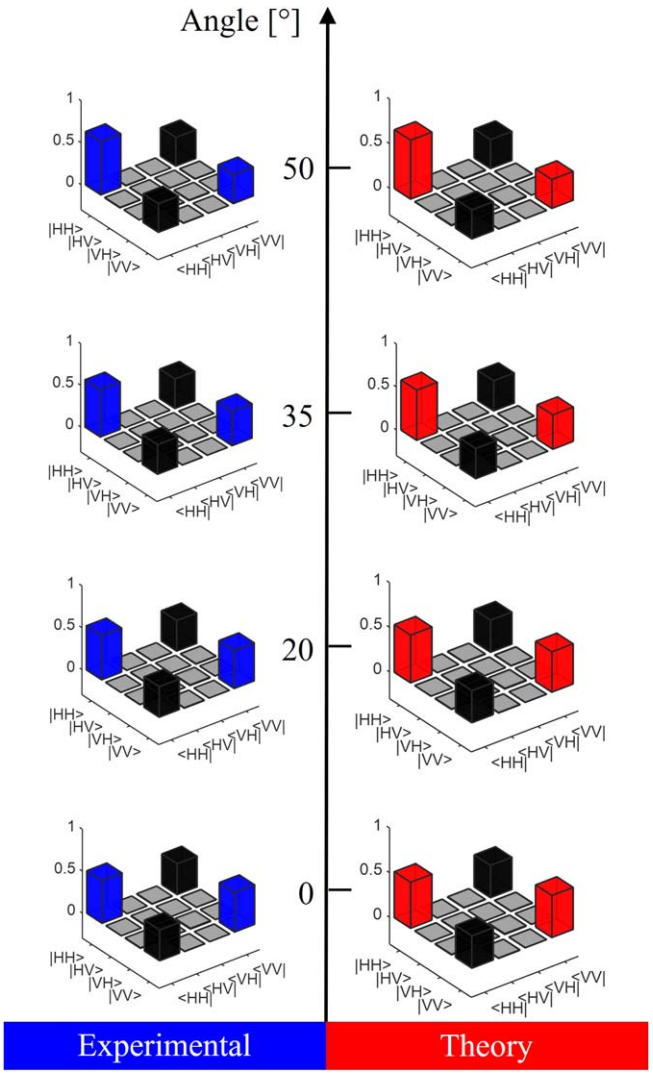

Figure 7. On the left (right), the graphical representation of the experimental (theoretical) values of the real parts of the density matrix $\tilde{\sigma}_i$ of the biphoton state after transmission through the continuous metallic film in function of the angle of incidence, i.e. of the rotation of the sample.

polarisation $|HH\rangle$ and $|VV\rangle$ of a system in an initially entangled state like the $|\phi_+\rangle$ Bell state. Each point represents the mean value of 30 measurements of 5 s.

We conclude that the introduction of the flat, metallic film sample at normal incidence decreases the coincidence rate (a loss of $\sim$55% theoretically and $\sim$57% experimentally) but it does not affect the entangled quantum state. Without perturbation of the polarisation of the system, the density matrix of the polarisation degree of freedom remains the same. This occurs at normal incidence, since the sample does not have any polarising property. For non-normal incidence, the polarisation entanglement decreases. It is related to the different transmission coefficients of *s* and *p* polarisation through the sample. This fact indicates that quantum correlations will be affected only if polarisation is affected. Although the nanostructured sample provides a transmission $\sim$50% better than the planar metallic film, the fidelities and trace distance between the initial and transmitted states at normal incidence indicate that the initial state preservation is nevertheless (marginally) better in the case of the planar metallic film. This effect could be the result of the anisotropy of the nanostructured sample that induces a small polarising effect upon transmission at normal incidence, contrary to the planar, isotropic film.

5. Conclusion

In the present work, we studied the preservation of polarisation entanglement in transmission through nanostructured and continuous planar gold films using quantum tomography. The quantum correlations survive after interaction with planar films and our finding clearly indicates that plasmonic resonances do not

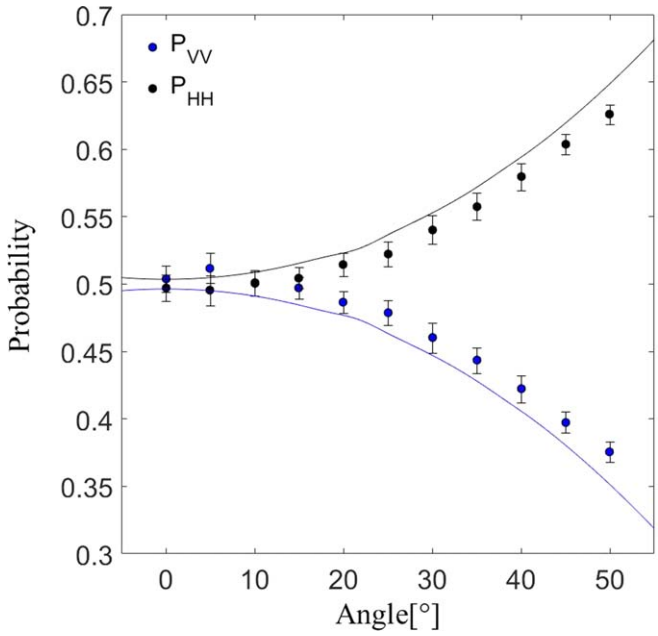

Figure 8. Probability of measuring a final polarisation $|HH\rangle$ (black) and $|VV\rangle$ (blue) after transmission through the continuous metallic film in function of the angle of incidence, i.e. of the rotation of the sample. Error bars represent the standard deviation of 30 measurements. Continuous curves represent the theoretical probabilities, P_{HH} and P_{VV}, as a function of the rotation of the sample.

play any significant role in the robustness of correlation preservation. They may only improve potentially the total coincidence rate by increasing the transmission coefficient through the film, while they do not play any role *per se* in the preservation of entanglement in the quantum state of the transmitted photon pairs.

Acknowledgments

All authors acknowledge Mr Adrien Nélis, Dr Sébastien Mouchet, Mr Bruno Majérus, and Dr Jean-François Colomer for their assistance in the characterization of the continuous metallic film. This work made use of the OLS, SIAM, and MORPH-IM technological platforms of the University of Namur, with support from the NISM and naXys Institutes. B K acknowledges financial support from the 'Action de Recherche Concertée' (BIOSTRUCT project, No. 10/15-033) of UNamur and from Interuniversity Attraction Pole: Photonics@be (P7-35, Belgian Science Policy Office). B K and B B acknowledge financial support of the Ministry of Science, Republic of Serbia (grant III 45016). B K and Y C acknowledge support from Nanoscale Quantum Optics COST-MP1403 action and from F R S-FNRS. Y C is a research associate of the Belgian Fund for Scientific Research F R S-FNRS.

ORCID iDs

Mathilde Remy https://orcid.org/0000-0002-4101-0454
Bojana Bokic https://orcid.org/0000-0002-9061-7201
Yves Caudano https://orcid.org/0000-0002-0805-4068
Branko Kolaric https://orcid.org/0000-0003-0203-7897

References

[1] Altewischer E, Van Exter M P and Woerdman J P 2002 *Nature* **418** 304–6
[2] Olislager L, Kubo W, Tanaka T, Ungureanu S, Vallée R, Kolaric B, Emplit P and Massar S 2015 *Nanophotonics* **4** 324–31
[3] Jacob Z 2012 Quantum plasmonics *Mrs Bull.* **37** 761–7
[4] Ebbesen T W, Lezec H J, Ghaemi H F, Thio T and Wolff P A 1998 *Nature* **391** 667–9
[5] Martín-Moreno L, García-Vidal F J, Lezec H J, Pellerin K M, Thio T, Pendry J B and Ebbesen T W 2001 *Phys. Rev. Lett.* **86** 1114
[38] Büse A, Juan M, Tischler N, D'Ambrosio V, Sciarrino F, Marrucci L and Molina-Terriza G 2018 *Phys. Rev. Lett.* **121** 173901
[39] Chen Y, Lee C, Lu L, Liu D, Wu Y, Feng L, Li M, Rockstuhl C, Guo G, Guo G, Tame M and Ren X 2018 *Optica* **5** 1229-1235
[6] Moreno E, Garcia-Vidal F J, Erni D, Cirac J I and Martín-Moreno L 2004 *Phys. Rev. Lett.* **92** 236801
[7] Fasel S, Robin F, Moreno E, Erni D, Gisin N and Zbinden H 2005 *Phys. Rev. Lett.* **94** 110501
[8] Ren X-F, Guo G-P, Huang Y-F, Li C-F and Guo G-C 2006 *Europhys. Lett.* **76** 753–9

[9] Schouten H F, Kuzmin N, Dubois G, Visser T D, Gbur G, Alkemade P F A, Blok H, 't Hooft G W, Lenstra D and Eliel E R 2005 *Phys. Rev. Lett.* **94** 053901
[10] Fasel S, Halder M, Gisin N and Zbinden H 2006 *New J. Phys.* **8** 13
[11] Akimov A V, Mukherjee A, Yu C L, Chang D E, Zibrov A S, Hemmer P R, Park H and Lukin M D 2007 *Nature* **450** 402–6
[12] Kolesov R, Grotz B, Balasubramanian G, Stöhr R J, Nicolet A A L, Hemmer P R, Jelezko F and Wrachtrup J 2009 *Nat. Phys.* **5** 470–4
[13] Di Martino G, Sonnefraud Y, Kéna-Cohen S, Tame M, Ozdemir S, Kim M S and Maier S A 2012 *Nano Lett.* **12** 2504–8
[14] Cai Y-J, Li M, Ren X-F, Zou C-L, Xiong X, Lei H-L, Liu B-H, Guo G-P and Guo G-C 2015 *Phys. Rev Applied* **2** 014004
[15] Huck A, Smolka S, Lodahl P, Sørensen A, Boltasseva A, Janousek J and Andersen U L 2009 *Phys. Rev. Lett.* **102** 246802
[16] Gonzalez-Tudela A, Martin-Cano D, Moreno E, Martin-Moreno L, Tejedor C and Garcia-Vidal F J 2011 *Phys. Rev. Lett.* **106** 020501
[17] Heeres R W, Kouwenhoven L P and Zwiller V 2013 *Nat. Nanotech.* **8** 719–22
[18] Dutta Gupta S and Agarwal G S 2014 *Opt. Lett.* **39** 390–3
[19] Fakonas J S, Lee H, Kelaita Y A and Atwater H A 2014 *Nat. Photon.* **8** 317–20
[20] Steel M 2014 *Nat. Photon.* **8** 273–5
[21] Di Martino G, Sonnefraud Y, Tame M S, Kéna-Cohen S, Dieleman F, Özdemir Ş K, Kim M S and Maier S A 2014 *Phys. Rev. Appl.* **1** 3
[22] Gorodetski Y, Bliokh K Y, Stein B, Genet C, Shitrit N, Kleiner V, Hasman E and Ebbesen T W 2012 *Phys. Rev. Lett.* **109** 013901
[23] Jacob Z and Shalaev V M 2011 Plasmonics goes quantum *Science* **334** 463–4
[24] Tame M S, McEnery K R, Özdemir Ş K, Lee J, Maier S A and Kim M S 2013 *Nat. Phys.* **9** 329–40
[25] Nielsen M A and Chuang I L 2010 *Quantum Computation and Quantum Information* (Cambridge: Cambridge university press) (https://doi.org/10.1017/CBO9780511976667)
[26] Aharonovich I, Greentree A D and Prawer S 2011 *Nat. Photon.* **5** 397–405
[27] Huck A, Kumar S, Shakoor A and Andersen U L 2011 *Phys. Rev. Lett.* **106** 096801
[28] Kubo W and Fujikawa S 2011 *Nano Lett.* **11** 8–15
[29] Kwiat P G, Waks E, White A G, Appelbaum I and Eberhard P H 1999 *Phys. Rev.* A **60** R773
[30] Cormann M, Remy M, Kolaric B and Caudano Y 2016 *Phys. Rev.* A **93** 042124
[31] Ungureanu S, Kolaric B, Chen J, Hillenbrand R and Vallée R A L 2013 *Nanophotonics* **2** 173–85
[32] van der Veen M A, Rosolen G, Verbiest T, Vanbel M K, Maes B and Kolaric B 2015 *J. Mater. Chem.* C **3** 1576–81
[33] Altepeter J B, James D F V and Kwiat P G 2004 4 Qubit Quantum State Tomography *Quantum State Estimation* (*Lect. Notes Phys.* 649) ed) ed M Paris and J Řeháček (Berlin, Heidelberg: Springer) 4 113–45
[34] Altepeter J B, Jeffrey E and Kwiat P G 2005 *Advances in Atomic, Molecular and Optical Physics* **52** 105–59
[35] Johnson P B and Christy R W 1972 *Phys. Rev.* B **6** 4370–9
[36] Johnson P B and Christy R W 1974 *Phys. Rev.* B **9** 5056–70
[37] Polyanskiy M Refractive index database https://refractiveindex.info/

jove

Uncovering Hidden Dynamics of Natural Photonic Structures using Holographic Imaging

Marina Simovic-Pavlovic[1,2], **Maja C. Pagnacco**[3], **Dusan Grujic**[1], **Bojana Bokic**[1], **Darko Vasiljevic**[1], **Sébastien Mouchet**[4,5], **Thierry Verbiest**[6], **Branko Kolaric**[1,7]

[1] Institute of Physics, Photonics Center, University of Belgrade [2] Faculty of Mechanical Engineering, University of Belgrade [3] Institute of Chemistry, Technology and Metallurgy, University of Belgrade [4] School of Physics, University of Exeter [5] Department of Physics & Namur Institute of Structured Matter (NISM), University of Namur [6] Chemistry Department, Laboratory of Molecular Imaging and Photonics, KULeuven [7] Université de Mons

Corresponding Authors

Maja C. Pagnacco
maja.pagnacco@nanosys.ihtm.bg.ac.rs
Branko Kolaric
branko.kolaric@umons.ac.be

Citation

Simovic-Pavlovic, M., Pagnacco, M.C., Grujic, D., Bokic, B., Vasiljevic, D., Mouchet, S., Verbiest, T., Kolaric, B. Uncovering Hidden Dynamics of Natural Photonic Structures using Holographic Imaging. *J. Vis. Exp.* (), e63676, doi:10.3791/63676 (2022).

Date Published

March 31, 2022

DOI

10.3791/63676

URL

jove.com/t/63676

Abstract

In this method, the potential of optics and holography to uncover hidden details of a natural system's dynamical response at the nanoscale is exploited. In the first part, the optical and holographic studies of natural photonic structures are presented as well as conditions for the appearance of the photophoretic effect, namely, the displacement or deformation of a nanostructure due to a light-induced thermal gradient, at the nanoscale. This effect is revealed by real-time digital holographic interferometry monitoring the deformation of scales covering the wings of insects induced by temperature. The link between geometry and nanocorrugation that leads to the emergence of the photophoretic effect is experimentally demonstrated and confirmed. In the second part, it is shown how holography can be potentially used to uncover hidden details in the chemical system with nonlinear dynamics, such as the phase transition phenomenon that occurs in complex oscillatory Briggs-Rauscher (BR) reaction. The presented potential of holography at the nanoscale could open enormous possibilities for controlling and molding the photophoretic effect and pattern formation for various applications such as particle trapping and levitation, including the movement of unburnt hydrocarbons in the atmosphere and separation of different aerosols, decomposition of microplastics and fractionation of particles in general, and assessment of temperature and thermal conductivity of micron-size fuel particles.

Introduction

To fully understand and notice all the unique phenomena in the nanoworld, it is crucial to employ techniques that are capable of revealing all details regarding structures and dynamics at the nanoscale. On this account, the unique combination of linear and nonlinear methods, combined with the power of holography to reveal the system's dynamics at the nanoscale are presented.

The described holographic technique can be viewed as the triple rec method (rec is the abbreviation for recording), since at a given time the signal is simultaneously recorded by a photographic camera, a thermal camera, and an interferometer. Linear and nonlinear optical spectroscopy and holography are well-known techniques, the fundamental principles of which are extensively described in the literature[1,2].

To cut a long story short, holographic interferometry allows the comparison of wavefronts recorded at different moments in time to characterize the dynamics of the system. It was previously used to measure vibrational dynamics[3,4]. The power of holography as the simplest interferometry method is based on its ability to detect the smallest displacement within the system. First, we exploited holography to observe and reveal the photophoretic effect[5] (i.e., the displacement of deformation of a nanostructure due to a light-induced thermal gradient), in different biological structures. For a true presentation of the method, representative samples were selected from a number of tested biological specimens[6]. Wings of the Queen of Spain fritillary butterfly, *Issoria lathonia* (Linnaeus, 1758; *I. lathonia*), were used in the framework of this study.

After having successfully demonstrated the occurrence of photophoresis at the nanoscale in biological tissues, a similar protocol was applied to monitor the spontaneous symmetry breaking process[7] caused by a phase transition in an oscillatory chemical reaction. In this part, the phase transition from a low concentration of iodide and iodine (called state I) to a high concentration of iodide and iodine with solid iodine formation (defined as state II) that occurs in a chemically nonlinear BR reaction was studied[8,9]. Here, we reported for the first time a holographic approach that allows studying such a phase transition and spontaneous symmetry breaking dynamics at the nanoscale occurring in condensed systems.

Protocol

1. Precharacterization

1. Perform a full precharacterization of the sample.
    1. Perform all experiments on dry specimens purchased from a commercial source. Store the samples in the laboratory, in a dry and dark place, at room temperature.
    2. Prior to holographic measurements, perform a complete sample characterization by scanning electronic microscope (SEM), linear optical spectroscopy, and nonlinear optical microscopy (NOM)[10] (**Figure 1**).
    3. In addition to the optical properties of samples measured by linear techniques, gather supplementary information with higher intensity laser beams that allow characterization of their nonlinear optical properties.
    4. Use the corresponding nonlinear optical susceptibilities to quantify the nonlinear optical response and form the basis of nonlinear optical techniques such as nondestructive multiphoton excitation fluorescence and second harmonic generation (SHG), which are used to characterize various biological samples.
    5. For the nonlinear chemical phenomena occurring in the oscillating BR reaction, carry out the study of interferometric monitoring of the *in situ* phase transition from state I to state II with the following concentrations of reactants: $[CH_2(COOH)_2]_0$ =

0.0789 mol dm^{-3}, $[MnSO_4]_0$ = 0.0075 mol dm^{-3}, $[HClO_4]_0$ = 0.03 mol dm^{-3}, $[KIO_3]_0$ = 0.0752 mol dm^{-3}, and $[H_2O_2]_0$ = 1.269 mol dm^{-3} (0 after the bracket stands for the initial concentration at the beginning of the process). Make the total volume used for the BR reaction equal to 2.5 mL.

NOTE: The concentration values used here are equal to the ones in the study by Pagnacco et al.[8], but with reaction volume divided by 10.

2. Prepare the sample for the experiment.

    1. Use wings of the Queen of Spain fritillary butterfly, *I. lathonia,* for this experiment. Place the wing on a hard surface and make a section with a 10 mm diameter cutter. Place the sample in the sample box, which can be any container with a lid.

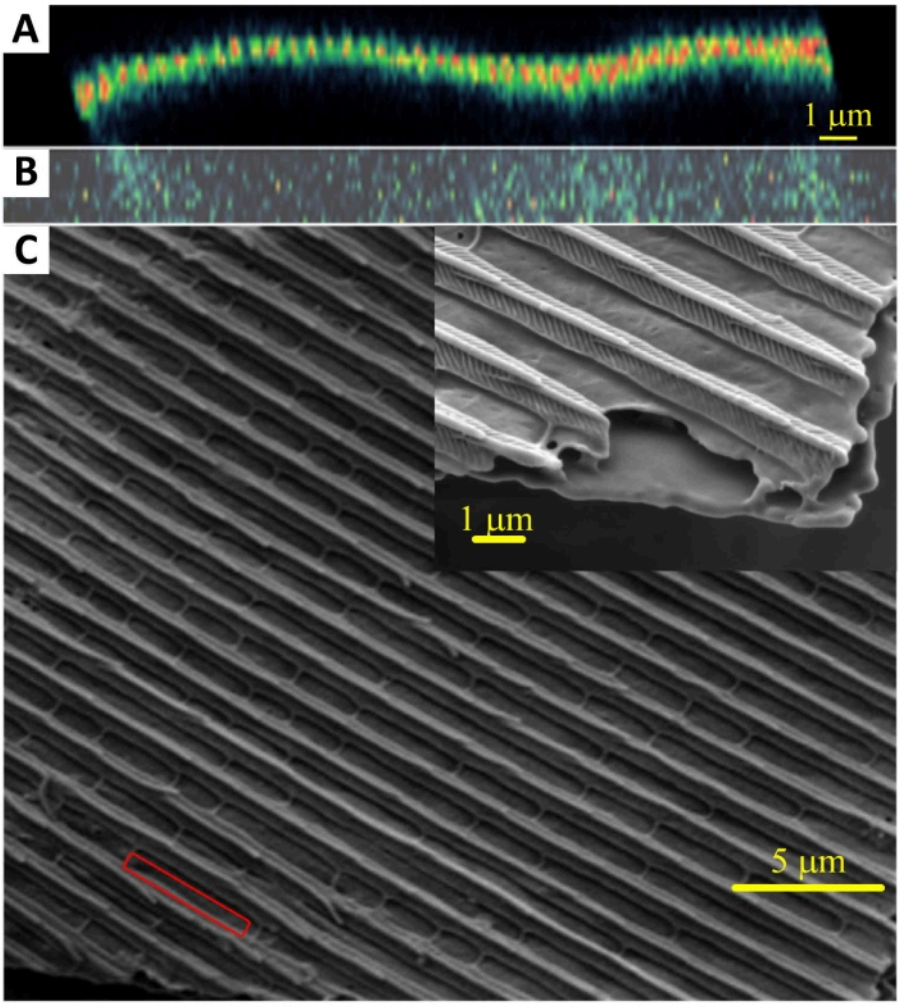

Figure 1: Wavy cross-section of butterfly wing scale. The cross-section was recorded on a nonlinear optical scanning microscope (**A,B**). A SEM observation (**C**) of a wing of the Queen of Spain fritillary butterfly, *I. lathonia*, was also done. This figure has been modified from[14]. Please click here to view a larger version of this figure.

2. Experimental setup

1. Holographic setup

   NOTE: The holographic interferometry measurements were performed with a tailor-made optical setup (**Figure 2**).

   1. Adjust the laboratory temperature to be 23 °C ± 0.2 °C. Turn the laser on. Use a laser (details given in the **Table of Materials**) with an excitation wavelength of 532 nm for these holographic observations.
   2. Check the alignment of the optical elements (**Figure 2**). First, check that setup is made according to the scheme in **Figure 2**.
   3. Align the laser beam perfectly with the concave mirror M. Check and adjust the position of the optical beam expander (L).
   4. Determine the beam part that impinges on sample S and ensure that it forms a reflex beam O. Check if the rest of the beam is collected on a spherical mirror CM, to be used to generate the reference beam R. Check if the detector C is placed within the interference zone of the two specified beams.

      NOTE: A complementary metal oxide semiconductor (CMOS) sensor is used as detector.
   5. Set up the cameras according to the instructions for the camera used. Set up an optical/photographic camera for the holographic experiment as shown in **Figure 2** (C is the camera; details given in the **Table of Materials**). Set up a second optical/photographic camera to view visible changes in BR reaction and a thermal camera with a thermal resolution of 50 mK and a focal length of 13 mm above the optical table.

      NOTE: The camera used in the holographic experiment does not use an objective lens; the light directly impinges on the chip.

2. Prepare the sample into holographic setup.

   1. Prepare the wing sample as in step 1.2.1. Place the prepared sample on a round metal support with a diameter of 15 mm. The support has three existing holes for the screws to which the metal ring holding the sample is attached.
   2. Attach the ring to the support. Place the attached sample in the part of the sample mount located on the optical table.
   3. Prepare the sample for chemical reaction monitoring. On the optical table, in the intended place, place a support with a flat adhesive surface on which the cuvette/vessel will be placed.
   4. Prepare the reagent used to initialize the reaction as in step 1.1.5. Fill the reactants into the cuvette, and mix in cuvette in the following order of volumes and concentrations: 0.7 mL of 0.2817 mol dm^{-3} $CH_2(COOH)_2$; 0.5 mL of 0.0375 mol dm^{-3} $MnSO_4$; 0.5 mL of 0.15 mol dm^{-3} $HClO_4$; 0.5 mL of 0.376 mol dm^{-3} KIO_3 ; and 0.3 mL of 10.575 mol dm^{-3} H_2O_2.
   5. Ensure that the total volume in the cuvette is 2.5 mL, and place it on the support in the setup.

6. Set up additional instruments if needed. For monitoring the photophoretic effect, use an additional laser (details given in **Table of Materials**) for local heating.

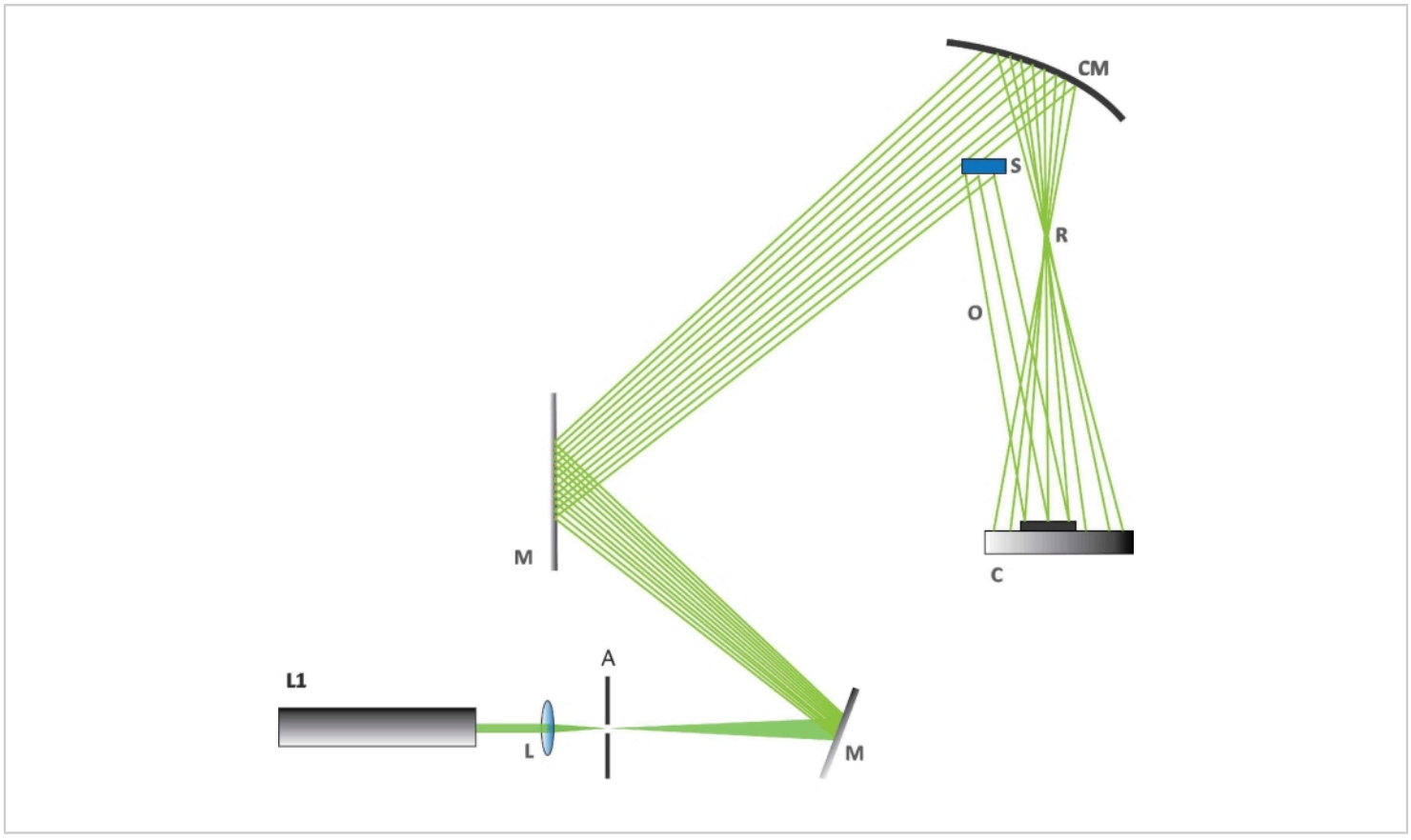

Figure 2: The holographic setup. The figure shows how the various components are arranged for the holographic experiment. Abbreviations: L1 = laser at 532 nm, L = biconvex lens, A = aperture, M = a flat mirror used to deflect the laser beam, CM = concave mirror, C = CMOS camera, S = butterfly wing section, R = reference beam, O = object beam. Please click here to view a larger version of this figure.

3. Setup of the software used

NOTE: Home-built C++ software based on Fresnel approximation[11] is used to analyze data from holographic experiments. The software developed for the presented study can be found at .[12] The details of software cannot be published at the moment; however, additional information will be provided on request. Fresnel approximation is extremely useful in digital holography since it focuses on different surfaces and zooms in on the area of the first diffraction order, which contains complete information about the recorded scene.

1. Turn on the computer and run the software.
   NOTE: The step for running the software depends on the software itself. There is no commercial software for this purpose.

4. Perform the experiment

1. Switch off the external lights. Carry out the whole experiment in a dark room.
2. Synchronize the cameras by using a chosen interval. For this experiment, start the holographic camera after 60 s, and the two other cameras immediately after it, using either a software or manually.
3. Press the recording buttons and define in the software when the recording starts.
4. Induce dynamical changes in the system of interest. The method of initiation depends on the type of sample; in the case of photophoretic effect, externally heat the sample by using the available lasers: 450 nm, 532 nm, 660 nm, 980 nm. In the case of the BR reaction, start the reaction by mixing the chemical reactants. Observe the holographic experiment.
5. Set the photographic and thermal camera to follow the whole experiment and determine the moment of the end of the holographic recording from the optical and thermal measurements.
6. Pronounce the end of the process. The end of the recording is preprogrammed, according to the estimated duration of the process. For the BR reaction, use solidification as the end of the reaction. In the case of the photophoretic effect, there is no such specific moment. In any case, this step emphasizes the importance of triple recording.

5. Acquisition of results[12]

1. Save the results. Precisely sort the files as a function of time for reconstructing holograms and deeper data analysis.

   NOTE: In this step, the data is transferred from the camera used for holography to the computer (hard disk) in folders named after the shooting dates. Use copy/paste and rename buttons.

2. Check the probe hologram for appropriate settings. In this way, the best settings are selected on the first hologram by looking at it, and then used for the reconstruction of all holograms.
   1. Choose one hologram by clicking on one of them from the folder you previously made (step 5.1) and make a reconstruction by clicking on the **Reconstruct** button.
   2. Change the settings to achieve the best image and make the reconstruction again. Options for adjusting parameters such as sampling, offset, and Fresnel distance will appear on the screen (software menu). Repeat these steps until the best settings are defined.
   3. Perform the reconstructions. Choose all the holograms by clicking the **Open File** button and choosing all files. Apply the desired parameters for numerical reconstruction of holograms; they remain unchanged after the step 5.2.1, so do not perform any action this time.
   4. Carry out the reconstructions using the **Reconstruct** button, and the interferograms by inserting the file names in the start with/end with field and then by clicking the button **Batch**. The interferograms appear in the previously made folder (in step 5.1).

      NOTE: After recording a series of holograms in time, the first hologram represents an unperturbed state, while the action of an external force causes subsequent holograms. It is necessary to

reconstruct the holograms using shifted Fresnel transform[13].

5. Obtain the interferograms by subtraction (in terms of complex numbers) of a particular hologram in time with the first hologram obtained.

   NOTE: This protocol allows observing the effect of the force on the object. The change in the interference pattern as a function of time is a consequence of deformation or displacement that occurs within the system during the measurement. These changes are used to monitor the system's dynamics at the nanoscale.

6. Analyses of the results

1. Perform a visual analysis as the first quality control step of the process. In this step, look for visible changes in interference pattern and try to match the changes in the interference pattern with results obtained by optical and thermal measurements.

2. Perform a cross-examination of all recordings. In this second phase of the analysis, thoroughly analyze the images visually from both the optical and thermal cameras with the holographic reconstructions in order to reveal dynamics at the nanoscale. In this way, the reaction moment is seen simultaneously in holographic, thermal, and photographic images.

3. Make a graphical representation of results based on numerical/software analysis and present them in the form of graphs (1D, 2D, or 3D), charts, histograms etc. After a complete analysis of results, draw conclusions and anticipate further research based on this.

Representative Results

A photophoretic effect was induced and monitored in a first experiment on the wing of a *Morpho menelaus* butterfly[5]. The effect was initiated by the action of LED lasers of different wavelengths (450 nm, 532 nm, 660 nm, and 980 nm). Here, the wings from an *I. lathonia* butterfly[14] were used. After the recording procedure, the hologram image was reconstructed.

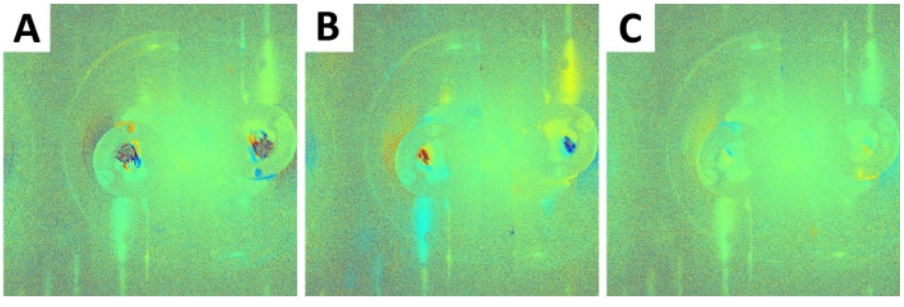

Figure 3: *I. lathonia* wings' holographic reconstructions. The reconstruction was done at 450 nm initiation (**A**), 532 nm initiation (**B**), and 980 nm initiation (**C**). The images show an obvious difference in the visual sense, where depending on the wavelength, the colored area appears in different sizes. Please click here to view a larger version of this figure.

The fringes observed in **Figure 3A-C** are the consequence of the interference. This figure clearly shows that changes occur only during the irradiation of the sample with a second laser (placed to hit the sample with a beam that does not interfere with the beam from the primary laser; put into operation at any time during the recording), and confirms that holographic interferometry can be used to monitor the deformation or displacement of the biological tissues.

Figure 3A-C shows how different wavelengths between 450 nm (**Figure 3A**), 532 nm (**Figure 3B**), and 980 nm (**Figure 3C**) affect the interferometric pattern by causing different morphological displacements within the tissues.

In the second experiment regarding the oscillatory BR reaction, this reaction started immediately after the addition of hydrogen peroxide, producing a large amount of oxygen (**Figure 4A**). As the transition from state I to state II (**Figure 4**) is essentially irreproducible for an individual kinetic run[8], the moment of transition is very difficult to monitor. Therefore, the presented results are the consequence of a large number of attempts. In the analysis of interferograms, a change in the fringe pattern was noticed at the exact moment when the reaction occurred (i.e., when transition from state I to state II occurred). **Figure 4E** shows a moment before the reaction occurred (left) and the exact moment (right). The wavelength used here is 573 nm. When calculating the displacement data from the amplitude image, the method of direct fringe counting was used. One fringe corresponds to a displacement of half the wavelength (i.e., 286.5 nm). If the displacement data is calculated from the phase, the following relation applies: $\Delta l/\lambda = \Delta\Phi/2\pi$.

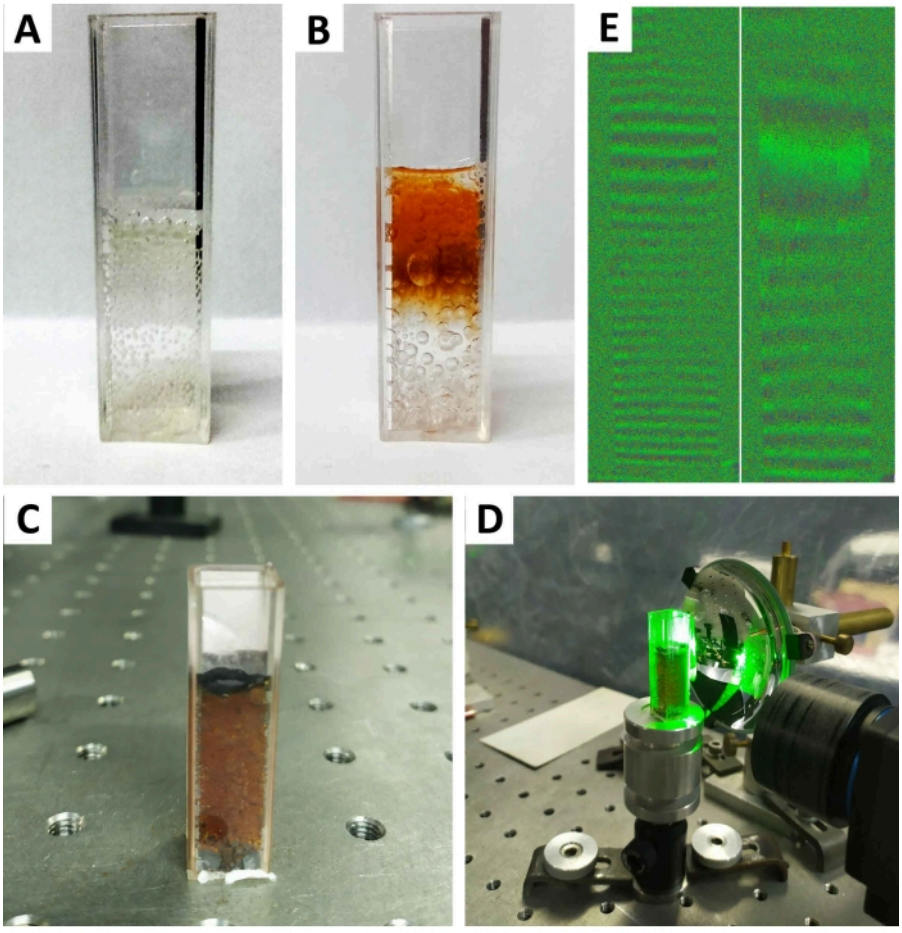

Figure 4: The transition from state I to state II in Briggs-Rauscher (BR) reaction. The different recordings for the transition from state I to state II in Briggs-Rauscher (BR) reaction. (**A**) The beginning of the BR reaction with bubbles corresponds to oxygen and carbon dioxide formation. (**B**) The state I to state II reaction course. (**C**) The end of state I to state II transition. (**D**) Cuvette in setup. (**E**) Interferogram of the moment before reaction (left) and the moment of reaction (right). Please click here to view a larger version of this figure.

Nonlinear chemical phenomena have been known for more than 100 years[15], but despite this, there are still doubts about their full mechanism and dynamics[16,17]. The results obtained open new possibilities for the investigation and monitoring of such complex chemical phenomena *in situ* by a holographic technique.

Discussion

In the presented biophotonic study, it is shown that a novel holographic method can be used to detect minimal morphological displacement or deformation caused by low-level thermal radiation.

The most critical step in holographic measurement with biological samples is the preparation step. The preparation

of the sample (cutting/gluing to match the size of the holder) depends on the sample's mechanical properties, and it is not possible to have a standard protocol for this step.

Regarding the BR study, it is vital to have a transparent reaction vessel and relatively clear optical path, since every obstacle during a chemical reaction, or physical transformation (like the release of oxygen, impurity) will affect interference pattern and therefore recorded results.

In general, the most significant limitation of the described method is the sample size that can be studied. The sample must have an appropriate dimension to be inserted within the optical setup.

Here we show that holographic interferometry (HI) should be considered as an essential complementary tool for the characterization of samples. For example, a classic optical/IR image captures information only regarding the intensity, while the information about the phase is totally lost[18]. Holographic interferometry provides all information regarding the intensity and phase, and additionally can be used to monitor their changes in real time.

The importance of exploiting this method in condensed matter science is to reveal *in situ* the slightest changes in system dynamics. For example, the BR reaction can reveal the first cause of the symmetry-breaking process. Is the symmetry-breaking process predetermined by physical constraints connected with nonlinear dynamics, or is the process truly random? On the other hand, in another way, can the minor differences in BR oscillatory period duration cause a significant deviation in transition appearance?

The presented results are the first step that will lead to a deeper understanding of dynamics at the nanoscale. Since the potential of holography in condensed science research has still not been fully recognized, the purpose of this article is to highlight the power of holography for future material science research and applications; for example, particle trapping and levitation such as movement of unburnt hydrocarbons in the atmosphere or separation of various aerosols[19], breaking down of microplastics in water and fractionation of particles in general[20], and characterisation of temperature and thermal conductivity properties of micron-size fuel particles[21].

Disclosures

The authors declare no conflict of interests.

Acknowledgments

M. S. P., D. G., D. V., and B. K. acknowledge support of the Biological and bioinspired structures for multispectral surveillance, funded by NATO SPS (NATO Science for Peace and Security) 2019-2022. B. K., D. V., B. B., D. G., and M. S. P. acknowledge funding provided bythe Institute of Physics Belgrade, through the institutional funding bythe Ministry of Education, Science, and Technological Development of theRepublic of Serbia. Additionally, B. K. acknowledges support from F R S - FNRS. M. P. acknowledges support from the Ministry of Education, Science and Technological Development of the Republic of Serbia, Contract number 451-03-9/2021-14/200026. S. R. M. was supported by a BEWARE Fellowship of the Walloon Region (Convention n °2110034), as a postdoctoral researcher. T. V. acknowledges financial support from the Hercules Foundation. D.V., M.S.P., D.G., M.P., B.B., and B.K. acknowledge the support of the Office of Naval Research Global through the Research Grant N62902-22-1-2024. This study was conducted in partial fulfillment of the requirements for the PhD degree of Marina

Simović Pavlović at the University of Belgrade, Faculty of Mechanical Engineering.

References

1. Pietrzyk, D. J., Frank, C. W. Development of an analytical method. *Analytical Chemistry.* 10-19 (1979).
2. Ostrovsky, Y. I., Shchepinov, V. P., Yakovlev, V. V. *Holographic Interferometry in Experimental Mechanics.* Volume 60. Springer (2013).
3. Pedrini, G., Osten, W., Gusev, M. E. High-speed digital holographic interferometry for vibration measurement. *Applied Optics.* **45** (15), 3456-3462 (2006).
4. Pantelić, D. V., Grujić, D. Ž., Vasiljević, D. M. Single-beam, dual-view digital holographic interferometry for biomechanical strain measurements of biological objects. *Journal of Biomedical Optics.* **19** (12), 127005 (2014).
5. Grujić, D. et al. Infrared camera on butterfly's wing. *Optics Express.* **26** (11), 14143-14158 (2018).
6. Mouchet, S. R., Deparis, O. *Natural Photonics and Bioinspiration.* Artech House (2021).
7. Pagnacco, M. C. et al. Spontaneous symmetry breaking: the case of crazy clock and beyond. *Symmetry.* **14**, 413 (2022).
8. Pagnacco, M. C., Maksimovic, J. P., Potkonjak, N. I., Božić, B. Đ., Horvath, A. K. Transition from low to high iodide and iodine concentration states in the Briggs-Rauscher reaction: evidence on crazy clock behavior. *The Journal of Physical Chemistry A.* **122** (2), 482-491 (2018).
9. Pagnacco, M. C., Maksimović, J. P., Janković, B. Ž. Analysis of transition from low to high iodide and iodine state in the Briggs-Rauscher oscillatory reaction containing malonic acid using Kolmogorov-Johnson-Mehl-Avrami (KJMA) theory. *Reaction Kinetics, Mechanisms and Catalysts.* **123** (1), 61-80 (2018).
10. Mouchet, S. R. et al. Unveiling the non-linear optical response of Trichtenotoma childreni longhorn bestle. *Journal of Biophotonics.* **12** (9), e201800470 (2019).
11. Shimobaba, T. et al. Computational wave optics library for C++: CWO++ library. *Computer Physics Communications.* **183** (5), 1124-1138 (2012).
12. Grujic, D. Application of digital holography for detection of infrared radiation on biophotonic structures. Ph. D. Thesis, Faculty of Physics, University of Belgrade, (2022); Available online after the Novembar (2022).
13. Muffoletto, R. P., Tyler, J. M., Tohline, J. E. Shifted Fresnel diffraction for computational holography. *Optical Express.* ***15*** .(9), 5631-5640 (2007).
14. Pavlović, D. et al. Naturally safe: Cellular noise for document security. *Journal of Biophotonics.* **12** (12), e201900218 (2019).
15. Bray, W. C. A periodic reaction inhomogeneous solution and its relation to catalysis. *Journal of the American Chemical Society.* **43** (6), 1262-1267 (1921).
16. Nicolis, G. Self-organization in nonequilibrium systems. *Dissipative Structures to Order through Fluctuations.* 339-426 (1977).
17. Prigogine, I., Hiebert, E. N. From being to becoming: Time and complexity in the physical sciences. *Physics Today.* **35** (1), 69 (1982).
18. Nikolova, L., Ramanujam, P. S. *Polarization Holography.* Cambridge University Press (2009).

19. Haisch, C., Kykal, C., Niessner, R. Photophoretic velocimetry for the characterization of aerosols. *Analytical Chemistry.* **80** (5), 1546-1551 (2008).

20. Kononenko, V. L., et al. Feasibility studies on photophoretic effects in field-flow fractionation of particles. *Journal of Liquid Chromatography & Related Technologies.* **20** (16-17), 2907-2929 (1997).

21. Zhang, X., Bar-Ziv, E. A novel approach to determine thermal conductivity of micron-sized fuel particles. *Combustion Science and Technology.* **130** (1-6), 79-95 (1997).

Airy beams propagation in optically induced photonic lattices

Bokić, Bojana, Diebel, Falko, Timotijević, Dejan, Piper, Aleksandra, Boguslawski, Martin, et al.

Bojana Bokić, Falko Diebel, Dejan Timotijević, Aleksandra Piper, Martin Boguslawski, Dragana Jović, Cornelia Denz, "Airy beams propagation in optically induced photonic lattices," Proc. SPIE 9136, Nonlinear Optics and Its Applications VIII; and Quantum Optics III, 91360S (1 May 2014); doi: 10.1117/12.2052272

SPIE.

Event: SPIE Photonics Europe, 2014, Brussels, Belgium

Airy beams propagation in optically induced photonic lattices

Bojana Bokić*[a], Falko Diebel[b], Dejan Timotijević[a], Aleksandra Piper[a], Martin Boguslawski[b], Dragana Jović[a] and Cornelia Denz[b]

[a]Institute of Physics, University of Belgrade, P.O. Box 68, 11001 Belgrade, Serbia;
[b]Institut für Angewandte Physik and Center for Nonlinear Science (CeNoS), Westfälische Wilhelms-Universität Münster, 48149 Münster, Germany

Abstract

We show both experimentally and numerically, control over the acceleration of two-dimensional Airy beam propagating in optically induced photonic lattice. Varying the lattice strength and including various defects we can reach a state, where the acceleration is completely stopped. We find an additional class of discrete lattice beams, localized and defect modes observed with Airy beams propagating in diamond optically induced photonic lattice.

Keywords: accelerating beams, photonic lattices, defects

1. INTRODUCTION

Airy beams are a well-known type of accelerating optical beams [1]. Unlike ordinary optical wave fields, Airy beams show an accelerated transverse intensity distribution which remains invariant along their parabolic trajectories [2]. Originally, Airy beams were introduced as wave functions solving the one-dimensional Schrödinger equation for free particles. Due to the equivalence between the Schrödinger equation in quantum mechanics and the paraxial equation of diffraction in optics these concepts can be transferred to optics. The ballistic-like properties of Airy beams qualify them for various applications ranging from particle trapping along curved paths [3] and self-bending plasma channels [4] to ultrafast self-accelerating pulses [5] and Airy light bullets accelerating in both transverse dimensions and in time [6]. Over the years, two-dimensional Airy beams have been systematically investigated, particularly in the field of optics and atom physics. In terms of experimental realization, optics provides a fertile ground to directly observe and study the properties of such non-spreading waves in detail. One of the features of these beams is their potential for applications in nonlinear optics: nonlinear interaction of light with some material and a study of accelerating beam dynamics inside nonlinear media. Formation of accelerating self-trapped optical beams has been proposed employing the different self-focusing nonlinearities, ranging from Kerr to quadratic nonlinearities, and also using an optically induced refractive-index potential [7, 8].

The key for the realization of all-optical guiding and switching architectures is control of the propagating light with light itself. Propagation dynamics of light is dramatically changed with the presence of photonic lattice. Recently, defect guiding Airy beams in optically induced waveguide arrays is studied [9]. The propagation of such accelerated beams inside a two-dimensional optically induced photonic lattice has not been observed yet.

We analyze theoretically and experimentally how an optically induced photonic lattice affects and modifies acceleration of Airy beams. Various conditions for the propagation and preservation of the Airy beam shape are considered. The acceleration of Airy beams is controlled by varying the lattice strength (refractive index modulation) and by introducing positive and negative single-side defects. We find that a modification of refractive index modulation leads to reduced Airy beam acceleration and formation of discrete lattice beams. However, inclusion of lattice defects changes the beam dynamics completely: with the negative defect Airy beams experience a strong repulsion, while in the presence of positive defect they form localized defect modes.

*bojana@ipb.ac.rs; phone +381 11 3713161; fax +381 113162190

Nonlinear Optics and Its Applications VIII; and Quantum Optics III, edited by Benjamin J. Eggleton, Alexander L. Gaeta, Neil G. R. Broderick, Alexander V. Sergienko, Arno Rauschenbeutel, Thomas Durt,
Proc. of SPIE Vol. 9136, 91360S · © 2014 SPIE · CCC code: 0277-786X/14/$18 · doi: 10.1117/12.2052272

2. THEORETICAL BACKGROUND AND EXPERIMENT

To study the propagation behavior of Airy beams in optical systems with induced photonic lattice, we start with considering the following scaled paraxial equation of diffraction for electric field Ψ

$$i\partial_\zeta \Psi + \frac{1}{2}(\partial_\chi^2 \Psi + \partial_\nu^2 \Psi) + \frac{1}{2} k_0^2 w_0^2 \Delta n^2 (\mathrm{I}_{indu}) \Psi = 0 \quad . \tag{1}$$

Here, $\chi=x/w_0$ and $\nu=y/w_0$ are dimensionless transverse coordinates scaled by the characteristic length w_0. $\zeta=z/kw_0^2$ represents the dimensionless propagation distance with $k=2\pi n/\lambda$. The photonic lattice enters this equation in terms of an intensity-dependent refractive index modulation Δn^2 (I_{indu}), which represents the optical induction process. This equation is also suitable to cover nonlinear light propagation in the case the inducting intensity becomes a function of field Ψ itself. In this contribution, however, we restrict ourselves to linear effects.

Considering the case for light propagation in homogenous, linear medium, where $\Delta n^2=0$ holds, the wave equation (1) can always be separated into two parts, each depending only on one transverse coordinate χ or ν, respectively. Therefore, the solution Ψ is also separated and can be written as a product in the following form: $\Psi(\chi,\nu,\zeta)=\Psi_1(\chi,\zeta)\Psi_2(\nu,\zeta)$. As firstly shown in [1] each part of the wave equation is fulfilled by a non-dispersive Airy solution. Thus, the overall solution of Eq. (1) reads as:

$$\Psi(\chi,\nu,\zeta) = \prod_{X=\{\chi,\nu\}} Ai(\mathrm{X} - (\zeta/2)^2) \exp(\mathrm{i}(\mathrm{X}\zeta/2) - \mathrm{i}(\zeta^3/12)) \quad . \tag{2}$$

We have to consider truncated solution with finite extent and energy, like $\Psi_\chi(\chi,0)=\mathrm{Ai}(\chi)\exp(a_\chi\chi)$, with the positive decay length a_χ, typically $a_\chi<<1$. It has been shown, that this kind of solution still solves the wave equation [1] and the distinguished properties of Airy beams are preserved. Although, the transverse intensity pattern is now non-spreading over a limited propagation distance, this easily covers the longitudinal range necessary to observe sufficient transverse displacement of the truncated Airy beams.

Our experimental setup for all measurements is sketched in Fig. 1(a). We use the beam from frequency-doubled, continuous wave laser ($Nd:YVO_4$) emitting at λ = 532 nm. The beam is split into two partial beams, each illuminating a high-resolution, programmable, phase-only spatial light modulator (SLM1, SLM2). The first one (SLM1), in combination with two lens and Fourier mask, is employed for making of nondiffracting induction beam. By using the calculated phase patterns, addressed to spatial light modulators, we modulate the phase and amplitude of incident plane wave and thereby obtain the complex field of desired nondiffracting induction beam. This modulated beam is then sent through the 20 mm long $Sr_{0.60}Ba_{0.40}Nb_2O_6$ (SBN:Ce) photorefractive crystal, externally biased with $E_{ext}\approx$2000 V/cm, an electric dc field. The induction beam is set to be ordinarily polarized with respect to the crystal's optical axis, to minimize the feedback of the written refractive index structure onto the induction beam itself. Because of the high polarization anisotropy of electro-optic coefficients of SBN:Ce crystal we are able to induce sufficient refractive index modulations to affect the propagation of extraordinarily polarized Airy beam. The Airy beam is made the same way as the nondiffracting induction beam by means of the second modulator (SLM2) and the encoded complex field, calculated in real space with the Eq. (2). To accurately overlay two beams in the crystal, we place a beam splitter directly in front of the SBN crystal. In addition, by illuminating the crystal homogeneously with white light, we can erase modulations of the written refractive index. With an imaging lens and a camera, mounted on a translation stage, we record the intensity distribution in different transverse planes.

The propagation characteristics of 2D Airy beam propagating in a homogeneous medium are shown experimentally in Fig. 1. The intensity distributions at the front and back face of the SBN:Ce crystal are shown in Fig. 1(b) and 1(c), respectively. To experimentally realize the photonic lattice which should control the propagation trajectory of Airy beam we use the technique of optical induction [10, 11]. Figure 1(d) shows the recorded intensity distribution of experimentally realized nondiffracting beam used to optically induce a two-dimensional square lattice. The lattice period $\Lambda=\pi/k_t\approx$25μm is chosen to match exactly the distance between the main and the first neighboring lobes of Airy beam.

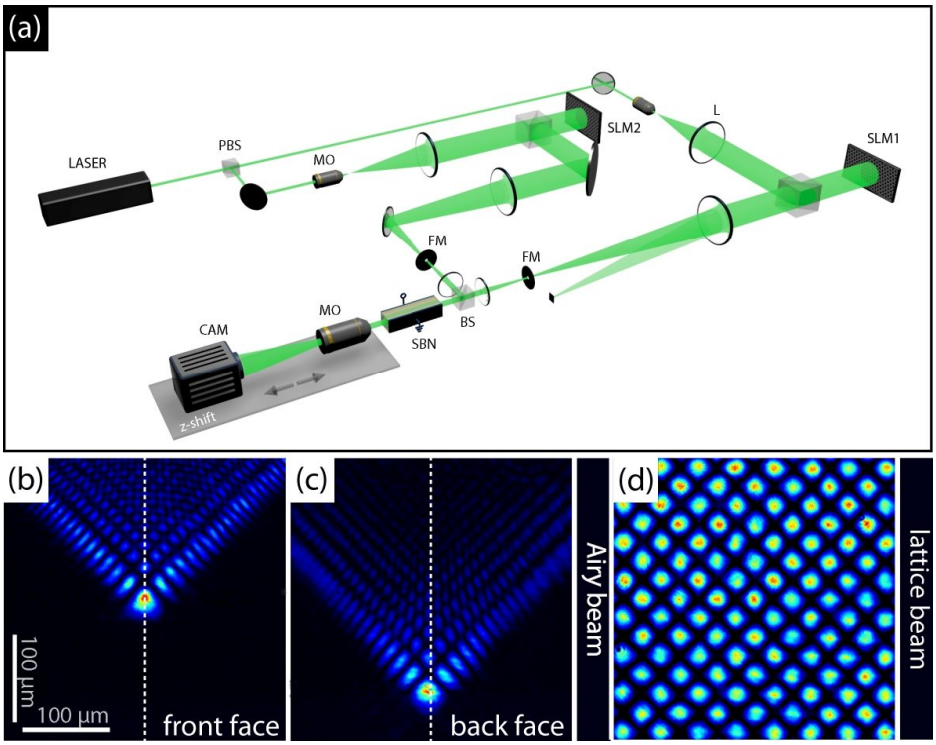

Figure 1. Experimental realization of two-dimensional Airy beams and photonic lattices. (a) Experimental setup. LASER: Nd:YVO_4 at λ = 532 nm, (P)BS: (polarizing) beam splitter, FM: Fourier mask, L: lens, MO: microscope objective, SBN: strontium barium niobate crystal, SLM1, SLM2: spatial light modulators. (b) Experimentally recorded intensity distribution of the Airy beam at the front face and (c) intensity distribution at the back face. (d) Lattice intensity distribution of the induced refractive index modulation.

We support our experiments with comprehensive numerical simulations by solving the paraxial wave equation (1), which models the light propagation in media with inhomogeneous refractive index modulations. The process of optical induction into a photorefractive material like SBN is represented by $\Delta n^2(I_{indu})$, which can be calculated in the full anisotropic model with a relaxation method. Since only linear effects are considered, the inducing intensity I_{indu} is solely given by the intensity of nondiffracting beam, $I_{indu}=|E_{ndB}|^2$ (cf. Eq. (3)). Even though the paraxial wave equation stays in the linear regime, it is not solvable analytically and we need to rely on proven beam propagation methods. The propagation equation (1) is solved numerically, using a split-step Fourier method described earlier in [12, 13].

3. CONTROL OF AIRY BEAM SELF-ACCELERATION WITH PHOTONIC LATTICES

Here, we observe the way that optically induced photonic lattice affects the acceleration of two-dimensional Airy beams. We have the self-bending of Airy beams on one side and the waveguiding and discrete diffraction effects of the photonic lattice on the other. By increasing the modulation of refractive index we affect the beam's acceleration and by increasing the lattice strength we affect the slowing down of the beam until we make it stops for a certain value.

In our investigation of propagation behavior of two-dimensional Airy beams in a regular photonic lattice, we are observing the influence of defect lattices as well. We consider single-site defect lattices with positive and negative variable defect strength.

Defect lattices are realized using the nondiffracting zero-order Bessel beam. We are increasing or decreasing the modulation of refractive index thus making a different defect lattices. We use the effective intensity distribution of incoherent superposition of two nondiffracting beams, the lattice beam and the Bessel beam, and make two-dimensional

defect lattice. Since we have incoherent superposition of the two nondiffracting beams we don't need to take care about the phase relation between them and potential unwanted intensity modulation in longitudinal direction. As shown earlier, this multiplexing method is suitable for fabrication of a whole set of different two-dimensional super and defect lattices, including negative defects [14]. For the realization of negative defect we apply the electric dc field, anti-parallel to the optical c-axis and obtain defocusing nonlinearity at the site where the Bessel beam is set to propagate.

Figure 2 illustrates the basic scheme of defect realization. The regular lattice is made by the intensity distribution shown in Fig. 2(a). Afterwards, the Bessel beam (Fig. 2(b)), illuminates the crystal and depending on the direction of applied electric field, the refractive index at one particular site gets increased or decreased. The resulting effective intensity distributions for the positive and negative defect lattices are shown in Fig. 2(c) and Fig. 2(d), respectively. Figures 2(e) and 2(f) show the numerically calculated refractive modulations for both defect lattices.

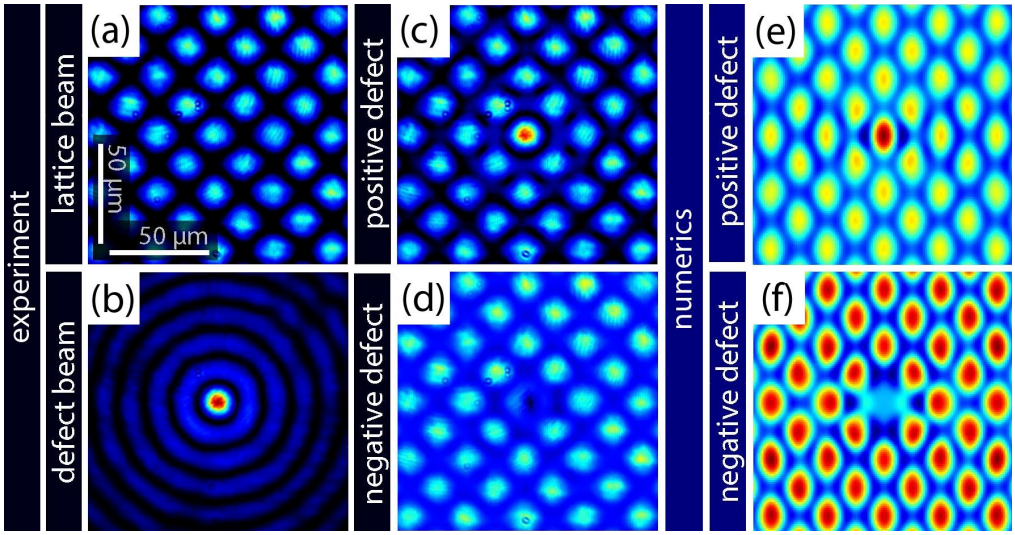

Figure 2. Defect generation in optically induced photonic lattice. (a) Experimental realization of the diamond lattice, (b) the Bessel beam, (c) the positive defect lattice and (d) the negative defect lattice. (e) Numerical realization of the positive and (f) negative lattice defects.

Figure 3 summarizes our numerical results regarding the propagation of Airy beam in regular photonic lattice as well as positive and negative defects. To get a more detailed insight into this propagation dynamics, we monitor the ratio between the power guided in the central waveguide and the total power of Airy beam as a function of the lattice strength and propagation distance. The numerical results for this power ratio are shown in Fig. 2(a) for a regular lattice, (d) negative defect and (g) positive defect. These graphs clearly demonstrates the impact of optically induced photonic lattice and apropriate defects on the formation of discrete structures, as well as suppression of the acceleration and bending of Airy beam. The Airy beam is launched into the induced photonic lattice with the main lobe exactly located at one lattice site. As the refractive index modulation strength grows, the interaction of Airy beam with lattice sites becomes stronger and consequently the bending of Airy beam is decreased. In the case of regular lattice, for higher refractive index modulations Δn, one can observe the localization of beam power to central waveguide at the back face of crystal. Our results clearly show the slowing down of the self-acceleration of Airy beam (Fig. 3(b),(c)). The corresponding intensity profiles at the back face are indicated with the letters at the respective positions. Depending on the different lattice strengths various kinds of discrete structures arises until the lattice finally suppress the acceleration of Airy beam. Most of the energy then stays in the lattice site, where the main lobe of Airy beam was initially launched.

Then we keep all parameters, but change the refractive index modulation Δn to both, positive and negative defects. The Airy beam is positioned with the main lobe exactly located at the defect site. For the different defects we record the intensity profiles of propagated Airy beam at the back face and monitor the percentage of power guided in the central waveguide, as described previously. Figures 3(d) and 3(g) show the numerical results of power ratio for the negative and

positive defect as a function of the propagation distance and refractive index modulation. The negative defect (Fig. 3(d)) significantly reduces the power guided in defect site and finally repels nearly all power, while the positive defect (Fig. 3(g)) strongly enhances the slowing-down and localization process of Airy beam. Corresponding intensity profiles are shown in the right panel of Fig. 3 for two values of Δn for the negative (e), (f) and positive defect (h), (i).

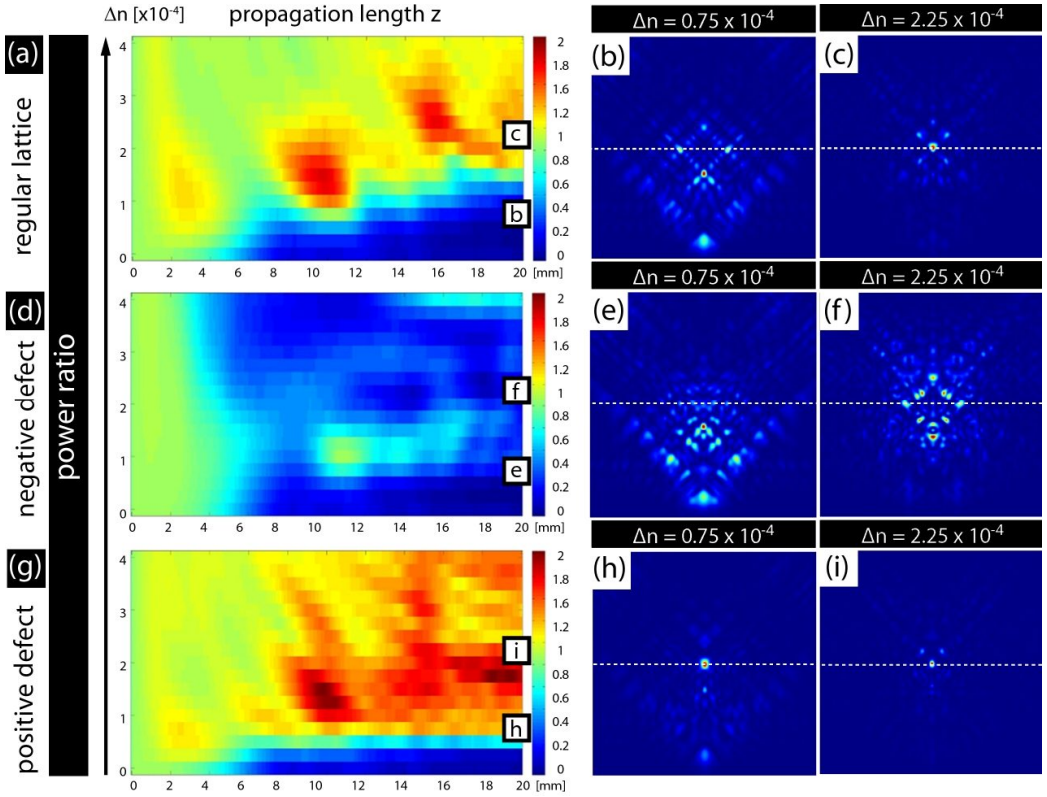

Figure 3. Airy beam propagation in diamond lattice, with and without defects. Dependence of the percentage of Airy beam power in the incident waveguide on refractive index change Δn and propagation length z for a (a) regular lattice, (d) negative defect and (g) positive defect. Numerical results for intensity distributions at the back face for different refractive index change Δn for: (b), (c) regular lattice, (e), (f) negative defect and (h), (i) positive defect.

To experimentally control the index modulation depth we take advantage of the time-dependent build up of induced lattice, which grows monotonously with the writing time. Because in experiments is not possible to record the intensity pattern inside the crystal, we are restricted to the profiles at the back face. In Fig. 4(d) the experimentally measured power ratio at the back face is plotted as a function of the refractive index modulation and defect strength. Therefore, we have repeated the experiments for 11 different defect strengths S_d = -1…1 and recorded the intensity profile at the back face. The modulus of defect strength S_d is given by the ratio of peak intensities of the discrete and the Bessel nondiffracting beam, while the sign is determined by the direction of applied electric field. These results illustrate the strong dependency of propagation and acceleration properties of Airy beam on the lattice depths, as well as the defect strength. The first and third row contains the experimental results – intensity distributions at the back face for two different values of Δn. The corresponding intensity profiles at the back face are indicated with the letters at the respective positions on graph, and presented in: (a), (e) for negative defect, (b), (f) regular lattice and (c), (g) positive defect. The experimental results fully agree with the theoretical analysis. Comparing the numerical intensity distributions of Airy beam at the back phase (Fig. 3) with corresponding experimental results (Fig. 4), one can see a very good qualitative agreement. Also, comparing the numerical graphs for percentage of Airy beam in incident waveguide for propagation distance of 20 mm with experimental graph in Fig. 4(d), very good agreement is observed for defect strength -1, 0 and +1, which corresponds to negative defect, regular lattice and positive defect, respectively.

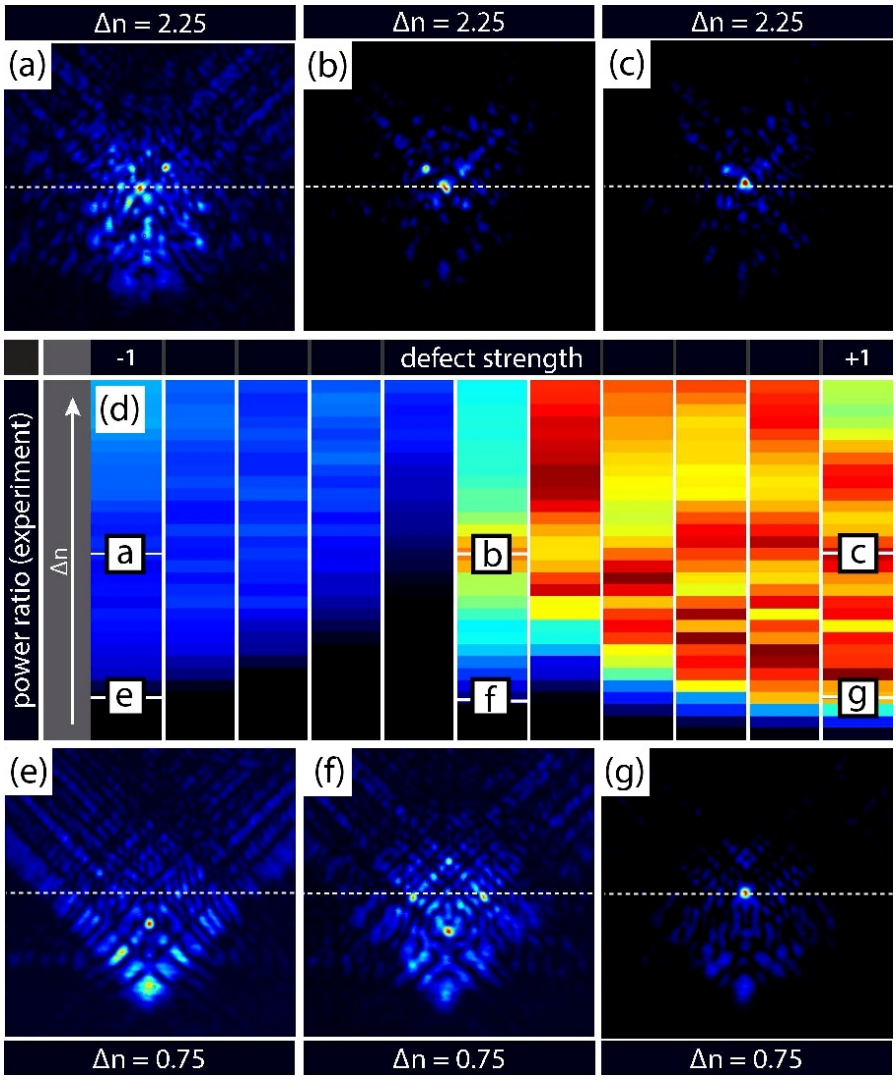

Figure 4. Experimentally observed Airy beam propagation in photonic lattice. (d) Percentage of the Airy beam power propagating in incident waveguide or defect site as a function of refractive index change Δn and defect strength. Exemplary experimental results of Airy beam intensity distribution at the back face for negative defect (a),(e), regular lattice (b),(f) and positive defect(c),(g).

4. CONCLUSIONS

In summary, we have shown, both theoretically and experimentally, that the propagation dynamics of two-dimensional Airy beams could be controlled by optically induced photonic lattices. We demonstrated a way to change the trajectory and shape of finite optical Airy beams. The results depend on the depth of the induced lattice which changes the acceleration and bending of Airy beam. The beam acceleration is slowed down and finally completely stopped for a certain amount of index modulation. Moreover, various single-side defects further affect the beam dynamics as well. By changing the defect strength, as well as the defect type, we can either increase the localization for positive defects, or repel all the power from a defect site, for the negative case. All our presented experimental results fully agree with the supporting numerical simulations.

Acknowledgements

This work is supported by the German Academic Exchange Service (Project 56267010) and Ministry of Education, Science and Technological Development, Republic of Serbia (Project OI 171036).

References

[1] Siviloglou, G. A., Broky, J., Dogariu, A. and Christodoulides, D. N.,"Observation of accelerating Airy beams," Phys. Rev. Lett. 99, 213901 (2007).
[2] Siviloglou, G. A., Broky, J., Dogariu, A. and Christodoulides, D. N., "Self-healing properties of optical Airy beams,"Opt. Lett. 33, 207 (2008).
[3] Baumgartl, J., Mazilu, M. and Dholakia, K., „Optically mediated particle clearing using Airy wavepackets," Nat. Photonics 2, 675–678 (2008).
[4] Polynkin, P., Kolesik, M., Moloney, J. V., Siviloglou, G. A. and Christodoulides, D. N.,"Curved plasma channel generation using ultraintense Airy beams,"Science 324, 229–232 (2009).
[5] Chong, A., Renninger, W. H., Christodoulides, D. N. and Wise, F. W.,"Airy–Bessel wave packets as versatile linear light bullets," Nat. Photonics 4, 103–106 (2010).
[6] Abdollahpour, D., Suntsov, S., Papazoglou, D. G. and Tzortzakis, S.,"Spatiotemporal Airy light bullets in the linear and nonlinear regimes," Phys. Rev. Lett. 105, 253901 (2010).
[7] Kaminer, I., Segev, M., and Christodoulides, D. N.,"Self-accelerating self-trapped optical beams," Phys. Rev. Lett. 106, 213903 (2011).
[8] Ye, Z., Liu, S., Lou, C., Zhang, P., Hu, Y., Song, D., Zhao, J. and Chen, Z., "Acceleration control of Airy beams with optically induced refractive-index gradient," Opt. Lett. 36, 3230 (2011).
[9] Lučić, N. M., Bokić, B. M., Grujić, D. Ž., Pantelić, D. V., Jelenković, B. M., Piper, A., Jović, D. M. and Timotijević, D. V., "Defect-guided Airy beams in optically induced waveguide arrays," Physical Review A 88, 063815(2013).
[10] Terhalle, B., Desyatnikov, A. S., Bersch, C., Träger, D., Tang, L., Imbrock, J., Kivshar, Y. S. and Denz, C., "Anisotropic photonic lattices and discrete solitons in photorefractive media," Applied Physics B 86, 399–405 (2006).
[11] Rose, P., Boguslawski, M. and Denz, C., "Nonlinear lattice structures based on families of complex nondiffracting beams," New Journal of Physics 14, 033018 (2012).
[12] Belić, M. R., Leonardy, J., Timotijević, D. and Kaiser, F., "Spatiotemporal effects in double phase conjugation," Journal of the Optical Society of America B 12, 1602 (1995).
[13] Belić, M., Petrović, M., Jović, D., Strinić, A., Arsenović, D., Motzek, K., Kaiser, F., Jander, P., Denz,C., Tlidi, M. and Mandel, P., "Transverse modulational instabilities of counterpropagating solitons in photorefractive crystals," Optics express 12, 708–16 (2004).
[14] Boguslawski, M., Kelberer, A., Rose, P. and Denz, C., "Multiplexing complex two-dimensional photonic superlattices," Optics Express 20, 27331–43 (2012).

UNIVERZITET U BEOGRADU
FIZIČKI FAKULTET

Bojana M. Bokić

DINAMIKA PROSTIRANJA EIRIJEVIH SNOPOVA U FOTOREFRAKTIVNIM SREDINAMA

doktorska disertacija

Beograd, 2021

UNIVERSITY OF BELGRADE
FACULTY OF PHYSICS

Bojana M. Bokić

DYNAMICS OF AIRY BEAMS PROPAGATION IN PHOTOREFRACTIVE MEDIA

Doctoral Dissertation

Belgrade, 2021

Mentor:

- **dr Branislav Jelenković**, naučni savetnik,
  Institut za fiziku, Univerzitet u Beogradu

Komentor:

- **dr Dragana Jović Savić**, naučni savetnik,
  Institut za fiziku, Univerzitet u Beogradu

Članovi komisije:

- **Prof. dr Bratislav Obradović**, redovni profesor,
  Fizički fakultet, Univerzitet u Beogradu
- **Prof. dr Đorđe Spasojević**, redovni profesor,
  Fizički fakultet, Univerzitet u Beogradu
- **Prof. dr Goran Poparić**, redovni profesor,
  Fizički fakultet, Univerzitet u Beogradu
- **dr Dragana Jović Savić**, naučni savetnik,
  Institut za fiziku, Univerzitet u Beogradu
- **dr Branko Kolarić**, naučni savetnik,
  Institut za fiziku, Univerzitet u Beogradu

Datum odbrane:

SPISAK RADOVA KORIŠĆENIH U DISERTACIJI

- Falko Diebel, **Bojana M. Bokić**, Martin Boguslawski, Aleksandra Piper, Dejan V. Timotijević, Dragana M. Jović, Cornelia Denz, „Control of Airy-beam self-acceleration by photonic lattices", Physical Review A **90**, br. 3, (2014).
- Falko Diebel, **Bojana M. Bokić**, Dejan V. Timotijević, Dragana M. Jović Savić, Cornelia Denz, "Soliton formation by decelerating interacting Airy beams", Optics Express **23**, br. 19, str. 24351-24361, (2015).

RADOVI KOJI NISU U VEZI SA DISERTACIJOM

- D. Pantelić, S. Ćurčić, S. Savić-Šević, A. Korać, A. Kovačević, B. Ćurčić, and **B. Bokić**, "High angular and spectral selectivity of purple emperor (Lepidoptera: *Apatura iris* and *A. ilia*) butterfly wings", Optics Express **19**, 5817, (2011).
- N. M. Lučić, **B. M. Bokić**, D. Ž. Grujić, D. V. Pantelić, B. M. Jelenković, A. Piper, D. M. Jović, D. V. Timotijević, "Defect-guided Airy beams in optically induced waveguide arrays", Physical Review A **88**, br. 6, (2013).
- A. G. Kovačević, S. M. Petrović, **B. M. Bokić**, B. M. Gaković, M. T. Bokorov, B. Z. Vasić, R. B. Gajić, M. S. Trtica, B. M. Jelenković, „Surface nanopatterning of Al/Ti multilayer thin films and Al single layer by a low-fluence UV femtosecond laser beam", Applied Surface Science **326**, str. 91-98, (2015).
- Monika M. Živković, Milesa Ž. Srećković, Tomislav M. Stojić, **Bojana M. Bokić**, "Influence of electromagnetic and nuclear radiation in medicine for therapy and diagnosis through processes, facts and statistical analysis", Nuclear Technology and Radiation Protection **32**, br.1, pp. 91-98, (2017).
- M. Remy, M. Cormann, W. Kubo, **B. Bokic**, Y. Caudano and B. Kolaric, „Transmission of entangled photons studied by quantum tomography: do we need plasmonic resonances?", Journal of Physics Communications **3**, 065011, (2019).
- D. Mara, F. Artizzu, J. Goura, M. Jayendran, **B. Bokić**, B. Kolaric, T. Verbiest and R. V. Deun, „Molecular dysprosium complexes for white-light and near-infrared emission controlled by the coordination environment", Journal of Luminescence **243**, 118646, (2022).

Sažetak disertacije

Tema ove teze je izučavanje fenomena koji su vezani za prostiranje dvodimenzionalnih Eirijevih svetlosnih snopova u nelinearnoj fotorefraktivnoj sredini. Istraživanje obuhvata proučavanje dinamike prostiranja više superponiranih dvodimenzionalnih Eirijevih snopova raspoređenih u simetrične konfiguracije od dva i četiri snopa, sa istim ili različitim faznim distribucijama, u linearnom i nelinearnom režimu kao i proučavanje prostiranja pojedinačnog dvodimenzionalnog Eirijevog snopa u optički indukovanoj kvadratnoj fotonskoj rešetci sa i bez optičkih defekata.

Disertacija je podeljena u sedam poglavlja, a sadržaj pojedinačnih poglavlja je dat u nastavku teksta.

U uvodnom poglavlju dat je pregled dosadašnjih rezultata u oblasti kompleksne svetlosti i nelinearne fotonike povezanih sa nedifragujućim snopovima uopšte a posebno u vezi sa samoubrzavajućim Eirijevim snopovima kao posebnom klasom nelinearno propagirajućih nedifragujućih snopova.

U drugom poglavlju opisan je detaljno koncept nedifragujućih snopova, a posebno klasa samoubrzavajućih Eirijevih snopova. Počevši od nedisperzivnog rešenja Šredingerove jednačine u domenu kvantne mehanike i analogije sa paraksijalnom talasnom jednačinom dolazi se do realizacije kvazi-nedifragujućih optičkih Eirijevih snopova u jednoj a zatim i u dve dimenzije.

U sledećem poglavlju opisan je koncept fotonskih struktura sa posebnim osvrtom na optički indukovane fotonske rešetke i tehniku optičke indukcije koja koristi koncept nedifragujućih snopova. Dat je i kratak uvid na značaj postojanja defekata u fotonskoj strukturi i mogućnosti koje nam takva struktura pruža za manipulaciju svetlošću, kao i metod multipleksiranja kojim se tehnikom optičke indukcije pomoću nekoherentne superpozicije više nedifragujućih snopova mogu realizovati optički defekti u dvodimenzionalnim optički indukovanim fotonskim rešetkama.

U četvrtom poglavlju prikazan je teorijski model za opisivanje i modelovanje propagacije dvodimenzionalnog Eirijevog snopa u nelinearnom materijalu. Teorijski model obuhvata propagaciju više Eirijevih snopova kroz nelinearni materijal kao i propagaciju pojedinačnog dvodimenzionalnog Eirijevog snopa kroz optički indukovanu kvadratnu fotonsku rešetku u nelinearnom materijalu. Ovo poglavlje sadrži i objašnjenje fotorefraktivnog efekta i modulacije indeksa prelamanja u fotorefraktivnom materijalu stroncijum barijum niobata (SBN). Nakon toga dat je detaljniji uvid u samu tehniku optičke indukcije i opisan numerički model za modelovanje linearnog i nelinearnog prostiranja Eirijevih snopova kroz SBN kristal sa i bez upisane fotonske strukture.

U petom poglavlju prikazane su eksperimentalne metode za ispitivanje dinamike prostiranja Eirijevog snopa u fotorefraktivnim sredinama. Poglavlje je podeljeno na dva dela. Prvi deo se odnosi na ispitivanje linearne i nelinearne interakcije više superponiranih dvodimenzionalnih Eirijevih snopova u fotorefraktivnom SBN kristalu. Drugi deo se odnosi na ispitivanje dinamike prostiranja jednog dvodimenzionalnog Eirijevog snopa kroz optički indukovanu fotonsku rešetku sa i bez defekata.

U šestom poglavlju prikazani su rezultati eksperimentalnog i teorijskog istraživanja. Ovo poglavlje je takođe podeljeno na više celina. U prvoj celini dati su rezultati linearne interakcije dva i četiri superponirana Eirijeva snopa. U slučaju linearne interakcije dva snopa kada su snopovi u fazi usled konstruktivne interferencije dolazi do formiranja fokusa u preseku trajektorija dva snopa. Kada snopovi nisu u fazi dolazi do vertikalne separacije uzrokovane destruktivnom

interferencijom. U oba slučaja mogu se jasno identifikovati parabolične trajektorije snopova. Kod ispitivanja linearne interakcije četiri superponirana Eirijeva snopa situacija je slična sa razlikom što ovde dolazi do formiranja jačeg fokusa jer je sada u pitanju interferencija četiri snopa. U drugoj celini dati su rezultati nelinearne interakcije dva i četiri superponirana Eirijeva snopa. U slučaju nelinearne interakcije povećavajući snagu probnog snopa možemo videti prelaz od linearne interferencione slike do dobro lokalizovanog solitarnog stanja za veće vrednosti nelinearnosti. U slučaju kada su faze snopova pomerene za π, ne dolazi do spajanja glavnih lobova već se usled destruktivne interferencije javljaju dva lokalizovana solitarna stanja. U slučaju nelinearne interakcije četiri snopa, kada su snopovi u fazi, situacija je ista kao i kod interakcije dva snopa. Situacija je totalno drugačija kada su snopovi pomerenih faza. Nasuprot ostalim slučajevima ovde ne dolazi do formiranja solitarnih stanja. Pošto su sva četiri snopa različitih faza u ovom slučaju ne dolazi do dovoljno velikog inteziteta koji bi usled interferencije mogao da formira solitarno stanje. Kod ispitivanja prostiranja pojedinačnog Eirijevog snopa u kristalu sa upisanom fotonskom rešetkom dobijeni su sledeći rezultati. Kako modulacija indeksa prelamanja rešetke raste interakcija Eirijevog snopa sa rešetkom postaje jača i kao posledica toga dolazi do usporavanja Eirijevog snopa. U zavisnosti od jačine rešetke javljaju se različite diskretne strukture sve dok sa pojačanjem rešetke ne dođe do kompletnog potiskivanja ubrzanja Eirijevog snopa. U slučaju defekata u jednom kanalu fotonske rešetke, situacija je sledeća. Jačina defekata kao i jačina fotonske rešetke dramatično utiču na oblik i transverzalno ubrzanje Eirijevog snopa. U slučaju pozitivnog defekta dolazi do povećanja lokalizacije u tom kanalu rešetke dok u slučaju negativnog defekta dolazi do delokalizacije polja Eirijevog snopa.

U poslednjem poglavlju sumirani su rezultati istraživanja i njihova potencijalna primena u drugim srodnim oblastima. Prikazana je prva eksperimentalna i numerička studija o nelinearnoj interakciji više dvodimenzionalnih Eirijevih snopova. Kao najvažniji rezultat, demonstrirana je izgradnja solitarnih struktura iz nelinearne interakcije više ubrzanih snopova. Ispitivanjem nelinearne dinamike superponiranih Eirijevih snopova za različite konfiguracije (broj snopova, fazne relacije), može se u zavisnosti od intenziteta demonstrirati formiranje pravolinijskih propagirajućih solitarnih stanja ili parova. Ovi eksperimentalni rezultati i metode omogućavaju dalje ispitivanje interakcije ostalih tipova nedifragujućih snopova i povrh toga nalaze primene u modernim optičkim arhitekturama za procesuiranje informacija. Takođe, u drugom delu disertacije, po prvi put je ispitivana i analizirana dinamika propagacije samoubrzavajućih dvodimenzionalnih Eirijevih snopova u dvodimenzionalnim fotonskim rešetkama uključujući defekte, teoretski i eksperimentalno. Ovi rezultati se takođe mogu generalizovati i na druge tipove optički indukovanih rešetki i tipove defekata, uključujući i nešto kompleksnije ili čak i trodimenzionalne rešetke. Isto tako, i druge klase samoubrzavajućih optičkih snopova se mogu kontrolisati koristeći prezentovane ideje i metode.

Ključne reči: Eirijevi snopovi, fotorefraktivni kristal, transverzalno ubrzanje, solitarna stanja, optički indukovane fotonske rešetke, optički indukovani defekti, protok energije, diskretna difrakcija, lokalizacija energije, delokalizacija energije.

Naučna oblast: Fotonika i laseri

Uža naučna oblast: Nelinearna fotonika

Abstract of dissertation

The main topic of this thesis is the study of phenomena related to the propagation of two-dimensional Airy light beams in a nonlinear photorefractive medium. The research includes the study of the propagation dynamics of several superimposed two-dimensional Airy beams arranged in symmetrical configurations of two and four beams, with the same or different phase distributions, in linear and nonlinear regime, as well as the study of the propagation of a single two-dimensional Airy beam in an optically induced square photonic lattice with and without optical defects.

The dissertation is divided into seven chapters, and the content of the individual chapters is given below.

The introductory chapter provides an overview of previous results in the field of complex light and nonlinear photonics related to non-diffracting beams in general and in relation to self-accelerating Airy beams as a special class of nonlinear propagating non-diffracting beams.

The second chapter describes in detail the concept of non-diffracting beams, and especially the class of self-accelerating Airy beams. Starting from the non-dispersive solution of the Schrödinger equation in the domain of quantum mechanics and analogy with the paraxial wave equation, the realization of quasi-non-diffracting optical Airy beams in one and then in two dimensions is realized.

The following chapter describes the concept of photonic structures with special reference to optically induced photonic lattices and the optical induction technique that uses the concept of non-diffracting beams. A brief insight is given into the importance of the existence of defects in the photonic structure and the possibilities that such a structure provides for light manipulation, as well as the multiplexing method by which optical defects can be realized in two-dimensional optically induced photonic lattices by incoherent superposition of several non-diffracting beams.

The fourth chapter presents a theoretical model for describing and modeling the propagation of a two-dimensional Airy beam in nonlinear material. The theoretical model includes the propagation of several Airy beams through a nonlinear material as well as the propagation of a two two-dimensional Airy beam through an optically induced square photonic lattice in a nonlinear material. This chapter also contains an explanation of the photorefractive effect and the modulation of the refractive index in the photorefractive material strontium barium niobate (SBN). After that, a more detailed insight into the optical induction technique itself is given and a numerical model for modeling the linear and nonlinear propagation of Airy beams through an SBN crystal with and without an inscribed photonic structure is described.

In the fifth chapter, experimental methods for examining the dynamics of Airy beam propagation in photorefractive media are presented. The chapter is divided into two parts. The first part deals with the investigation of the linear and nonlinear interaction of several superimposed two-dimensional Airy beams in a photorefractive SBN crystal. The second part refers to the investigation of the dynamics of propagation of a two - dimensional Airy beam through an optically induced photonic lattice with and without defects.

The sixth chapter presents the results of experimental and theoretical research. This chapter is also divided into several sections. In the first part, the results of the linear interaction of two and four superimposed Airy beams are given. In the case of linear interaction of two beams when the beams are in phase due to constructive interference, a focus is formed in the intersection of the trajectory of the two beams. When the beams are not in phase, vertical separation caused by destructive interference occurs. In both cases, parabolic beam trajectories can be clearly identified.

When examining the linear interaction of the four superimposed Airy beams, the situation is similar with the difference that a stronger focus is formed here because the interference of the four beams is now in question. In the second part, the results of nonlinear interaction of two and four superimposed Airy beams are given. In the case of a nonlinear interaction, increasing the strength of the probe beam, we can see the transition from a linear interference image to a well - localized solitary state for higher values of nonlinearity. In the case when the phases of the beams are shifted by π, the main lobes do not merge, but due to destructive interference, two localized solitary states occur. In the case of nonlinear interaction of four beams, when the beams are in phase, the situation is the same as in the interaction of two beams. The situation is totally different when the beams are shifted phases. In contrast to other cases, there is no formation of solitary states here. Since all four beams are of different phases, in this case there is not a large enough intensity that could form a solitary state due to the interference. When examining the propagation of a single Airy beam in a crystal with an inscribed photonic lattice, the following results were obtained. As the modulation of the lattice refractive index increases, the interaction of the Airy beam with the grid becomes stronger and as a consequence the Airy beam slows down. Depending on the strength of the lattice, different discrete structures appear until the acceleration of the Airy beam is completely suppressed with the reinforcement of the lattice. In the case of defects in one channel of the photonic lattice, the situation is as follows. The strength of the defects as well as the strength of the photonic lattice dramatically affects the shape and transverse acceleration of the Airy beam. In the case of a positive defect, there is an increase in the localization in that channel of the lattice, while in the case of a negative defect, there is a delocalization of the Airy beam field.

The last chapter summarizes the research results and their potential application in other related fields. The first experimental and numerical study on the nonlinear interaction of several two-dimensional Airy beams is presented. As the most important result, the construction of solitary structures from the nonlinear interaction of several accelerated beams is demonstrated. By examining the nonlinear dynamics of superimposed Airy beams for different configurations (number of beams, phase relations), the formation of rectilinear propagating solitary states or pairs can be demonstrated, depending on the intensity. These experimental results and methods enable further investigation of the interaction of other types of non - diffracting beams and, in addition, find applications in modern optical architectures for information processing. Also, in the second part of the dissertation, the dynamics of propagation of self - accelerating two - dimensional Airy beams in two - dimensional photonic lattices, including defects, is investigated and analyzed for the first time, theoretically and experimentally. These results can also be generalized to other types of optically induced lattices and types of defects, including somewhat more complex or even three-dimensional lattices. Likewise, other classes of self-accelerating optical beams can be controlled using the ideas and methods presented.

Keywords: Airy beams, photorefractive crystal, transverse acceleration, solitary states, optically induced photonic lattices, optically induced defects, energy flow, discrete diffraction, energy localization, energy delocalization.

Scientific field: Photonics and lasers

Research area: Nonlinear photonics

Ovim putem želim da iskažem zahvalnost svom mentoru, dr Branislavu Jelenkoviću, na rukovođenju mojom doktorskom disertacijom i, pre svega, pruženoj prilici da budem deo ovog zanimljivog istraživanja iz kojeg je ova disertacija proistekla.

Posebnu zahvalnost dugujem dr Dragani Jović Savić, mom komentoru i rukovodiocu projekta koji se bavio ovim istraživanjem. Bila mi je čast sarađivati sa njom kao jednim od vrhunskih stručnjaka iz oblasti nelinearne fotonike, zahvaljujem se na velikoj pomoći prilikom formiranja i izrade disertacije kao i korisnim savetima i sugestijama.

Zahvalnost dugujem i dr Branku Kolariću na pregledu i konsultacijama prilikom izrade disertacije kao i velikoj podršci u proteklom periodu.

Zahvaljujem se i profesorima dr Bratislavu Obradoviću, dr Đorđu Spasojeviću i dr Goranu Popariću na pregledu i oceni ove doktorske disertacije

Najveću zahvalnost dugujem svojoj porodici na velikom razumevanju i podršci.

Bojana Bokić

Sadržaj

Poglavlje 1

Uvod i motivacija

Svetlost na jedinstveni način povezuje infinitno sa infinitezimalnim, prenoseći istovremeno informacije o beskrajno velikim galaktičkim strukturama i događajima koji su se desili posle *Velikog praska* [1] kao i informacije iz mikro i nano sveta, sveta atoma, molekula i kristala [2]. Integracija tih infomacija dovela je do koherentnog opisa interakcija između polja i materije, interakcija koje opisuju veliki deo nama poznate fizike i hemije.

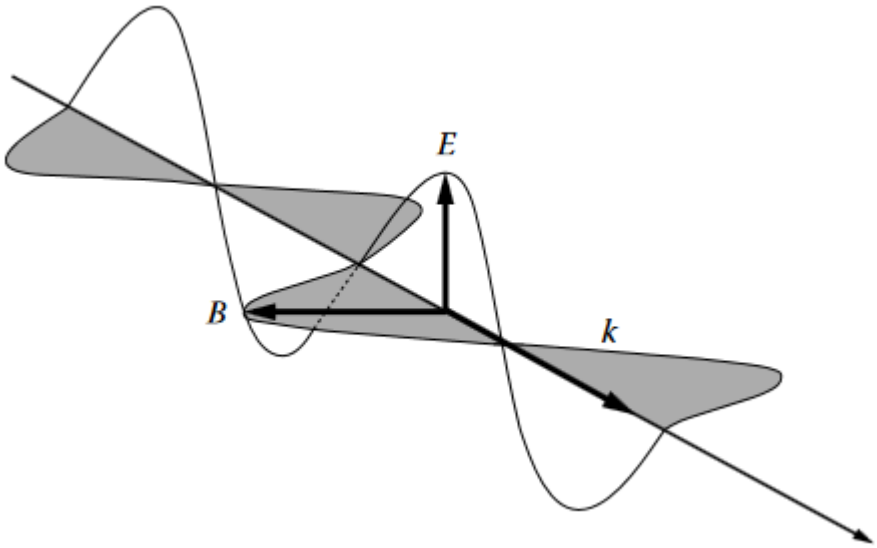

Slika 1.1 Šema elektromagnetnog talasa. [3]

Svetlost najčešće opisujemo kao vektor elektromagnetnog polja koji ima svoj intenzitet i pravac prostiranja (polarizaciju), frekvenciju i brzinu (Slika 1.1). Interakcija svetlosti sa materijom dovodi do difrakcije, refleksije, apsorpcije i disperzije, pojava koje su dobro poznate vekovima i prepoznate kao ključni elementi u umetnosti (Slika 1.2) ili kao ključni a nekada i ograničavajući faktori u mnogim modernim industrijskim i tehnološkim aplikacijama zasnovanim na kontroli elektromagnetnih talasa [4]. Uz pomoć svetlosti, otkriveno je i opisano mnoštvo fizičkih pojava, od optičke komunikacije visokog propusnog opsega do polarizovanih sunčanih naočara, fotosinteze u biljkama do primarnih molekulskih procesa kod čula vida.

Difrakcija (interakcija svetlosti sa materijom/preprekom) modifikuje prostiranje svetlosnog talasa. Interakcija sa materijom povezana je i sa disperzijom koja je posledica zavisnosti indeksa

prelamanja materijala od frekvencije i koja dovodi do toga da se svaka spektralna komponenta prostire različitom faznom brzinom [5].

Poznato je da difrakcija i disperzija mogu biti ozbiljno ograničenje za primene u kojima je veoma poželjno da snop ili impuls zadrži svoju transverzalnu lokalizaciju i/ili širinu u vremenu tokom propagacije [6-11]. Kao posledica toga, razvoj metoda kojima bi se ublažili efekti degradacije signala izazvane od strane ova dva efekta je od presudnog značaja.

Slika 1.2. *Likurgov pehar* (Iz doba starog Rima IV vek). Pehar od stakla sa primesama nanočestica zlata i kalaja (tehnologija razvijena u Antičkom Rimu) nije samo umetnički predmet već i objekat koji pokazuje složenost interakcije svetlosti sa materijom. Kada se posmatra u reflektovanom svetlu, na primer na dnevnom svetlu, izgleda zeleno. Međutim, kada se svetlo ubaci u šolju i prenese kroz staklo, pehar izgleda crveno. [12]

Laseri kao izvori koherentnog zračenja doveli su do revolucije u modernoj tehnologiji od hemije do optike. Prostiranje laserskih snopova predmet je aktivnog istraživanja već više od 50 godina, ali je tek pre nešto više od 20 godina doživelo značajan pomak sa razvojem novih metoda za opisivanje i karakterizaciju laserskih zraka. Paralelno, tehnike oblikovanja laserskog snopa napredovale su zbog povećane snage računara i mogućnosti izrade difrakcionih optičkih elemenata standardnim litografskim tehnikama. Poslednjih godina oblikovanje laserskih snopova je dodatno napredovalo zahvaljujući primeni tehnologije na bazi tečnih kristala [13]. Takva tehnologija omogućila je stvaranje laserskih snopova specifične strukture pomoću kompleksne modulacije svetlosti. Istraživanja su dovela do novih otkrića o laserskim snopovima i njihovim svojstvima prostiranja, uključujući orbitalni ugaoni momenat svetlosti, nedifrakcionu prirodu svetlosti, svetlost koja se prostire zakrivljenim putevima i rekonstruiše nakon prepreka [14]. Takvi laserski snopovi primenjeni su u mnogim disciplinama, od fizike do biologije, od klasičnih do kvantnih studija.

Novi pravac istraživanja, takozvano polje kompleksne (ili strukturirane) svetlosti, opisuje apstraktna topološka svojstva svetlosti - tj. snopove posebno dizajniranog intenziteta, polarizacije i faze - i upravo ta svojstva uvode renesansu u mnogim oblastima optičke nauke i tehnologije i predstavljaju centralnu tačku za fundamentalne proboje u optici. Napredak u fundamentalnom razumevanju, zajedno sa najnovijim dostignućima u proizvodnji svetlosti kompleksne strukture, translira se i na niz različitih i interdisciplinarnih primena koje obuhvataju mikroskopiju [15,16], komunikaciju sa velikim brzinama prenosa podataka [17], optičko zarobljavanje [18] i kvantnu optiku [19]. Može se očekivati i više primena u budućnosti, jer istraživači nastoje da manipulišu i kontrolišu brzinu prostiranja kompleksnih svetlosnih snopova, a javljaju se i egzotičnije mogućnosti koje pruža kompleksna svetlost u eksperimentima kvantnih uvezanih stanja.

Lokalizovani talasni paketi, poznati i kao nedifragujući talasi, nastali su u početku kao pokušaj da se dobiju snopovi i impulsi sposobni da se odupru difrakciji u slobodnom prostoru na velikim udaljenostima. Takvi talasi su u početku dobijeni teoretski kao rešenja talasne jednačine početkom 1940-ih [20], a eksperimentalno su demonstrirani 1987. [21]. Danas, lokalizovani talasi predstavljaju

rastuću i dinamičnu oblast istraživanja, ne samo u vezi sa nedisperzivnim slobodnim prostorom (ili vakuumom), već i za disperzivne, nelinearne i medije bez gubitaka.

Najpoznatiji talasni paket bez difrakcije je Beselov snop koji su prvi uveli J. Durnin i saradnici [21,22]. Ovaj pionirski rad otvorio je put otkriću drugih nedifragujuíh rešenja [23], uključujući Matjeove i parabolične Veberove snopove, kao i Matjeove i Beselove snopove viših redova.

U poslednje vreme, samoubrzavajući talasni paketi koji se mogu prostirati po zakrivljenoj putanji privukli su veliko interesovanje. Među njima, posebno Eirijev snop (ili impuls) (Slika 1.3), koji se prostire duž parabolične putanje bez ikakve difrakcije (ili disperzije) [24,25]. Za razliku od konvencionalnog laserskog snopa koji se prostire po pravoj liniji, Eirijev snop koji sam ubrzava ima karakteristiku da prati zakrivljenu putanju u linearnom homogenom medijumu, čime se uvodi pojam transverzalnog ubrzanja. Za razliku od drugih nedifragujućih snopova, Eirijev talasni paket takođe može postojati i u jednoj dimenziji.

Eirijevi snopovi predstavljaju prvu eksperimentalno proučavanu klasu samoubrzavajućih optičkih talasa. Teorija Eirijevih snopova je razvijena na osnovu geometrijske optike i morfologije kaustičnih površina određenih na osnovu bifurkacione teorije dinamičkih sistema, poznate kao teorija katastrofe [26,27]. Kaustična površina, na koju su zraci fokusirani, je envelopa familije parcijalnih zraka i ona predstavlja sam Eirijev snop. Kaustične površine su zakrivljene čak iako su zraci pravolinijski. Kaustična površina opisana Eirijevom funkcijom (Slika 1.3a) jedna je od sedam elementarnih prirodnih katastrofa – tzv. „nabor“ katastrofa (*engl.* ***fold catastrophy***) opisana potencijalom $V(x) = \frac{1}{3}x^3 - ax$.

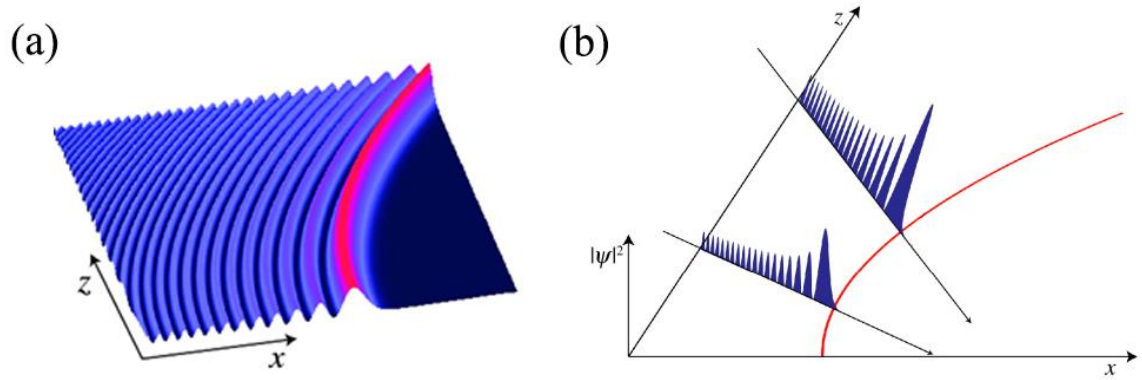

Slika 1.3 (a) Primer dinamike jednodimenzionalnog nedifragujućeg Eirijevog snopa [28]; **(b)** Prikaz osobine samoubrzavanja Eirijevog snopa duž parabolične trajektorije [28].

Treba naglasiti da se Eirijevi snopovi prvi put pojavljuju u domenu kvantne mehanike 1979. kao nedisperzivno rešenje Šredingerove jednačine koja opisuje kretanje slobodne čestice konačne mase [40]. Analogija između Šredingerove jednačine i paraksijalne talasne jednačine bila je inspiracija za dobijanje optičkih Eirijevih snopova, koji su eksperimentalno realizovani prvi put tek 2007. godine [41].

Ono zbog čega su posebno zanimljivi su njihove specifične osobine: nedifragujući su snopovi, kreću se po zakrivljenoj paraboličnoj putanji, tj. imaju sposobnost samoubrzanja u transverzalnoj ravni prostiranja kao i mogućnost samorekonstrukcije ukoliko naiđu na prepreku. Otkriće optičkih Eirijevih snopova otvorilo je široko polje istraživanja njihovih potencijalnih primena u različitim oblastima fizike, teoretski i eksperimentalno [29-31], počevši od mikromanipulacije česticama i ćelijama, kao optički raspršivači [32], laserske mikroobrade materijala [33], optičkih rutera [34], autofokusirajućih snopova [35], pa do ultrabrzih samoubrzavajućih impulsa [36].

Glavni cilj ove disertacije je izučavanje propagacije i lokalizacije dvodimenzionalnih Eirijevih snopova u fotorefraktivnim sredinama, da se sagleda u kojoj meri možemo da kontrolišemo prostiranje nedifragujućeg Eirijevog snopa radi potencijalne buduće primene u naprednim optičkim i informacionim tehnologijama.

Od svoje prve demonstracije, raste interesovanje za Eirijeve snopove i njihove moguće primene. Poznato je da je kontrolisanje osobina prostiranja svetlosti samom svetlošću ključna za realizaciju naprednih potpuno optičkih tehnologija. Postoji mnogo načina koji se mogu koristiti kako bi se one unapredile. Jedan od obećavajućih pristupa ovom cilju koji se predlaže u ovoj disertaciji jeste primena Eirijevih snopova i mogućnost da se modulacijom transverzalnog ubrzanja Eirijevih snopova kontroliše prostiranje svetlosti u fotorefraktivnom materijalu. U ovom istraživanju to je rađeno na dva načina.

Jedan od njih se zasniva na formiranju optičkih solitona [37], koji predstavljaju lokalizovane strukture koje održavaju svoj oblik balansirajući između efekata difrakcije i nelinearnog samofokusiranja. Ideja i motivacija u ovoj disertaciji je bila da se koherentnom superpozicijom više Eirijevih snopova modulišu njihova transverzalna ubrzanja tako da dođe do formiranja solitona ili solitarnih struktura. U ovom delu disertacije je rađeno ispitivanje i analiza linearne i nelinearne interakcije dva i četiri dvodimenzionalna Eirijeva snopa u nelinearnom materijalu, kao i potencijalne primene dobijenih efekata.

Drugi način je kontrolisanje prostiranja Eirijevih svetlosnih snopova pomoću fotonskih rešetki. Poznato je da prisustvo diskretnih fotonskih struktura u fotorefraktivnom materijalu dramatično menja dinamiku propagacije svetlosti [38]. Zato, jedan od obećavajućih pristupa ovom cilju jeste mogućnost modulisanja transverzalnog ubrzanja Eirijevih snopova koristeći fotonske rešetke. Fotonske rešetke su jedan od načina realizacije fotonskih kristala i predstavljaju optičke talasovode sa periodičnom promenom indeksa prelamanja sredine u kojima se fotoni ponašaju poput elektrona u poluprovodniku. Zbog svojih osobina pogodan su optički sistem za manipulaciju i kontrolu prostiranja svetlosti. Fotonske rešetke se mogu kreirati modulacijom indeksa prelamanja sredine što uključuje direktno lasersko upisivanje, optičku litografiju ili tehniku bušenja. Veoma praktična metoda je tehnika optičke indukcije [39] u fotorefraktivnom materijalu korišćenjem nedifragujućih zraka, koja stvara trajne, reverzibilne fotonske strukture reprezentovane profilom intenziteta nedifragujućeg svetlosnog polja. U drugom delu disertacije rađeno je ispitivanje i analiza dinamike prostiranja dvodimenzionalnih Eirijevih snopova u optički indukovanoj fotonskoj rešetci sa i bez različitih optičkih defekata, kao i ispitivanje njihove postojanosti u funkciji od modulacije indeksa prelamanja fotonske rešetke.

Poglavlje 2

Nedifragujući snopovi

U ovom poglavlju dat je pregled naučnog koncepta nedifragujućih snopova sa posebnim akcentom na nelinerno propagirajuće Eirijeve snopove, u oblasti kvantne mehanike gde su se prvobitno pojavili a kasnije i u optici, gde su sa izvesnim modifikacijama idealnih Eirijevih snopova realizovani kvazi-nedifragujući Eirijevi svetlosni snopovi. Na kraju su predstavljeni dvodimenzionalni optički Eirijevi snopovi koji predstavljaju glavni predmet istraživanja prikazanog u ovoj doktorskoj disertaciji.

2.1 Koncept nedifragujućih snopova

Polazna tačka za proučavanje "nedifragujućih" snopova (pri čemu razlikujemo linearno i nelinearno propagirajuće) je skalarna Helmholcova jednačina:

$$\frac{\partial^2 u}{\partial x^2}+\frac{\partial^2 u}{\partial y^2}+\frac{\partial^2 u}{\partial z^2}+\frac{\omega^2}{c^2}u=0 \tag{2.1}$$

Ova jednačina opisuje prostiranje monohromatskih talasa, gde je *c* brzina talasa, *ω* monohromatska ugaona frekvencija posmatranog talasa i *u* jedna od komponenti elektromagnetnog polja.

Prvo je opisan slučaj ***linearno propagirajućih nedifragujućih snopova*** i specifična forma te vrste svetlosnih snopova. Radi praktičnosti, za smer prostiranja bira se z-osa. U ovom slučaju, linearno polarizovana svetlost duž *x*-smera se može opisati postavljanjem da je $u = E_x$.

Rešenje Helmholcove jednačine je ravanski talas

$$u(x,y,z)=e^{-ik_z z-ik_t(x\cos(\phi)+y\sin(\phi))} \tag{2.2}$$

pod uslovom da je $\omega^2 = c^2k^2 = c^2k_z^2 + c^2k_t^2$ uslov ispunjen. Ovde, k_z predstavlja aksijalnu komponentu talasnog vektora dok k_t odgovara transverzalnoj komponenti talasnog vektora. Azimutalni ugao ϕ definiše ugao ravanskog talasa u odnosu na z-osu. Razmatraju se superpozicije više ravanskih talasa od kojih svi imaju isti aksijalni talasni vektor. Ova superpozicija definiše "nedifragujuće" snopove koji se mogu opisati preko Vitakerovog integrala

$$u(x,\psi,z)=e^{-ik_z z}\int_0^{2\pi} d\phi g(\phi)e^{-ik_t(x\cos(\phi)+y\sin(\phi))} \tag{2.3}$$

gde kompleksna funkcija $g(\phi)$ definiše fazu i amplitudu različitih ravanskih talasa koji formiraju određeni "nedifragujući" snop.

Vitakerov integral ima sledeću interpretaciju. "Nedifragujući" snop je određen superpozicijom višestrukih ravanskih talasa čiji se transverzalni vektori k_t nalaze na kružnici. Bilo koja kompleksna funkcija $g(\phi)$ definiše nedifragujući snop, međutim, samo za određene funkcije $g(\phi)$ se Vitakerov integral može opisati analitički.

U zavisnosti od koordinatnog sistema u kojima su opisani, postoje generalno četiri familije nedifragujućih snopova [42]. Prvu familiju predstavljaju snopovi opisani u Dekartovom koordinatnom sistemu, koji se nazivaju ravni talasi. U cilindričnom koordinatnom sistemu su opisani Beselovi snopovi (Slika 2.1a), u eliptično-cilindričnom Matjeovi (Slika 2.1b) a u parabolično-cilindričnom koordinatnom sistemu Veberovi snopovi (Slika 2.1c). Pored nedifragujućeg karaktera, ovi snopovi se odlikuju i svojom robusnošću i sposobnošću samorekonstrukcije.

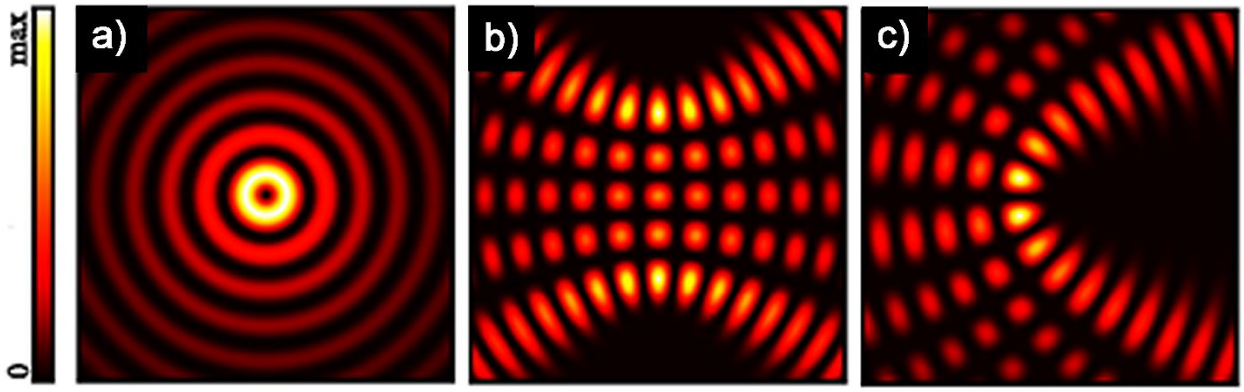

Slika 2.1. Primeri **a)** Beselovog, **b)** Matjeovog, i **c)** Veberovog nedifragujućeg snopa [42].

2.1.1 Eirijeva funkcija i samoubrzavajući talasni paketi

Nelinearno propagirajući "nedifragujući" snopovi, koji se još nazivaju ubrzavajući ili samoubrzavajući nedifragujući snopovi, su takođe rešenja paraksijalne Helmholcove jednačine (2.1) koja uzimaju u obzir sporo promenljiva rešenja prostiranja u jednom pravcu. To su snopovi koji se prostiru duž parabolične putanje. Ako nam je z-osa pravac prostiranja onda imamo sledeći izraz

$$\frac{\partial^2 u}{\partial x^2} + \frac{\partial^2 u}{\partial y^2} + 2ik\frac{\partial u}{\partial z} = 0 \tag{2.4}$$

gde k predstavlja dužinu talasnog vektora i $u(x, y, z)$ sporo promenljivu envelopu nosećeg talasa $exp\,(i(\omega t - kz))$. Birajući $x - z$ ravan za ravan formiranja nelinearno ubrzavajuće parabolične trajektorije, može se definisati nedifragujuće rešenje integrala u formi

$$u(x,y,z) = \int_{-\infty}^{\infty} dk_y Ai\left(\frac{x}{x_0} + x_0^2 k_y^2 - \frac{z^2}{4k^2 x_0^4}\right) g(k_y) e^{-ik_y\gamma + \frac{ixz}{(2kx_0^3)} - \frac{iz^3}{(12k^3 x_0^6)}} \tag{2.5}$$

gde $Ai(x)$ predstavlja Eirijevu funkciju, x_0 karakterističnu skalu dužine koja daje transverzalno ubrzanje snopa i $g(k_y)$ koje predstavlja bilo koju kompleksnu funkciju. Ako ova funkcija ima Dirakovu distribuciju $g(k_y) = \delta(k_y)$ dobija se standardni Eirijev snop (Slika 2.2) dok se za sve ostale varijante dobijaju daleko komplikovaniji snopovi: pri čemu svi ti snopovi predstavljaju nedifragujuće snopove koji se kreću paraboličnom putanjom. Integral (2.5) ima sličnu interpretaciju kao Vitakerov integral. Ovde, integral unosi lateralni pomeraj definisan izrazom $\delta_x = -x_0^3 k_y^2$. Ovaj pomeraj, zajedno sa izrazom za relativnu fazu i amplitudu $g(k_y)e^{-ik_y Y}$ definiše iskošene Eirijeve snopove koji imaju identično ubrzanje i interferiraju na isti način duž parabolične putanje. Ovaj argument je identičan onom argumentu u slučaju Vitakerovog integrala koji opisuje linearno propagirajuće nedifragujuće snopove.

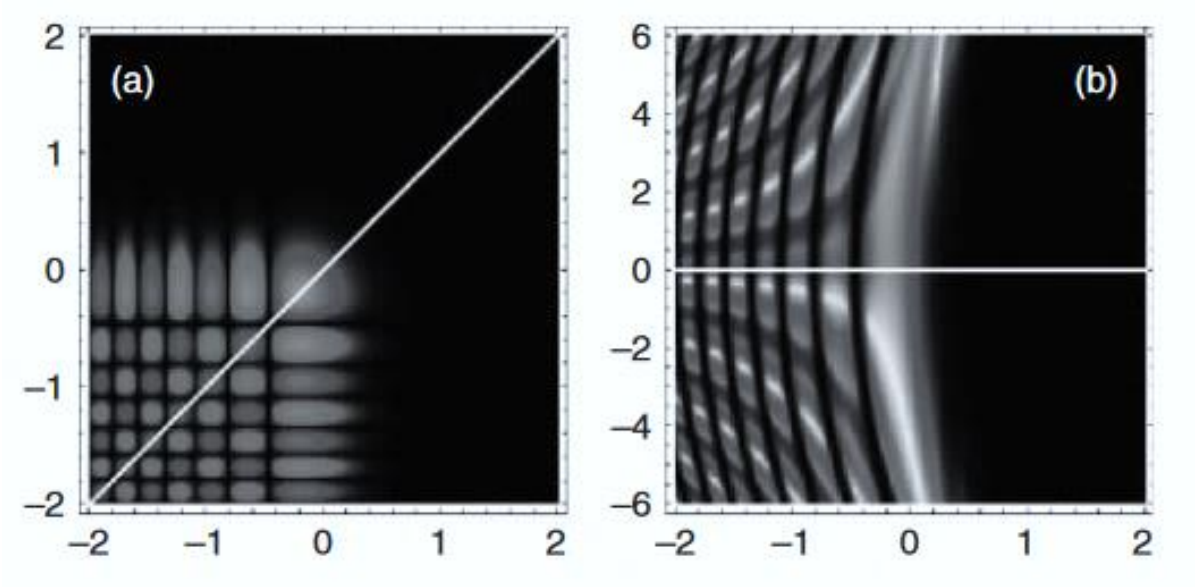

Slika 2.2 (a) Transverzalni i **(b)** longitudinalni poprečni presek Eirijevog snopa. [43]

2.2 Idealni Eirijev snop beskonačne energije

Eirijeve funkcije, u obliku talasnog rešenja, se prvi put pojavljuju 1979. u radu Berija i Balaža [40], koji su pokazali da jednodimenzionalna Šredingerova jednačina (2.6), koja opisuje kretanje slobodne čestice, mase *m*, ima nedisperzivno rešenje u formi idealne Eirijeve funkcije (2.7),

$$-\frac{\hbar^2}{2m}\frac{\partial^2\psi}{\partial x^2} = i\hbar\frac{\partial\psi}{\partial t} \tag{2.6}$$

$$\psi(x,t) = Ai\left[\frac{B}{\hbar^{2/3}}\left(x - \frac{B^3t^2}{4m^2}\right)\right] e^{\left(\frac{iB^3t}{2m\hbar}\right)\left[x - \left(\frac{B^3t^2}{6m^2}\right)\right]} \tag{2.7}$$

gde je *x* – prostorna koordinata, *t* - vreme, *m* – masa slobodne čestice, $\hbar$ - redukovana Plankova konstanta, *Ai* – Eirijeva funkcija, *B* – konstanta veća od nule. Takvo rešenje predstavljalo je talasni paket koji ima osobinu da ne menja svoj oblik u transverzalnoj ravni i da se kreće po zakrivljenoj

putanji, tj. da ubrzava. Izraz „samoubrzavajući“ korišćen je iz razloga što takav talasni paket ima osobinu ubrzanja bez prisustva spoljašnjeg potencijala.

Za realizaciju optičkih Eirijevih snopova, istraživači [41] su iskoristili korespondenciju između kvantno-mehaničke Šredingerove jednačine i paraksijalne talasne jednačine koja se koristi u optici.

Analiza počinje od normalizovane jednodimenzionalne paraksijalne Helmholcove jednačine koja opisuje dinamiku prostiranja envelope električnog polja $\varphi(s,\xi) = E(s,\xi)$ optičkog snopa:

$$i\frac{\partial\varphi}{\partial\xi} + \frac{1}{2}\frac{\partial^2\varphi}{\partial s^2} = 0 \tag{2.8}$$

gde $s = x/x_0$ i $\xi = z/k_0 n_0 x_0^2$ označavaju normalizovane transverzalne i longitudinalne koordinate, k_0 je talasni broj u vakuumu, i x_0 arbitrarna skala dužine. Ova jednačina pretpostavlja da je ugao između ose prostiranja i talasnih vektora dovoljno mali da talas ne odstupa značajno od njega. Rešenje jednačine (2.8) je nedifragujući Eirijev snop [40, 41]:

$$\varphi(s,\xi) = Ai\left[s - \frac{\xi^2}{4}\right] exp\left(is\frac{\xi}{2}\right) exp\left(-i\frac{\xi^3}{12}\right) \tag{2.9}$$

gde Ai označava Eirijevu funkciju [44] a $\varphi(s,0) = Ai(s)$ envelopu električnog polja na početku ($\xi = 0$). Jednačina (2.9) pokazuje da je rešenje u obliku Eirijeve funkcije bez difrakcije, i da se kod njega javlja transverzalni pomeraj duž parabolične krive ($s = \xi^2/4$) tokom prostiranja (Slika 2.3a). Idealni Eirijev snop karakteriše asimetrični profil amplitude, formiran od značajno intenzivnijeg glavnog loba i oscilirajućeg repa sastavljenog od sublobova čije vrednosti amplitude opadaju veoma sporo za negativne vrednosti *s*, (tj. $Ai(-s) \approx \pi^{-1/2}s^{-1/4}sin\left(2/3s^{3/2} + \pi/4\right)$ za s $\rightarrow+\infty$) [44].

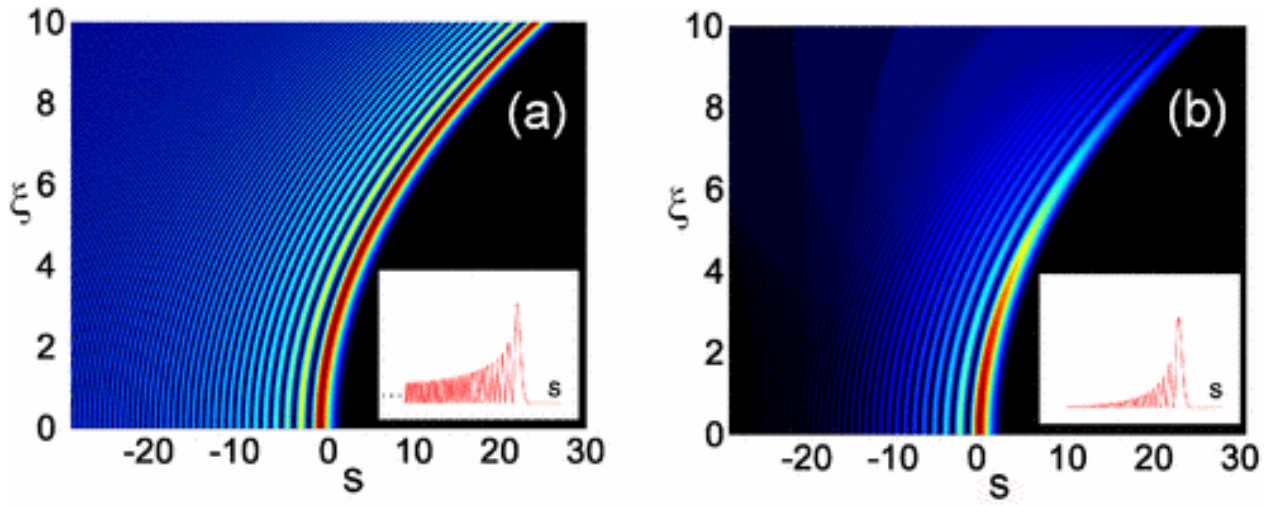

Slika 2.3 Dinamika propagacije Eirijevog snopa. Prostorna evolucija intenziteta Eirijevog snopa **(a)** beskonačne energije, i **(b)** konačne energije. Crvenom bojom je prikazan odgovarajući profil intenziteta na ulazu. [53]

Za pozitivne vrednosti *s*, Eirijevo rešenje opada eksponencijalno. Interpretacija procesa nelinearnog ili ubrzanog prostiranja je objašnjena od strane D. Greenberger-a preko principa ekvivalencije [45]. Ostala fizička objašnjenja se odnose na poreklo zakrivljenog prostiranja kao posledice interferencije pravolinijskih parcijalnih zraka u kaustičnu površinu [46-50]. Osobina prostiranja bez difrakcije je esencijalno povezana sa činjenicom da ovakav profil snopa (Slika 2.3a)

poseduje beskonačnu energiju. Zapravo, Eirijev snop nije kvadratno integrabilan ($\int_{-\infty}^{+\infty} |Ai(s)|^2 ds \rightarrow +\infty$), i kao posledica toga ne može mu se definisati centar mase. Ovo znači da se samoubrzanje ne suprotstavlja Erenfestovoj teoremi [51], koja opisuje kretanje centra mase. U praksi, "idealni" Eirijev snop je nemoguće eksperimentalno realizovati, pošto bi to zahtevalo neograničenu količinu energije. Eirijev snop je ipak moguće sintetizovati pomoću korišćenja funkcije koja bi predstavljala neki vid aperture i tako omogućila realizaciju Eirijevog snopa konačne energije (Slika 2.3b) [24-25,52].

2.3 Optički Eirijev snop konačne energije

Kao što je već pomenuto, jedini način dobijanja Eirijevog snopa konačne energije je uvođenjem funkcije eksponencijalne aperture na ulazu u sistem [41,53]:

$$\varphi(s,0) = Ai\,(s) exp\,(\alpha s) \tag{2.10}$$

gde $\alpha > 0$ predstavlja faktor trunkacije/zarubljivanja (Slika 2.4a).

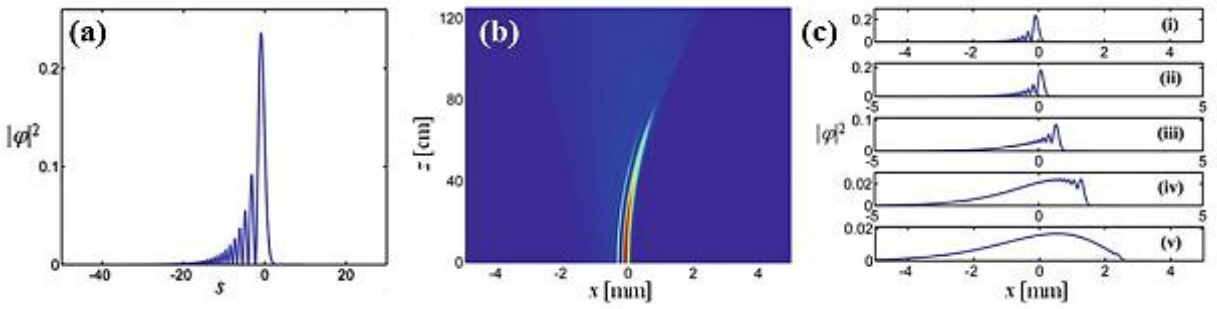

Slika 2.4 Dinamika propagacije Eirijevog snopa konačne energije. **(a)** Profil intenziteta snopa kao funkcija normalizovane transverzalne koordinate *s*. **(b)** Distribucija intenziteta Eirijevog snopa konačne energije. **(c)** Profili intenziteta Eirijevog snopa kao funkcija transverzalne koordinate *x* na selektovanim dužinama propagacije *z* ((i) z = 0 cm, (ii) 31.4 cm, (iii) 62.8 cm, (iv) 94.3 cm, i (v) 125.7cm). [41]

Rešenje jednačine (2.5) sa početnim uslovima jednačine (2.10) je sledeći izraz:

$$\varphi(s,\xi) = Ai\left[s - \frac{\xi^2}{4} + i\alpha\xi\right] exp\left(\alpha s - \alpha\frac{\xi^2}{2}\right) exp\left(-i\frac{\xi^3}{12} + i\alpha^2\frac{\xi}{2} + is\frac{\xi}{2}\right) \tag{2.11}$$

koji može da se redukuje na idealni slučaj kada je $\alpha = 0$. Za razliku od idealnog slučaja, ukupna snaga koju nosi ovaj zarubljeni Eirijev snop ima konačnu vrednost koja zavisi od parametra α na sledeći način:

$$\int_{-\infty}^{+\infty} |Ai(s) exp\,(\alpha s)|^2 ds = \sqrt{\frac{1}{8\pi\alpha}}\, exp\left(\frac{2\alpha^3}{3}\right) \tag{2.12}$$

I pored inicijalne eksponencijalne aperture, ovakav Eirijev snop konačne energije i dalje poseduje osobine idealnog Eirijevog snopa. Nastoji da samoubrzava duž iste parabolične trajektorije sa kvazi-nedifragujućim prostiranjem.

2.3.1 Dvodimenzionalni Eirijev snop konačne energije

Rezultati dobijeni za jednodimenzionalne Eirijeve snopove su lako generalizovani i na dve dimenzije. U ovom slučaju, rešenje se nalazi rešavanjem normalizovane dvodimenzionalne paraksijalne jednačine:

$$i\frac{\partial\hat{\varphi}}{\partial\xi}+\frac{1}{2}\frac{\partial^2\hat{\varphi}}{\partial s_x^2}+\frac{1}{2}\frac{\partial^2\hat{\varphi}}{\partial s_y^2}=0 \tag{2.13}$$

gde $\hat{\varphi}(s_x,s_y,\xi)$ predstavlja envelopu električnog polja, $s_x=x/w_0$ i $s_y=y/w_0$ su, respektivno, normalizovane transverzalne koordinate (sa w_0 faktorom skaliranja) duž x i y pravaca, i $\xi=z/k_0n_0x_0^2$ označava normalizovanu longitudinalnu koordinatu. α_x i α_y su parametri trunkacije duž x i y. Lak način za pronalaženje dvodimenzionalnog Eirijevog snopa se dobija proizvodom dva jednodimenzionalna Eirijeva snopa, respektivno duž *x* i *y* pravaca na sledeći način:

$$\hat{\varphi}(s_x,s_y,0)=Ai(s_x)Ai(s_y)exp\,(\alpha_x s_x)exp\,(\alpha_y s_y) \tag{2.14}$$

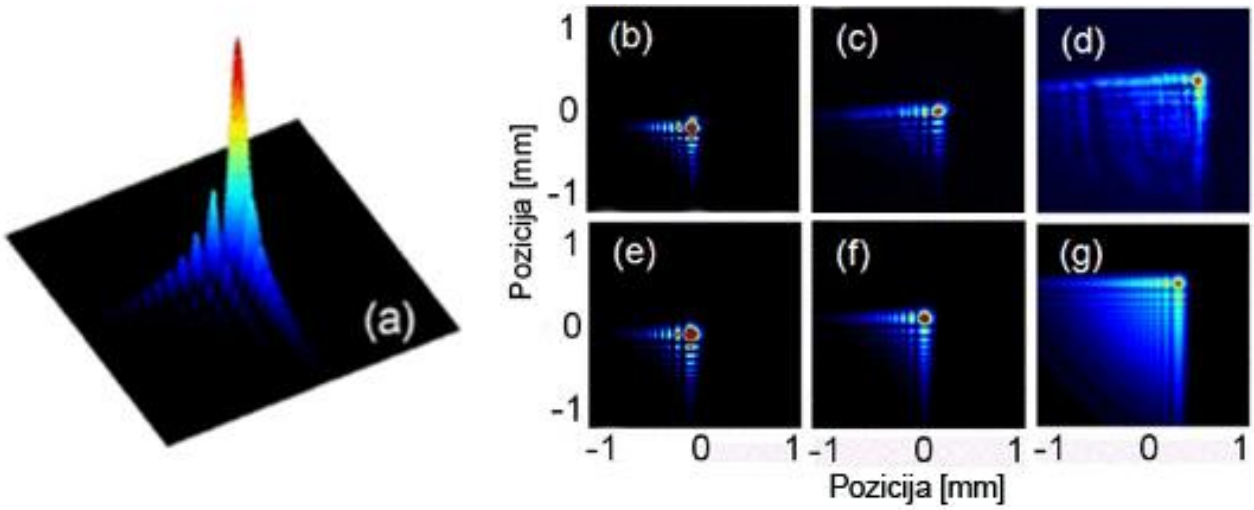

Slika 2.5 Dinamika propagacije dvodimenzionalnog Eirijevog snopa konačne energije. **(a)** Šematski prikaz dvodimenzionalnog Eirijevog paketa. Distribucija transverzalnog intenziteta dvodimenzionalnog Eirijev snopa konačne energije na rastojanju od **(b)** z = 0 cm, **(c)** z = 10 cm, i **(d)** z = 20 cm. Odgovarajući teoretski prikaz za ista rastojanja, **(e)** z = 0 cm, **(f)** z = 10 cm, i **(g)** z = 20 cm. [53]

Evolucija dvodimenzionalnog Eirijevog snopa prikazana je sledećim izrazom:

$$\hat{\varphi}(s_x,s_y,\xi)=\varphi(s_x,\xi)\varphi(s_y,\xi) \tag{2.15}$$

gde $\varphi(s_i, \xi)$ $(i = x \text{ ili } y)$ predstavljaju jednodimenzionalne profile električnog polja (2.11). Ovaj dvodimenzionalni Eirijev snop ima asimetrični profil intenziteta sastavljen od visoko-konfinirane tačke glavnog loba u $(x - y)$ ravni, i dva dugačka repa (Slika 2.5).

Pored ove analitičke i numeričke studije, eksperimentalno je demonstrirana i prva generacija optičkih Eirijevih snopova koristeći pristup pomoću Furijeove transformacije [54], ilustrovan na Slici 2.6a. Ovaj metod se zasnivao na osobinama Furijeovog prostornog spektra Eirijevog snopa, opisanim izrazom (2.10):

$$\Phi(k, 0) = exp\,(\alpha k^2) exp\left(\frac{i}{3}(k^3 - 3\alpha^2 k - i\alpha^3)\right) \tag{2.16}$$

Ovakav spektar poseduje amplitudu Gausovog snopa i uključuje i kubnu spektralnu fazu.

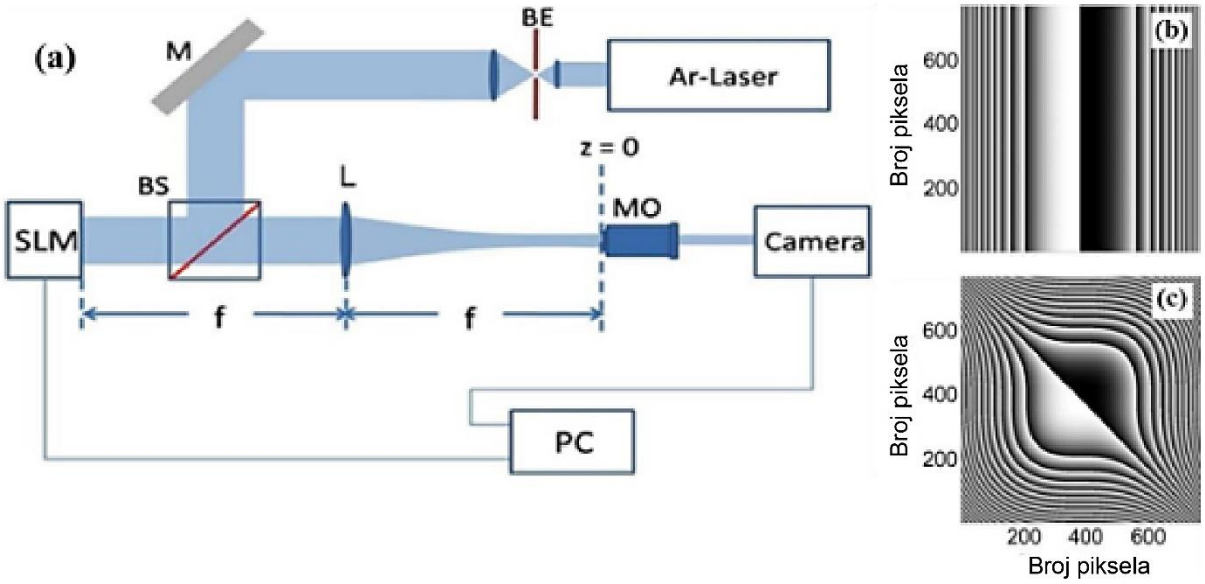

Slika 2.6 Eksperimentalna demonstracija jednodimenzionalnog i dvodimenzionalnog Eirijevog snopa. **(a)** Šema eksperimentalne postavke. [55] **(b, c)** Kubne fazne maske pomoću kojih se moduliše Gausov snop i dobija (b) jednodimenzionalni, i (c) dvodimenzionalni Eirijev snop. [53]

Kao rezultat, Eirijev snop se lako može generisati fazno modulisanim Gausovim snopom sa distribucijom kubne faze u Furijeovom prostoru (Slika 2.6b,c), i zatim proračunavanjem njegove inverzne Furijeove transformacije. Isti princip se može generalizovati i za dvodimenzionalne Eirijeve snopove koji su korišćeni u ovoj tezi. Spektar koji određuje envelopu polja određen je izrazom:

$$\widehat{\Phi}\big(k_x, k_y, 0\big) = \Phi(k_x, 0)\Phi\big(k_y, 0\big) \tag{2.17}$$

Iz izraza se vidi da se dvodimenzionalni Eirijev snop takođe može generisati fazno modulisanim Gausovim snopom sa distribucijom dvodimenzionalne kubne faze u Furijeovom prostoru (Slika 2.6c).

Poglavlje 3

Fotonske strukture

Fotoni su odličan medijum za prenos informacija. Prednosti fotona leže u velikom kapacitetu i brzini prenosa. Jedan od ciljeva fotonske tehnologije je postići izuzetno brzu obradu informacija i potpuno optičko računanje zasnovano na mikro/nano-fotonskim uređajima [56]. Kontrola i modulacija informacija pomoću fotonskih struktura ima izuzetan fundamentalan i praktičan značaj i zbog toga fotoniku kao granu fizike možemo smestiti u sam centar tehnološke revolucije u oblasti telekomunikacija i informacionih tehnologija.

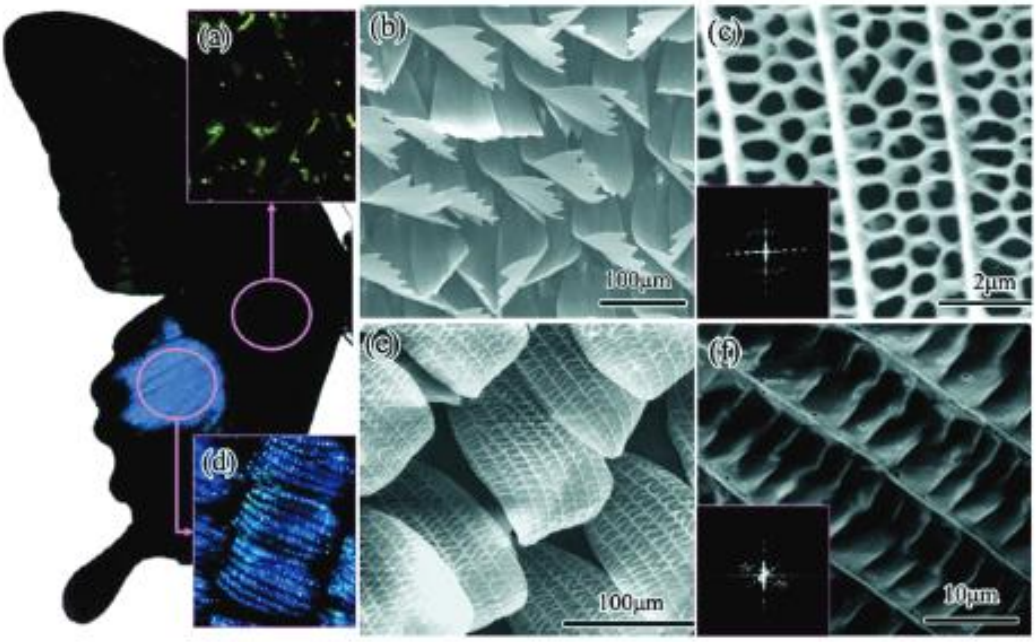

Slika 3.1 Morfo leptir - amblem prirodne fotonike. Na slici su prikazani uvećani delovi krila sa crno **(a, b, c)** i plavo **(d, e, f)** obojene površine sa različitim uvećanjima. Slike pokazuju da su različite boje uzrokovane različitim nanostrukturama. [57]

Fotonski kristali su najstariji i najpoznatiji materijali koji se koriste za pasivnu i aktivnu modulaciju svetlosti [58]. Od davnina su ljudska bića bila fascinirana izuzetnim optičkim svojstvima koloidnih kristala. Mistični opali i insekti koji pokazuju prelive boja (Slika 3.1), nerazumljivi za naše pretke, pretvorili su se u modele za proučavanje fotonskih kristala.

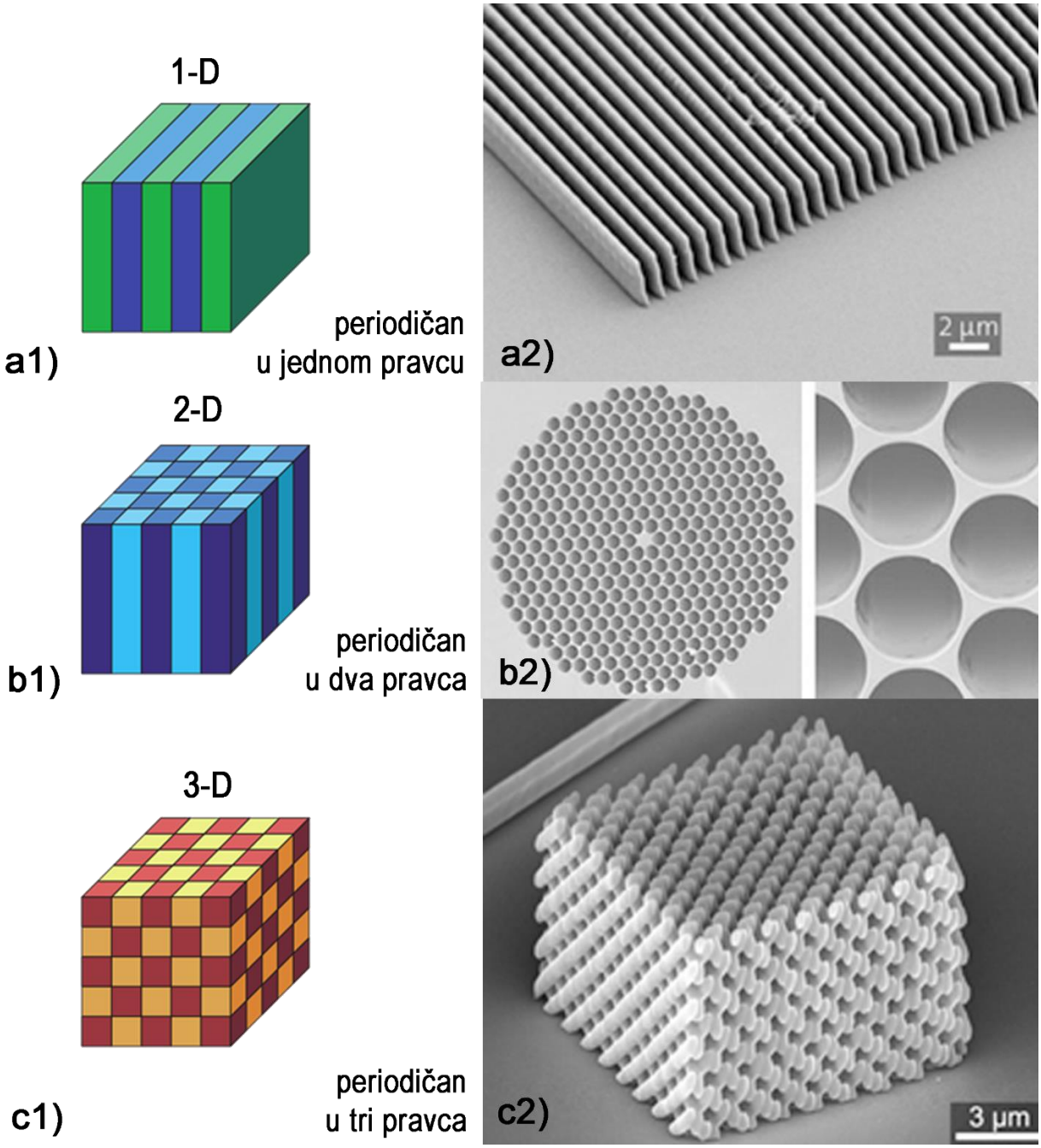

Slika 3.2 (**1**) Jednostavan prikaz jednodimenzionalnog (**a1**), dvodimenzionalnog (**b1**) i trodimenzionalnog (**c1**) fotonskog kristala. Različite boje predstavljaju materijale sa različitim dielektričnim konstantama. [38] (**2**) Primeri izrade fotonskih kristala u jednoj (**a2**), dve (**b2**) i tri (**c2**) dimenzije [60].

Fotonski kristali su zapravo dielektrične strukture sa periodičnom modulacijom indeksa prelamanja i smatraju se optičkim analogonom poluprovodnika. Dielektrične strukture koje po dimenziji odgovaraju talasnoj dužini svetlosti raspoređene su u 1D, 2D i 3D konfiguracijama (Slika 3.2), periodično različitih (visokih i niskih) dielektričnih konstanti duž jedne, dve ili tri ose. Fotoni se

prostiru kroz takvu strukturu ili ne, u zavisnosti od njihove talasne dužine. Talasne dužine koje se mogu prostirati kroz određeni fotonski kristal nazivaju se modovima, a grupa dozvoljenih modova formiraće fotonski pojas kristala (engl. ***band***). Pojasevi talasnih dužina koje ne mogu proći kroz fotonski kristal čine fotonske pojasne procepe (engl. ***photonic band gaps***) i fizički odgovaraju difrakcionom piku kristala.

Analogno poluprovodničkim materijalima i njihovoj ulozi u kontroli kretanja elektrona, fotonski kristali predstavljaju materijale koji su u mogućnosti da kontrolišu mnoge aspekte prostiranja elektromagnetnih talasa [59].

U jednodimenzionalnoj konfiguraciji fotonski kristali imaju već široku primenu u obliku tankih filmova, nisko i visoko reflektivnih slojeva na sočivima i ogledalima, kao Bragg-ove rešetke, zatim farbe i mastila promenljivih boja itd. Što se tiče dvodimenzionalne konfiguracije prvi komercijalni proizvodi bili su rupičasti fiberi specifične mikrostrukture, a u pogledu trodimenzionalne konfiguracije još uvek nema komercijalne primene upravo zbog teškoća u tehnologiji njihove izrade a jedna od potencijalnih primena bi bila u oblasti optičkih kompjutera. Za fotonske kristale pravljene za talasne dužine iz vidljivog dela spektra reč je o strukturama od par stotina nanometara što sa stanovišta tehnologije izrade nije ni malo lak zadatak. U zavisnosti od dimenzije periodičnosti postoje različite tehnike izrade fotonskih kristala [60].

3.1 Optički indukovane fotonske rešetke

Fotonske rešetke predstavljaju jedan način realizacije koncepta dvodimenzionalnih fotonskih kristala s tim što je razlika u modulacijama indeksa prelamanja između susednih dielektričnih slojeva jako mala (< 0.01). Fotonske rešetke se mogu kreirati modulacijom indeksa prelamanja sredine što uključuje direktno lasersko upisivanje, optičku litografiju ili tehniku bušenja.

Tehnikom optičke indukcije [39], koja će biti detaljnije opisana u narednom poglavlju, dobijaju se takozvane ***optički indukovane fotonske rešetke***. Ovakva vrsta fotonskih rešetki omogućava kontrolu svetlosti samom svetlošću, a pored toga one poseduju značajne prednosti u odnosu na klasične fotonske kristale. Na primer, optički indukovane fotonske rešetke, u različitim konfiguracijama i veličinama, se mogu upisati (i izbrisati) bez ikakvih teškoća, jednostavnim osvetljavanjem kristala belom svetlošću. Zatim, mogu interagovati sa propagirajućim snopovima. U njima se mogu demonstrirati mnogi fenomeni prostiranja talasa [61] uključujući fenomene fizike čvrstog stanja kao što su Blohove oscilacije, Zenerovo tunelovanje i Andersenova lokalizacija.

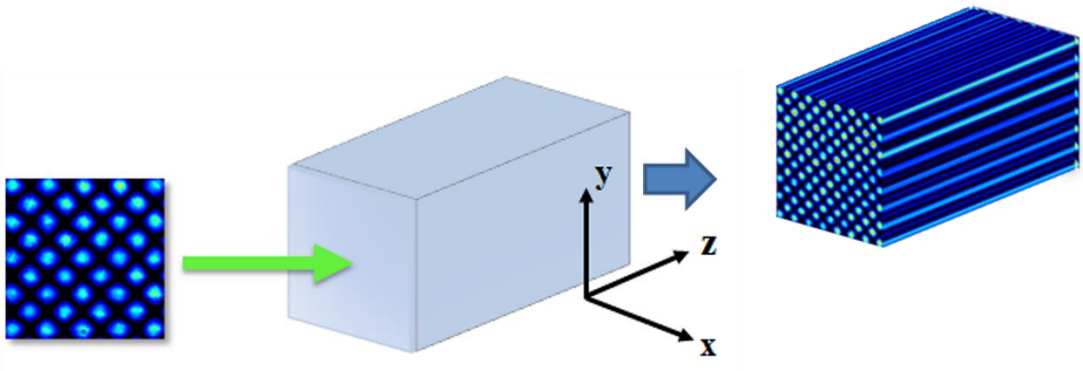

Slika 3.3 Šema realizacije fotonske rešetke tehnikom optičke indukcije pomoću koncepta nedifragujućih snopova (primer fotonske rešetke korišćene u ovoj tezi).

Koristeći nedifragujuće talase optička indukcija u fotorefraktivnom materijalu predstavlja pogodan način za kreiranje nelinearnih, rekonfigurabilnih fotonskih rešetki (Slika 3.3) za fundamentalna ispitivanja propagacije talasa u periodičnim strukturama. Osnovna ideja je da se modifikuje indeks prelamanja u zapreminskom nelinearnom materijalu propuštanjem svetlosnog snopa nepromenljivog intenziteta u transverzalnoj ravni propagacije. Ako je svetlosni snop periodičan u prostoru, u materijalu će doći do periodične modulacije indeksa prelamanja što predstavlja fotonski kristal [39].

3.2 Optički indukovane fotonske strukture sa defektima

Fotonski kristali kao i fotorefraktivni materijali nalaze mnogobrojne primene u optičkim tehnologijama, uključujući lasere niskog praga [62], talasovode sa malim gubicima, [63–65] optička kola na čipu [66], optička vlakna [67,68] itd.

Većina ovih primena ne zahteva samo fotorefraktivni materijal, već i precizno, kontrolisano ugrađivanje unapred projektovanih defekata. Ovi defekti remete periodičnost kristala, stvarajući optička stanja unutar inače zabranjenih frekvencija pojasnog procepa. Stoga, spajanje svetlosti sa ovim stanjima može biti lokalizovano unutar defektnih regiona, a projektovanjem geometrije i pozicije defekata u fotorefraktivnom materijalu u mogućnosti smo da manipulišemo svetlošću.

Napravljeni su veliki pomaci u kontrolisanoj inkorporaciji defekata u fotonske kristale, čime je proširena njihova funkcionalnost i održivost za primene zasnovane na fotonskom pojasnom procepu. Defekti se ugrađuju u fotonske kristale različitim tehnikama, uključujući samoorganizaciju, holografiju, kontrolisano graviranje i litografske procedure (Slika 3.4) [60]. Razvoj reproduktivnih tehnika za proizvodnju visokokvalitetnih fotonskih kristala koji bi sadržali kontrolisane defekte otvara vrata novoj eri u kojoj će se mikrofotonski uređaji kombinovati sa, ili čak zameniti trenutne mikroelektronske uređaje.

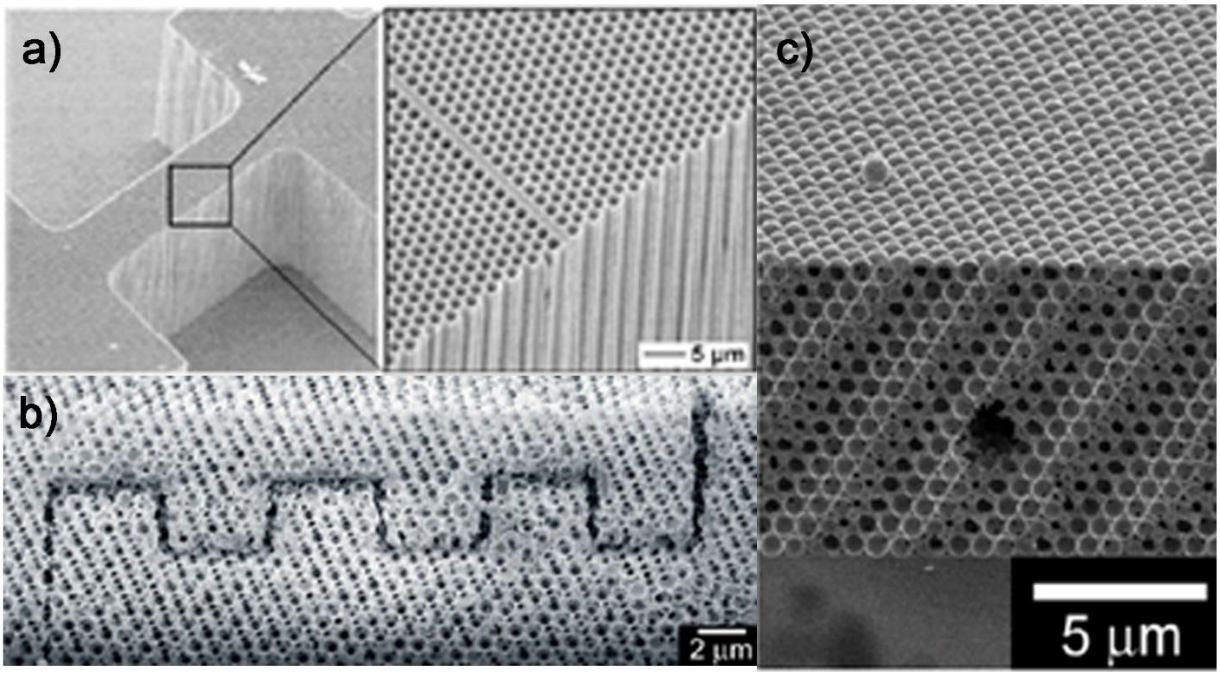

Slika 3.4 SEM fotografije različitih defekata u fotonskim strukturama [60].

Pored uticaja fotonske kvadratne rešetke, upisane u kristal SBN:Ce, na prostiranje dvodimenzionalnog Eirijevog snopa, u ovoj disertaciji ispitivana je i dinamika prostiranja Eirijevog snopa u sistemu sa pozitivnim i negativnim defektom u jednom kanalu rešetke. U ovoj tezi za realizaciju ***optički indukovanih defekata*** korišćena je tehnika optičke indukcije i metod multipleksiranja [69-71]. Cela procedura biće detaljnije opisana u nastavku teksta u Poglavlju 5 gde se opisuju eksperimentalne metode korišćene u ovoj disertaciji.

Poglavlje 4

Teorijski model

U ovom poglavlju prikazan je teorijski model za opisivanje i modelovanje propagacije dvodimenzionalnog Eirijevog snopa u nelinearnom materijalu. Teorijski model obuhvata propagaciju više Eirijevih snopova kroz nelinearni materijal kao i propagaciju pojedinačnog dvodimenzionalnog Eirijevog snopa kroz optički indukovanu kvadratnu fotonsku rešetku u nelinearnom materijalu. Ovo poglavlje sadrži i objašnjenje fotorefraktivnog efekta i modulacije indeksa prelamanja u fotorefraktivnom materijalu stroncijum barijum niobata (SBN). Nakon toga dat je detaljniji uvid u samu tehniku optičke indukcije i opisan numerički model za modelovanje linearnog i nelinearnog prostiranja Eirijevih snopova kroz SBN kristal sa i bez upisane fotonske strukture.

4.1 Osnovne jednačine prostiranja svetlosti u nelinearnom fotorefraktivnom medijumu

Teorijsko razmatranje prostiranja svetlosnog talasa u nelinearnom fotorefraktivnom medijumu kreće od Maksvelovih jednačina, osnovnih jednačina talasne optike:

$$\nabla \cdot \boldsymbol{D} = \rho \tag{4.1}$$

$$\nabla \cdot \boldsymbol{B} = \boldsymbol{0} \tag{4.2}$$

$$\nabla \times \boldsymbol{E} = -\frac{\partial \boldsymbol{B}}{\partial t} \tag{4.3}$$

$$\nabla \times \boldsymbol{H} = \frac{\partial \boldsymbol{D}}{\partial t} + \boldsymbol{j} \tag{4.4}$$

U nemagnetnom materijalu, električno $\boldsymbol{E}$ i magnetno polje $\boldsymbol{H}$ su povezani poljem dielektričnog pomeraja $\boldsymbol{D}$ i magnetne indukcije $\boldsymbol{B}$ na sledeći način:

$$\boldsymbol{D} = \epsilon_0 \boldsymbol{E} + \boldsymbol{P} \tag{4.5}$$

$$\boldsymbol{B} = \mu_0 \boldsymbol{H} \tag{4.6}$$

gde ε_0 predstavlja dielektričnu konstantu vakuuma, permitivnost, i $\boldsymbol{P}$ indukovanu polarizaciju materijala. Pošto nas interesuju rešenja ovih jednačina za slučaj kada u materijalu nema slobodnih nosilaca naelektrisanja a samim tim i struja, pretpostavićemo da su $\rho = 0$ i $\boldsymbol{j} = 0$. Uvodeći brzinu svetlosti u vakuumu kao $c = 1/\sqrt{\mu_0 \epsilon_0}$ i kombinovanjem (4.3)-(4.6) dolazimo do opšte talasne jednačine:

$$\nabla \times \nabla \times \boldsymbol{E} + \frac{1}{c^2}\frac{\partial^2 \boldsymbol{E}}{\partial t^2} = -\frac{1}{\epsilon_0 c^2}\frac{\partial^2 \boldsymbol{P}}{\partial t^2} \tag{4.7}$$

U ovoj jednačini, odziv materijala na električno polje je povezan sa upadnim svetlosnim talasom određenim polarizacijom $\boldsymbol{P}$. Za linearni dielektrični materijal polarizacija se može prikazati sledećim izrazom

$$\boldsymbol{P} = \epsilon_0 \chi^{(1)} \boldsymbol{E} \tag{4.8}$$

gde $\chi^{(1)}$ predstavlja (linearnu) električnu susceptibilnost medijuma. Iako se često može tretirati kao skalarna konstanta u slučaju propagacije kroz anizotropni medijum, $\chi^{(1)}$ predstavlja tenzor ranga 2. Zamenom (4.8) u (4.5) dobijamo sledeći izraz

$$\boldsymbol{D} = \epsilon_0\left(1 + \chi^{(1)}\right)\boldsymbol{E} = \epsilon_0 \epsilon \boldsymbol{E} \tag{4.9}$$

sa dielektričnom permitivnošću ϵ. U slučaju da električno polje upadnog svetlosnog talasa postane uporedivo sa poljem unutar kristala, linearna relacija (4.8) prestaje da bude validna. U tom slučaju, polarizaciju predstavljamo razvojem u Tejlorov red

$$\boldsymbol{P} = \epsilon_0\left(\chi^{(1)}\boldsymbol{E} + \chi^{(2)}\boldsymbol{E}\boldsymbol{E} + \chi^{(3)}\boldsymbol{E}\boldsymbol{E}\boldsymbol{E} + \cdots\right) \tag{4.10}$$

gde $\chi^{(i)}$ sa $i \geq 2$ predstavlja nelinearnu susceptibilnost n-tog reda. Nelinearni izrazi u (4.10) dovode do niza zanimljivih fenomena [72]. Na primer, susceptibilnost drugog reda je odgovorna za generaciju drugog harmonika ili zbira i razlike frekvencija dok u slučaju susceptibilnosti trećeg reda javljaju se fenomeni kao što je generacija trećeg harmonika ili optička fazna konjugacija.

Radi pogodnosti izraz (4.10) se prikazuje kao

$$\boldsymbol{P} = \epsilon_0 \chi_{eff} \boldsymbol{E} \tag{4.11}$$

sa efektivnom, zavisnom od intenziteta susceptibilnošću $\chi_{eff}(I \equiv |E|^2)$. Koristeći ovu relaciju i uvodeći izraz za efektivni indeks prelamanja $n(I) = \sqrt{1 + \chi_{eff}}$, Helmholcova jednačina se može dobiti iz izraza (4.7):

$$-\nabla^2 \boldsymbol{E} + \frac{n^2}{c^2}\frac{\partial^2 \boldsymbol{E}}{\partial t^2} = 0 \tag{4.12}$$

U ovom izvođenju, korišćena je relacija $\nabla \times \nabla \times \boldsymbol{E} = \nabla(\nabla \cdot \boldsymbol{E}) - \nabla^2 \boldsymbol{E}$ zajedno sa činjenicom da je izraz $\nabla(\nabla \cdot \boldsymbol{E})$ jako mali i može se zanemariti [72]. U sledećem koraku, indeks prelamanja se može podeliti na njegovu vrednost u odsustvu svetlosti n_0^2 i svetlošću indukovanu promenu vrednosti indeksa prelamanja $\Delta n^2(I)$:

$$n^2 = n_0^2 + \Delta n^2(I) \tag{4.13}$$

Štaviše, razmatra se talas linearno polarizovan u *x*-pravcu koji se prostire duž *z*-pravca, tj.

$$\boldsymbol{E}(\boldsymbol{r},t) = A(\boldsymbol{r})e^{i(k_z z-\omega t)} \cdot \boldsymbol{e}_x \tag{4.14}$$

sa $\boldsymbol{r} = (x, y, z)$ i $k_z = n_o\omega/c$. U standardnoj paraksijalnoj aproksimaciji, pretpostavlja se da envelopa polja $A(x, y, z)$ varira sa z na skali mnogo većoj od talasne dužine. U ovom slučaju, drugi izvod po z se može zanemariti tako da ubacivanjem izraza (4.14) u (4.12) dolazimo do ***dvodimenzionalne nelinearne paraksijalne Šredingerove jednačine***

$$i\frac{\partial A}{\partial z} + \frac{1}{2k_z}\nabla_\perp^2 A + \frac{k_z}{2n_0^2}\Delta n^2(I)A = 0 \tag{4.15}$$

sa $\nabla_\perp^2 = (\partial^2/\partial x^2 + \partial^2/\partial y^2)$. Uvođenjem bezdimenzionih varijabli $x' = x/x_0$, $y' = y/y_0$ i $z' = z/k_z x_0^2$ sa transverzalnim faktorom skaliranja x_0 dobija se

$$2i\frac{\partial A}{\partial z'} + \nabla_\perp'^2 A + \frac{k_z^2 x_0^2}{n_0^2}\Delta n^2(I)A = 0 \tag{4.16}$$

sa $\nabla_\perp'^2 = (\partial^2/\partial x'^2 + \partial^2/\partial y'^2)$.

Za modelovanje propagacije Eirijevih snopova u nelinearnom materijalu sa i bez fotonske rešetke u ovoj disertaciji, polazi se od skalirane paraksijalne jednačine difrakcije (4.16) električnog polja dvodimenzionalnog Eirijevog snopa $A(\boldsymbol{r})$.

Propagaciona jednačina (4.16) se koristi i za ispitivanje interakcije superponiranih dvodimenzionalnih Eirijevih snopova kao i za modelovanje interakcije Eirijevog snopa sa optički indukovanom kvadratnom fotonskom rešetkom sa i bez defekata. Razlika je samo u članu $\Delta n^2(I)$, tj. nelinearnoj promeni indeksa prelamanja u zavisnosti od indukovanog intenziteta I ukupnog električnog polja.

U prvom slučaju kada je reč o interakciji više Eirijevih snopova $I = |A|^2$, envelopa električnog polja $A(\boldsymbol{r})$ predstavlja koherentnu superpoziciju više snopova iste ili različite fazne distribucije, tj. $A = \sum_i A_i \mathrm{e}^{i\varphi_i}$.

Kada se modeluje interakcija Eirijevog snopa sa kvadratnom fotonskom rešetkom $I = |A_{latt}|^2 + |A|^2$, tj. sabiraju se intenziteti Eirijevog snopa i snopa kojim se formira kvadratna rešetka, pri čemu se envelopa električnog polja snopa kvadratne rešetke može prikazati sledećim izrazom

$$A_{latt}(x, y, z) = \sum_{n=1}^{4} A_n e^{ik_t(x\cos\varphi_n + y\sin\varphi_n)} e^{ik_z z} \tag{4.17}$$

sa $\varphi_n = \frac{\pi}{4}(2n + 1)$ i $k^2 = k_t^2 + k_z^2$, gde je k_t – longitudinalni talasni vektor.

4.2 Fotorefraktivni efekat

Fotorefraktivni efekat je veoma značajan efekat u nelinearnoj optici. Efekat opisuje fenomene povezane sa prostiranjem laserskih zraka u nelinearnim fotorefraktivnim materijalima. Uglavnom su to transparentni i anizotropni feroelektrični kristali, čisti ili sa određenim primesama, čija se energetska stanja nalaze između valentne i provodne zone kristala. Primese specifičnih elemenata nazivaju se akceptorima ili donorima u kristalu. Kada se kroz fotorefraktivni materijal pošalje prostorno-modulisani intenzitet elektromagnetnog polja (laserski zrak) nosioci naelektrisanja se pobuđuju fotojonizacijom i dolazi do njihove redistribucije pod uticajem spoljašnjeg električnog polja. Neki od elektrona ili šupljina koji potiču od donora ili akceptora se fotojonizuju i podižu iz valentne u provodnu zonu (Slika 4.1). U osvetljenim oblastima kristala se tada stvaraju slobodni elektroni i šupljiine, a naelektrisanja koja su prešla u provodnu zonu se onda kreću pod uticajem difuzije ili drifta.

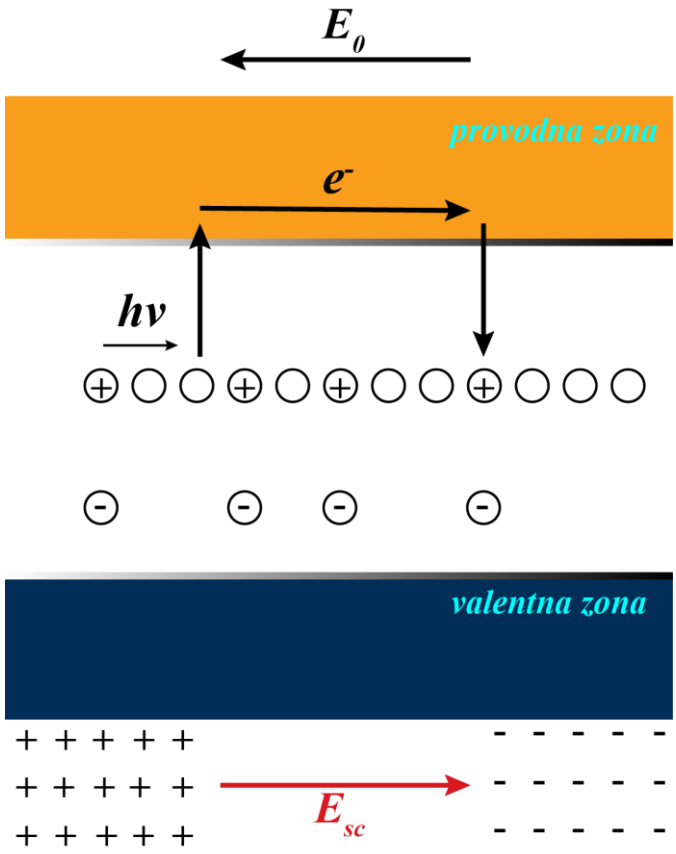

Slika 4.1 Šematska ilustracija transporta naelektrisanja u fotorefraktivnom kristalu.

Prilikom difuzije, naelektrisanja se rekombinuju sa suprotnim nosiocem naelektrisanja (donorima ili akceptorima). Tokom procesa rekombinacije stvara se statičko polje prostornog naelektrisanja E_{sc} koje moduliše indeks prelamanja materijala pomoću linearnog elektro-optičkog efekta (Pokelsovog efekta). Jačina modulacije indeksa prelamanja zavisi od intenziteta osvetljenja upadne svetlosti i intrinzičnih parametara kristala.

Drugi mehanizam za modulaciju indeksa je drift. Nasuprot difuziji, drift se javlja samo ako se na kristal primeni spoljašnje električno polje. Pobuđeni elektroni i šupljine se ubrzavaju spoljašnjim poljem i kreću, sve dok sila stvorena spoljašnjim poljem ne bude kompenzovana unutrašnjim poljem, koje je stvoreno rezultujućom nehomogenom raspodelom naelektrisanja.

Fotorefraktivni efekat koji opisuje lokalnu promenu indeksa prelamanja u materijalu koja nastaje kao rezultat optički indukovane redistribucije nosilaca naelektrisanja je efekat visoke osetljivosti. Može se uočiti pri niskim intenzitetima svetlosti a zavisi od više faktora kao što su intenzitet svetlosti, pokretljivost naelektrisanja dopiranog elementa kao i intenziteta spoljašnjeg polja primenjenog na kristal. Modulacija indeksa prelamanja je obično veoma postojana u mraku. Takođe, može se izbrisati homogenim osvetljenjem poput LED svetla ili visoke temperature, bez oštećenja kristala.

Fotorefraktivni efekat je prvi put posmatran 1966. u vidu distorzije talasnog fronta koherentnog svetlosnog snopa koji se prostirao kroz kristal Litijum Niobata ($LiNbO_3$) [73]. Od tada, ovaj efekat je posmatran i u mnogim drugim materijalima kao što su Barijum Titanat ($BaTiO_3$), Litijum Tantalat ($LiTaO_3$), Potasium Niobat ($KNbO_3$), i Stroncijum Barijum Niobat (SBN) koji je izabran kao fotorefraktivni materijal u istraživanju prikazanom u ovoj tezi.

4.2.1 Linearni elektro-optički efekat

U elektro-optičkim kristalima, prisustvo stacionarnog električnog polja utiče na promenu dielektrične permitivnosti ϵ što je ekvivalentno promeni dimenzije i pravca optičke indikatrise [74]. U fotorefraktivnim materijalima, ova promena zavisi linearno od jačine indukovanog polja prostornog naelektrisanja pa je zato opisana linearnim elektro-optičkim efektom (Pokelsovim efektom). Matematički ovaj efekat se opisuje kao promena tenzora impermeabilnosti

$$\Delta\eta_{ij} = \Delta\left(\frac{1}{n^2}\right) = \sum_k r_{ijk}E_k \tag{4.18}$$

Konstante r_{ijk} su elementi elektrooptičkog tenzora a E_k predstavlja k-tu komponentu ukupnog električnog polja $\boldsymbol{E} = \boldsymbol{E}_0 + \boldsymbol{E}_{sc}$ koje predstavlja sumu eksterno primenjenog stacionarnog električnog polja $\boldsymbol{E}_0$ i polje prostorog naelektrisanja $\boldsymbol{E}_{sc}$ generisano unutar kristala. Odgovarajuća promena dielektrične permitivnosti opisana je izrazom

$$\Delta\epsilon_{ij} = -\epsilon_0 n_i^2 n_j^2 \Delta\eta_{ij} \tag{4.19}$$

U ovoj tezi, svi eksperimenti su rađeni u kristalu Stroncijum Barijum Niobata dopiranom Cerijumom (SBN:Ce) (Slika 4.2).

SBN kristal ($Sb_xBa_{1-x}Nb_2O_6$, $0{,}25 \leq x \leq 0{,}75$) čist, kao i dopiran različitim elementima (Ce, Cr, Co, Fe) je odličan optički i fotorefraktivni materijal koji se često koristi u elektro-optici, akusto-optici ili fotorefraktivnoj nelinearnoj optici. Dopiranjem SBN kristala otkriveno je primetno poboljšanje njegovih fotorefraktivnih svojstava [75]. Mogućnost indukovanja reverzibilne modulacije indeksa prelamanja nehomogenim osvetljenjem (fotorefraktivnim efektom) je najvažnija karakteristika SBN kristala. Takav kristal poseduje ogromnu fleksibilnost, jer se upisane strukture lako mogu izbrisati homogenom belom svetlošću. SBN kristal je kristal sa dvojnim prelamanjem, uniaksijalni i anizotropni materijal sa tetragonalnom kristalografskom strukturom (simetrijska grupa 4mm). Za SBN kristal dominantan efekat koji dovodi do modulacije indeksa prelamanja je linearni elektro-optički efekat, gde je modulacija indeksa prelamanja povezana sa linearnim elektro-optičkim koeficijentima.

U skraćenoj notaciji, elektrooptički koeficijenti za ovu određenu klasu simetrije se mogu prikazati izrazom

$$r_{SBN} = \begin{bmatrix} 0 & 0 & r_{13} \\ 0 & 0 & r_{13} \\ 0 & 0 & r_{33} \\ 0 & r_{42} & 0 \\ r_{42} & 0 & 0 \\ 0 & 0 & 0 \end{bmatrix} \tag{4.20}$$

Za SBN kristale važi relacija $r_{33} \gg r_{13}, r_{42}$ koja nam govori da se svetlošću indukovane promene dielektrične permitivnosti ϵ mogu opisati efektivnim elektrooptičkim koeficijentom $r_{eff} = r_{33} = r_{333}$. Ako je upadna svetlost polarizovana kao neredovan zrak u odnosu na *c*-osu kristala, efektivna promena indeksa prelamanja je određena sledećim izrazom

$$\Delta n^2 = -n_0^4 r_{eff} \boldsymbol{E} \cdot \boldsymbol{e}_c \tag{4.21}$$

gde $\boldsymbol{e}_c$ predstavlja jedinični vektor duž pravca c-ose kristala.

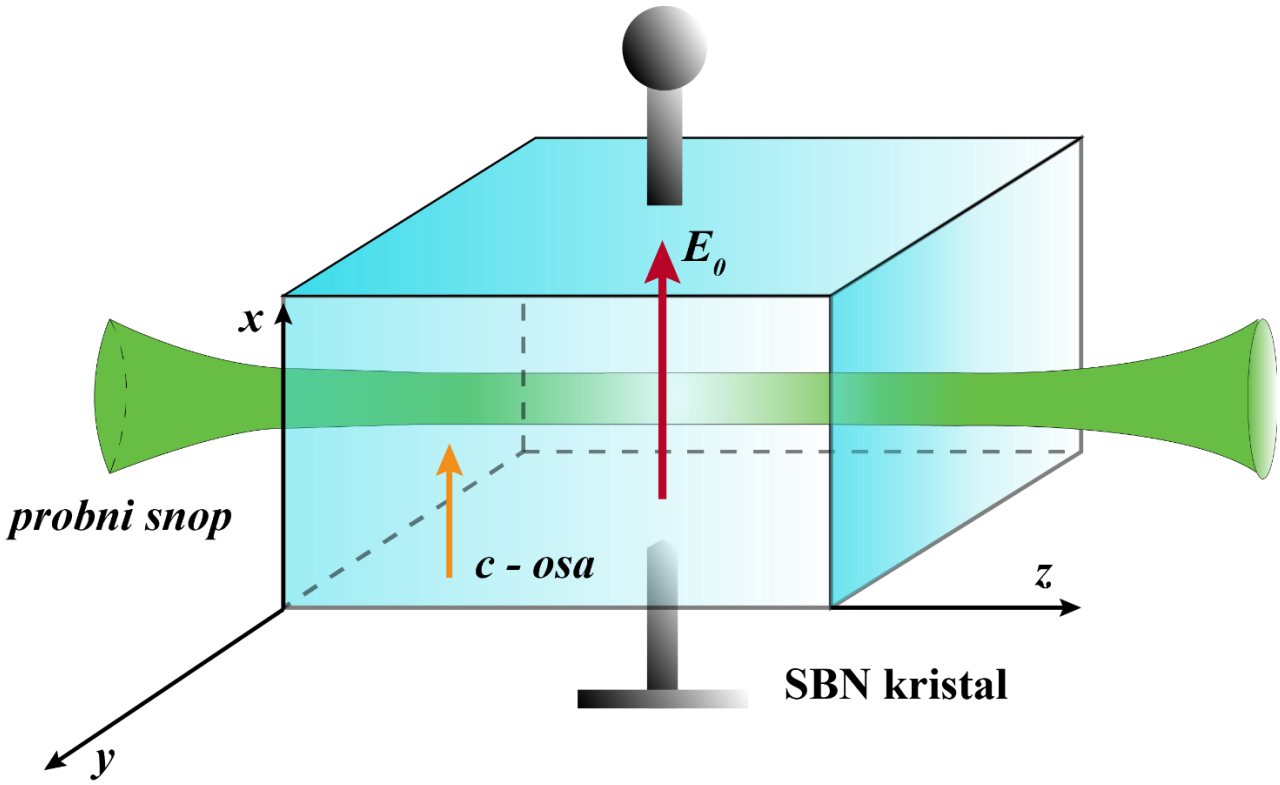

Slika 4.2 Prikaz geometrije SBN kristala i orijentacije osa

U ovoj disertaciji za eksperimentalnu realizaciju kao i u numeričkim simulacijama korišćen je SBN ($Sb_{0.6}Ba_{0.4}Nb_2O_6$) kristal dopiran cerijumom (2‰ CeO_2), tipičnih geometrijskih dimenzija 5 × 5 × 20 mm^3. Takav kristal karakterišu neperturbovani indeksi prelamanja n_o = 2,358 i n_e = 2,325 sa odgovarajućim elektro-optičkim koeficijentima r_{13} = 47,1 pm/V i r_{33} = 237,0 pm/V za redovan i neredovan zrak [76].

4.3 Tehnika optičke indukcije u fotorefraktivnom SBN kristalu

Kao što je već pomenuto, optička indukcija u fotorefraktivnom medijumu predstavlja idealan alat za kreiranje nelinearnih, rekonfigurabilnih fotonskih rešetki za fundamentalna istraživanja prostiranja talasa u periodičnim strukturama [39].

Koristeći koncept nedifragujućih talasa, ovom tehnikom se realizuju fotonske strukture unutar fotorefraktivnog medijuma. Tehnika se bazira na fotorefraktivnom efektu. Unutar fotorefraktivnog kristala, kao što je stroncijum barijum niobat dopiran cerijumom, SBN:Ce, redistribucija naelektrisanja rezultuje formiranjem reverzibilnog makroskopskog polja prostornog naelektrisanja koje moduliše indeks prelamanja pomoću elektrooptičkog Pokelsovog efekta.

Kako je reč o SBN:Ce kristalu, materijalu sa velikom fotorefraktivnom nelinearnošću (odnosno izraženoj polarizacionoj anizotropiji), sledi da se svetlošću indukovane promene mogu opisati efektivnim elektrooptičkim koeficijentom $r_{eff} = r_{33}$ i zavise od polarizacije upadne svetlosti [31].

Ako je upadna svetlost neredovan zrak (linearno polarizovani snop koji se kreće paralelno sa *c*-osom kristala sa pravcem prostiranja električnog polja paralelnim u odnosu na *c*-osu kristala) u odnosu na optičku c-osu kristala, efektivna promena indeksa prelamanja je određena izrazom (4.21). Kako Δn^2 zavisi od r_{eff} i $\vec{E}$, važno je znati kako izgleda polje prostornog naelektrisanja generisano upadnom svetlošću.

Da bi u materijalu sa nelinearnom promenom indeksa prelamanja (duž pravca neredovnog zraka u odnosu na optičku *c*-osu kristala) upisali fotonsku strukturu koja odgovara obliku upadnog indukcionog nedifragujućeg snopa neophodno je da se upadni snop prostire kao redovan zrak (linearno polarizovan zrak koji se kreće paralelno duž c-ose kristala sa pravcem prostiranja električnog polja normalnim u odnosu na optičku *c*-osu kristala) kako ne bi došlo do promene geometrije rešetke usled nelinearnih efekata. Dakle, takav upadni snop će se prostirati u linearnom režimu. Ako se intenzitet upadnog snopa dovoljno poveća dolazi do nelinearne propagacije kroz periodičnu strukturu. Dakle, u zavisnosti od intenziteta probnog snopa, moguće je proučavati i linearne i nelinearne efekte propagacije.

U drugoj fazi istraživanja optički je indukovana dvodimenzionalna kvadratna fotonska rešetka u SBN:Ce kristalu radi ispitivanja dinamike prostiranja dvodimenzionalnog Eirijevog snopa. Za generisanje dvodimenzionalne fotonske rešetke potrebno je da imamo distribuciju intenziteta indukcionog snopa koja je nepromenljiva u transverzalnoj ravni propagacije. Jasno je da snop mora pripadati klasi nedifragujućih snopova. Kao što je prethodno opisano u Poglavlju 2, nedifragujući snopovi predstavljaju skalarno rešenje vremenski nepromenljive Helmholcove jednačine i dele osobinu da u Furijeovom prostoru transverzalni vektori, k_x i k_y leže na kružnici radijusa k_t i određuju dimenzije strukture u realnom prostoru kao i period rešetke (Slika 4.3) [78]. Nedifragujući snop kojim je indukovana kvadratna fotonska rešetka formiran je superpozicijom četiri ravanska talasa. Električno polje takvog indukcionog snopa opisano je izrazom (4.17) sa $\varphi_n = \frac{\pi}{4}(2n+1)$ i $k^2 = k_t^2 + k_z^2$, gde je k_t – longitudinalni talasni vektor.

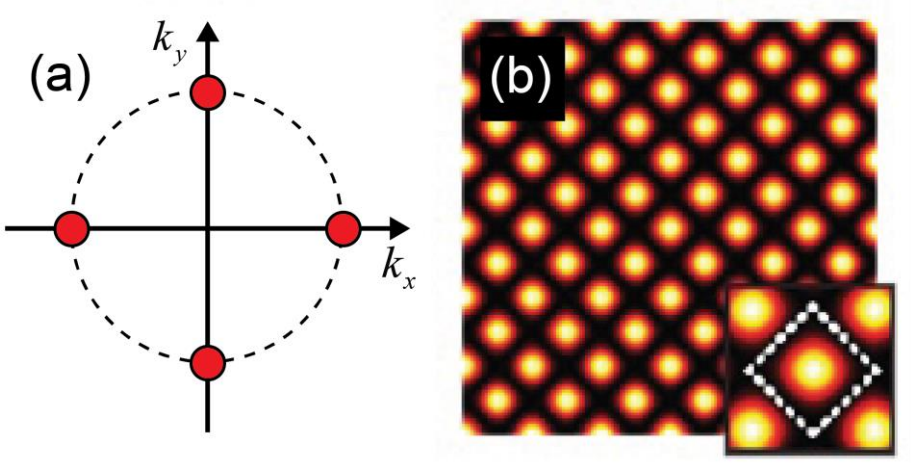

Slika 4.3. (a) Ilustracija talasnog polja nedifragujućeg snopa kvadratne rešetke u Furijeovom prostoru; **(b)** Transverzalna distribucija faze nedifragujućeg snopa kvadratne rešetke - oblik snopa za upisivanje rešetke [78].

4.4 Numerički metod za rešavanje propagacione jednačine

Generalno, propagaciona jednačina (4.16) kao nelinearna parcijalna diferencijalna jednačina ne dozvoljava analitička rešenja i mora se rešiti numerički. Pored različitih pristupa rešavanju ovog tipa jednačina, numerički propagacioni metod podeljenih koraka (SSFM – *Split Step Fourier Method*) se pokazao dosta brzim i pouzdanim [79].

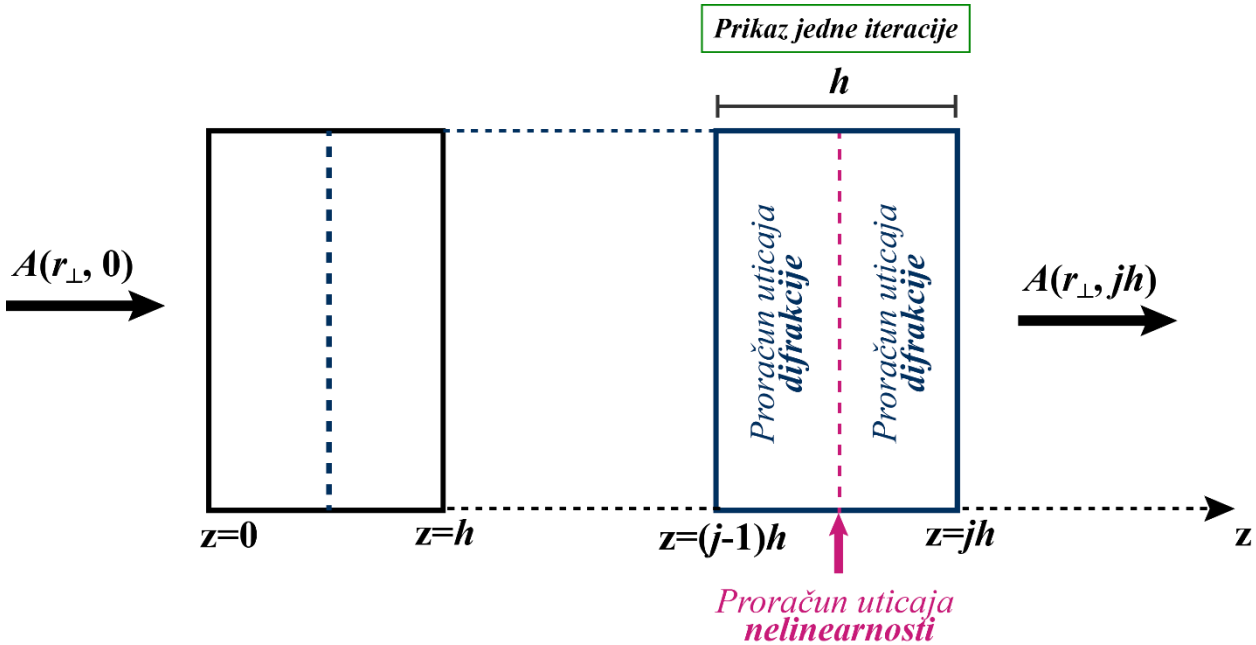

Slika 4.4. Prikaz šeme proračunavanja jednog koraka pomoću simetričnog Furijeovog metoda podeljenih koraka.

U ovom pristupu, aproksimativno rešenje jednačine (4.16) se dobija pod pretpostavkom da se difrakcija i nelinearni efekti mogu tretirati nezavisno za malo rastojanja propagacije h. Pod ovom pretpostavkom, propagacija od z do $z + h$ se računa u dva alternativna koraka gde se bilo difrakcioni efekti uzimaju u obzir a nelinearni zanemaruju i obrnuto (zbog čega i nosi naziv da je metod podeljenih koraka). Da bi razumeli osnovnu proceduru, zgodno je napisati propagacionu jednačinu (4.16) u sledećoj formi

$$\frac{\partial A}{\partial z} = (\boldsymbol{D} + \boldsymbol{N})A \tag{4.41}$$

sa dva operatora $\boldsymbol{D} = i\nabla_{\perp}^2/2$ i $\boldsymbol{N} = ik_z^2 x_0^2 \Delta n^2(I)/2$ koji se odnose na difrakciju i nelinearnost, respektivno. Formalno rešenje ove jednačine je za propagaciju od z do $z + h$ dato je izrazom

$$A(x, y, z + h) = e^{[h(\boldsymbol{D}+\boldsymbol{N})]} A(x, y, z) \tag{4.42}$$

Na osnovu ovog izraza, numerički model se izvodi primenom dobro poznate Baker—Hausdorff fomule [80]

$$e^{h\boldsymbol{D}} e^{h\boldsymbol{N}} = e^{h(\boldsymbol{D}+\boldsymbol{N}) + \frac{1}{2}h^2[\boldsymbol{D},\boldsymbol{N}] + \cdots} \tag{4.43}$$

gde $[\boldsymbol{D}, \boldsymbol{N}] = \boldsymbol{DN} - \boldsymbol{ND}$. Usled nekomutativne prirode operatora $\boldsymbol{D}$ i $\boldsymbol{N}$, proračun difrakcionih i nelinearnih efekata u dva koraka, tj. zamena $e^{h(\boldsymbol{D}+\boldsymbol{N})}$ sa $e^{h\boldsymbol{D}} e^{h\boldsymbol{N}}$ rezultuje lokalnom preciznošću od $\mathcal{O}(h^2)$ koja se pokazala sasvim dovoljnom u većini slučajeva. Ukoliko je potrebno, preciznost se može unaprediti uključujući izraze viših redova [79].

Difrakcija se dobija koristeći pseudospektralni metod uključujući Furijeov transform envelope na dužini propagacije z da bi se obezbedio proračun diferencijalnih operatora $\nabla_{\perp}^2 \rightarrow -\left(k_x^2 + k_y^2\right)$. Nakon toga inverzni Furijeov transform nam daje envelopu difraktovanog polja na propagacionoj udaljenosti od $z + h$. Odgovarajuća nelinearna korekcija se naknadno primenjuje u realnom prostoru tako da se proračun propagacije može sumirati na sledeći način

$$A(x, y, z + h) = e^{ik_z^2 x_0^2 \Delta n^2(I) h/2} \mathcal{F}^{-1}\left[e^{-i\left(k_x^2 + k_y^2\right)h/2} \mathcal{F}[A(x, y, z)]\right] \tag{4.44}$$

Poglavlje 5

Eksperimentalne metode za ispitivanje dinamike prostiranja Eirijevih snopova u fotorefraktivnim sredinama

U ovom poglavlju prikazane su eksperimentalne metode za ispitivanje dinamike prostiranja Eirijevog snopa u fotorefraktivnim sredinama. Poglavlje je podeljeno na dva dela. Prvi deo se odnosi na eksperimentalne metode korišćene za ispitivanje linearne i nelinearne interakcije više superponiranih dvodimenzionalnih Eirijevih snopova u fotorefraktivnom SBN kristalu. Opisana je korišćena eksperimentalna postavka kao i detalji i relevantni parametri vezani za eksperiment, kao što je veličina snopa, položaj Eirijevih snopova u simetričnim konfiguracijama, njihova fazna distribucija kao i ostali detalji eksperimenta. Drugi deo se odnosi na eksperimentalne metode korišćene za ispitivanje dinamike prostiranja pojedinačnog dvodimenzionalnog Eirijevog snopa kroz optički indukovanu fotonsku rešetku sa i bez defekata. Pored esperimentalne postavke i relevantnih parametara opisan je i metod multipleksiranja koji je korišćen za generisanje optičkih defekata.

5.1 Interakcija dvodimenzionalnih Eirijevih snopova u fotorefraktivnom kristalu

Za ispitivanje linearne i nelinearne interakcije dva i četiri Eirijeva snopa korišćena je postavka eksperimenta sa Slike 5.1.

Kao svetlosni izvor korišćen je frekvencijski-udvojen Nd:YVO_4 (neodimijum itrijum vanadat) laser koji daje kontinualnu svetlost talasne dužine $\lambda = 532nm$. Laserski snop se proširi i kolimiše tako da na prostorni modulator svetlosti (SLM) pada kao ravanski talas. SLM (*Holoeye Pluto VIS*) je programabilni reflektivni fazni modulator svetlosti visoke HD rezolucije (displeja od 1920×1080 px^2), sa veličinom piksela od $8 \times 8\ \mu m^2$ i dimenzija $11.25 \times 8.64\ mm^2$.

Pomoću modulatora svetlosti se moduliše i amplituda i faza snopa [80]. Pri refleksiji dolazi do prostorne fazne modulacije Gausovog snopa koja u kombinaciji sa dva sočiva i Furijevom maskom (koja se postavlja u difrakcionu ravan i služi da snop koji je formiran posle difrakcije sa SLM očisti od svih parazitnih difrakcionih redova ostavljajući samo nulti difrakcioni red koji je najjačeg intenziteta) dovodi do željenog kompleksnog svetlosnog polja na ulazu u nelinearni fotorefraktivni medijum. Na ovaj način, realizuju se različita kompleksna svetlosna polja formirana kao superpozicija dva i četiri dvodimenzionalna Eirijeva snopa iste ili različite fazne distribucije.

Za sve konfiguracije enkodira se ukupna fazna slika i šalje na modulator svetlosti. Na kristal se primenjuje spoljašnje električno polje E_{ext}=1000V/cm^{-1}, a snop iz lasera se polarizuje tako da se prostire kao neredovan zrak (linearno polarizovani snop koji se kreće paralelno sa c-osom kristala sa pravcem prostiranja električnog polja paralelnim u odnosu na c-osu kristala), tj. duž efektivnog elektro-optičkog koeficijenta kristala kako bi se u kristalu obezbedila dovoljno velika nelinearnost.

Iza SBN kristala nalazi se mikroskopski objektiv (MO) i kamera, koji nam služe za dobijanje slike intenziteta na izlazu iz kristala. Kamera se može pomerati u z-pravcu. Kako je indeks prelamanja u kristalu prostorno modulisan, u eksperimentu se ne može snimiti distribucija intenziteta kroz kristal već samo na izlazu iz kristala. Numeričke simulacije se upravo koriste da bi moglo da se predvidi određeni efekat u kristalu i da onda na osnovu poređenja slika na izlazu iz kristala iz numerike i eksperimenta možemo da znamo da li je došlo do potvrđivanja željenog efekta prethodno dobijenog u numeričkoj simulaciji. Kada se dobije dobro slaganje slika dobijenih na izlazu iz kristala između eksperimenta i numerike, može se iskoristiti numerička simulacija za prikazivanje distribucije intenziteta kroz kristal.

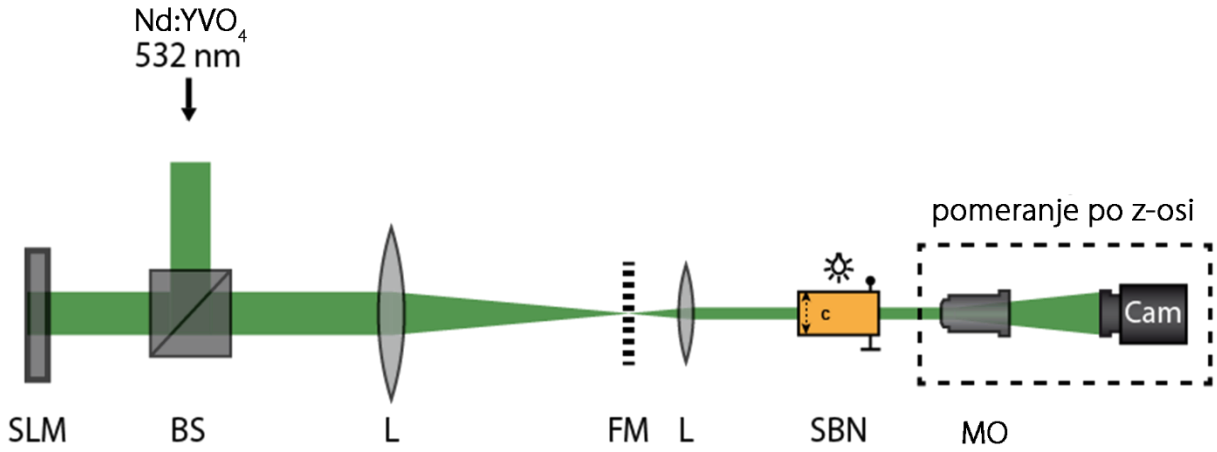

Slika 5.1 Eksperimentalna postavka za ispitivanje interakcije više dvodimenzionalnih Eirijevih snopova u SBN kristalu. **BS**: delitelj snopa; **FM**: Furijeova maska; **L**: sočiva; **MO**: mikroskopski objektiv; **SBN**: kristal Stroncijum Barijum Niobata; **SLM**: prostorni modulatori svetlosti; **Cam**: kamera.

5.1.1 Linearna interakcija više Eirijevih snopova

Karakteristike propagacije samog Eirijevog snopa su bile predmet mnogih eksperimentalnih i numeričkih studija poslednjih godina, uzimajući u obzir linearne i nelinearne efekte, ili propagaciju u nehomogenom ili periodično strukturisanom medijumu. Kao što je dobro poznato, za linearnu propagaciju u homogenom okruženju Eirijevi snopovi prate paraboličnu trajektoriju tokom propagacije. Ovo ponašanje se jasno može videti iz eksperimentalno snimljenog profila intenziteta jednog Eirijevog snopa (Slika 5.2a-c) realizovanog prikazanom eksperimentalnom postavkom (Slika 5.1).

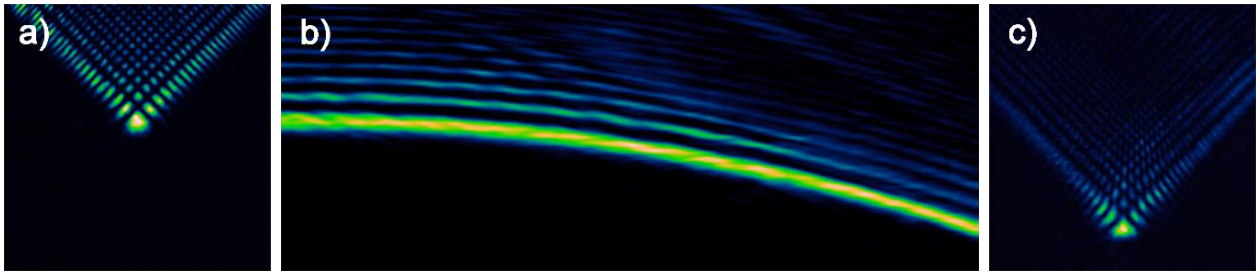

Slika 5.2 Linearna propagacija jednog dvodimenzionalnog Eirijevog snopa kroz homogeni kristal. **(a)** Distribucija intenziteta na ulazu u kristal; **(b)** Poprečni presek prostiranja snopa kroz kristal; **(c)** Distribucija intenziteta na izlazu iz kristala.

Da bi se sistematski ispitivala propagacija i interakcija više dvodimenzionalnih Eirijevih snopova, počinje se uzimajući u obzir najfundamentalniji slučaj dva kopropagirajuća Eirijeva snopa u linearnom režimu. Snopovi su koherentno superponirani sa inicijalnim rastojanjem od d≈50μm i rotirani za 180º, da bi se njihove parabolične trajektorije ukrstile tokom propagacije (Slika 5.3). Longitudinalna pozicija tačke ukrštanja strogo zavisi od krivine Eirijevog snopa koja je određena njegovom veličinom, ali takođe zavisi i od inicijalne separacije. Nastoji se da se posmatra ovo ukrštanje unutar zapremine 20mm dugog SBN kristala. Iz tog razloga, podešava se veličina Eirijevog snopa, merena kao rastojanje između glavnog loba i njegovog susednog, na s≈25μm.

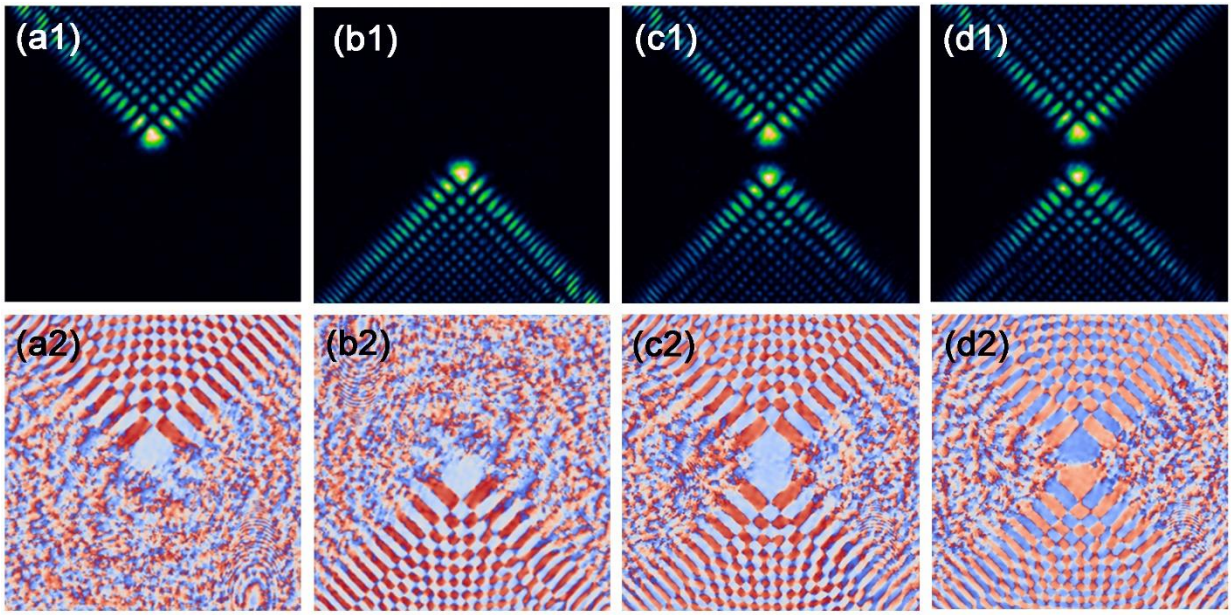

Slika 5.3 Superpozicija dva dvodimenzionalna Eirijeva snopa sa inicijalnim rastojanjem od d≈50μm. **(a, b)** Pojedinačni Eirijevi snopovi zarotirani za 180º stepeni (intenzitet (**a1**, **b1**) i faza (**a2**, **b2**)); **(c)** Superpozicija dva Eirijeva snopa u fazi (intenzitet **(c1)** i faza **(c2)**); **(d)** Superpozicija dva Eirijeva snopa sa π faznom razlikom (intenzitet **(d1)** i faza (**d2**)).

Posle konfiguracije od dva kopropagirajuća Eirijeva snopa u linearnom režimu prelazi se na prvi sledeći složeniji simetrični slučaj, kopropagaciju četiri dvodimenzionalna Eirijeva snopa. Snopovi su takođe koherentno superponirani sa inicijalnim rastojanjem od d≈50μm i rotirani za 90º, da bi se njihove parabolične trajektorije ukrstile tokom propagacije (Slika 5.4). Longitudinalna pozicija tačke ukrštanja i u ovom slučaju strogo zavisi od krivine Eirijevog snopa koja je određena njegovom veličinom, ali takođe zavisi i od inicijalne separacije. Nastoji se da se posmatra ovo

ukrštanje unutar zapremine 20mm dugog SBN kristala. Iz tog razloga, podešava se i ovde veličina Eirijevog snopa, merena kao rastojanje između glavnog loba i njegovog susednog, na s≈25μm.

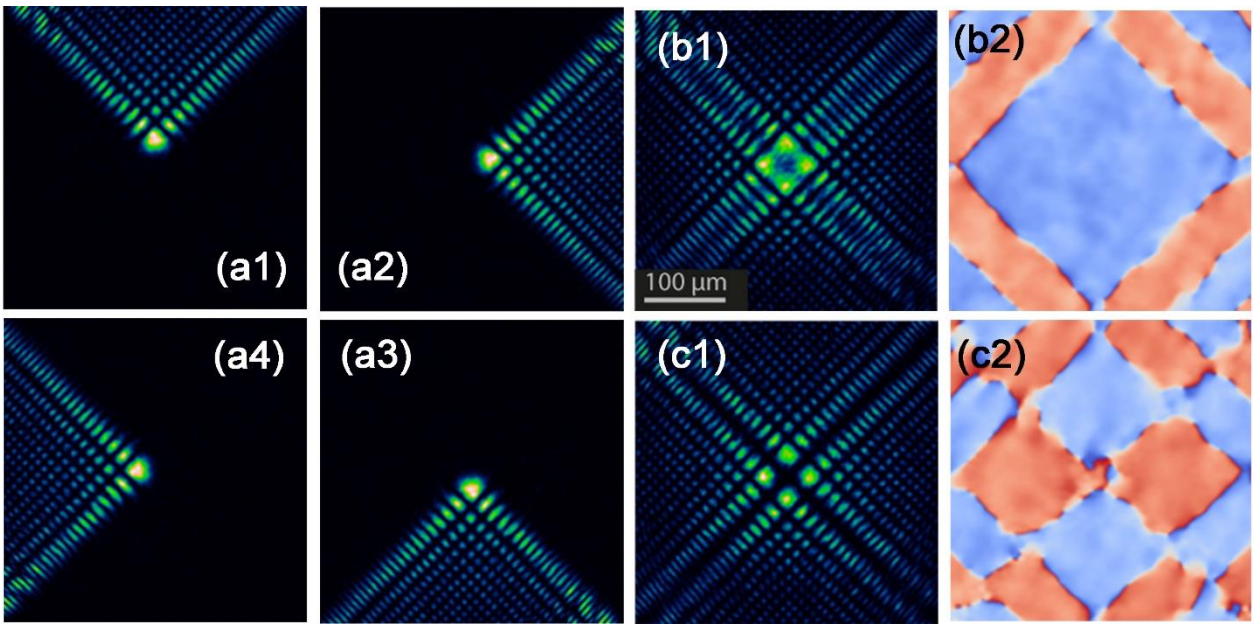

Slika 5.4 Superpozicija četiri dvodimenzionalna Eirijeva snopa sa inicijalnim rastojanjem od d≈50μm. **(a)** Intenzitet pojedinačnih Eirijevih snopova zarotiranih za 90º stepeni; **(b)** Superpozicija četiri Eirijeva snopa u fazi (intenzitet **(b1)** i faza **(b2)**); **(c)** Superpozicija četiri Eirijeva snopa sa π faznom razlikom (intenzitet **(c1)** i faza **(c2)**).

5.1.2 Nelinearna interakcija više Eirijevih snopova

U narednom delu, ispitivaće se i analizirati nelinearna propagacija i interakcija više Eirijevih snopova u fotorefraktivnom SBN kristalu.

Ispitivanje nelinearne interakcije počinje sa fundamentalnom konfiguracijom dva razmeštena Eirijeva snopa (Slika 5.3). Korišćeni su isti parametri snopa opisani za linearni slučaj. Na ulazu, dva snopa su razdvojena za d≈50μm i orijentisana tako da ubrzavaju jedan ka drugom. Na taj način, trajektorije Eirijevih snopova će se ukrstiti i snopovi će imati jaku interakciju. Nasuprot linearnom eksperimentu, sada se povećava snaga snopa, kao i vreme upisivanja radi dobijanja dovoljno velike nelinearnosti. Da bi se posmatrala zavisnost intenziteta od dinamike propagacije podešene su četiri različite snage za probni snop: $P_{in} \approx \{237, 475, 950, 1.425\}$nW i izveden je eksperiment za svaku vrednost, pri čemu su svi ostali parametri ostali nepromenjeni, kao što je jačina eksterno primenjenog stacionarnog polja, vreme indukcije, i iluminacija pozadine.

Posle ispitivanja nelinearnih procesa za osnovni slučaj dva interagujuća Eirijeva snopa, sada se uzima malo komplikovanija konfiguracija, slučaj gde se sintetizuju četiri snopa. Četiri Eirijeva snopa se kombinuju na isti način kao i u slučaju propagacije četiri snopa u linearnom režimu (Slika 5.4). U osnovi, četiri snopa dozvoljavaju više od dve fazne konfiguracije, ali se uprkos tome ovde ograničava na dva slučaja: bilo da su svi snopovi u fazi, bilo da su π fazno pomereni u odnosu na susedni snop. Da bi se posmatrala zavisnost intenziteta od dinamike propagacije podešene su tri različite snage za probni snop: $P_{in} \approx \{0.5, 1.0, 3.0\}$μW i izveden je eksperiment za svaku vrednost, pri čemu su svi ostali parametri ostali nepromenjeni, kao što je jačina eksterno primenjenog stacionarnog polja, vreme indukcije, i iluminacija pozadine.

5.2 Dinamika prostiranja Eirijevog snopa kroz optički indukovanu fotonsku rešetku

Za ispitivanje dinamike prostiranja pojedinačnog dvodimenzionalnog Eirijevog snopa u SBN:Ce kristalu sa optički indukovanom kvadratnom fotonskom rešetkom korišćena je eksperimentalna postavka prikazana na Slici 5.5.

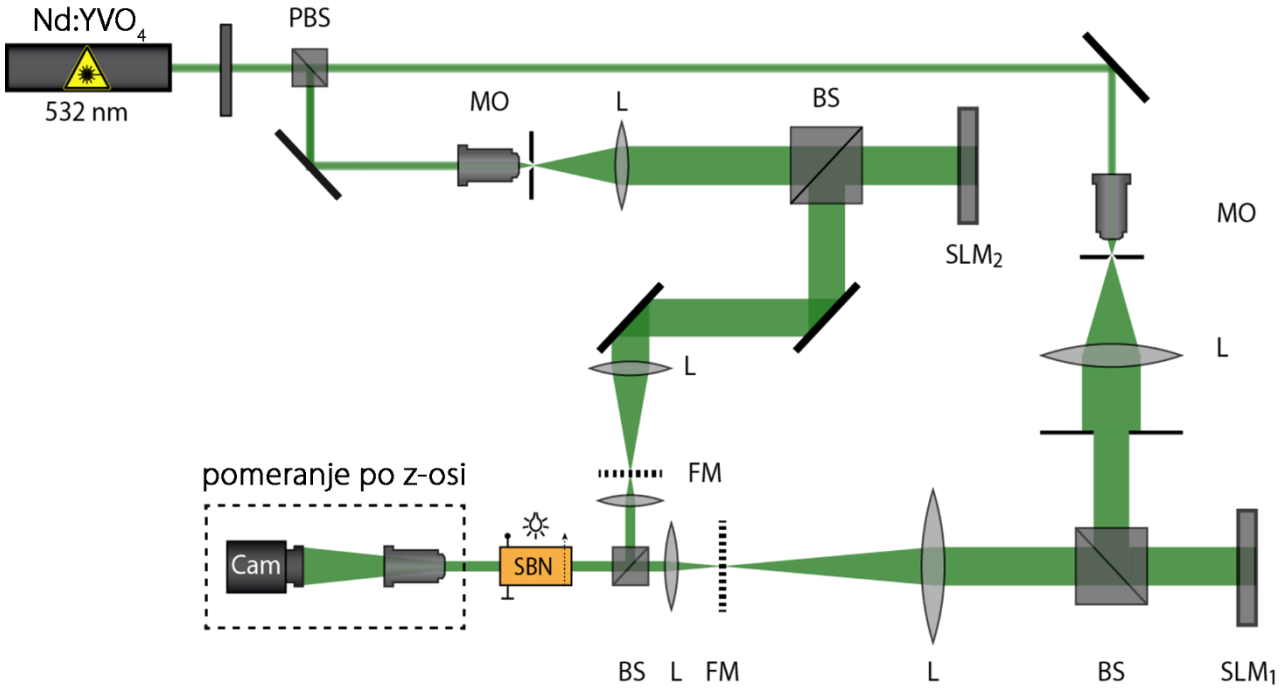

Slika 5.5 Eksperimentalna postavka za realizaciju interakcije dvodimenzionalnog Eirijevog snopa i fotonske kvadratne rešetke. (P)**BS**: (polarizujući) delitelj snopa; **FM**: Furijeova maska; **L**: sočiva; **MO**: mikroskopski objektiv; **SBN**: kristal Stroncijum Barijum Niobata; **SLM1**, **SLM2**: prostorni modulatori svetlosti; **Cam**: kamera.

Laserski snop iz Nd:YVO_4 lasera, talasne dužine 532nm, deli se na dva snopa. Jedan snop služi za formiranje snopa kvadratne rešetke, pomoću prostornog modulatora svetlosti SLM_1. Modulator (SLM_1), u kombinaciji sa sočivima i Furijeovom maskom se koristi za oblikovanje nedifragujućeg snopa za indukovanje kvadratne rešetke (Slika 5.6d) tako što se proračunatom faznom slikom moduliše faza i amplituda Gausovog snopa i na taj način dobija kompleksno optičko polje nedifragujućeg snopa kvadratne rešetke [82]. Nakon toga ovaj modulisani snop pada na polarizujući delitelj snopa i kao redovan zrak (linearno polarizovan zrak koji se kreće paralelno duž c-ose kristala sa pravcem prostiranja električnog polja normalnim u odnosu na optičku c-osu kristala) pada na 20 mm dug nelinearni kristal, SBN:Ce, na koji deluje spoljašnje električno polje jačine E_{ext}=2000V/cm duž optičke c-ose. Dakle, takav upadni snop će se prostirati u linearnom režimu i doći će do kvazi-linearnog upisivanja rešetke.

Drugi snop koji dolazi na modulator SLM_2 se koristi za generisanje dvodimenzionalnog Eirijevog snopa (Slika 5.6a) tako što se na SLM_2 šalje proračunata fazna slika kompleksnog optičkog polja, pa Gausov snop posle difrakcije sa SLM_2 nastavlja prostiranje modulisan u formi dvodimenzionalnog Eirijevog snopa. Posle prolaska kroz Furijeovu masku izdvaja se nulti difrakcioni

red snopa koji dalje pada na polarizacioni delitelj snopa i kao neredovan zrak u odnosu na c-osu kristala pada na nelinearni SBN:Ce kristal.

Slika 5.6d pokazuje snimljenu distribuciju intenziteta eksperimentalno realizovanog nedifragujućeg snopa koji se koristi za optičku indukciju dvodimenzionalne kvadratne rešetke. Period rešetke $\Lambda = \pi / k_t \approx 25\mu m$ je odabran tako da se direktno poklapa sa veličinom Eirijevog snopa (rastojanje između glavnog i njemu susednog loba Eirijevog snopa). Da bi se realizovale rešetke različite jačine Δn, korišćena je činjenica da optički indukovana modulacija indeksa prelamanja u SBN:Ce kristalu raste ako se poveća vreme iluminacije kristala. Osvetljavanjem kristala intenzitetom snopa rešetke za različita vremena trajanja iluminacije dobijene su fotonske rešetke različite jačine. Da bi se verifikovalo da je u kristal upisana odgovarajuća rešetka kristal se osvetljava ravanskim talasom. Prvobitno homogeni intenzitet ravanskog talasa se redistribuira upisanom prostornom modulacijom indeksa prelamanja (optički indukovanom rešetkom) u materijalu koji se zatim lokalizuje u delovima kristala sa većim indeksom prelamanja (Slika 5.6e).

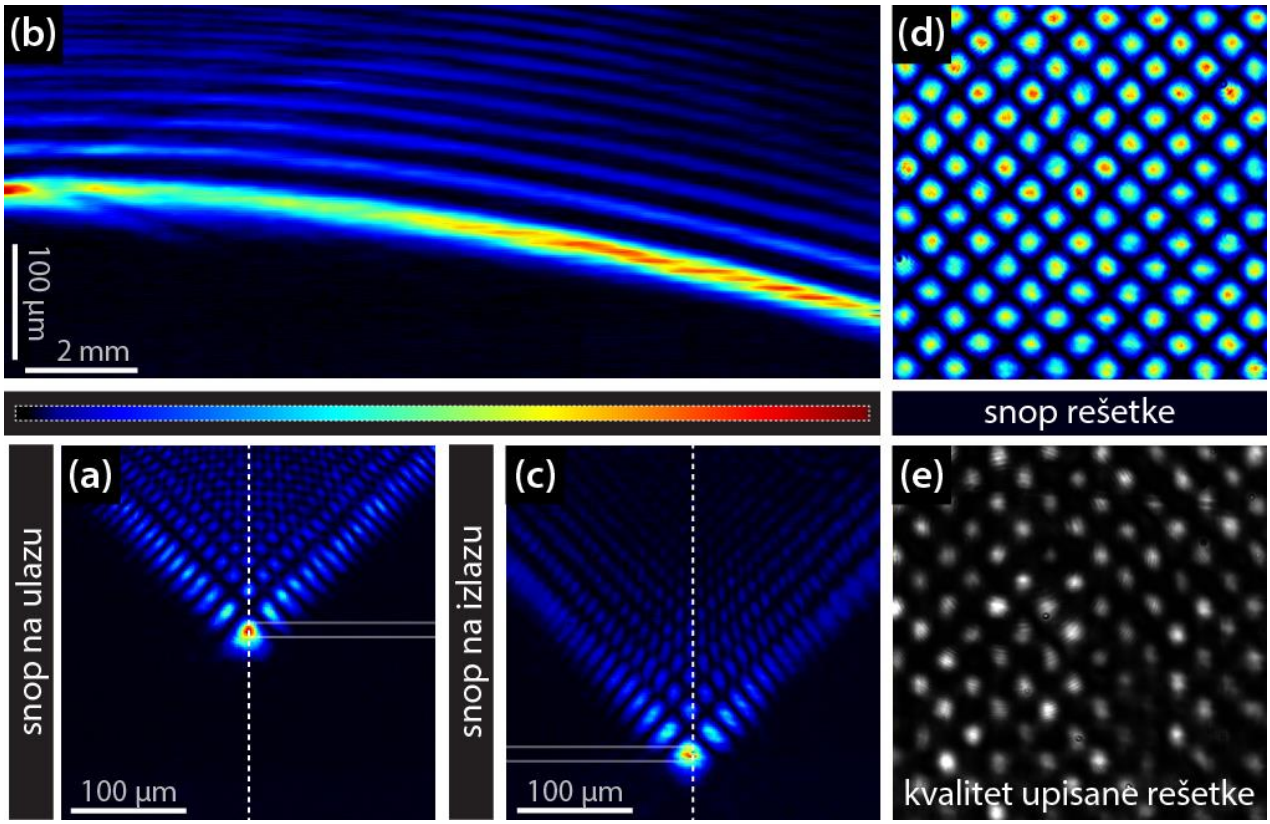

Slika 5.6 Eksperimentalna realizacija interakcije dvodimenzionalnog Eirijevog snopa i fotonske kvadratne rešetke. **(a)** Distribucija intenziteta Eirijevog snopa na ulazu u kristal; **(b)** Eksperimentalno snimljen profil snopa tokom propagacije kroz kristal; **(c)** Distribucija intenziteta Eirijevog snopa na izlasku iz kristala; **(d)** Intenzitet snopa rešetke; **(e)** Slika indukovanog indeksa prelamanja u kristalu dobijena kada se kroz upisanu rešetku propusti svetlosni snop.

Da bi dva snopa u kristalu bila precizno preklopljena, delitelj snopa se postavlja direktno ispred kristala. Ozračavanjem kristala homogeno belom svetlošću, moguće je izbrisati indukovanu modulaciju indeksa prelamanja u celoj zapremini kristala. Pomoću kamere montirane na translacionom postolju snimana je distribucija intenziteta Eirijevog snopa u transverzalnoj ravni na izlasku iz kristala.

5.3 Dinamika prostiranja Eirijevog snopa u fotonskoj rešetci sa različitim defektima

Pored uticaja fotonske kvadratne rešetke, upisane u kristal SBN:Ce, na prostiranje dvodimenzionalnog Eirijevog snopa, ispitivana je i dinamika snopa u sistemu sa pozitivnim i negativnim defektom u jednom kanalu rešetke. Za realizaciju defekata u ovom slučaju korišćen je metod multipleksiranja [69-71] Beselovog snopa nultog reda i snopa za formiranje kvadratne rešetke, za lokalizovano povećavanje ili smanjivanje modulacije indeksa prelamanja u jednom kanalu rešetke.

Princip je sledeći: nekoherentnom superpozicijom osvetljava se kristal naizmenično diskretnim (Slika 5.7a) i Beselovim nedifragujućim snopom (Slika 5.7b). Nekoherencija je neophodna radi izbegavanja neželjenih modulacija intenziteta koji bi nastali usled koherentne superpozicije. Kod SBN:Ce kristala primenjuje se spoljašnje elektrostatičko polje duž optičke *c*-ose kojim se utiče na jačinu elektrooptičkog efekta, odnosno povećanje/smanjenje efektivne modulacije indeksa prelamanja u materijalu. Za razliku od modulacije Beselovim snopom koja je lokalna, modulacija električnim poljem je opšta za celu rešetku. U slučaju pozitivnog defekta primenjuje se spoljašnje elektrostatičko polje orijentacije paralelne u odnosu na *c*-osu kristala i multipleksiranjem snopa kvadratne rešetke i Beselovog snopa postiže se fokusirajuća nelinearnost/modulacija indeksa prelamanja u određenom kanalu rešetke ($n_{defekta} = n_{rešetke} + \Delta n$), dok u slučaju negativnog defekta spoljašnje elektrostatičko polje se orijentiše antiparalelno u odnosu na *c*-osu kristala i dobija se defokusirajuća nelinearnost ($n_{defekta} = n_{rešetke} - \Delta n$).

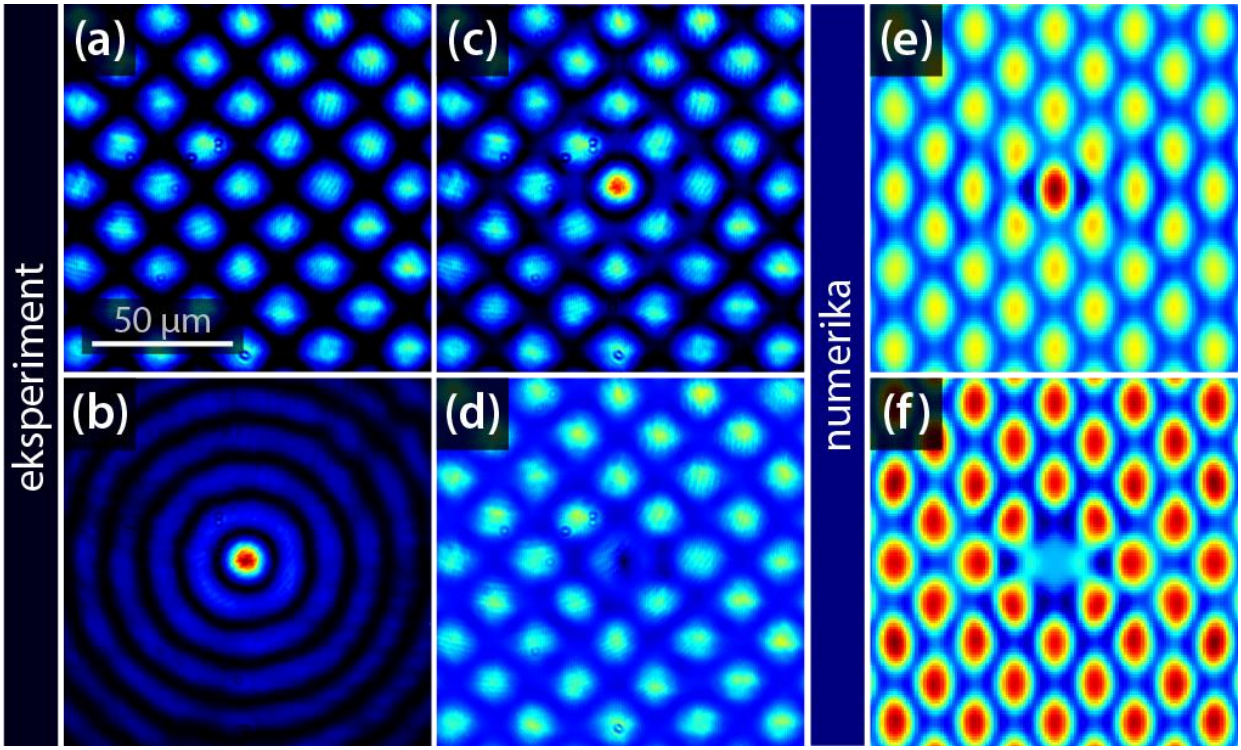

Slika 5.7 Generisanje defekata u optički indukovanoj fotonskoj rešetci. **(a)** Eksperimentalna realizacija kvadratne fotonske rešetke; **(b)** Beselovog snopa; **(c)** pozitivnog defekta rešetke, i **(d)** negativnog defekta rešetke. Numerička realizacija **(e)** pozitivnog i **(f)** negativnog defekta.

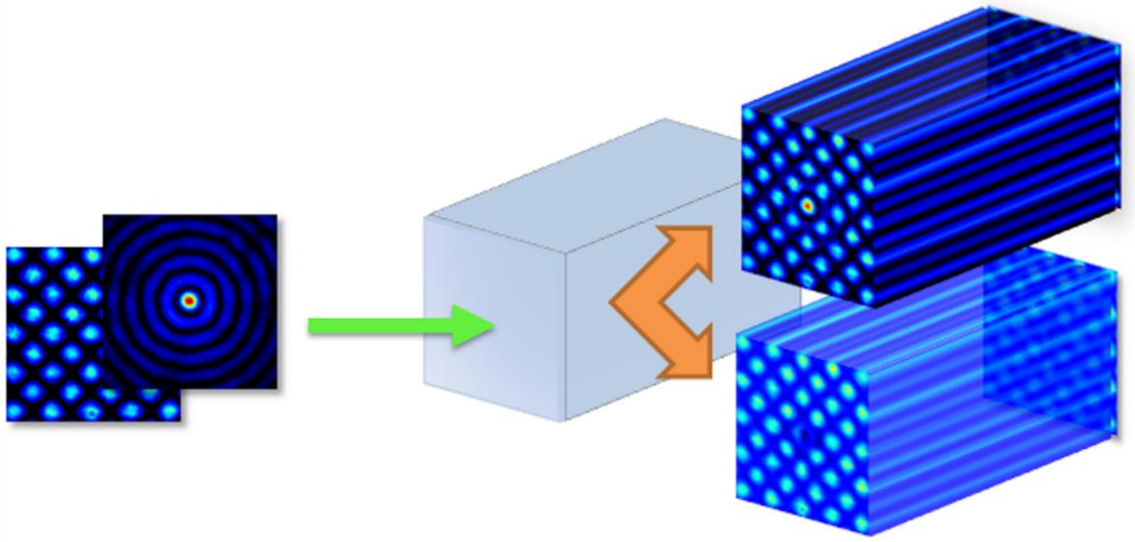

Slika 5.8 Šema generisanja defekata u optički indukovanoj fotonskoj rešetci pomoću nedifragujućih snopova.

Slika 5.8 ilustruje osnovnu šemu realizacije defekta koristeći multipleksirane nedifragujuće snopove. Regularna rešetka se indukuje distribucijom intenziteta prikazanom na Slici 5.7a. Simultano, intenzitet Beselovog snopa prikazan na Slici 5.7b povećava ili smanjuje indukovani indeks prelamanja u jednom talasovodu rešetke, u zavisnosti od pravca primenjenog električnog polja. Rezultujuća efektivna distribucija intenziteta za pozitivni i negativni defekt rešetke prikazana je na Slici 5.7c i 5.7d, respektivno. Slike 5.7e i 5.7f prikazuju numerički proračunate modulacije indeksa prelamanja za oba tipa rešetki sa defektom.

Kada se jednom realizuje rešetka sa defektom, može se ispitivati kako različiti defekti utiču na propagaciju i ubrzanje Eirijevog snopa. Ovde su takođe zadržavani svi parametri iz prethodnih eksperimenata i samo menjan znak defekta, za pozitivni kao i za negativni. Eirijev snop je pozicioniran sa glavnim lobom tačno lociranim na mesto defekta. Za različite defekte, snimljeni su profili intenziteta propagacije Eirijevog snopa na izlazu iz kristala i posmatran je procenat snage Eirijevog snopa vođene u centralnom talasovodu.

Poglavlje 6

Rezultati i diskusija

U ovom poglavlju prikazani su rezultati eksperimentalnog i teorijskog istraživanja. Poglavlje je podeljeno na više celina. U prvoj i drugoj celini prikazani su rezultati međusobne interakcije više dvodimenzionalnih Eirijevih snopova. U prvoj celini dati su rezultati ***linearne interakcije*** dva i četiri superponirana Eirijeva snopa dok su u drugoj celini prikazani rezultati ***nelinearne interakcije*** takođe dva i četiri superponirana Eirijeva snopa.

U trećoj i četvrtoj celini prikazani su rezultati interakcije pojedinačnog Eirijevog snopa sa fotonskim strukturama upisanim u SBN kristalu. U trećoj celini dati su rezultati ispitivanja prostiranja pojedinačnog Eirijevog snopa u SBN kristalu sa upisanom kvadratnom fotonskom rešetkom. U četvrtoj celini dati su rezultati ispitivanja prostiranja pojedinačnog Eirijevog snopa u SBN kristalu sa upisanom fotonskom rešetkom u kojoj je indukovan pozitivni kao i negativni optički defekt. Pokazano je da jačina defekata kao i jačina fotonske rešetke dramatično utiče na oblik i transverzalno ubrzanje Eirijevog snopa.

6.1 Linearna interakcija više dvodimenzionalnih Eirijevih snopova

Kao što je dobro poznato, za linearnu propagaciju u homogenom okruženju Eirijevi snopovi prate paraboličnu trajektoriju tokom propagacije. Ovde se sada može videti šta se dešava ako se izvrši simetrična superpozicija više Eirijevih snopova u različitim konfiguracijama.

6.1.1 Linearna interakcija dva Eirijeva snopa

Polazi se prvo od najjednostavnijeg slučaja, linearne interakcije dva Eirijeva snopa. Razmatramo dva slučaja gde su snopovi bilo u fazi, ili za π izvan faze. Ovi različiti inicijalni uslovi rezultuju različitim transverzalnim profilima intenziteta tokom propagacije usled interferencije. Eksperimentalni rezultati za dva Eirijeva snopa prikazani su na Slikama 6.1a, 6.1b, sa odgovarajućim numeričkim simulacijama na Slikama 6.1c, 6.1d. Za konfiguraciju „u fazi“, oslikanu na Slikama 6.1a, 6.1c, jako izražen fokus se formira konstruktivnom interferencijom snopova u oblasti ukrštanja obe parabolične trajektorije. Ovo svojstvo veoma visokog lokalnog intenziteta u poređenju sa okolinom je prethodno opisano kao ključna prednost tzv autofokusirajućih snopova. Za slučaj „π fazne razlike“, prikazanom na Slikama 6.1b, 6.1d, fazna razlika od π između snopova na ulazu dovešće do vertikalne separacije tamnom linijom destruktivne interferencije koja je očuvana tokom cele propagacije. U oba slučaja, parabolične trajektorije dva superponirana Eirijeva snopa se jasno mogu identifikovati. Kako

je za sada propagacija kompletno linearna, kompleksni paterni intenziteta su rezultat samo interferencije, ali snopovi ne interaguju i ne utiču jedan na drugog. Iz tog razloga, njihove inicijalne osnovne parabolične trajektorije su očuvane iako se trajektorije snopova ukrštaju.

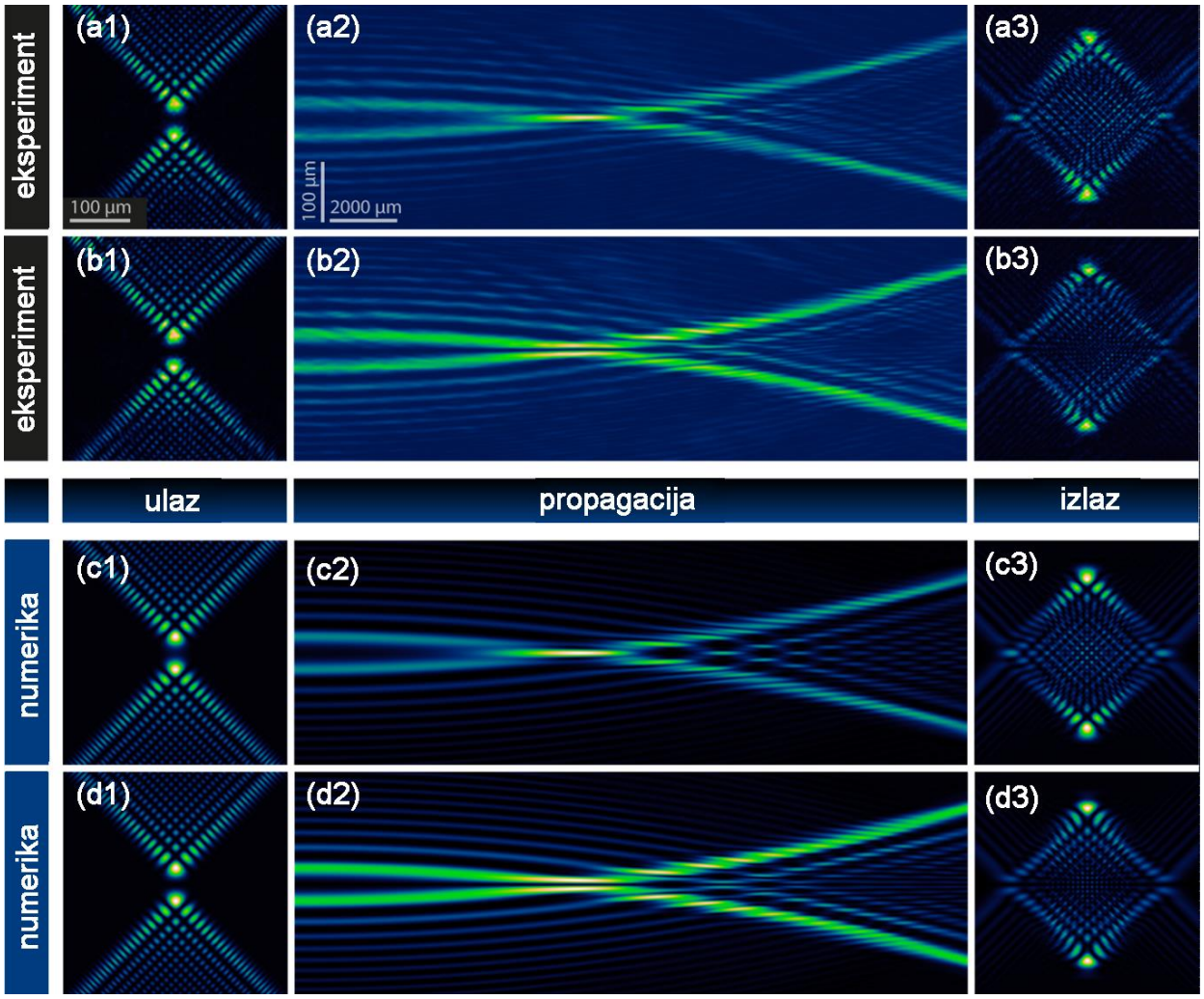

Slika 6.1 Linearna interakcija dva Eirijeva snopa u homogenom linearnom medijumu. **(a)** Eksperimentalni rezultati interferencije dva Eirijeva snopa u fazi - [**(a1)** intenzitet superpozicije dva Eirijeva snopa u fazi na ulazu u SBN kristal, **(a2)** prikaz propagacije kroz 20mm dug SBN kristal, **(a3)** intenzitet superpozicije dva Eiriieva snopa na izlazu iz kristala]; **(b)** Eksperimentalni rezultati interferencije dva Eirijeva snopa sa π faznom razlikom - [**(b1)** intenzitet superpozicije dva Eirijeva snopa u fazi na ulazu u SBN kristal, **(b2)** prikaz propagacije kroz 20mm dug SBN kristal, **(b3)** intenzitet superpozicije dva Eiriieva snopa na izlazu iz kristala]; **(c)** Numerički rezultati interferencije dva Eirijeva snopa u fazi - [**(c1)** intenzitet superpozicije dva Eirijeva snopa u fazi na ulazu u SBN kristal, **(c2)** prikaz propagacije kroz 20mm dug SBN kristal, **(c3)** intenzitet superpozicije dva Eiriieva snopa na izlazu iz kristala]; **(d)** Numerički rezultati interferencije dva Eirijeva snopa sa π faznom razlikom - [**(d1)** intenzitet superpozicije dva Eirijeva snopa u fazi na ulazu u SBN kristal, **(d2)** prikaz propagacije kroz 20mm dug SBN kristal, **(d3)** intenzitet superpozicije dva Eiriieva snopa na izlazu iz kristala].

6.1.2 Linearna interakcija četiri Eirijeva snopa

Povećanjem broja superponiranih snopova, sledeća simetrična konfiguracija se može konstruisati sa četiri razmeštena Eirijeva snopa, gde je svaki zarotiran za 90^0, kao što je prikazano na Slikama 6.2a1 i 6.2c1.

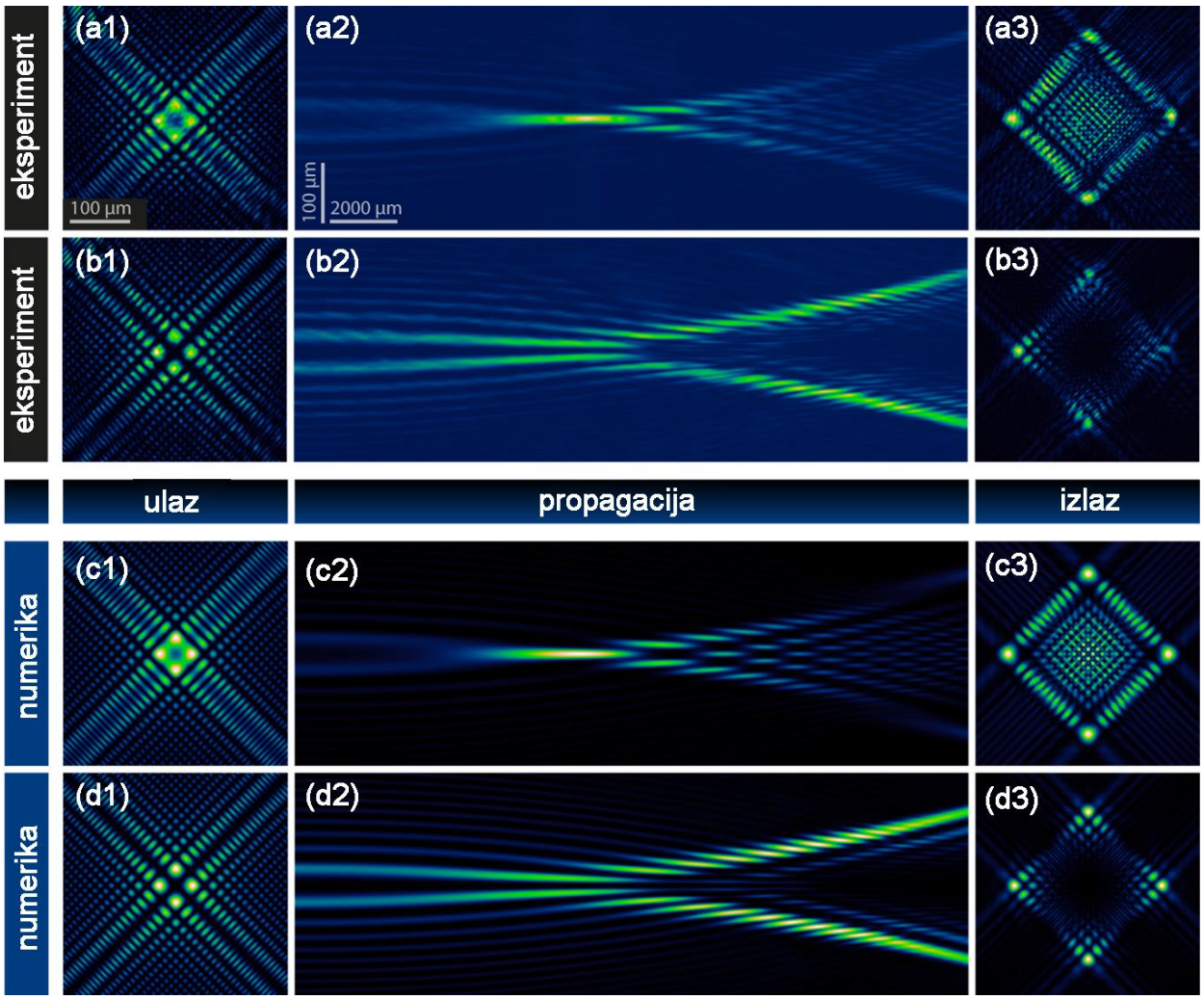

Slika 6.2 Linearna interakcija četiri Eirijeva snopa u homogenom linearnom medijumu. **(a)** Eksperimentalni rezultati interferencije četiri Eirijeva snopa u fazi - [**(a1)** intenzitet superpozicije dva Eirijeva snopa u fazi na ulazu u SBN kristal, **(a2)** prikaz propagacije kroz 20mm dug SBN kristal, **(a3)** intenzitet superpozicije četiri Eiriieva snopa na izlazu iz kristala]; **(b)** Eksperimentalni rezultati interferencije četiri Eirijeva snopa sa π faznom razlikom - [**(b1)** intenzitet superpozicije četiri Eirijeva snopa u fazi na ulazu u SBN kristal, **(b2)** prikaz propagacije kroz 20mm dug SBN kristal, **(b3)** intenzitet superpozicije četiri Eiriieva snopa na izlazu iz kristala]; **(c)** Numerički rezultati interferencije četiri Eirijeva snopa u fazi - [**(c1)** intenzitet superpozicije četiri Eirijeva snopa u fazi na ulazu u SBN kristal, **(c2)** prikaz propagacije kroz 20mm dug SBN kristal, **(c3)** intenzitet superpozicije četiri Eiriieva snopa na izlazu iz kristala]; **(d)** Numerički rezultati interferencije četiri Eirijeva snopa sa π faznom razlikom - [**(d1)** intenzitet superpozicije četiri Eirijeva snopa u fazi na ulazu u SBN kristal, **(d2)** prikaz propagacije kroz 20mm dug SBN kristal, **(d3)** intenzitet superpozicije četiri Eiriieva snopa na izlazu iz kristala].

U principu postoji više mogućnosti za postavku relativnih faza snopova, ali je istraživanje ograničeno na sledeća dva slučaja: ili su snopovi u fazi (Slike 6.2a, 6.2c), ili su susedni snopovi sa π faznom razlikom (Slike 6.2b, 6.2d). Dok transverzalni profili intenziteta sada izgledaju dosta drugačije u poređenju sa situacijom gde su dva snopa superponirana, longitudinalni poprečni preseci otkrivaju slično ponašanje tokom propagacije. Opet, dolazi do formiranja fokusa velikog intenziteta u oblasti gde četiri Eirijeva snopa koja su u fazi konstruktivno interferiraju, dok se tamna linija destruktivne interferencije javlja kao separator snopova u slučaju π fazne razlike. Usled činjenice da sada četiri snopa interferira, relativna jačina fokusa za konstruktivnu interferenciju je mnogo veća nego kod dva snopa. Broj interferirajućih Eirijevih snopova se može dalje povećavati dok se kontrast između fokalnog intenziteta i pozadine kontinualno povećava do granice koja se postiže radijalnom distribucijom Eirijevih snopova.

Svi prikazani eksperimentalni rezultati su podržani odgovarajućim numeričkim simulacijama. Za propagaciju više Eirijevih snopova u linearnom režimu numerički rezultati se savršeno poklapaju sa eksperimentalnim merenjima.

6.2 Nelinearna interakcija više dvodimenzionalnih Eirijevih snopova

Iz gore navedenih rezultata vidi se da tokom linearne propagacije više Eirijevih snopova sama interferencija već vodi do zanimljivih distribucija intenziteta, čak iako snopovi ne interaguju i ne utiču jedni na druge. Prema teoretskim modelima i eksperimentima pri nelinearnoj interakciji svetlosti i materije mogu se očekivati zanimljivi novi efekti kao što je na primer formiranje solitona, što je i predviđeno na osnovu numeričkih rezultata [83, 84].

Ova kompleksna nelinearnost značajno menja dinamiku propagacije Eirijevih snopova i dovodi do fascinantnih novih tipova evolucije snopa koje za razliku od linearnog režima zavise i od broja superponiranih snopova, njihove relativne faze i intenziteta. U ovoj sekciji prikazani su eksperimentalni i numerički rezultati za nelinearnu interakciju dva i četiri superponirana dvodimenzionalna Eirijeva snopa.

6.2.1 Nelinearna interakcija dva Eirijeva snopa

Kao i u slučaju linearne interakcije polazi se od najjednostavnije konfiguracije, tj. dva snopa, i posmatraju slučajevi sa različitim faznim distribucijama. Eksperimentalni i numerički rezultati za snopove "u fazi" prikazani su na Slici 6.3. U eksperimentu, Slika 6.3a, prilikom povećavanja snage probnog snopa, $P_{\text{in}} \approx \{237, 475, 950, 1.425\}$ nW (Slike 6.3a1-a4, respektivno), može se videti prelaz sa gotovo linearnog paterna interferencije (Slika 6.3a1) na dobro lokalizovano, solitarno stanje izlaza za veće nelinearnosti (Slike 6.3a3 i 6.3a4). Ovo lokalizovano stanje potiče od tačke ukrštanja trajektorija snopova, gde se javlja konstruktivna interferencija Eirijevih snopova "u fazi". Interferencija dovodi do strogo lokalizovanog i pojačanog intenziteta. Posle toga, propagacija je gotovo nepromenjena, osim malog oscilovanja, usled kompenzacije difrakcije i nelinearnog samofokusiranja. Ovo spojeno lokalizovano stanje dalje propagira ravno očigledno bez bilo kakvog transverzalnog momenta zaostalog od inicijalnih snopova sa paraboličnom putanjom. Nelinearnost dovodi do toga da za ovu kompleksnu interakciju između dva snopa kao posledica dolazi do kompenzacije ubrzanja. Intenzitet pika rezultujućeg stanja na izlazu je naravno veći nego na ulazu gde se individualni snopovi ne preklapaju značajno. Faktor $r = I_{max,out}/I_{max,in}$ predstavlja odnos između maksimalnog intenziteta na izlazu i ulazu, respektivno. Kako u ovom eksperimentu nije moguće imati uvid u distribuciju intenziteta kroz nehomogeni medijum, dostupan nam je samo intenzitet na izlazu iz kristala. Faktor $\boldsymbol{r}$ nam pomaže u kvantitativnoj komparaciji eksperimenta i numerike. U slučaju eksperimenta faktor intenziteta je iznosio $r = \{1.2, 1.1, 3.1, 2.6\}$ (Slike 6.3a1-a4, respektivno).

Poređenje između eksperimentalnih rezultata (Slika 6.3a) i numeričke simulacije prikazane na Slici 6.3b i 6.3c pokazuje veoma dobro ukupno slaganje. Prema različitim snagama probnog snopa u eksperimentu, simulirana je nelinearna propagacija za odgovarajuće ulazne intenzitete $I_{\text{in}} \approx \{0.33, 0.65, 1.30, 1.95\}$ (Slike 6.3b1-b4, respektivno). Izlazni profili, kao i faktor intenziteta, koji u slučaju numerike iznosi $r = \{1.0, 1.1, 3.4, 2.6\}$ (Slike 6.3b1-b4, respektivno) savršeno se slažu sa realnom obzervacijom u eksperimentu. Ovo verifikuje da implementirane numeričke metode egzaktno opisuju realnu situaciju i opravdavaju uključivanje numeričkih simulacija radi dobijanja detalja o tome do kakve dinamike dolazi prilikom nelinearne propagacije u SBN kristalu. Kao što je i prethodno navedeno, u eksperimentu ovi podaci nisu dostupni usled osnovnih fizičkih razloga.

Slika 6.3c prikazuje zapreminsko renderovanje numerički dobijenih distribucija intenziteta tokom nelinearne propagacije. Formacija solitarnog stanja je jasno vidljiva. Dok se tokom procesa izgradnje mogu primetiti modulacije u obliku i intenzitetu solitarnog stanja (usled prolaženja ostalih susednih lobova inicijalnih Eirijevih snopova), posle nekog rastojanja propagacije situacija se stabilizuje i solitarno stanje propagira gotovo nepromenjeno osim malog oscilovanja. Označena ravan

na Slici 6.3c odgovara dužini SBN kristala (20 mm) i slikama intenziteta na izlazu iz kristala (Slike 6.3a i 6.3b).

Slično ponašanje lokalizacije se javilo i u numerici za jednostavne idealizovane izotropne Kerove i saturabilne Kerove nelinearnosti [83]. Za prikazane eksperimentalne i numeričke rezultate u realističnom fotorefraktivnom SBN kristalu, situacija je mnogo više komplikovana, usled anizotropne, saturabilne i drift-dominantne nelinearnosti. Neznatni pomeraj pikova intenziteta u horizontalnom pravcu se može objasniti dodatnim uzimanjem u obzir i dufuzionih efekata u numeričkom modelu.

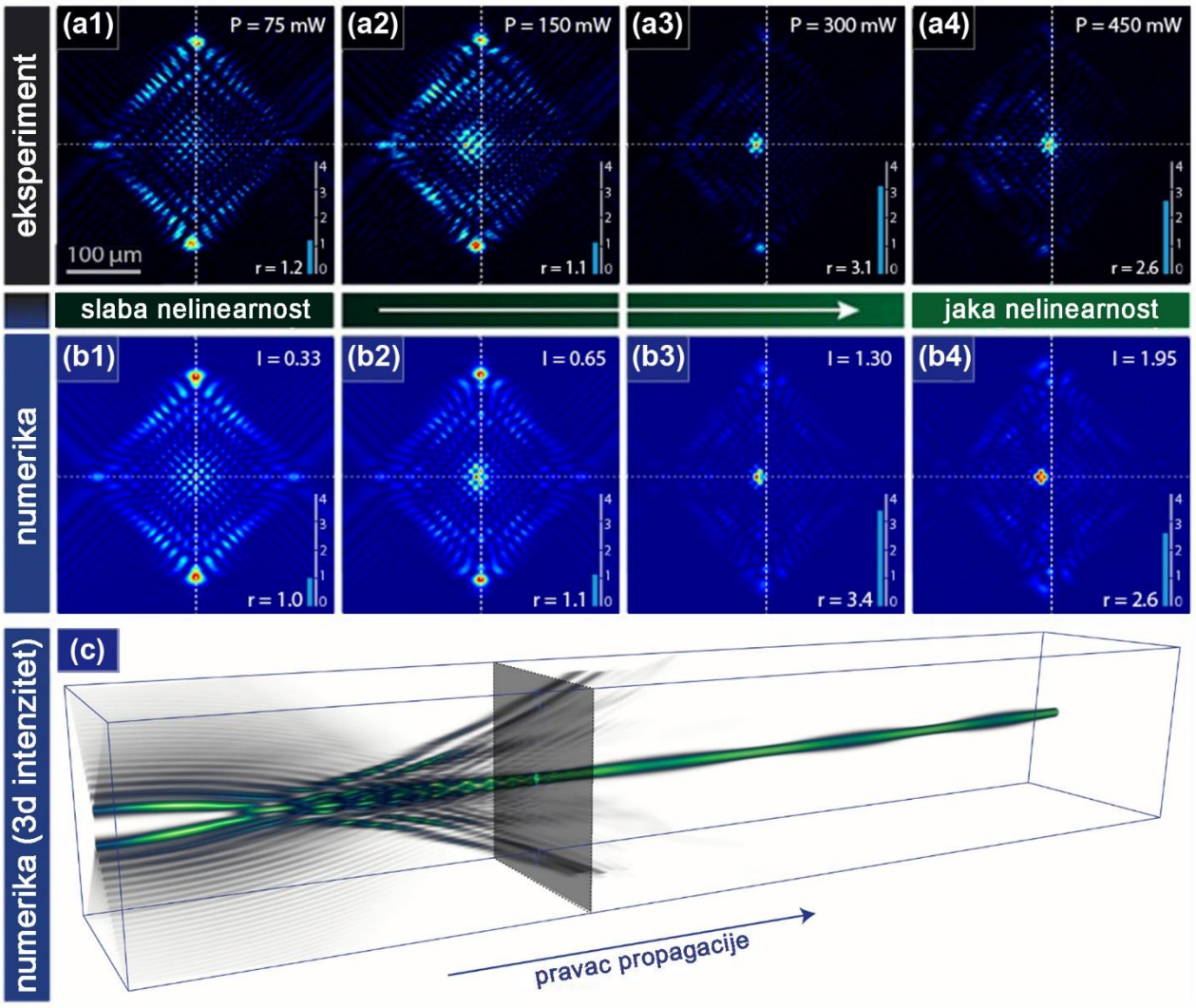

Slika 6.3 Nelinearna interakcija dva Eirijeva snopa u fazi. **(a)** Eksperimentalni rezultati za različite vrednosti snage probnog snopa P_{in} i faktora intenziteta ***r***, [**(a1)** $P_{in} \approx 237$ nW i $r = 1.2$; **(a2)** $P_{in} \approx 475$ nW i $r = 1.1$; **(a3)** $P_{in} \approx 950$ nW i $r = 3.1$; **(a4)** $P_{in} \approx 1{,}425$ nW i $r = 2.6$] **(b)** Rezultati iz odgovarajućih numeričkih simulacija za različite vrednosti intenziteta snopa I_{in} i faktora intenziteta ***r***, [**(b1)** $I_{in} \approx 0.33$ i $r = 1.0$; **(b2)** $I_{in} \approx 0.65$ i $r = 1.1$; **(b3)** $I_{in} \approx 1.30$ i $r = 3.4$; **(b4)** $I_{in} \approx 1.95$ i $r = 2.6$] **(c)** trodimenzionalni prikaz numerički proračunate distribucije intenziteta za nelinearnost pri kojoj dolazi do formiranja solitarnog stanja.

Eksperimentalni i numerički rezultati za snopove različitih faznih distribucija, sa π faznom razlikom, prikazani su na Slici 6.4. Prilikom povećavanja snage probnog snopa u eksperimentu, $P_{in} \approx$ {237, 475, 950, 1.425} nW (Slike 6.4a1-a4, respektivno) situacija se kompletno menja. Dva glavna

loba se ne preklapaju usled linije separacije destruktivne interferencije u sredini između snopova. Kao posledica toga, grade se dva lokalizovana solitarna stanja i stabilno propagiraju kao par tokom velikih rastojanja. Nelinearnost dovodi do toga da za ovu kompleksnu interakciju između dva snopa kao posledica dolazi do kompenzacije ubrzanja. U slučaju eksperimenta faktor intenziteta je iznosio r = {1.0, 0.9, 1.1, 2.0} (Slike 6.4a1-a4, respektivno).

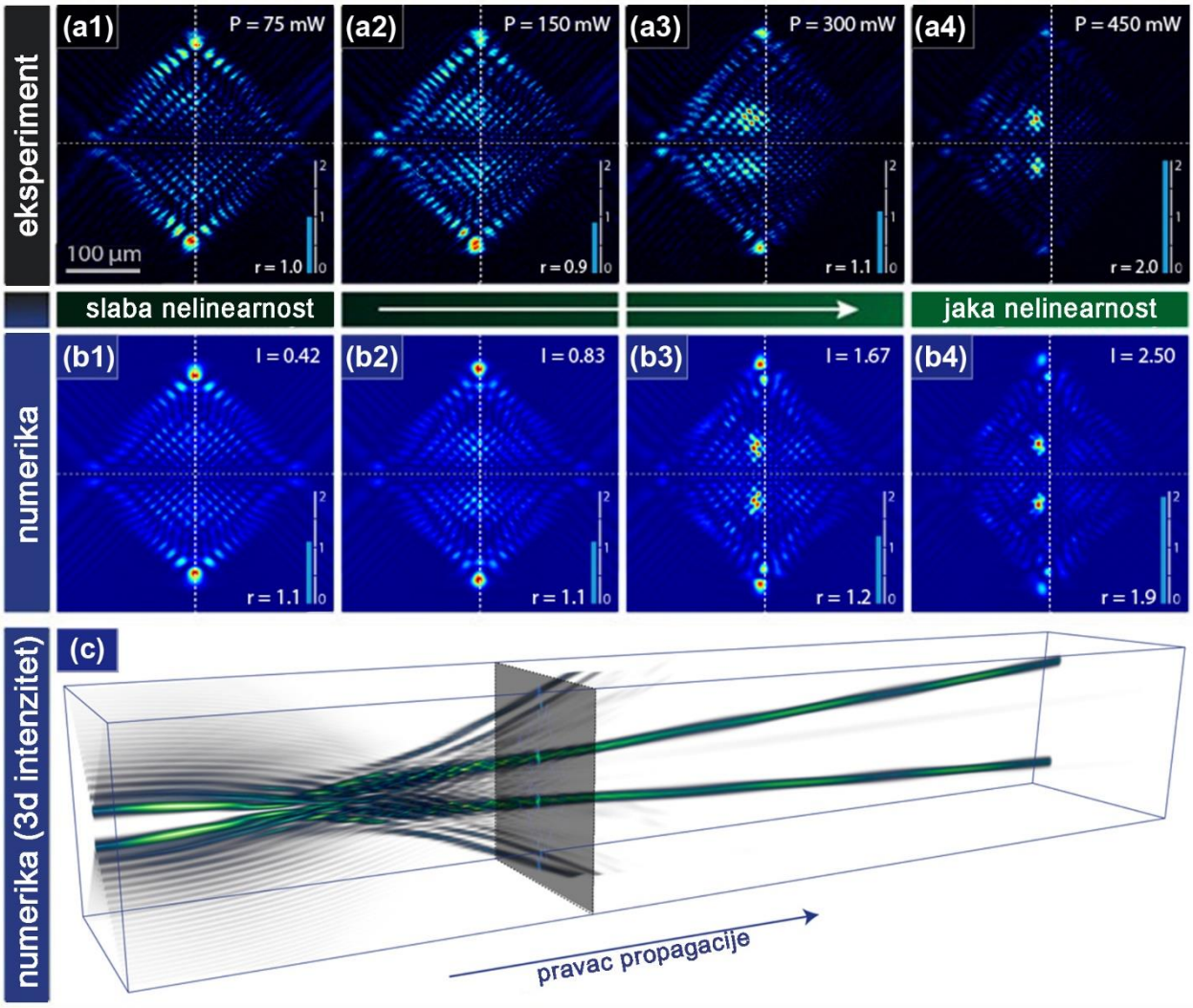

Slika 6.4 Nelinearna interakcija dva Eirijeva snopa sa π faznom razlikom. **(a)** Eksperimentalni rezultati za različite vrednosti snage probnog snopa P_{in} i faktora intenziteta ***r*** [**(a1)** $P_{in} \approx 237$ nW i r = 1.0; **(a2)** $P_{in} \approx 475$ nW i r = 0.9; **(a3)** $P_{in} \approx 950$ nW i r = 1.1; **(a4)** $P_{in} \approx 1.425$ nW i r = 2.0] **(b)** Rezultati iz odgovarajućih numeričkih simulacija za različite vrednosti intenziteta snopa I_{in} i faktora intenziteta ***r***, [**(b1)** $I_{in} \approx 0.42$ i r = 1.1; **(b2)** $I_{in} \approx 0.83$ i r = 1.1; **(b3)** $I_{in} \approx 1.67$ i r = 1.2; **(b4)** $I_{in} \approx 2.50$ i r = 1.9] **(c)** trodimenzionalni prikaz numerički proračunate distribucije intenziteta za nelinearnost pri kojoj dolazi do formiranja stanja solitarnog para.

Poređenje između eksperimentalnih rezultata (Slika 6.4a) i numeričke simulacije prikazane na Slici 6.4b i 6.4c pokazuje veoma dobro ukupno slaganje. Prema različitim snagama probnog snopa u eksperimentu, simulirana je nelinearna propagacija za odgovarajuće ulazne intenzitete $I_{in} \approx$ {0.42, 0.83, 1.67, 2.50} (Slike 6.4b1-b4, respektivno). Izlazni profili, kao i faktor intenziteta, koji u slučaju numerike iznosi r = {1.1, 1.1, 1.2, 1.9} (Slike 6.4b1-b4, respektivno) savršeno se slažu sa realnom obzervacijom u eksperimentu. Ovo verifikuje da implementirane numeričke metode i u ovom slučaju

egzaktno opisuju realnu situaciju i opravdavaju uključivanje numeričkih simulacija radi dobijanja detalja o tome do kakve dinamike dolazi prilikom nelinearne propagacije u SBN kristalu. Kao što je i prethodno navedeno, u eksperimentu ovi podaci nisu dostupni usled osnovnih fizičkih razloga.

Slika 6.4c prikazuje zapreminsko renderovanje numerički dobijenih distribucija intenziteta tokom nelinearne propagacije. Formacija dva lokalizovana stanja, solitarnog para, je jasno vidljiva. Dok se tokom procesa izgradnje mogu primetiti modulacije u obliku i intenzitetu kod oba solitarna stanja (takođe usled prolaženja ostalih susednih lobova inicijalnih Eirijevih snopova), posle nekog rastojanja propagacije situacija se stabilizuje i solitarni par propagira gotovo nepromenjeno osim malog oscilovanja. Označena ravan na Slici 6.4c odgovara dužini SBN kristala (20 mm) i slikama intenziteta na izlazu iz kristala (Slike 6.4a i 6.4b).

Uvedeni sa inicijalnom faznom razlikom, ova dva solitona takođe imaju faznu razliku od π i samim tim odbijaju jedan drugog, kao što je slučaj i kod fundamentalnih solitona [85]. Dakle, oni propagiraju na ravnim linijama ali sa malom divergencijom, kao što se može videti na Slici 6.4c. Preostali lobovi inicijalno lansiranih Eirijevih snopova dalje prate svoje parabolične trajektorije i ubrzo odlaze van zapremine kristala.

6.2.2 Nelinearna interakcija četiri Eirijeva snopa

Posle ispitivanja nelinearnih procesa za osnovni slučaj dva interagujuća Eirijeva snopa, sada se prelazi na malo složeniju konfiguraciju, slučaj gde se sintetizuju četiri snopa. Četiri Eirijeva snopa se kombinuju na način da se njihove trajektorije ukrste, kao i u linearnom režimu. U osnovi, četiri snopa dozvoljavaju više od dve fazne konfiguracije, uprkos tome istraživanje je ograničeno na dva slučaja: bilo da su svi snopovi u fazi, bilo da su π fazno pomereni u odnosu na susedni snop. Ova dva slučaja daju kompletno različite rezultate.

Za slučaj gde su svi snopovi u fazi, rezultati su prikazani na Slici 6.5. Iako struktura transverzalnog intenziteta na izlazu iz kristala izgleda drugačije u slučaju četiri superponirana snopa, generalno, nelinearno ponašanje je jako slično slučaju sa dva Eirijeva snopa u fazi (Slika 6.3). Sa povećavanjem nelinearnosti, intenzitet se lokalizuje u sredini i formira stabilno solitarno stanje koje nastaje iz konstruktivne interferencije snopova u oblasti ukrštanja njihovih trajektorija. Eksperimentalni rezultati za tri različita intenziteta snopa $P_{in} \approx \{0.5, 1.0, 3.0\}\mu W$ (Slike 6.5a1-a3, respektivno) jasno pokazuju opisano formiranje solitarnog stanja kao prelaz od četiri odvojena Eirijeva glavna loba (Slika 6.5a1) do lokalizovanog stanja visokog intenziteta (Slika 6.5a3). Ovde, odnos ***r*** između maksimalnog intenziteta na ulazu u intenziteta pika izgrađenog solitarnog stanja je mnogo veće u poređenju sa slučajem od dva snopa, što je razumljivo jer je u pitanju spajanje četiri snopa. U slučaju eksperimenta faktor intenziteta je iznosio $r = \{1.6, 2.4, 6.9\}$ (Slike 6.5a1-a3, respektivno).

Poređenje između eksperimentalnih rezultata (Slika 6.5a) i numeričke simulacije prikazane na Slici 6.5b i 6.5c pokazuje i ovaj put veoma dobro ukupno slaganje. Prema različitim snagama probnog snopa u eksperimentu, simulirana je nelinearna propagacija za odgovarajuće ulazne intenzitete $I_{in} \approx \{0.125, 0.25, 0.75\}$ (Slike 6.5b1-b3, respektivno). Izlazni profili, kao i faktor intenziteta, koji u slučaju numerike iznosi $r = \{1.9, 2.7, 7.0\}$ (Slike 6.5b1-b3, respektivno) savršeno se slažu sa realnom obzervacijom u eksperimentu.

Situacija se kompletno menja za konfiguraciju četiri snopa sa π faznom razlikom između susednih snopova. Odgovarajući rezultati su prikazani na Slici 6.6. Eksperimentalni rezultati za tri različita intenziteta snopa $P_{in} \approx \{0.5, 1.0, 3.0\}\mu W$ (Slike 6.6a1-a3, respektivno) jasno pokazuju da ovde u suprotnosti sa ostalim prikazanim slučajevima, ovde ne dolazi do formiranja ni pravilnog solitona ni para ili grupe solitona. U slučaju eksperimenta faktor intenziteta je iznosio $r = \{1.9, 1.7, 3.3\}$ (Slike 6.6a1-a3, respektivno).

Poređenje između eksperimentalnih rezultata (Slika 6.6a) i numeričke simulacije prikazane na Slici 6.6b i 6.6c pokazuje veoma dobro ukupno slaganje. Prema različitim snagama probnog snopa u eksperimentu, simulirana je nelinearna propagacija za odgovarajuće ulazne intenzitete $I_{in} \approx \{0.25, 0.50, 1.50\}$ (Slike 6.6b1-b3, respektivno). Izlazni profili, kao i faktor intenziteta, koji u slučaju numerike iznosi $r = \{1.8, 1.7, 2.4\}$ (Slike 6.6b1-b3, respektivno) savršeno se slažu sa realnom obzervacijom u eksperimentu.

Usled faznih razlika, ne javlja se mesto visokog intenziteta usled interferencije na preseku trajektorija snopova koje bi moglo da proizvede soliton. Čak štaviše, zaostali susedni lobovi četiri Eirijeva snopa sprečavaju izgradnju solitarnog stanja ili klastera, kao što je posmatrano u prethodnom slučaju za dva snopa (Slika 6.4). Kod većih intenziteta, intenzitet teži da se lokalizuje pretežno sa jedne strane (Slika 6.6a3) i nastavlja prostiranje sve dalje od centra.

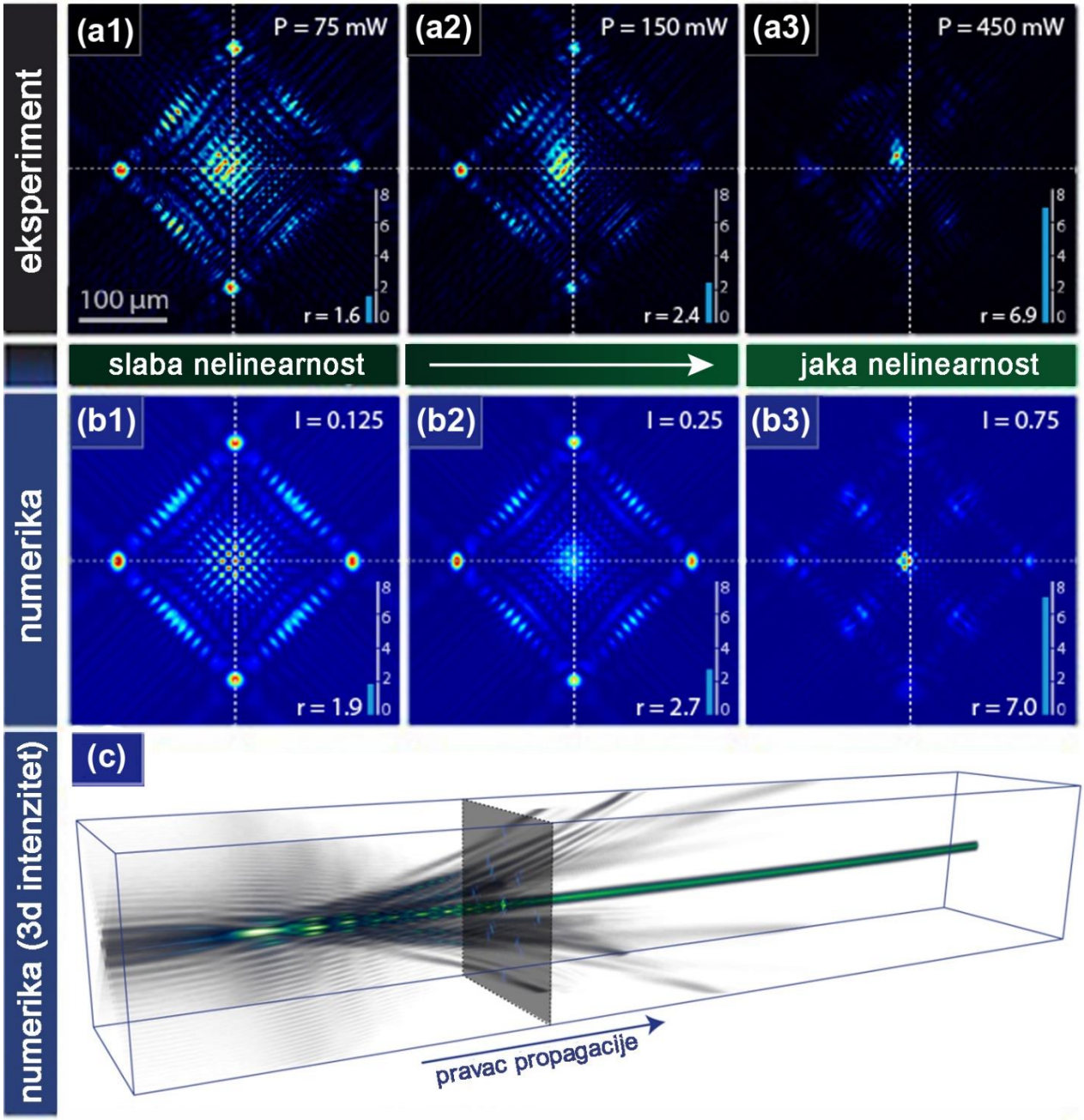

Slika 6.5 Nelinearna interakcija četiri Eirijeva snopa u fazi. **(a)** Eksperimentalni rezultati za različite vrednosti snage probnog snopa P_{in} i faktora intenziteta ***r***, [**(a1)** $P_{in} \approx 0.5$ µW i $r = 1.6$; **(a2)** $P_{in} \approx 1.0$ µW i $r = 2.4$; **(a3)** $P_{in} \approx 3.0$ µW i $r = 6.9$] **(b)** Rezultati iz odgovarajućih numeričkih simulacija za različite vrednosti intenziteta snopa I_{in} i faktora intenziteta ***r***, [**(b1)** $I_{in} \approx 0.125$ i $r = 1.9$; **(b2)** $I_{in} \approx 0.25$ i $r = 2.7$; **(b3)** $I_{in} \approx 0.75$ i $r = 7.0$] **(c)** trodimenzionalni prikaz numerički proračunate distribucije intenziteta za jaku nelinearnost pri kojoj dolazi do formiranja solitarnog stanja.

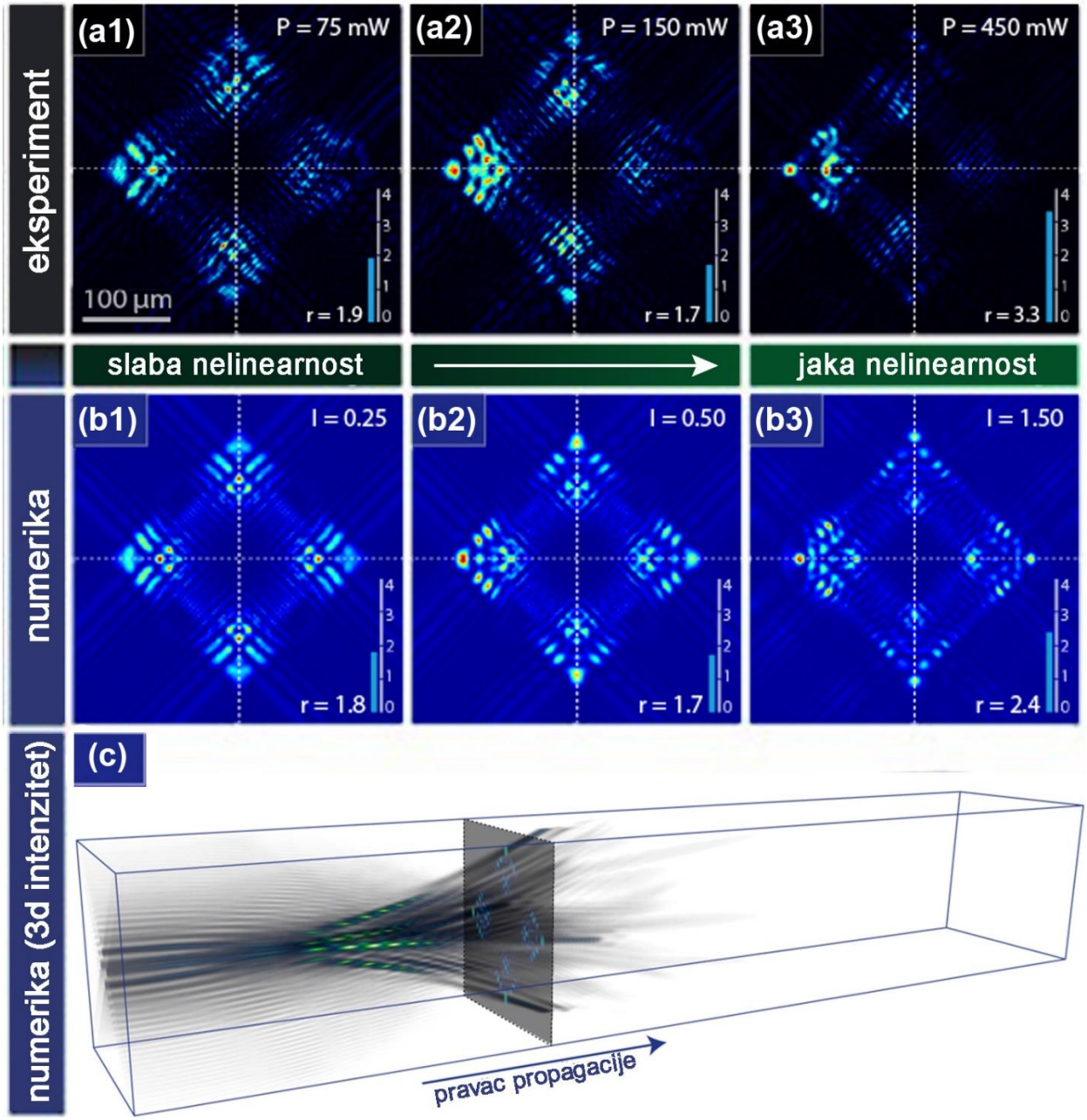

Slika 6.6 Nelinearna interakcija četiri Eirijeva snopa sa π faznom razlikom. **(a)** Eksperimentalni rezultati za različite vrednosti snage probnog snopa P_{in} i faktora intenziteta ***r***, [**(a1)** $P_{in} \approx 0.5$ µW i $r = 1.9$; **(a2)** $P_{in} \approx 1.0$ µW i $r = 1.7$; **(a3)** $P_{in} \approx 3.0$ µW i $r = 3.3$] **(b)** Rezultati iz odgovarajućih numeričkih simulacija za različite vrednosti intenziteta snopa I_{in} i faktora intenziteta ***r***, [**(b1)** $I_{in} \approx 0.25$ i $r = 1.8$; **(b2)** $I_{in} \approx 0.50$ i $r = 1.7$; **(b3)** $I_{in} \approx 1.50$ i $r = 2.4$] **(c)** trodimenzionalni prikaz numerički proračunate distribucije intenziteta za jaku nelinearnost.

Ako se uporede svi rezultati nelinearne interakcije dva i četiri Eirijeva snopa, može se identifikovati tri različita tipa nelinearne dinamike. Prvo, u svim slučajevima gde se sintetizuju snopovi u fazi, interakcija vodi do ***formiranja jednog stabilnog prostornog solitarnog stanja*** iniciranog visokim intenzitetom koji je rezultat konstruktivne interferencije glavnih lobova. Drugi tip, ***formiranje solitarnog para***, može se posmatrati ako dođe do superponiranja sa faznom razlikom od π. Za ova dva tipa ubrzanje inicijalnih Eirijevih snopova je kompenzovano, vodeći do pravolinijskih oblika propagacije. Interesantno da postoji i treći tip gde ***ne dolazi do javljanja***

solitarnih struktura, čak i za iste intenzitete i nelinearnosti. Ovo se može posmatrati ako četiri Eirijeva snopa superponiramo sa π faznom razlikom kao što je urađeno u primeru. Za ovu konfiguraciju nelinearna dinamika pokazuje trend razbijanja simetrije koje zavisi kritično od malih perturbacija i asimetrija u sistemu. Usmerena difuzija slobodnih nosilaca unutar fotorefraktivnog SBN kristala uzrokuje takvu asimetriju, koja je takođe odgovorna za horizontalni pomeraj ostalih solitarnih rešenja, kao što je iznad navedeno.

6.3 Dvodimenzionalni Eirijevi snopovi u fotonskim rešetkama

U ovom delu, ispitivan je uticaj optički indukovane fotonske rešetke na transverzalno samoubrzanje pojedinačnog dvodimenzionalnih Eirijevog snopa. Fokus je postavljen na kompeticiju između samo-savitljive propagacije Eirijevih snopova i vođenja talasa i diskretnih difrakcionih efekata na fotonsku rešetku. Iz tog razloga, sukcesivno je povećavana jačina indukovane modulacije indeksa prelamanja i posmatran efekat na samoubrzanje snopa. Tokom povećavanja jačine rešetke, Eirijev snop efikasnije pobuđuje različite linearne Blohove modove rešetke koji sprečavaju transverzalno samoubrzavanje Eirijevog snopa. Ovo rezultuje efektivnim smanjivanjem samoubrzanja, koje se za određenu vrednost indukovane modulacije indeksa prelamanja kompletno zaustavlja.

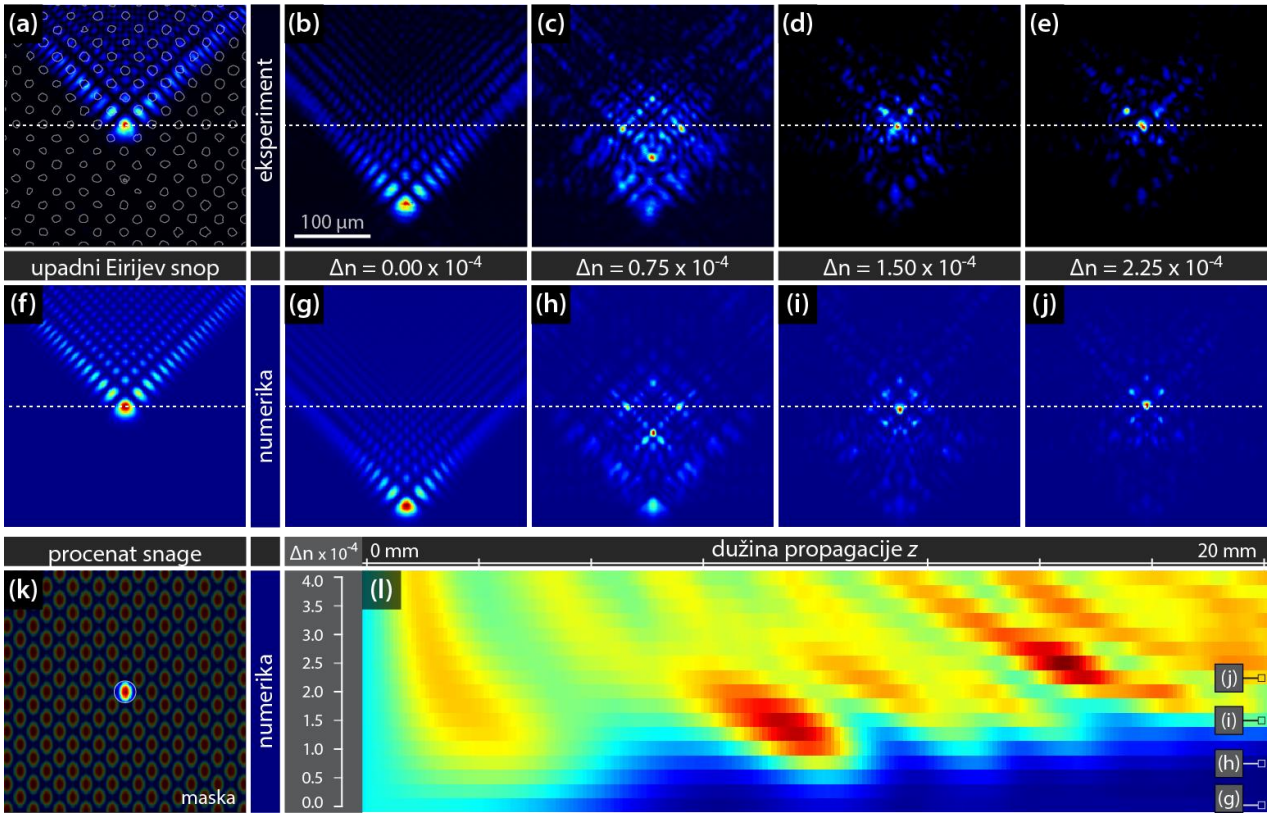

Slika 6.7 Prostiranje Eirijevog snopa u regularnoj kvadratnoj rešetci. **(a)** Eirijev snop na ulazu u kristal, u eksperimentu, (položaj rešetke u odnosu na snop je prikazan matricom belih kružnica); **(b)-(e)** Eksperimentalno zabeležena distribucija intenziteta na izlazu iz kristala za različite vrednosti promene indeksa prelamanja Δn. **(f)** Eirijev snop na ulazu u kristal u numerici; **(g)-(j)** Distribucija intenziteta na izlazu iz kristala za različite vrednosti promene indeksa prelamanja Δn, dobijena u numerici; **(k)** Maska za proračun procenta snage snopa koji prođe kroz centralni talasovod rešetke; **(l)** Prikaz zavisnosti procenta snage Eirijevog snopa u upadnom talasovodu rešetke od promene indeksa prelamanja Δn i dužine propagacije.

Slika 6.7 sumira rezultate u odnosu na propagaciju Eirijevog snopa unutar regularne fotonske rešetke. Gornji red (Slike 6.7a-e) sadrži eksperimentalne rezultate, dok su odgovarajuće numeričke simulacije prikazane u drugom redu (Slike 6.7f-j). Prve dve kolone predstavljaju rekapitulaciju tipičnog transverzalnog pomeraja Eirijevog snopa koji propagira između prednje (Slike 6.7a i 6.7f) i zadnje strane (Slike 6.7b i 6.7g) homogenog SBN kristala. Zatim se Eirijev snop propušta kroz indukovanu fotonsku rešetku sa glavnim lobom postavljenim naspram centralnog talasovoda rešetke.

Kako modulacija indeksa prelamanja raste, interakcija Eirijevog snopa sa delovima rešetke postaje jača i kao posledica toga javlja se efekat sprečavanja savijanja snopa. Eksperimentalni rezultati (Slike 6.7c-e), kao i numerika (Slike 6.7h-j) jasno pokazuju ometanje samoubrzanja Eirijevog snopa. U zavisnosti od jačine rešetke, različite vrste diskretnih struktura se javljaju sve do onog trenutka kad jačina rešetke konačno totalno potisne samoubrzanje Eirijevog snopa.

Da bi se dobila detaljnija slika dinamike propagacije, posmatra se odnos između vođene snage u centralnom talasovodu rešetke i ukupne snage Eirijevog snopa kao funkcija jačine rešetke i dužine propagacije. Na Slici 6.7l prikazani su numerički rezultati ovog odnosa. Pomoću ove redukovane prezentacije u mogućnosti smo da prikažemo ključni potpis kompleksne evolucije Eirijevog snopa tokom propagacije za različite jačine rešetke. Ovo nam ilustruje, prostorno razlučeno, koliko energije je vođeno centralnim talasovodom rešetke i samim tim koliko jako je Eirijev snop ometen od strane rešetke. Zasenčena površina na Slici 6.7k predstavlja masku za proračun snage u centralnom talasovodu. Ovaj graf jasno demonstrira uticaj optički indukovane fotonske rešetke kao i potiskivanje samoubrzanja i savijanje Eirijevog snopa. Za određene vrednosti Δn mogu se videti oscilacije snage snopa u centralnom talasovodu duž rastojanja propagacije. Ovo se dešava usled osobine samozakretanja Eirijevog snopa i uticaja centralnog talasovoda ne samo na glavni već i na okolne lobove koji se preklapaju sa ovim određenim talasovodom tokom propagacije. Kao rezultat, javlja se deo snage koji potiče iz okolnih lobova a koji možemo da posmatramo u centralnom talasovodu za neka rastojanja propagacije. Za veće modulacije indeksa prelamanja, Δn, može se posmatrati lokalizacija velikog dela snage snopa u centralnom talasovodu pošto snop napusti kristal. Opet, da bi eksperimentalno kontrolisali dubinu modulacije indeksa prelamanja koristi se vremenska zavisnost upisivanja indukovane rešetke, koja raste monotono sa vremenom upisivanja.

Nasuprot odgovarajućoj situaciji propagacije jednodimenzionalnog Eirijevog snopa u nizu talasovoda [86], ovde lokalizacija dvodimenzionalnog Eirijevog snopa na izlazu iz kristala strogo zavisi od jačine fotonske rešetke, što se takođe može videti sa desne strane Slike 6.7l. Ovo različito ponašanje se može objasniti činjenicom da u dve dimenzije svaki talasovod rešetke ima četiri susedna talasovoda (u jednoj dimenziji samo dva). Iz tog razloga, u ovom slučaju se interakcija Eirijevog snopa koji se propušta glavnim lobom kroz centralni talasovod rešetke drugačije izražava. Ovakva zavisnost lokalizacije snopa od jačine rešetke se može iskoristiti za realizaciju brzih prekidača ili rutera za Eirijeve snopove bazirano na njihovoj polarizaciji.

6.4 Propagacija Eirijevog snopa u fotonskoj rešetci sa različitim defektima

Na Slikama 6.8 i 6.9 prikazani su eksperimentalni i numerički rezultati prostiranja pojedinačnog dvodimenzionalnog Eirijevog snopa kroz SBN kristal sa optički indukovanom kvadratnom rešetkom sa pozitivnim ili negativnim optičkim defektom u centralnom talasovodu rešetke. Numerički rezultati za procenat snage u centralnom talasovodu rešetke kao funkcija dužine propagacije ζ i modulacije indeksa prelamanja Δn prikazani su kao paneli na Slikama 6.8a i 6.9a. Izabrane su dve vrednosti promene indeksa prelamanja u centralnom talasovodu (optičkog defekta), $\Delta n=0.75\text{x}10^{-4}$ (Slika 6.8c i 6.9c) i $\Delta n=2.25\text{x}10^{-4}$(Slika 6.8d i 6.9d) i za njih je prikazan profil intenziteta Eirijevog snopa na izlazu iz kristala. Pozicije koje odgovaraju ovim profilima intenziteta su označene slovima (c) i (d) na grafiku procenta snage (Slike 6.8a i 6.9a).

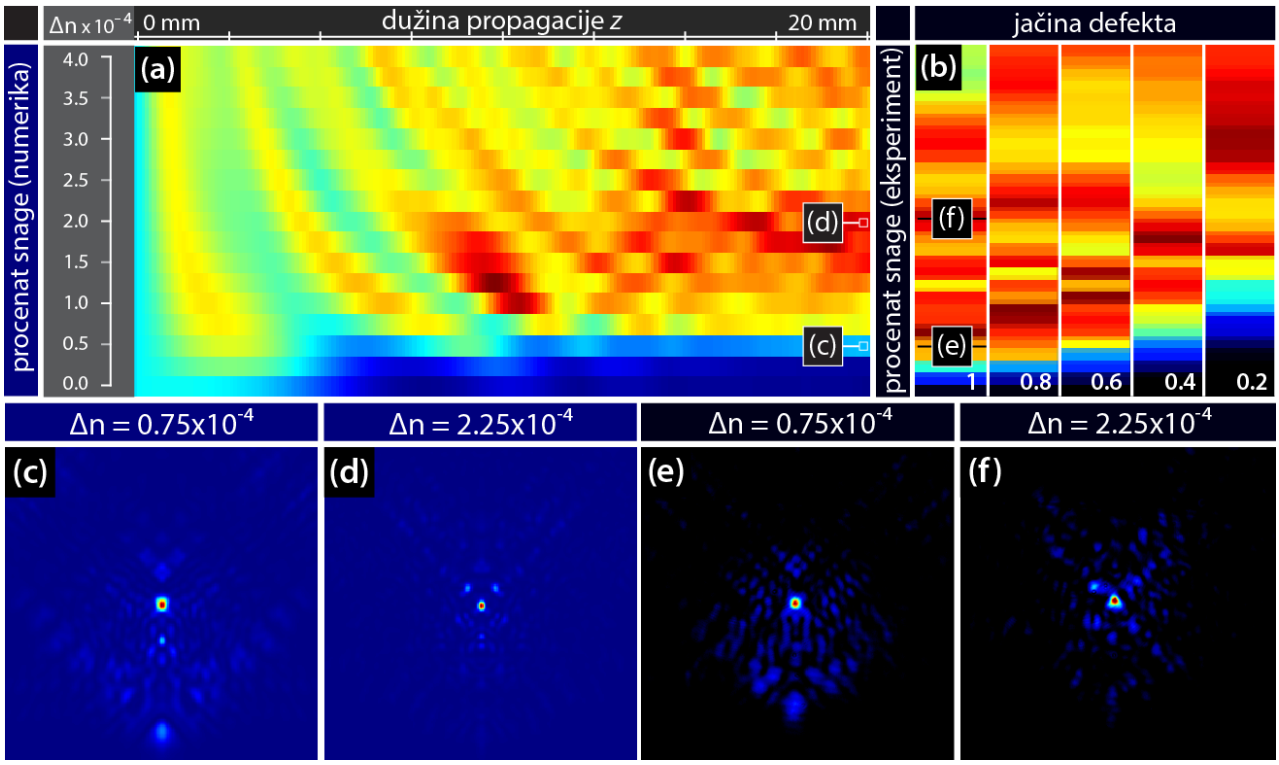

Slika 6.8 Prostiranje Eirijevog snopa kroz rešetku sa različitim jačinama pozitivnih optičkih defekata. **(a)** Numerički rezultati ispitivanja zavisnosti snage Eirijevog snopa u određenom defektu od promene indeksa prelamanja Δn i dužine propagacije z; **(b)** Eksperimentalno posmatran procenat snage Eirijevog snopa kroz određeni defekt kao funkcije promene indeksa prelamanja Δn i jačine defekta S_d; **(c, d)** Numerički rezultati distribucije intenziteta Eirijevog snopa na izlazu iz kristala za dve jačine defekta; **(e, f)** Eksperimentalni rezultati distribucije intenziteta na izlazu iz kristala za odgovarajuće dve jačine defekta.

Pošto u eksperimentu nije moguće snimiti longitudinalni intenzitet unutar i duž nehomogenog SBN kristala ograničenje je samo na profilima intenziteta snopa na izlasku iz kristala. Na Slikama 6.8b i 6.9b prikazan je eksperimentalno mereni odnos snage na izlazu iz kristala prikazan u funkciji modulacije indeksa prelamanja i jačine defekta. Eksperiment je ponovljen za pet različitih jačina defekata i to za obe vrste defekata, pozitivne i negativne, i snimljen profil intenziteta Eirijevog snopa na izlazu iz kristala. Moduo jačine defekta S_d je dat preko odnosa intenziteta pika diskretnog (snopa za formiranje kvadratne rešetke) i Beselovog nedifragujućeg snopa, dok je znak određen pravcem

primenjenog električnog polja. U eksperimentu su selektovane dve reprezentativne jačine rešetke Δn kako bi se pokazao profil intenziteta Eirijevog snopa na izlazu iz kristala (paneli (e) i (f)). Njihove pozicije u plotu eksperimentalno dobijenog odnosa snage (Slike 6.8b i 6.9b) označene su slovima (e) i (f).

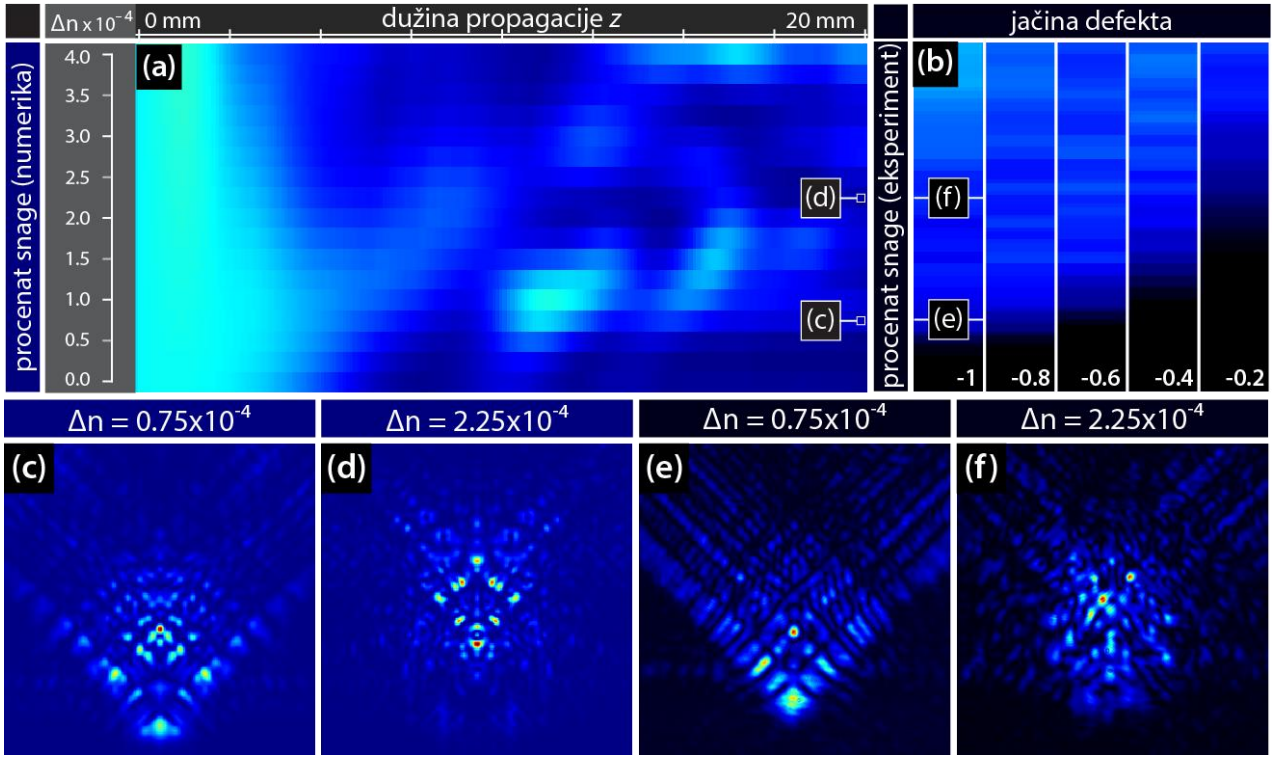

Slika 6.9 Prostiranje Eirijevog snopa kroz rešetku sa različitim jačinama negativnih optičkih defekata. **(a)** Numerički rezultati ispitivanja zavisnosti snage Eirijevog snopa u određenom defektu od promene indeksa prelamanja Δn i dužine propagacije z; **(b)** Eksperimentalno posmatran procenat snage Eirijevog snopa kroz određeni defekt kao funkcija promene indeksa prelamanja Δn i jačine defekta S_d. **(c, d)** Numerički rezultati distribucije intenziteta Eirijevog snopa na izlazu iz kristala za dve jačine defekta. **(e, f)** Eksperimentalni rezultati distribucije intenziteta na izlazu iz kristala za odgovarajuće dve jačine defekta.

Ovi rezultati ilustruju jaku zavisnost propagacije i osobina Eirijevog snopa, pre svega transverzalnog ubrzanja, od dubine rešetke, kao i jačine defekata. Pozitivni defekat (Slika 6.8a) strogo pojačava lokalizaciju snage Eirijevog snopa u talasovodu defekta, dok u slučaju negativnog defekta (Slika 6.9a) dolazi do redukcije snage snopa i totalne delokalizacije za dovoljno veliku jačinu defekta.

Poglavlje 7

Zaključak

Istraživanje interakcije svetlosti sa materijom dovelo je do mogućnosti dizajniranja snopova sa kontrolisanom fazom, polarizacijom i intenzitetom i do rađanja nove discipline fizike, ***fizike kompleksne svetlosti.***

Otkriće Eirijevih snopova i mogućnost njihove manipulacije otvorilo je široko polje istraživanja potencijalnih primena Eirijevih snopova u različitim oblastima fizike, počevši od mikromanipulacije česticama i ćelijama, kao optički raspršivači, laserske mikroobrade materijala, optičkih rutera, autofokusirajućih snopova, pa do ultrabrzih samoubrzavajućih impulsa.

Poznato je da je kontrolisanje propagacije svetlosti samom svetlošću (nelinearnom interakcijom) ključan faktor za realizaciju naprednih potpuno optičkih tehnologija. Jedan od obećavajućih pristupa ovom cilju koji je bio i jedan od osnovnih ciljeva istraživanja opisanih u ovoj tezi jeste primena Eirijevih snopova i mogućnost da se modulacijom transverzalnog ubrzanja Eirijevih snopova kontroliše prostiranje svetlosti u fotorefraktivnom materijalu.

Rezultati opisani u ovoj tezi predstavljaju originalni doprinos istraživanjima kompleksne svetlosti u modernoj linearnoj i nelinearnoj fotonici kao i u fizici optičkih materijala. U uvodu ove teze objašnjene su osnovne osobine kompleksne svetlosti i nedifragujućih talasa i dat je pregled dosadašnjih istraživanja u ovoj oblasti. Posle detaljnog opisa koncepta nedifragujućih snopova i posebne klase samoubrzavajućih Eirijevih snopova kao i kratkog osvrta na značaj fotonskih kristala u istraživanjima nelinearne optike, teorijskog modela i eksperimentalnih metoda korišćenih u opisanim eksperimentima, dat je prikaz rezultata.

U prvom delu prikazanih rezultata disertacije, predstavljena je prva eksperimentalna i numerička studija o nelinearnoj interakciji više dvodimenzionalnih Eirijevih snopova. Kao najvažniji rezultat, demonstrirana je mogućnost dizajniranja kompleksnih solitarnih struktura kontrolišući nelinearne interakcije više ubrzanih snopova. Ispitivanje nelinearne dinamike superponiranih Eirijevih snopova za različite konfiguracije (broj snopova, fazne relacije, intenzitet), otvorilo je mogućnost kontrole formiranja pravolinijskih propagirajućih solitarnih stanja ili parova.

U drugom delu prikazanih rezultata disertacije, opisano je ispitivanje dinamike propagacije samoubrzavajućih dvodimenzionalnih Eirijevih snopova u dvodimenzionalnim fotonskim rešetkama sa i bez defekata. Eksperimentalno je otkriveno a teorijskim modelom i potvrđeno da povećanje modulacije indeksa prelamanja (“dubine” rešetke – globalne promene indeksa prelamanja rešetke reda veličine 10^{-4}) redukuje ubrzanje Eirijevog snopa i dovodi do formiranja diskretnih snopova rešetke (što predstavlja dvodimenzionalni Eirijev snop usporen pod uticajem modulacije indeksa prelamanja na mestu upisane kvadratne fotonske rešetke u SBN:Ce kristalu).

Takođe je potvrđeno da optički defekti (koji predstavljaju lokalnu promenu indeksa prelamanja rešetke) značajno utiču na promenu dinamike snopa. Za pozitivne defekte ($n > n_{rešetke}$), lokalizacija je značajno povećana, dok se kod negativnih defekata ($n < n_{rešetke}$), situacija menja i dolazi do značajnog slabljenja intenziteta Eirijevog snopa (snage) duž pravca optičkog defekta.

Izuzetno je značajno da se rezultati dobijeni i opisani u ovoj tezi mogu generalizovati i na druge tipove optički indukovanih rešetki i defekata, uključujući i nešto kompleksnije ili čak i trodimenzionalne rešetke. Isto tako, i druge klase samoubrzavajućih nedifragujućih optičkih snopova se mogu kontrolisati koristeći prezentovane ideje i metode, što prikazane rezultate čini posebno značajnim i atraktivnim.

Prikazani eksperimentalni rezultati i metode nisu samo osnova za dalja fundamentalna ispitivanja interakcije ostalih tipova nedifragujućih snopova već takođe nude praktično neograničene mogućnosti za kontrolu, obradu i prenos informacija u modernim optičkim tehnologijama.

Pored toga, opisani rezultati su značajni i za druge oblasti fizike kao što je kvantna gravitacija gde bi mogli da pomognu u ispitivanju postojanja nelinearne samointerakcije (opisane Šredinger-Njutnovom jednačinom) kao i u kvantnoj holografiji, spektroskopiji i fizici materijala (interakciji kompleksne svetlosti sa materijom).

Mogućnost kontrolisanja talasnog fronta, tzv. strukturiranja svetlosti i njene propagacije kroz materijalnu sredinu predstavlja jedno od najznačajnijih dostignuća ljudskog duha u modernoj fotonici i fizici optičkih materijala. Ova teza predstavlja jedan od prvih koraka ka dubljem razumevanju propagacije posebne klase Eirijevih snopova, samoubrzavajućih nedifragujućih snopova, njihove međusobne interakcije kao i njihove interakcije sa materijom u linearnom i nelinearnom režimu.

Literatura

[1] THE FERMI-LAT COLLABORATION, "A gamma-ray determination of the Universe's star formation history", Science, Vol **362**, Issue 6418, pp. 1031-1034, (2018).

[2] M. V. Trushin, "Light-mediated "conversation" among microorganisms", Microbiological Research, Volume **159**, Issue 1, 2004, Pages 1-10, ISSN 0944-5013, (2004).

[3] T. Verbiest, K. Clays, V. Rodriguez, ***Second-Order Nonlinear Optical Characterization Techniques: An introduction***, (Taylor & Francis, 2009).

[4] R. Bansal, ***Fundamentals of Engineering Electromagnetics*** 1st Edition, (CRC Press, 2006).

[5] M. Born and E. Wolf, ***Principles of Optics: Electromagnetic Theory of Propagation, Interference and Diffraction of Light***, 6th ed., (Cambridge University Press, 1998).

[6] H. A. Willebrand and B. S. Ghuman, "Fiber optics without fiber", IEEE Spectrum 38(8) (2001).

[7] J. W. Goodman, ***Introduction to Fourier Optics***, 2nd ed., (McGraw-Hill, New York, 1996).

[8] S. Okazaki, "Resolution limits of optical lithography", J. Vac. Sci. Technol. B **9**, 2829–2833 (1991).

[9] T. Ito and S. Okazaki, "Pushing the limits of lithography", Nature **406**, 1027–1031 (2000).

[10] A.Ashkin, J. M. Dziedzic, J. E. Bjorkholm, and S. Chu, "Observation of a single-beam gradient force optical trap for dielectric particles", Opt. Lett. **11**, 288–290 (1986).

[11] J. E. Curtis, B. A. Koss, and D. G. Grier, "Dynamic holographic optical tweezers", Opt. Commun. **207**, 169–175 (2002).

[12] https://www.britishmuseum.org

[13] Iam-Choon Khoo, Bahaa E. A. Saleh, ***Liquid Crystals***, 2nd Edition, (Wiley, 2007).

[14] Dr Jeff Secor, Prof Robert Alfano, Dr Solyman Ashrafi, ***Complex Light***, (IOP Publishing Ltd 2017).

[15] Klar T. A., Jakobs S., Dyba M., Egner A. and Hell S. W., "Fluorescence microscopy with diffraction resolution barrier broken by stimulated emission", Proc. Natl. Acad. Sci. USA **97** 8206–10, (2000).

[16] M. G. L. Gustafsson, “Nonlinear structured-illumination microscopy: wide-field fluorescence imaging with theoretically unlimited resolution”, Proc. Natl. Acad. Sci. USA **102** 13081–6, (2005).

[17] A. E. Wilner et al, “Optical communications using orbital angular momentum beams”, Adv. Opt. Photonics **7** 66–106, (2015).

[18] M. Padgett and R. Bowman, “Tweezers with a twist”, Nat. Photonics **5** 343, (2011).

[19] K. Y. Bliokh, F. J. Rodríguez-Fortuño, F. Nori and A. V. Zayats, “Spin–orbit interactions of Light”, Nat. Photonics **9**, 796–808, (2015).

[20] J. A. Stratton, ***Electromagnetic Theory***, (McGraw-Hill, New York, 1941).

[21] J. Durnin, J. J. Miceli i J. H. Eberly, „Diffraction-free beams“, Phys. Rev. Lett., Vol **58**, str. 1499–1501, (1987).

[22] J. Durnin, “Exact solutions for nondiffracting beams. I. The scalar theory”, J. Opt. Soc. Am. A **4**, 651 (1987).

[23] Z. Bouchal, “Nondiffracting optical beams: physical properties, experiments, and applications”, Czechoslovak Journal of Physics, **53**, 537 (2003).

[24] G. A. Siviloglou and D. N. Christodoulides, “Accelerating finite energy Airy beams,” Opt. Lett. **32**, 979-981 (2007).

[25] G. A. Siviloglou, J. Broky, A. Dogariu, and D. N. Christodoulides, “Observation of accelerating Airy beams,” Phys. Rev. Lett. **99**, 213901, (2007).

[26] M. V. Berry and C. Upstill, „IV catastrophe optics: morphologies of caustics and their diffraction patterns,“ Progress in optics **18**, 257-346, (1980).

[27] Y. A. Kravtsov and Y. I. Orlov, ***Caustics, Catastrophes and Wave Fields***, (Springer, Berlin, 1999).

[28] N. K. Efremidis, Z. Chen, M. Segev, and D. N. Christodoulides, “Airy beams and accelerating waves: an overview of recent advances”, Optica **6**, 686-701, (2019).

[29] J. Broky, G. A. Siviloglou, A. Dogariu, and D. N. Christodoulides, „Self-healing properties of optical Airy beams,“ Opt. Express **16**, 12880-12891, (2008).

[30] Z. Bouchal, J. Wagner, and M. Chlup. “Self-reconstruction of a distorted nondiffracting beam,” Opt. Commun. **151**, 207-211, (1998).

[31] X. Chu, “Evolution of Airy beam in turbulence,” Opt. Lett. **36**, 2701-2703 (2011).

[32] J. Baumgartl, M. Mazilu, and K. Dholakia, „Optically mediated particle clearing using Airy wavepackets,“ Nat. Photon. **2**, 675 (2008).

[33] A. Mathis, F. Courvoisier, L. Froehly, L. Furfaro, M. Jacquot, P. Lacourt, and J. Dudley, “Micromachining along a curve: Femtosecond laser micromachining of curved profiles in diamond and silicon using accelerating beams,” Appl. Phys. Lett. **101** (2012).

[34] P. Rose, F. Diebel, M. Boguslawski, and C. Denz, “Airy beam induced optical routing” Appl. Phys. Lett. **102**, 101101 (2013).

[35] N. K. Efremidis, “Airy trajectory engineering in dynamic linear index potentials,” Opt. Lett. **36**, 3006-3008 (2011).

[36] A. Chong, W. H. Renninger, D. N. Christodoulides, and F. W. Wise, “Airy-Bessel wave packets as versatile linear light bullets,” Nat. Photonics **4**, 103 (2010).

[37] Y. S. Kivshar and G. P. Agrawal, ***Optical Solitons: From Fibers to Photonic Crystals***, (Academic Press, San Diego, 2003).

[38] J. D. Joannopoulos, S. G. Johnson, J. N. Winn, and R. D. Meade, ***Photonic crystals: Molding the Flow of Light***, 2nd ed. (Princeton University, 1995).

[39] N. K. Efremidis, S. Sears, D. N. Christodoulides, J. W. Fleischer and M. Segev, “Discrete solitons in photorefractive optically induced photonic lattices”, Phys. Rev. E, **66**, 046602, (2002).

[40] M. V. Berry and N. L. Balazs, “Nonspreading wave packets”, Am. J. Phys. **47**, 264 (1979).

[41] G. A. Siviloglou and D. N. Christodoulides, “Accelerating finite energy Airy beams,” Opt. Lett. **32**, 979-981 (2007).

[42] P. Rose et. al., Nonlinear lattice structures based on families of complex nondiffracting beams, New Journal of Physics **14,** 033018(2012).

[43] H. E. Hernandez-Figueroa, E. Recami, and M. Zamboni-Rached, ***Non-diffracting Waves***, (Wiley, 2014).

[44] O. Vallée and M. Soares (eds), ***Airy functions and applications to physics***, (Imperial College Press, 2004).

[45] D. M. Greenberger, American Journal of Physics **48**, 256 (1980).

[46] L. Froehly, F. Courvoisier, A. Mathis, M. Jacquot, L. Furfaro, R. Giust, P. A. Lacourt, and J. M. Dudley, "Arbitrary accelerating micron-scale caustic beams in two and three dimensions," Optics Express **19** (17), 16455-16465 (2011).

[47] Y. Hu, D. Bongiovanni, Z. Chen, and R. Morandotti, "Multipath multicomponent self-accelerating beams through spectrum-engineered position mapping," Physical Review A **88**, 043809 (2013).

[48] Y. Kaganovsky and E. Heyman, "Wave analysis of Airy beams," Optics Express **18** (8), 8440-8452 (2010).

[49] I. D. Chremmos, Z. Chen, D. N. Christodoulides, and N. K. Efremidis, "Abruptly autofocusing and autodefocusing optical beams with arbitrary caustics," Physical Review A **85**, 023828 (2012).

[50] E. Greenfield, M. Segev, W. Walasik, and O. Raz, "Accelerating Light Beams along Arbitrary Convex Trajectories," Physical Review Letters **106**, 213902 (2011).

[51] L. I. Schiff, ***Quantum Mechanics*** 3rd, (New York: M cGraw-Hill, 1968).

[52] M. Zamboni-Rached, K. Z. Nóbrega, and C. A. Dartora, "Analytic description of Airy-type beams when truncated by finite apertures," Optics Express **20** (18), 19972-19977 (2012).

[53] G. A. Siviloglou, J. Broky, A. Dogariu, and D. N. Christodoulides, "Observation of Accelerating Airy Beams," Physical Review Letters **99**, 213901 (2007).

[54] J. W. Goodman, ***Introduction to Fourier Optics***. (Mc-Graw-Hill, New York, 1996).

[55] G. A. Siviloglou, J. Broky, A. Dogariu, and D. N. Christodoulides, "Ballistic dynamics of Airy beams," Optics Letters **33** (3), 207-209 (2008)

[56] Q. Gong, X. Hu, ***Photonic Crystals: Principles and applications***, (Taylor & Francis, 2013).

[57] W. Zhang, D. Zhang, T. Fan, J. Gu, J. Ding, H. Wang, Q. Guo, H. Ogawa, „Novel photoanode structure templated from butterfly wing scales", Chem. Mater. **21**, 33, (2009).

[58] L. Gonzales-Urbina, K. Baert, B. Kolaric, J. Perez-Mreno, and K. Clays, „Linear and Nonlinear Optical Properties of Colloidal Photonic Crystals", Chem. Rev. **112**, 2268-2285, (2012).

[59] A. Yariv, P. Yeh, ***Optical Waves in Crystals,Propagation and Control of Laser Radiation***, (Wiley, 2002).

[60] P. V. Braun et al., "Introducing defects in 3D photonic crystals: state of the art", Adv. Mater. **18**, 2665, (2006).

[61] F. Lederer, G. I. Stegeman, D. N. Christodoulides, G. Assanto, M. Segev, Y. Silberberg, "Discrete solitons in optics", Physics Reports **463**, 1–126, (2008).

[62] E. Yablonovitch, "Inhibited spontaneous emission in solid-state physics and electronics", Phys. Rev. Lett. **58**, 2059, (1987).

[63] R. D. Meade, A. Devenyi, J. D. Joannopoulos, O. L. Alerhand, D. A. Smith, K. Kash, "Novel applications of photonic band gap materials: Low-loss bends and high *Q* cavities", J. Appl. Phys. **75**, 4753, (1994).

[64] S. H. Fan, J. N. Winn, A. Devenyi, J. C. Chen, R. D. Meade, J. D. Joannopoulos, "Guided and defect modes in periodic dielectric waveguides", J. Opt. Soc. Am. B **12**, 1267, (1995).

[65] A. Mekis, J. C. Chen, I. Kurland, S. H. Fan, P. R. Villeneuve, J. D. Joannopoulos, "High transmission through sharp bends in photonic crystal waveguides", Phys. Rev. Lett. **77**, 3787, (1996).

[66] S. John, T. Quang, "Collective switching and inversion without fluctuation of two-level atoms in confined photonic systems", Phys. Rev. Lett. **78**, 1888, (1997).

[67] Y. Fink, J. N. Winn, S. H. Fan, C. P. Chen, J. Michel, J. D. Joannopoulos, E. L. Thomas, "A dielectric omnidirectional reflector", Science **282**, 1679, (1998).

[68] P. Russell, "Photonic crystal fibers", Science **299**, 358, (2003).

[69] F. Diebel, D. Leykam, M. Boguslawski, P. Rose, C. Denz, and A. Desyatnikov, "All-optical switching in optically induced nonlinear waveguide couplers", Appl. Phys. Lett. **104**, 261111 (2014).

[70] M. Boguslawski, A. Kelberer, P. Rose, and C. Denz, "Multiplexing complex two-dimensional photonic superlattices", Opt. Express **20**, 27331 (2012).

[71] M. Boguslawski, A. Kelberer, P. Rose, and C. Denz, "Photonic ratchet superlattices by optical multiplexing", Opt. Lett. **37**, 797 (2012).

[72] R. W. Boyd, ***Nonlinear Optics***, 3rd ed. (Academic press, Elsevier 2008).

[73] A. Ashkin, G. D. Boyd, J. M. Dziedzic, R. G. Smith, A. A. Ballman, J. J. Levinstein, K. Nassau, "Optically induced refractive index inhomogeneities in $LiNbO_3$ and $LiTaO_3$", Appl. Phys. Lett. **9**, 72 (1966).

[74] P. Yeh, ***Introduction to Photorefractive Nonlinear Optics***, (Wiley, New York, 1993).

[75] K. Megumi, H. Kozuka, M. Kobayashi, Y. Furuhata, „High-sensitive holographic storage in Ce-doped SBN", Appl. Phys. Lett. **30**, 631 (1977).

[76] D. Kip, S. Aulkemeyer, K. Buse, F. Mersch, R. Pankrath, E. Krätzig, "Refractive Indices of $Sr_{0.61}Ba_{0.39}Nb_2O_6$ Single Crystals", Phys. Stat. Sol. A, 154, K5 (1996).

[77] U. B. Dorfler, R. Piechatzek, T. Woike, M. K. Imlau, V. Wirth, L. Bohaty, T. Volk, R. Pankrath, and M. Wohlecke, „A holographic method for the determination of all linear electrooptic coefficients applied to Ce-doped strontium-barium-niobate," Appl. Phys. B: Lasers Opt. **68**, 843 (1999).

[78] M. Boguslawski, P. Rose, and C. Denz, „Increasing the structural variety of discrete nondiffracting wave fields," Phys. Rev. A **84**, 013832 (2011).

[79] G. P. Agrawal, ***Nonlinear Fiber Optics*** (2nd ed.) (Academic press, San Diego, 1995).

[80] J. A. Davis, D. M. Cottrell, J. Campos, M. J. Yzuel, I. Moreno, „Encoding amplitude information onto phase-only filters", Applied Optics **38**, 5004 (1999).

[81] G. H. Weiss, A. A. Maradudin, "The Baker-Hausdorff formula and a problem in crystal Physics". J. Math. Phys. **3**, 771–777 (1962).

[82] J. A. Davis, E. Carcole, and D. M. Cottrell, "Nondiffracting interference patterns generated with programmable spatial light modulators," Appl. Opt. **35**, 599-602 (1996).

[83] Y. Zhang, M. R. Belic, Z. Wu, H. Zheng, K. Lu, Y. Li, and Y. Zhang, "Soliton pair generation

in the interactions of Airy and nonlinear accelerating beams," Opt. Lett. **38**, 4585–4588 (2013).

[84] Y. Zhang, M. R. Belic, H. Zheng, H. Chen, C. Li, Y. Li, and Y. Zhang, "Interactions of Airy beams, nonlinear accelerating beams, and induced solitons in Kerr and saturable nonlinear media," Opt. Express **22**, 7160– 7171 (2014).

[85] W. Królikowski, C. Denz, A. Stepken, M. Saffman, and B. Luther-Davies, "Interaction of spatial photorefractive solitons," Quantum Semiclassical Opt. J. Eur. Opt. Soc. Part B **10**, 823 (1998).

[86] N. M. Lucic, B. M. Bokic, D. Z. Grujic, D. V. Pantelic, B. M. Jelenkovic, A. Piper, D. M. Jovic, and D. V. Timotijevic, "Defect-guided Airy beams in optically induced waveguide arrays", Phys. Rev. A **88**, 63815 (2013).

Biografija

Kandidat Bojana Bokić rođena je u Beogradu 05.07.1981. Osnovnu školu i gimnaziju, prirodno-matematički smer, završila je u Negotinu 2000. godine. Iste godine upisuje Elektrotehnički fakultet Univerziteta u Beogradu. Diplomira 2008. godine na studijskom programu Elektrotehnika i računarstvo – modul Nanoelektronika, optoelektronika i laserska tehnika, odbranivši diplomski rad na temu *Primena lasera u medicini – Dijagnostičke tehnike*, čime stiče zvanje diplomiranog inženjera elektrotehnike. 2010. godine završava Master akademske studije na Elektrotehničkom fakultetu Univerziteta u Beogradu, na studijskom programu Elektrotehnika i računarstvo – modul Biomedicinski i ekološki inženjering, odbranivši master rad na temu *Primena lasera i drugih snopnih tehnika u dijagnostičke i terapeutske svrhe u biomedicini.*

Od 1.oktobra 2010. je zaposlena u Centru za fotoniku Instituta za fiziku, kao istraživač-pripravnik u Laboratoriji za atomsku i kvantnu optiku, sa angažovanjem na projektu osnovnih istraživanja OI171038 Ministarstva prosvete, nauke i tehnološkog razvoja pod nazivom *Holografske metode generisanja specifičnih talasnih frontova za efikasnu kontrolu koherentnih efekata u interakciji atoma i lasera*, pod rukovodstvom dr Dejana Pantelića. 2011. godine kandidat upisuje Doktorske akademske studije na Fizičkom fakultetu Univerziteta u Beogradu, na smeru Kvantna optika i laseri, pod mentorstvom dr Branislava Jelenkovića. Od 2013-2014. godine bila je angažovana na bilateralnom projektu sa Saveznom Republikom Nemačkom pod nazivom *Propagacija i lokalizacija svetlosti u sistemima sa kompleksnim fotoničnim rešetkama* pod rukovodstvom dr Dragane Jović Savić.

Njena oblast istraživanja je kvantna optika sa posebnim interesovanjem za nelinearnu fotoniku i primenu kompleksnih struktura u istraživanjima iz oblasti fizike materijala i optičkih telekomunikacija. Rezultate svog istraživanja publikovala je u šest radova kategorije M21, dva rada kategorije M23, šest saopštenja sa međunarodnog skupa kategorije M33 i M34, i tri saopštenja sa skupa od nacionalnog značaja kategorije M64.

obrazac izjave o autorstvu

Izjava o autorstvu

Ime i prezime autora **Bojana Bokić**

Broj indeksa **8001/2019**

Izjavljujem

da je doktorska disertacija pod naslovom

Dinamika prostiranja Eirijevih snopova u fotorefraktivnim sredinama

- rezultat sopstvenog istraživačkog rada;
- da disertacija u celini ni u delovima nije bila predložena za sticanje druge diplome prema studijskim programima druhig visokoškolskih ustanova;
- da su rezultati korektno navedeni
- da nisam kršio/la autorska prava i koristio/la intelektualnu svojinu drugih lica.

Potpis autora

U Beogradu, _____

_____

obrazac izjave o istovetnosti štampane i elektronske verzije doktorskog rada

Izjava o istovetnosti štampane i elektronske verzije doktorskog rada

Ime i prezime autora **Bojana Bokić**

Broj indeksa **8001/2019**

Studijski program **Fotonika i laseri**

Naslov rada **Dinamika prostiranja Eirijevih snopova u fotorefraktivnim sredinama**

Mentor **dr Branislav Jelenković**

Izjavljujem da je štampana verzija mog doktorskog rada istovetna elektronskoj verziji koju predao/la radi pohranjivanja u **Digitalnom repozitorijumu Univerziteta u Beogradu**.

Dozvoljavam da se objave moji lični podaci vezani za dobijanje akademskog naziva doktora nauka, kao što su ime i prezime, godina i mesto rođenja i datum odbrane rada.

Ovi lični podaci mogu se objaviti na mrežnim stranicama digitalne biblioteke, u elektronskom katalogu i u publikacijama Univerziteta u Beogradu.

Potpis autora

U Beogradu, _____

_____

obrazac izjave o korišćenju

Izjava o korišćenju

Ovlašćujem Univerzitetsku biblioteku „Svetozar Marković“ da u Digitalni repozitorijum Univerziteta u Beogradu unesu moju doktorsku disertaciju pod naslovom:

Dinamika prostiranja Eirijevih snopova u fotrefraktivnim sredinama

koja je moje autorsko delo.

Disertaciju sa svim prilozima predao/la sam u elektronskom formatu pogodnom za trajno arhiviranje.

Moju doktorsku disertaciju pohranjenu u Digitalnom repozitorijumu Univerziteta u Beogradu i dostupnu u otvorenom pristupu mogu da koriste svi koji poštuju odredbe sadržane u odabranom tipu licence Kreativne zajednice (Creative Commons) za koju sam se odlučio/la.

Autorstvo (CC BY)

1. Autorstvo – nekomercijalno (CC BY-NC)

2. Autorstvo – nekomercijalno – bez prerada (CC BY-NC-ND)

3. Autorstvo – nekomercijalno – deliti pod istim uslovima (CC BY-NC-SA)

4. Autorstvo – bez prerada (CC BY-ND)

5. Autorstvo – deliti pod istim uslovima (CC BY-SA)

(Molimo da zaokružite samo jednu od šest ponuđenih licenci. Kratak opis licenci je sastavni deo ove izjave).

Potpis autora

U Beogradu, _____

_____

1. **Autorstvo.** Dozvoljavate umnožavanje, distribuciju i javno saopštavanje dela, i prerade, ako se navede ime autora na način određen od strane autora ili davaoca licence, čak i u komercijalne svrhe. Ovo je najslobodnija od svih licenci.

2. **Autorstvo – nekomercijalno**. Dozvoljavate umnožavanje, distribuciju i javno saopštavanje dela, i prerade, ako se navede ime autora na način određen od strane autora ili davaoca licence. Ova licenca ne dozvoljava komercijalnu upotrebu dela.

3. **Autorstvo – nekomercijalno – bez prerada**. Dozvoljavate umnožavanje, distribuciju i javno saopštavanje dela, bez promena, preoblikovanja ili upotrebe dela u svom delu, ako se navede ime autora na način određen od strane autora ili davaoca licence. Ova licenca ne dozvoljava komercijalnu upotrebu dela. U odnosu na sve ostale licence, ovom licencom se ograničava najveći obim prava korišćenja dela.

4. **Autorstvo – nekomercijalno – deliti pod istim uslovima**. Dozvoljavate umnožavanje, distribuciju i javno saopštavanje dela, i prerade, ako se navede ime autora na način određen od strane autora ili davaoca licence i ako se prerada distribuira pod istom ili sličnom licencom. Ova licenca ne dozvoljava komercijalnu upotrebu dela i prerada.

5. **Autorstvo – bez prerada**. Dozvoljavate umnožavanje, distribuciju i javno saopštavanje dela, bez promena, preoblikovanja ili upotrebe dela u svom delu, ako se navede ime autora na način odreen od strane autora ili davaoca licence. Ova licenca dozvoljava komercijalnu upotrebu dela.

6. **Autorstvo – deliti pod istim uslovima**. Dozvoljavate umnožavanje, distribuciju i javno saopštavanje dela, i prerade, ako se navede ime autora na način određen od strane autora ili davaoca licence i ako se prerada distribuira pod istom ili sličnom licencom. Ova licenca dozvoljava komercijalnu upotrebu dela i prerada. Slična je softverskim licencama, odnosno licencama otvorenog koda.

УНИВЕРЗИТЕТ У БЕОГРАДУ
ФИЗИЧКИ ФАКУЛТЕТ
Бр. 165/10
6. 4. 2022 год.
БЕОГРАД, СТУДЕНТСКИ ТРГ 12-16
П. ФАХ 44

На основу члана 29 Закона о општем управном поступку («Службени гласник РС» број 18/2016 и 95/2018), и члана 149 Статута Универзитета у Београду - Физичког факултета, по захтеву БОЈАНЕ БОКИЋ, дипломираног физичара, издаје се следеће

У В Е Р Е Њ Е

БОЈАНА БОКИЋ, дипломирани физичар, дана 4. априла 2022. године, одбранила је докторску дисертацију под називом

"ДИНАМИКА ПРОСТИРАЊА ЕИРЕЈЕВИХ СНОПОВА У ФОТОРЕФРАКТИВНИМ СРЕДИНАМА"

пред Комисијом Универзитета у Београду - Физичког факултета и тиме испунила све услове за промоцију у ДОКТОРА НАУКА – ФИЗИЧКЕ НАУКЕ.

Уверење се издаје на лични захтев, а служи ради регулисања права из радног односа и важи до промоције, односно добијања докторске дипломе.

Уверење је ослобођено плаћања таксе.

Република Србија * Универзитет у Београду - Физички факултет * Београд

ДЕКАН ФИЗИЧКОГ ФАКУЛТЕТА

Проф. др Иван Белча